ETP-KA/2019-18

Suche nach Zwei-Boson-Resonanzen im vollhadronischen Endzustand mit dem CMS-Detektor

Zur Erlangung des akademischen Grades eines

DOKTORS DER NATURWISSENSCHAFTEN

von der Fakultät für Physik
des Karlsruher Instituts für Technologie (KIT)

genehmigte

DISSERTATION

von

M.Sc. Daniela Schäfer
aus Karlsruhe

Referent:	P.D. Dr. Matthias Mozer
Korreferent:	Prof. Dr. Thomas Müller

Tag der mündlichen Prüfung: 6. Dezember 2019

Eidesstattliche Versicherung gemäß der Promotionsordnung des Karlsruher Instituts für Technologie (KIT) für die KIT-Fakultät für Physik:

1. Bei der eingereichten Dissertation zu dem Thema

   Suche nach Zwei-Boson-Resonanzen im vollhadronischen Endzustand mit dem CMS-Detektor

   handelt es sich um meine eigenständig erbrachte Leistung.

2. Ich habe nur die angegebenen Quellen und Hilfsmittel benutzt und mich keiner unzulässigen Hilfe Dritter bedient. Insbesondere habe ich wörtlich oder sinngemäß aus anderen Werken übernommene Inhalte als solche kenntlich gemacht.

3. Die Arbeit oder Teile davon habe ich bislang nicht an einer Hochschule des In- oder Auslands als Bestandteil einer Prüfungs- oder Qualifikationsleistung vorgelegt.

4. Die Richtigkeit der vorstehenden Erklärungen bestätige ich.

5. Die Bedeutung der eidesstattlichen Versicherung und die strafrechtlichen Folgen einer unrichtigen oder unvollständigen eidesstattlichen Versicherung sind mir bekannt.

Ich versichere an Eides statt, dass ich nach bestem Wissen die reine Wahrheit erklärt und nichts verschwiegen habe.

Karlsruhe, den 6. November 2019

. . . . . .

(Full name)

Zusammenfassung

Das Standardmodell (SM) der Teilchenphysik gehört, seit seiner Entwicklung in den sechziger Jahren des zwanzigsten Jahrhunderts, zu den erfolgreichsten und am genauesten vermessenen physikalischen Theorien. Mit seiner Beschreibung der drei fundamentalen Grundkräfte, der Elektromagnetischen-, Starken- und Schwachen-Kraft, können Wechselwirkungen zwischen Elementarteilchen mit erstaunlicher Präzision vorhergesagt werden. Die fundamentalen Kräfte des Standardmodells werden durch lokale Eichsymmetrien bestimmt, deren Übertragung von sogenannten Eichbosonen vermittelt wird. Mit diesen Prinzipien können elektromagnetische Wechselwirkungen zwischen geladenen Teilchen, radioaktive Zerfälle von Hadronen wie $\beta^{\pm}$ Zerfälle die über die Schwache-Kraft ablaufen, sowie die Vielfalt von Hadronen und Mesonen als aus Quarks zusammengesetzte Teilchen die von der Starken-Kraft zusammengehalten werden, erklärt werden. Im Jahr 2012 wurde das Higgs-Boson, der letzte bis dato nachgewiesene Baustein des Standardmodells, am Large Hadron Collider in Genf entdeckt. Damit wurde die Struktur des Standardmodells, die das Higgs-Feld zur Erhaltung der Eichsymmetrien benötigt, noch einmal auf beeindruckende Weise bestätigt. Trotz seines überwältigenden Erfolgs bleiben jedoch einige Fragen und Problemstellungen ungeklärt. Ein Beispiel hierfür ist die Tatsache, dass Gravitation nicht durch das Standardmodell beschrieben wird. Eine weitere Herausforderung für das Standardmodell ist die Frage, wie die gemessene Higgs Boson Masse von $125.10 \pm 0.14\,\text{GeV}$ [1], die stark von großen Schleifenkorrekturen abhängt, zustande kommt. Hier besteht die Möglichkeit das neue Phänomene, die bei Energien im TeV-Bereich auftreten, das Vakuum des Higgs-Feldes auf natürliche Art und Weise stabilisieren.

Diese und weitere Gründe motivieren die Suche nach Auswirkungen von theoretischen Modellen, die das Standardmodell in dem Versuch erweitern, die bekannten Schwächen auszubessern. Von besonderem Interesse sind hierbei Modelle die Gravitation als vierte Kraft ins Standardmodell integrieren, und gleichzeitig in der Lage sind, den großen Unterschied zwischen den Energieskalen von Gravitation und dem Elektroschwachen Sektor des Standardmodells zu erklären. Dies geschieht durch eine Erweiterung der uns bekannten Raum-Zeit durch eine weitere gekrümmte Dimension. Bekannte Representanten solcher Modelle sind Randall-Sumdrum (RS) Modelle [2–5], die die Existenz von neuen Spin-2 Resonanzen mit Massen im TeV-Bereich vorhersagen. Weitere wichtige Vertreter von theoretischen Erweiterungen des Standardmodells sind Modelle die den Elektroschwachen Sektor erweitern oder Modelle mit zusammengesetzten Higgs-Bosonen, in den letztgenannten werden neue geladene und ungeladene Spin-1 Resonanzen vorhergesagt [6–10].

Der Zwei-Boson-Zerfallskanal ist bei Suchen nach neuer Physik am Large Hadron Collider besonders interessant, da Einblicke in einen bis dato schwer zugänglichen Phasenraum ermöglicht werden bei gleichzeitiger hoher Sensitivität für verschiedenste theoretische Modelle. Im Fokus von Resonanz-Suchen nach neuer Physik liegen Studien mit geboosteten hadronischen Boson-Zerfällen. Diese bieten die höchsten Verzweigungsverhältnisse im Endzustand und ermöglichen daher einen vielversprechenden Einblick in von Erweiterungen des Standardmodells

favorisierte Phasenräume.

Ein wichtiger Aspekt dieser Suchen ist das Boson-Tagging, d.h. die Klassifizierung von Jets aus Vektorboson-Zerfällen und von Jets die von Untergrundprozessen erzeugt wurden. Für die Analyse der 2016 und 2017 vom Compact Muon Soleniod (CMS) Experiment aufgenommenen Daten, die in dieser Arbeit analysiert wurden, wurden Methoden des Boson-Taggings basierend auf der Untersuchung der Jet-Substruktur verwendet und optimiert. Eine wichtige Variable ist die sogenannte n-subjettiness, die die Kompatibilität eines gegebenen Jets mit n verschiedenen Jet-Achsen charakterisiert. Das Verhältnis von 2-subjettiness zu 1-subjettiness kann verwendet werden um Jets aus W- oder Z-Boson-Zerfällen von Untergrundprozessen zu unterscheiden. Eine weitere wichtige Variable im Boson-Tagging ist die Jetmasse, d.h. die invariante Masse der Konstituenten eines Jets, nachdem dieser von weitwinkligen und energiearmen Abstrahlungen befreit wurde.

Der im vollhadronischen Zwei-Boson-Zerfallskanal wichtigste Untergrundprozess sind Jets hervorgerufen von Prozessen der Qantenchromodynamik. Diese sind schwer mit theoretischen Modellen zu beschreiben, da farbgeladene Teilchen nicht frei vorkommen können. Es sind deshalb starke Abhängigkeiten der Simulation von Teilchenschauer und Hadronisierungsprozessen zu erwarten. Es werden deshalb datengetriebene Untergrundabschätzungen vorgenommen, um trotzdem verlässliche Modellierungen des Untergrunds zu erreichen. Hierfür wurde ein neuer multidimensionaler Maximum-Likelihood-Fit implementiert, der eine genauere Beschreibung der Standardmodell Untergründe erlaubt und Verbesserungen in der Sensitivität der Analyse von bis zu 30% zur Folge hat, wie in Abbildung 0.1 zu sehen.

Die Methode beruht auf einer Erweiterung herkömmlicher Suchmethoden nach Resonanzen in der invarianten Masse des rekonstruierten Zwei-Jet-Systems, auf zwei zusätzliche Dimensionen, die Massen der zwei Jets im Endzustand. Hiermit können die SM-Untergründe besser beschrieben werden, insbesondere die assoziierte SM-Produktion eines Vektorboson mit Jets, sowie Signale, die in allen drei Dimensionen resonant sind, können mit deutlich höherer Signifikanz nachgewiesen werden. Schon jetzt sind die mit der neuen Methode erreichten Ergebnisse von ähnlicher Signifikanz wie die Kombination [11] von allen Zwei-Boson-Zerfallskanälen basierend auf dem 2016 vom CMS Detektor aufgenommenen Datensatz. Die Ausschlussgrenzen als Funktion der Masse der hypothetischen neuen Resonanz sind in Abbildung 0.2 zu sehen. Die Abbildung zeigt die Ausschlussgrenzen auf den Produktionswirkungsquerschnitt für geladene und ungeladene Spin-1- und ungeladene Spin-2-Resonanzen für ein Konfidenzniveau von 95%. Die Ergebnisse werden mit Hilfe von zwei Modellen interpretiert: Dem Bulk Graviton Modell [5, 12] das zu den Randall-Sundrum Modellen gehört, sowie dem schweren Vektor-Triplett-Modell (HVT) [13], das die Phänomenologie vieler Modelle mit erweiterten elektroschwachen Sektoren beschreibt.

Die neue Methode erlaubt die gemeinsame Analyse der Kanäle WW, WZ, ZZ, WH, ZH, und HH oder sogar eine Verallgemeinerung auf Suchen nach exotischeren Teilchen, die in drei Vektorbosonen oder auch W(Z)X zerfallen, wobei X ein beliebiges, von neuen Theorien vorhergesagtes Teilchen ist. Somit besteht die Möglichkeit in Zukunft mit einer bereits erprobten Analysestrategie neue Phasenräume vollständig zu erschließen und auf Physik jenseits des SMs zu testen. Durch eine zukünftige Einbeziehung der 2018 aufgenommen Daten und eine Kombination verschiedener Zerfallskanäle kann somit eine noch nie zuvor erreichte Sensitivität in der Suche nach neuen Resonanzen erzielt werden.

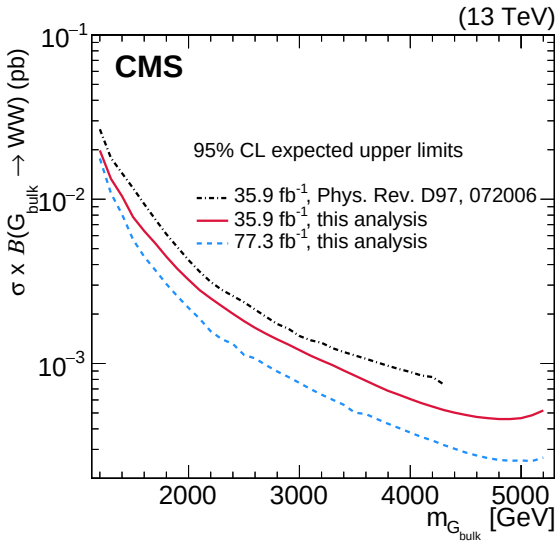

Abbildung 0.1.: Erwartete Ausschlussgrenzen auf das Produkt des Produktionswirkungsquerschnitts und des Verzweigungsverhältnisses mit einem Konfidenzintervall von 95% für die verbesserte Analyse-Methode dieser Arbeit (rot) verglichen mit der bisherigen Methode (schwarz) beruhend auf einer eindimensionalen Resonanz-Suche in der invarianten Zwei-Jet-Masse.

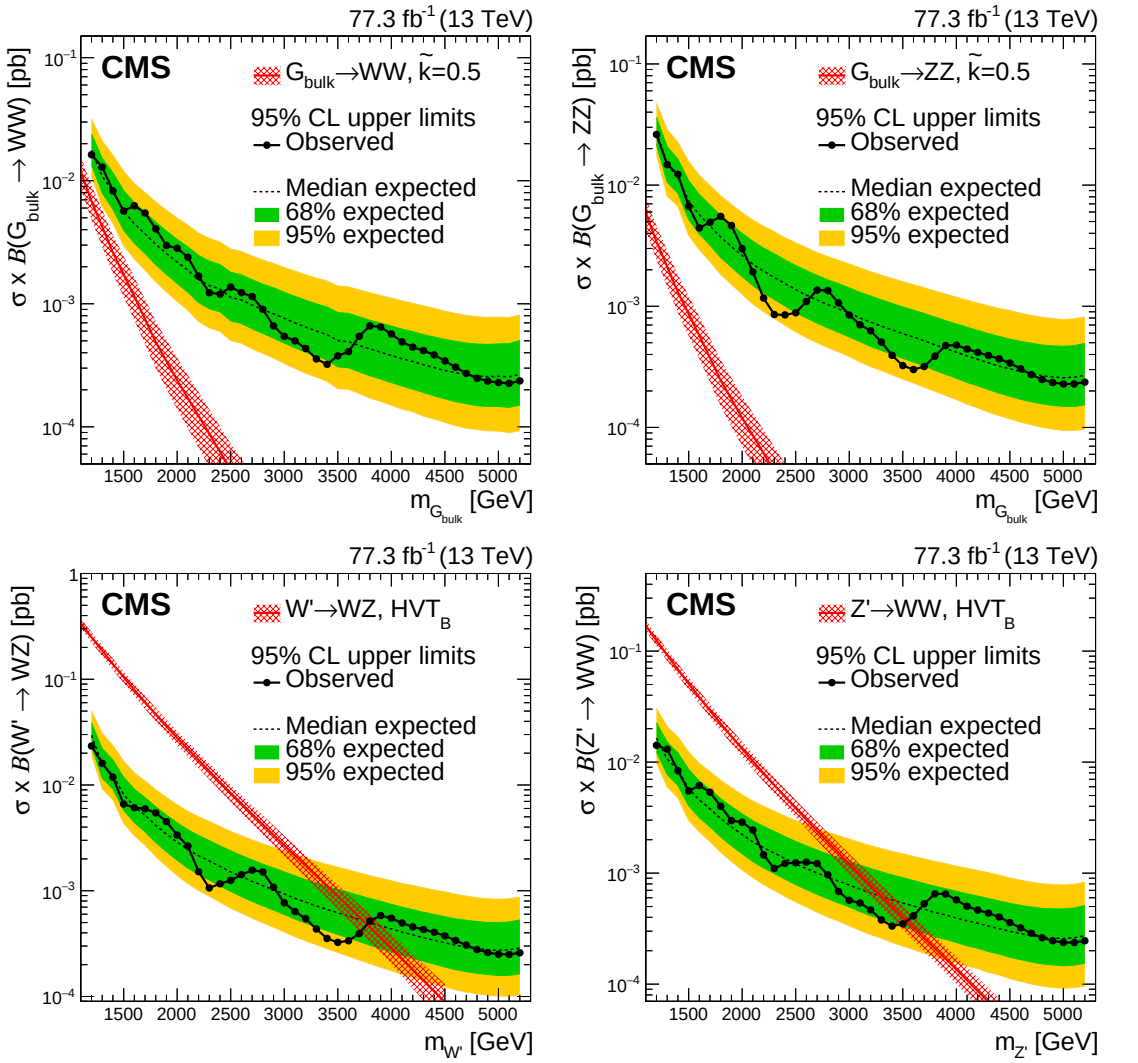

Abbildung 0.2.: Beobachtete (schwarz) und erwartete (gestrichelt schwarz) Ausschlussgrenzen auf den Produktionswirkungsquerschnitt mit einem Konfidenzintervall von 95% für Zwei-Boson Resonanzen im vollhadonischen Zerfallskanal. Die Unsicherheiten mit ein und zwei Standardabweichungen sind mit einem grünen und gelben Band eingezeichnete. Die rote Linie und der rot-gestrichelte Bereich zeigt den erwarteten Produktionswirkungsquerschnitt für die zum Vergleich herangezogenen Theoriemodelle, sowie die Unsicherheit dieses Wirkungsquerschnitts. Die Ausschlussgrenzen gelten für ungeladene Spin-2-Resonanzen die in zwei W-Bosonen zerfallen (links oben) sowie in zwei Z-Bosonen (rechts oben), als auch für geladen Spin-1-Resonanzen (links unten) und ungeladen Spin-1-Resonanzen (rechts unten).

Karlsruher Institut für Technologie

Search for Diboson Resonances in the Full-Hadronic Final State with the CMS Detector at $\sqrt{s}$ = 13 TeV

Zur Erlangung des akademischen Grades eines

DOKTORS DER NATURWISSENSCHAFTEN

von der Fakultät für Physik
des Karlsruher Instituts für Technologie (KIT)

genehmigte

DISSERTATION

von

M.Sc. Daniela Schäfer

aus Karlsruhe

Referent:	P.D. Dr. Matthias Mozer
Korreferent:	Prof. Dr. Thomas Müller

Tag der mündlichen Prüfung: 6. Dezember 2019

Abstract

A search for new resonances decaying to WW, WZ or ZZ in the all hadronic final state using 77.3 fb^{-1} of data taken with the CMS experiment at the CERN LHC at a center-of-mass energy of 13 TeV is presented. The search focuses on potential new particles with a mass at the TeV scale resulting in a high transverse momentum of the produced vector bosons. The subsequent decay products of the vector bosons are therefore highly collimated and reconstructed into a single large-radius jet, which are further classified using jet substructure methods. The analysis presented utilizes a new data-driven background modeling technique based on a template fit in a three-dimensional hyperspace spanned by the dijet invariant mass and the corrected jet masses of the two final state jets. This method allows the utilization of the full available signal yield while simultaneously constraining the background processes by including the mass sideband regions in the fit. This grants the opportunity to easily expand this framework to include VH, HH or more exotic signals with different messenger particles in the future.

No significant excess is observed above the estimated standard model background and limits are set at 95% confidence level on the cross section times branching fraction of a new particle, which are interpreted in terms of various models that predict spin-2 gravitons or spin-1 vector bosons. In a heavy vector triplet model, spin-1 Z' and W' resonances with masses below 3.5 and 3.8 TeV, respectively, are excluded at 95% confidence level. In a narrow-width bulk graviton model, upper limits on cross sections times branching fractions are set between 27 and 0.2 fb for resonance masses between 1.2 and 5.2 TeV, respectively. The limits presented in this thesis are the best to date in the dijet final state.

Introduction

Since its development in the 1960s, the Standard Model (SM) of particle physics has become the most successful and precise physical theory of all time. For all its merits, however, the SM is not without flaws in both phenomenology and theory. Prominent examples include the hierarchy problem, which introduces fine tuning of theory parameters, neutrino flavor mixing, which has been experimentally observed but is not described by the SM, and the absence of the fourth fundamental force of nature, gravity, in the SM.

As a consequence, even though SM predictions describe the data taken by generations of particle colliders very well, the general consensus within the particle physics community is that a multitude of new physical phenomena not described by the SM are expected to appear at high energy scales.

Since the spectacular discovery of the Higgs boson in 2012 at the Large Hadron Collider (LHC), a new data-taking period at a center-of-mass energy of $\sqrt{s} = 13$ TeV has begun in 2015, collecting data at energies never before reached in a laboratory. This opens new opportunities for searches of physical phenomena unexplained within the SM. Some interesting theories predict new resonances that decay with a high probability into two vector bosons, and have masses of a few TeV, which could be created in proton-proton (pp) collisions at the CERN LHC. Well-known representatives of such models are warped extra-dimensional models, which are able to include gravity into the framework of the SM. In this analysis, the bulk scenario of the Randall-Sundrum (RS) model [2–5], which predicts new spin-2 resonances, and the heavy vector triplet (HVT) framework [13], which serves as a generalization of models predicting spin-1 resonances, are considered.

No significant deviations from the SM background expectation have been observed previously in searches by the CMS and ATLAS collaborations for such particles decaying to two vector bosons, or to a vector boson and a Higgs boson [14–35]. The search presented here focuses on resonances with masses above 1.2 TeV, which decay into highly boosted vector boson pairs. Because of the large boost of the vector bosons, their decay products are merged into single, large-radius jets, leading to dijet final states. These jets are identified through dedicated jet substructure algorithms. Compared to previous analyses in this final state, an improved background estimation and signal extraction procedure based on a multi-dimensional maximum likelihood fit is employed, increasing the sensitivity of the analysis by up to 30% relative to previous methods. The method can be applied to any search with final states expected to cause resonant behavior in three observables, whereas previous methods used solely the invariant mass of the final decay products as the search variable.

The analysis is performed on a data set consisting of data collected by the CMS experiment during the 2016 and 2017 data taking periods, corresponding to a total integrated luminosity of 77.3 fb^{-1}.

This thesis is organized as follows: the first chapter provides the theoretical foundation and motivation for the search presented here. The second chapter introduces important concepts of statistical inference. Chapter three contains a brief description of the Large Hadron Collider and the Compact Muon Solenoid Detector, and chapter four is dedicated to the simulation and reconstruction of events. Chapter five describes a search for diboson resonances based on a novel multi-dimensional fit method. An outlook into the future of this analysis is given in chapter six.

Contents

1. Theoretical Foundations **3**
- 1.1. The Standard Model of Particle Physics . . . 3
  - 1.1.1. Particle Content . . . 4
  - 1.1.2. Gauge Symmetries . . . 5
- 1.2. Challenges of the Standard Model . . . 10
- 1.3. Extensions of the Standard Model . . . 12
  - 1.3.1. Warped Extra Dimensional Models . . . 12
  - 1.3.2. Heavy Vector Triplet Models . . . 16
- 1.4. Current Status of Diboson Resonance Searches at the LHC . . . 19

2. Statistical Inference **25**
- 2.1. Basic Principles . . . 25
- 2.2. Maximum Likelihood Estimation . . . 26
- 2.3. Template Morphing . . . 26
- 2.4. Hypothesis Tests . . . 27
- 2.5. Goodness-of-Fit Tests . . . 28
- 2.6. Systematic Uncertainties . . . 29
- 2.7. Exclusion Limits . . . 30
  - 2.7.1. The Test Statistic . . . 30
  - 2.7.2. CLs Limits . . . 31
  - 2.7.3. Asymptotic Approximation . . . 31

3. The Large Hadron Collider and the Compact Muon Solenoid Detector **33**
- 3.1. The Large Hadron Collider . . . 33
- 3.2. The Compact Muon Solenoid Experiment . . . 37
  - 3.2.1. Tracker . . . 38
  - 3.2.2. Calorimeters . . . 40
  - 3.2.3. Muon System . . . 43
  - 3.2.4. Trigger and Data Acquisition . . . 44
  - 3.2.5. Computing Infrastructure . . . 45

4. Event Reconstruction and Simulation **47**
- 4.1. Characteristics of Proton-Proton Collisions . . . 48
  - 4.1.1. Hard Process . . . 48
  - 4.1.2. Underlying Event . . . 49
  - 4.1.3. Parton Distribution Functions . . . 50
  - 4.1.4. Pileup . . . 50
  - 4.1.5. Parton Showers and Hadronization . . . 51
  - 4.1.6. Monte Carlo Event Generators . . . 52

4.2. Event Reconstruction . . . 54
4.2.1. Track Reconstruction . . . 54
4.2.2. Vertex Reconstruction . . . 55
4.2.3. Energy Reconstruction . . . 55
4.2.4. Long-Lived Leptons . . . 55
4.2.5. Photons, Charged Hadrons and Neutral Hadrons . . . 56
4.2.6. Missing Transverse Momentum . . . 56
4.2.7. Jets . . . 57

5. Search for Diboson Resonances in the Full-Hadronic Final State 69
5.1. Analysis Strategy . . . 69
5.1.1. Event Topology . . . 71
5.1.2. Selection and Reconstruction of Events . . . 75
5.1.3. V-tagging . . . 84
5.2. Signal Modeling . . . 87
5.3. Background Modeling . . . 94
5.3.1. Modeling of the QCD Multijet Background . . . 94
5.3.2. Alternative Background Shapes . . . 97
5.3.3. Modeling of the Subdominant Backgrounds . . . 106
5.4. Systematic Uncertainties . . . 114
5.4.1. Normalization Uncertainties . . . 114
5.4.2. Shape Uncertainties . . . 116
5.5. Closure and Bias Tests . . . 119
5.5.1. Tests in a Data Control Region . . . 119
5.5.2. Variations of the QCD Multijet Prediction . . . 120
5.5.3. Bias Tests in Pseudo-data . . . 126
5.6. Results . . . 130
5.6.1. Statistical Interpretation . . . 130
5.6.2. Exclusion Limits . . . 133

6. Conclusion and Outlook 141

A. Appendix: Data Sets and MC Samples 145

B. Appendix: Cross Checks for the Signal Modeling 149

C. Appendix: Post-Fit Results in the LPLP Data Sideband 159

D. Appendix: Tests of the Fitting Procedure 165

E. Appendix: Results of a previous Diboson Search Utilizing a Different Background Estimation Method with 35.9 fb^{-1} of Data Recorded in 2016 175

List of Figures 183

List of Tables 186

Bibliography 187

1. Theoretical Foundations

As in any scientific endeavour, experimental particle physics needs a theoretical prediction to fully interpret its complex measurements. In high energy particle physics the theory describing the free behavior and interactions of fundamental particles is the *standard model* of particle physics (SM). Since its development in the 1970s it has been one of the most powerful theories in physics. Although the SM provides astoundingly precise predictions for three fundamental interactions – electromagnetism, strong and weak interaction – it is widely believed that the SM might only be an effective theory valid at relatively low energy scales, while physics at the Planck scale (10^{19} GeV) might be described by a different more encompassing theory. In this chapter, a brief introduction into the theoretical foundations on which this thesis is built is given. The first Section gives a brief introduction to the SM. In the second Section the idea of new phenomena beyond the SM is motivated. The third Section gives an overview of possible extensions of the SM that are relevant for this thesis, as well as their phenomenological predictions for the research program of the Large Hadron Collider (LHC). For brevity natural units are used throughout this thesis, i.e., $\hbar = c = 1$.

1.1. The Standard Model of Particle Physics

The SM of particle physics is a theoretical model, which is able to mathematically describe the behavior of elementary particles with astounding precision. It contains three fundamental interactions: the electromagnetic, weak, and strong force with associated mediator bosons, as well as a number of elementary particles, the behavior of which is completely governed by the charge they carry under any of the fundamental interactions, their mass and their spin. The SM is a quantum field theory (QFT) that is formulated using the principle of least action, thus all interactions between fundamental particles can in principle be described by

$$\delta S = \delta \int \mathrm{d}^4x \; \mathcal{L}_{\mathrm{SM}}(\phi, \partial_\mu \phi) = 0, \tag{1.1}$$

where $\mathcal{L}_{SM}$ is the Lagrangian density of the SM which will be discussed in a little more detail in the following sections and ϕ is a stand-in for the fields of the SM. For now two things are important to note: firstly the mathematical formulation allows for the identification of conserved quantities as symmetries of the Lagrangian, or conversely, the formulation of the Lagrangian will be governed by symmetry arguments, and secondly the equations of motion for the SM Lagrangian cannot be solved, instead particle physics must rely on a perturbation series approach for practical calculations.

To ensure invariance under Lorentz-transformations, the Poincaré group is included as a *global* symmetry of the SM, i.e., the SM Lagrangian density $\mathcal{L}_{\mathrm{SM}}$ is invariant under global coordinate

transformations of the Poincaré group. The Poincaré group includes rotations, Lorentz-boosts, and translation in time and space, giving rise to the familiar energy, momentum and angular momentum conservation. However, a trademark of quantum field theories is their relationship to *local* coordinate transformations, which are called *gauge transformations*. Each of the three aforementioned interactions will be described by an invariance under a gauge transformation giving rise to "mediator particles", the bosons. Apart from the gauge bosons, the SM contains twelve "matter particles". In the context of quantum field theories, a "particle" is actually an excitation of a field, which in turn is an operator assigning values to each point in the four-dimensional space-time. In Section 1.1.1 the particle content of the SM will be briefly described while the significance of gauge transformations will be discussed in more detail in Section 1.1.2.

1.1.1. Particle Content

Fermions

The fermions are particles with spin 1/2, thus governed by the Pauli-principle. The SM contains twelve different fermion flavors, however it does not make a clear prediciton of how many such particles must be included. They are arranged into groups and families according to their charges belonging to the fundamental gauge symmetries of the SM and in generations according to an increase in the masses of the particles. The grouping of particles according to their weak isospin and electric charge as shown in table 1.1 and 1.2 is customary even though the weak and electromagnetic interactions are a low energy approximation of a combined electroweak force. Since the second and third generations are unstable, all matter in the universe consists of particles of the first generation. There is also an associated antiparticle for each particle, with the same mass but opposite charges. For brevity only the particles and not the antiparticles are listed in the tables.

The *quarks*, which are shown in Table 1.1 couple to all three interactions and are arranged in pairs of two according to their charges mandated by the weak and electromagnetic force and in three generations according to their increasing mass. Quarks can carry three different *colors*, their charge generated by the strong force, which is ommitted in the table in this simplified depiction. Due to a property of the strong interaction, color-charged states cannot exist freely, instead only color-neutral bound states called *hadrons* can be found in nature.

A second kind of fermions called *leptons* are grouped in a similar way in generations according to their mass and in pairs according to their weak and electromagnetic charge. They are listed in Table 1.2. Neutrinos are the only fermions that couple to the weak force exclusively.

Bosons

Particles with an integral spin are called bosons. The SM contains the mediator bosons and the Higgs boson as elementary particles with integral spin. The mediators of the fundamental forces that arise naturally from the mathematical structure of the SM are spin-1 particles,

while the Higgs boson (H) has a spin of zero. There are the photons (γ) that mediate the electromagnetic interaction, the W and Z bosons (in this thesis the shorthand V bosons is used whenever a W or Z bosons is meant) that govern the weak interaction, which describes radioactive decays, and the gluons that belong to the strong force, which governs the formation of composite particles such as neutrons or protons. An overview of the gauge bosons of the SM is shown in Table 1.3. There is also the Higgs boson which is not a mediator of a fundamental force, however the couplings to the Higgs field give rise to the spontaneous symmetry breaking of the electroweak force into the electromagnetic and weak force and are the origin of fermion masses and the masses of the weak bosons.

1.1.2. Gauge Symmetries

As mentioned before, there are a number of local coordinate transformations that have a special meaning within the SM. A local symmetry means that the transformation acting on the fields depends on the position in space-time, while the Lagrangian must still be invariant under the transformation. A gauge transformation therefore relates two field configurations

Table 1.1.: The quark content of the SM, the listing includes the mass, electric charge and the third component of the weak isospin T^3, values taken from Ref. [1]. The values for the electric charge are given in units of $e = 1.602 \cdot 10^{-19}$ C.

		Mass	**Electric Charge**	**Weak Isospin T^3**
		1. Generation		
up	(u)	2.2 ± 0.6 MeV	$+2/3$	$+1/2$
down	(d)	4.7 ± 0.5 MeV	$-1/3$	$-1/2$
		2. Generation		
charm	(c)	1.28 ± 0.03 GeV	$+2/3$	$+1/2$
strange	(s)	96 ± 8 MeV	$-1/3$	$-1/2$
		3. Generation		
top	(t)	173.1 ± 0.6 GeV	$+2/3$	$+1/2$
bottom	(b)	4.18 ± 0.04 GeV	$-1/3$	$-1/2$

Table 1.2.: The lepton content of the SM, the listing includes the mass, electric charge and the third component of the weak isospin T^3, values taken from Ref. [1]. The values for the electric charge are given in units of $e = 1.602 \cdot 10^{-19}$ C.

		Mass	**Electric Charge**	**Weak Isospin T^3**
		1. Generation		
electron neutrino	(ν_e)	< 1 keV	0	$+1/2$
electron	(e)	0.5 MeV	-1	$-1/2$
		2. Generation		
muon neutrino	(ν_μ)	< 1 keV	0	$+1/2$
muon	(μ)	105.658 MeV	-1	$-1/2$
		3. Generation		
tauon neutrino	(ν_τ)	< 1 keV	0	$+1/2$
tauon	(τ)	1.776 GeV	-1	$-1/2$

that result in the same physical observables. In fact, each of the fundamental interactions is completely determined by picking a symmetry group, and requiring the Lagrangian density to be invariant under local coordinate transformations of this symmetry group. This automatically leads to the introduction of *gauge fields* that determine the interactions between matter fields depending on what representation of the symmetry group they belong to.

The full symmetry group of the SM is $\mathrm{SU(3)_C \times SU(2)_L \times U(1)_Y}$ with the group $\mathrm{U}(n)$ generated by unitary $n \times n$ matrices, and the group $\mathrm{SU}(n)$ containing all hermitian traceless matrices M with $\det(\mathrm{M}) = 1$. All these symmetries are Lie groups which can be described by a Lie algebra of the form

$$[T^a, T^b] = f^{abc} T^c \ , \tag{1.2}$$

with the group generators T and the structure constants f^{abc}. In case of the symmetry group SU(2), the generators are more commonly known as the Pauli matrices $\sigma_a = 2T^a$, for SU(3) they are known as the Gell-Mann matrices λ_a. Each gauge symmetry leads to a conserved charge and a number of gauge fields equal to the number of generators of the underlying symmetry group.

In the end, the SM Lagrangian density consists of two different parts, a part $\mathcal{L}_{\text{free}}$ that is quadratic in the matter fields and accounts for the "free" propagation of the matter field in space-time, and a part containing at least three fields, the interaction Lagrangian $\mathcal{L}_{\text{int}}$ that accounts for field interactions. Once the interaction part $\mathcal{L}_{\text{int}}$ is added the Lagrangian cannot be solved analytically without approximation. In many cases, notably in calculations for scattering experiments, the interaction Lagrangian can be perturbatively expanded since the couplings relating the strength of the interactions are small. The terms in this perturbation series can be written down pictorially as *Feynman diagrams*, which also serve as an assistance for calculations, as well as visual representations.

The SM has the additional peculiarity that it contains a series of ultraviolet (UV) divergences that have to be dealt with. This is done using regularization, a mathematical recipe to parameterize the divergences, and renormalization, a procedure to relocate the divergences into counter-terms. In principle this means that QFTs can predict the evolution of the behavior of the particles between two energy scales, but can make no absolute predictions at one particular scale. This procedure leads to the introduction of a *renormalization scale*, which is an artificial scale entering the calculations during renormalization and is in principle unphysical, i.e., the obervables of the theory do not depend on this scale. However, since the calculations are only approximate and the perturbation series is only calculated up to a fixed order of perturbation theory, the calculated observables might still have a residual

Table 1.3.: The boson content of the SM, the listing includes the mass, charge and spin, values taken from Ref. [1].

		Mass	**Charge**	**Spin**
Higgs boson	(H)	125.09 ± 0.24 GeV	$\pm 1/2$ isospin	0
W boson	($\mathrm{W}^{\pm}$)	80.385 ± 0.015 GeV	± 1 electric charge, ± 1 isospin	1
Z boson	(Z)	91.188 ± 0.002 GeV	0	1
photon	(γ)	0	0	1
gluon	(g)	0	color charge	1

dependence on the renormalization scale. This is mitigated in parts by choosing this scale in a meaningful way for each scattering process.

In addition to the UV divergences, QFTs contain also infrared (IR) divergences, which arise in the limit of zero momentum of massless particles. These divergencies consist of two parts, either there is a massless particle of essentially zero momentum in a loop, or a zero momentum massless particle is radiated. The sum of all IR divergent contributions, however, is again finite. One can think about this as follows: since in a given process there is always the possibility of emitting a particle with low energy (soft), which is virtually indistinguishable from the same process without the emission of a soft particle. For an exhaustive calculation of any process these emissions have to be considered for any physical result. Practically, these divergencies can be removed by introducing a cutoff scale called *factorization scale*, which can be thought of as considering the finite resolution of any experimental setup.

Free Lagrangian

Starting from the principle of least action, the Euler-Lagrange equations for the Lagrangian density can be derived

$$\partial_\mu \frac{\partial \mathcal{L}}{\partial(\partial_\mu \phi)} - \frac{\partial \mathcal{L}}{\partial \phi} = 0 \ , \tag{1.3}$$

with the space-time derivative $\partial_\mu = \frac{\partial}{\partial x^\mu}$. These equations can be solved for the free part of the SM Lagrangian resulting for example in equations of motion for spin-1/2 fermions

$$i\partial\!\!\!/ \Psi - m\Psi = 0 \ , \tag{1.4}$$

with the particle field Ψ and $\partial\!\!\!/ = \gamma_\mu \partial^\mu$, where γ_μ are the gamma matrices. Equation (1.4) is called the Dirac equation and is solved by the fermion fields

$$\Psi(x) = \int \frac{\mathrm{d}^3 k}{(2\pi)^3} \sum_s \left(e^{ikx} v_s(\vec{k}) b_s^\dagger(\vec{k}) + e^{-ikx} u_s(\vec{k}) a_s(\vec{k}) \right) \ . \tag{1.5}$$

The operators a_s ($b_s^\dagger$) annihilate (create) a particle (antiparticle) excitation of the field with spin s, momentum k, and two component spinor u_s (v_s).

Very similarly, the equation of motion for a spin-0 field, in the SM Lagrangian this would be the Higgs field, can be obtained. It is called the Klein-Gordon equation

$$\partial_\mu \partial^\mu \Phi + m^2 \Phi = 0 \ , \tag{1.6}$$

and has the solutions

$$\Phi(x) = \int \frac{\mathrm{d}^3 k}{(2\pi)^3} \left(e^{ikx} \frac{a^\dagger(\vec{k})}{2k^0} + e^{-ikx} \frac{a(\vec{k})}{2k^0} \right) \ , \tag{1.7}$$

where the operators $a(\vec{k})$ ($a^\dagger(\vec{k})$) again annihilate (create) a particle with momentum k. Fermions posses an additional property called *chirality*, which is directly related to the representation of the spinor in the Poincaré group. The Dirac-spinors in equation (1.5) can be projected on a subspace of right-, and left-handed spinors $\frac{(1\pm\gamma_5)}{2}\Psi = \Psi_{\mathrm{R/L}}$. The *helicity* is determined by the projection of the spin along the momentum of the particle, this is therefore not a well-defined quantity for massive particles. However, chirality and helicity are the same for massless particles.

Electroweak Interaction

The electroweak interaction is more familiar in its low energy form (energies below the W boson mass) where it seemingly splits into two distinct forces: the electromagnetic interaction and the weak interaction, governing radioactive decays [36, 37]. This form is only reached after the symmetry breaking triggered by the Higgs mechanism [38, 39]. Before the symmetry breaking, two unbroken gauge symmetries for the groups $\mathrm{SU(2)_L \times U(1)_Y}$ form the electroweak interaction terms. The non-abelian nature of this symmetry group leads to the appearance of interactions between the gauge bosons themselves in the form of triple and quartic couplings. The interaction Lagriangian for the electroweak force is

$$\mathcal{L}_{\text{weak}} = -\frac{1}{4}\left(F^a_{W,\mu\nu}F^{a,\mu\nu}_W\right) + \sum_{\text{generations}} \bar{I}_{\mathrm{L}} \not{D} I_{\mathrm{L}} \ , \tag{1.8}$$

$$D_\mu = \partial_\mu - \frac{ig}{2} W^a_\mu \sigma^a \ , \tag{1.9}$$

$$F^a_{W,\mu\nu} = \partial_\mu W^a_\nu - \partial_\nu W^a_\mu + g\epsilon^{abc} W^b_\mu W^c_\nu \ , \tag{1.10}$$

$$\mathcal{L}_{\mathrm{Y}} = \frac{1}{4} B_{\mu\nu} B^{\mu\nu} + \sum_{\text{flavors, generations}} \bar{\Psi} \not{D} \Psi \ , \tag{1.11}$$

$$D_\mu = \partial_\mu + ig' Y B_\mu \ , \tag{1.12}$$

$$B^a_{\mu\nu} = \partial_\mu B_\nu - \partial_\nu B_\mu \ , \tag{1.13}$$

where W^a and B^a are the gauge fields, g and g' the coupling constants, σ^a the three generators of SU(2) and Ψ are the fermion fields. The quantity I is an SU(2) doublet containing two matter fields Ψ in the combination of one up- and one down-type quark, or one charged lepton and one neutrino. The charge Y is called the hypercharge, while the charge belonging to the generators of $\mathrm{SU(2)_L}$ is called isospin. This interaction has a different coupling behavior for left- and right-handed fields. The vector triplet W^a only couples to left-handed fields, while B^a couples to right- and left-handed fields, however, the hypercharges of left-handed fields is different to those of right-handed fields. After the spontaneous symmetry breaking a massive mediator boson triplet emerges, the $\mathrm{W^{\pm}}$ bosons, which couple only to left-handed fermions and right-handed anti-fermions, the Z boson, which couples to both chiralities with different coupling strengths, and one massless mediator boson, the photon (γ), which couples to both chiralities equally.

Spontaneous Symmetry breaking and the Higgs Boson

One of the major accomplishments of the recent years was the discovery of the Higgs boson in 2012. This field was initially introduced in the 1960s in order to allow the unification of electromagnetic and weak force at energy scales above m_{W}, which solved the issue of the massive weak mediator bosons breaking their gauge symmetry. Another challenge was the Dirac mass term for fermions, which also breaks the gauge symmetry of the weak force. In order to resolve these issues, the Higgs mechanism was proposed in 1964 [39] to break the exact gauge symmetries of the electroweak force into a residual U(1) gauge symmetry corresponding to electromagnetism and the weak force with massive mediator bosons. The mechanism is introduced via a new scalar field ϕ, which is also an isospin doublet, and has

a special potential term such that its ground state has a non-vanishing vacuum expectation value. The Higgs Lagrangian is

$$\mathcal{L}_{\text{Higgs}} = (D^\mu \phi)^\dagger D_\mu \phi + \mu^2 \phi^\dagger \phi - \lambda (\phi^\dagger \phi)^2 \ , \tag{1.14}$$

$$D_\mu = \partial_\mu - \frac{ig}{2} \tau^a W_\mu^a + i \frac{g'}{2} B_\mu \ , \tag{1.15}$$

with the Higgs field ϕ. This potential leads to ground states of the form of $\phi_0 = (0, v/\sqrt{2})^T$, with the vacuum expectation value $v/\sqrt{2}$. The complex field can be parameterized as

$$\phi = \begin{pmatrix} \phi_+ \\ \frac{v+H+i\varphi_z}{\sqrt{2}} \end{pmatrix} \ , \tag{1.16}$$

around its ground state with the two real fields H, φ_z and the complex field ϕ_+. The parameterization is chosen in order to emphasize the ground state ϕ_0 and allow for an approximation of small excitations around the ground state. The quantities λ and μ are constant parameters of the theory and it immediately follows $v = \mu/\sqrt{\lambda}$. The ground state of the Lagrangian breaks the $\mathrm{SU(2)_L} \times \mathrm{U(1)_Y}$ gauge symmetry of the electroweak force to a residual U(1) symmetry, effectively leaving one massless U(1) gauge boson and three massive gauge bosons, the $\mathrm{W}^\pm$ and Z bosons absorbing the degrees of freedom contained in ϕ_+ and ϕ_z in the process [40].

The gauge boson for this residual U(1) symmetry is known as the photon γ and it is a mixed state of both B and W^3 fields. The W and Z bosons arise from a mixture of the W^μ and B^μ fields parameterized with the Weinberg angle, or weak mixing angle $\sin\theta_\mathrm{W} = \frac{g'}{\sqrt{g^2+g'^2}} \approx 0.47$ [1] and the masses $m_\mathrm{W} = vg/2$ and $m_\mathrm{Z} = v\sqrt{g^2+g'^2}/2$. The Higgs boson (H) also carries a mass $m_\mathrm{H} = 2|\mu^2|$.

Quantum Chromodynamics

The interaction determining the formation of hadrons is the strong force. It is introduced via an $\mathrm{SU(3)_C}$ gauge symmetry with *color* as charge, thus explaining its name *quantum chromodynamics*. The Lagrangian density for this interaction can be written as

$$\mathcal{L}_\mathrm{QCD} = -\frac{1}{4} \left(F_{G,\mu\nu}^a F_G^{a,\mu\nu} \right) + \sum_{\text{quark flavors}} \bar{q}_i \not{D}_{ij} q_j \ , \tag{1.17}$$

$$D_{\mu,ij} = \partial_\mu \delta_{ij} - ig G_\mu^a T_{ij}^a \ , \tag{1.18}$$

$$F_{G,\mu\nu}^a = \partial_\mu G_\nu^a - \partial_\nu G_\mu^a + g f^{abc} G_\mu^b G_\nu^c \ , \tag{1.19}$$

with the gauge fields G, the quark spinor fields q, and the strong coupling g. The indices a, b, and c sum over the eight generators of the group, and the indices i and j denote the quark colors. A non-abelian gauge group like SU(3) gives rise to self couplings of the gauge fields, which leads to triple and quadruple vertices in the Feynman rules for QCD. The gauge bosons of the strong force, generally referred to as gluons, remain massless after the spontaneous symmetry breaking of the Higgs field. However, because of the special non-abelian structure of QCD, the strong coupling constant α_s, which is proportional to g^2 in first order perturbation theory, grows smaller at high energies and larger at small energies,

leading to the two phenomena of asymptotic freedom and confinement. Consequently at high energies or small distances, the quarks can be approximated as almost free particles (asymptotic freedom). At low energies or large distances, the interaction strength between colored particles increases, which ultimately leads to the confinement of color charges within a colorless object. When the coupling α_s grows too large, calculations via a perturbative approach are no longer valid, which makes the analytical calculation of the formation of hadrons impossible.

Fermion Mass Terms and the CKM Matrix

The last ingredient for the full SM Lagrangian are the mass terms for fermions, which are believed to originate from the symmetry breaking through a coupling to the Higgs field [41]. The (Dirac) mass terms for the SM fermions are

$$\mathcal{L}_{\text{Yukawa}} = -\bar{l}_{\text{L}}\phi Y_l l_{\text{R}} - \bar{q}_{\text{L}} Y_d \phi d_{\text{R}} - \bar{q}_{\text{L}} i\sigma_2 \phi^* Y_u u_{\text{R}} + h.c. \,, \tag{1.20}$$

where Y_i are the Yukawa couplings, q contains the left-handed quarks, and d_{R} (u_{R}) contain the right-handed down- (up)-type quarks, while l_{L} contains the left-handed leptons in an SU(2) doublett and l_{R} contains right-handed leptons in an SU(2) singlett. The Yukawa couplings are matrices in flavor space that are in general not diagonal, and in the SM up- and down-type Yukawa matrices cannot be diagonalized simultaneously. This gives rise to flavor-changing charged currents via the electroweak $\text{W}^{\pm}$ bosons proportional to the CKM [1] matrix elements [42] with $U_{\text{CKM}} = U_{\text{L},u} U_{\text{L},d}^{\dagger}$, where $U_{\text{L},u/d}$ is the unitary transformation matrix diagonalizing the u/d Yukawa matrix from the left side. In the SM neutrinos are massless, since the above terms do not introduce a mass term for neutrinos, and the SM does not require the existence of right-handed neutrinos. However, the observed mixing between neutrino flavors suggests that neutrinos do indeed have masses and a mixing matrix similar to the CKM matrix has to be introduced. This is, however, not part of the SM.

1.2. Challenges of the Standard Model

So far most experimental findings show an exceptional agreement with theoretical predictions from the SM. However, in addition to small disagreements in some observables, as for example found in the properties of B mesons, there are some open questions for which the SM has only unsatisfactory or sometimes no solutions to offer. These challenges lead to the conjecture that the SM is not the final theory describing particle interactions, but rather might be a low energy approximation of a larger, more encompassing theory. The challenges listed here are by no means exhaustive.

The Hierarchy Problem exists in two forms. One is connected with the small value of the Higgs boson mass, which is around 125 GeV. Self-energy corrections to the Higgs boson mass introduce divergent terms proportional to the square of the cut-off scale Λ. In

[1] CKM stands for Cabibbo, Kobayashi and Maskawa, after the physicists who first suggested to introduce a quark mixing matrix.

order to ensure a Higgs boson mass as found in measurements, some SM parameters have to be *fine-tuned* to orders of magnitude. This is not an unsolvable shortcoming of the SM, but rather a stretch of its plausibility. The other form of the hierarchy problem lies in the question why gravity is so much weaker than the other forces, or alternatively formulated why is $\frac{M_{\mathrm{W}}}{M_{\mathrm{Pl}}} \approx 10^{-16}$ so small. It is important to note here that although these two problems are connected, i.e., a closer gap between the Planck scale and the electroweak scale could resolve the fine tuning problem of the Higgs boson mass, a theory introducing a solution to the fine-tuning does not automatically answer the second hierarchy question.

Gravitation is not included in the SM as of yet. For typical particle interactions at low energies gravity can be neglected since it is much smaller than the other fundamental forces that are included in the SM. However, it stands to argue that a complete theory should also contain a description of the fourth fundamental interaction at particle level [43].

Grand Unification [44–46] is the idea that the fundamental forces might all be one unified force at sufficiently high energies. The idea is fueled by the unification of the weak and electromagnetic forces above the electroweak breaking scale, as well as the running of the couplings which almost suggests a grand unification at some higher energy. This is not so much a shortcoming of the SM as a beautification to satisfy a sense of elegance.

Dark Matter and Dark Energy [47–49] are necessary to explain astrophysical measurements within the existing framework. Dark matter, which is basically an invisible matter that only weakly interacts with known SM particles, is for example needed to describe the measured rotational curves of galaxies and galaxy clusters or gravitational lensing effects, which cannot be explained with the mass of visible matter alone. From these astrophysical measurements it can be inferred that about 27% [50] of the energy density of the universe consists of dark matter. Dark energy is also not directly observed but rather inferred from the measured accelerated expansion rate of the universe and cosmological models. As for dark matter, there is no explanation in the SM for dark energy, which is expected to make up around 68% [50] of the energy density of the known universe.

Neutrino Flavour Oscillations [1, 51] are another well-measured phenomenon that is not explained within the SM, since neutrinos in the SM are assumed to be massless. However, it is possible to incorporate neutrino masses into the SM by introducing right-handed neutrinos and a standard Dirac-mass term. This approach cannot explain the actual large measured numbers on the mixing angles or the small size of the neutrino masses compared to any other SM particles.

The Baryon Asymmetry of the Universe [52–54] is also unexplained within the SM. Predictions from Big Bang models assume the creation of equal amounts of matter and antimatter, which is a strong contrast to the observed imbalance between those two types of matter today. The mechanism behind this imbalance resulting in a matter-dominated universe is called baryogenesis. There are some processes in the SM which violate CP symmetry and can therefore contribute to the imbalance but the magnitude of these processes is too small to explain the observed imbalance between matter and

antimatter in the universe.

1.3. Extensions of the Standard Model

There are a multitude of theories that extend the SM in various ways in order to address some or all of the challenges discussed in the previous section. Depending on the particular model, different phenomenological predictions emerge that can be addressed by experimental searches at the LHC. In this work the main focus lies on new phenomena that lead to the resonant production of a new particle X, which decays to a large extent into SM vector bosons. Models that predict such resonances, and are used in the search presented in this thesis, are discussed in more detail in this section.

1.3.1. Warped Extra Dimensional Models

The theory models containing warped extra dimensions (WED) discussed in this thesis follow the Randall-Sundrum approach [2–5]. WED models incorporate a form of quantum gravity into the quantum field theory of the SM, and are able to provide solutions to the hierarchy problem and the flavor puzzle of the SM at the same time. Randall-Sundrum models introduce a fifth compact extra dimension with a curvature k and two *branes* of four dimensional Minkowski space-time that are connected via the fifth dimension. The compact extra dimension is also called the *bulk*.

WED models of the Randall-Sundrum kind extend the 3+1-dimensional Minkowski space to a five-dimensional space with the metric g_{MN}, with the two indices M, N running from 0 to 4. Using the five-dimensional Einstein equations in vacuum

$$R_{MN} - \frac{1}{2} R g_{MN} = 0 \ , \tag{1.21}$$

where R_{MN} is the Ricci tensor and $R = R^M_M$ is the Ricci scalar. The line segment of the five-dimensional metric is derived as

$$\mathrm{d}s^2 = e^{-2kL|\phi|} \eta_{\mu\nu} \mathrm{d}x^\mu \mathrm{d}x^\nu + L^2 \mathrm{d}\phi^2 \ . \tag{1.22}$$

Here ϕ parameterizes the extra dimension and $\eta_{\mu\nu}$ is the Minkowski metric, while L is the radius of the extra dimension and k its curvature. Curvature in this scenario can only be understood in a purely mathematical sense, where it is closely connected to the second derivative of a path with respect to its parameters [55].

The classical five-dimensional action is

$$S = S_{\text{Gravity}} + S_{\text{Matter}} = S_{\text{TeV}} + S_{\text{Planck}} + S_{\text{Bulk}} + S_{\text{Matter}} \ , \tag{1.23}$$

with the action of matter fields S_{Matter}, and the action for gravity split in three parts, the action of the gravity field in the bulk S_{Bulk} and the two parts of the gravitational action $S_{\text{TeV/Planck}}$ confined to the TeV or Planck brane see Ref. [56]. Starting from this five-dimensional action a

four dimensional effective action can be derived by integrating over the finite fifth dimension. This leads to an effective suppression of five-dimensional quantities with an exponential *warp factor* given by

$$w_f = e^{-2\pi kL} \ . \tag{1.24}$$

This leads to an exponential suppression of gravity at the TeV scale. The same exponential suppression can be reached for the five-dimensional Higgs vacuum expectation value v_0 if the SM Higgs potential is plugged into the five-dimensional action and confined to the TeV brane. Given

$$kL \approx 11 \ , \tag{1.25}$$

the hierarchy problem of the SM is solved. However, in principle k and L are free parameters of the theory.

Models of this kind introduce new resonances with interesting features. These resonances are the excitation modes of the five-dimensional metric g_{MN}. They can be decomposed into two different excitations

$$\delta g_{MN} = \begin{pmatrix} h(\phi,x)_{\mu\nu} & \vec{0} \\ \vec{0} & h(\phi,x)_5 \end{pmatrix} \ , \tag{1.26}$$

a spin-2 excitation $h(\phi,x)_{\mu\nu}$ of Minkowski space-time, in general these excitations are referred to as *gravitons*, and a spin-0 excitation $h(x,\phi)_5$ along the fifth dimension, called a *radion*. Such excitations X can be decomposed into their four dimensional wave functions $X^{(n)}(x)$ and the functions $f^{(i)}(\phi)$, called profile functions that describe the behavior in the extra dimension

$$X(x,\phi) = \sum_{n=0}^{\infty} X^{(n)}(x) f_X^{(n)}(\phi) \ . \tag{1.27}$$

Each mode n corresponds to a particle in the effective four-dimensional theory, leading to a tower of resonant states with increasing masses. These distinct resonances are called *Kaluza-Klein*[2] (KK) resonances. The zero mass solution of the five-dimensional profile function corresponds to the mediator of the gravitational force.

In order for $kL \approx 11$ to hold the first massive graviton is predicted to have a mass of a few TeV. The two parameters $\tilde{\mathrm{k}} = k/\overline{M}_{\mathrm{Pl}}$, with the reduced Planck mass $\overline{M}_{\mathrm{Pl}} = M_{\mathrm{Pl}}/\sqrt{8\pi} \approx 2.4 \times 10^{18}$ GeV, and the mass of the first KK-resonance $m_{\mathrm{X}} = x_1 \cdot \tilde{\mathrm{k}} e^{-kL} \overline{M}_{\mathrm{Pl}}$, are used as free parameters of the theory prediction. Here x_1 is a parameter corresponding to the first mode of the profile function. The parameter $\tilde{\mathrm{k}}$ is also commonly called coupling because it naturally appears as a parameter when the five-dimensional Lagrangian of matter fields is expanded around the excitation modes of g_{MN}.

There are two WED models widely utilized by experimental collaborations: the first is the RS1 model, the second is the *bulk graviton model*. In RS1 models all SM particles are confined to the TeV brane, while the KK-gravitons are allowed to propagate into the bulk, although the graviton profile function is localized mainly around the TeV brane.

[2] From a similar, but classical suggestion of Kaluza and Klein to unify gravity and electromagnetism, see Ref. [57].

The bulk-graviton model is a more sophisticated model of the RS kind. Here, SM fields such as SM bosons and fermions are allowed to propagate into the bulk, which leads to an overlap of their profile functions inside of the bulk. This overlap determines the coupling strength to gravitons. This ansatz replaces the fine tuning of parameters to orders of magnitude with the tuning of order one parameters, namely the placement of the particle fields inside the bulk, thus solving the hierarchy problem. A visualization of this concept for the bulk-graviton model is shown in Figure 1.1. Each SM particle allowed to propagate into the bulk causes a tower of KK-modes, where the SM particles are the first excitations of the KK-modes, while higher excitations only play a role in loop corrections at low energy scales. There are far more models suggesting a wide range of possible scenarios, however, for the case of high energy physics searches it is advantageous to take relatively simple models that can act as stand-ins for more sophisticated models.

Graviton Couplings to Matter

The effective interaction strength between the graviton and any SM field is proportional to the integral of their profiles in the fifth dimension

$$\mathcal{L}_{\text{eff}} = -\frac{x_1 \tilde{k}}{m_{\text{X}}} h^{\mu\nu(1)} d_i F^i_{\mu\nu} \ , \tag{1.28}$$

with the SM field $F^i_{\mu\nu}$, d_i is the overlap integral between the SM field i and the graviton in the fifth dimension. The field $h^{\mu\nu(1)}$ is the graviton field for the first heavy graviton resonance

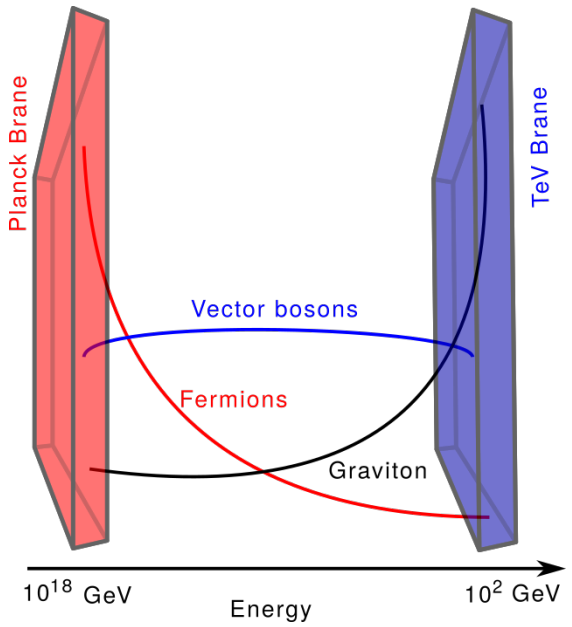

Figure 1.1.: Schematic picture of the two branes connected by a finite warped extra dimension, as predicted by bulk graviton RS models. The matter localization in the bulk determined by the profile functions is pictured for light fermions (red line), SM vector bosons (blue line) and KK gravitons (black line). For RS1 models the fermions and SM vector bosons are confined to the TeV brane.

with mass m_X. For the Higgs boson that is completely confined to the TeV brane the integral d_H is equal to 1. This is also the reason why the coupling of a bulk graviton to weak bosons is large. These couplings consist of two parts, the coupling to longitudinal vector bosons, which results from absorbing the Goldstone boson of the Higgs doublet and is not volume suppressed, and a volume suppressed term coming from the propagation of the vector bosons into the bulk. The profile of the vector bosons in the bulk is a flat profile, leading to a small coupling term to transverse modes proportional to $\frac{2}{k\pi L}$.

The coupling to fermions can be split into three parts that are driven by the overlap of wave functions in the bulk. A part corresponding to the overlap between left- and right-handed fields and the graviton and the third combining left and right-handed fields that is proportional to the mass of the fermions.

Phenomenology at the Large Hadron Collider

In order to discover the predicted resonances or set exclusion limits on their production cross section, the phenomenological consequences of the theory model for LHC physics are important. As seen in the last section, WED models predict two kinds of resonances: massive

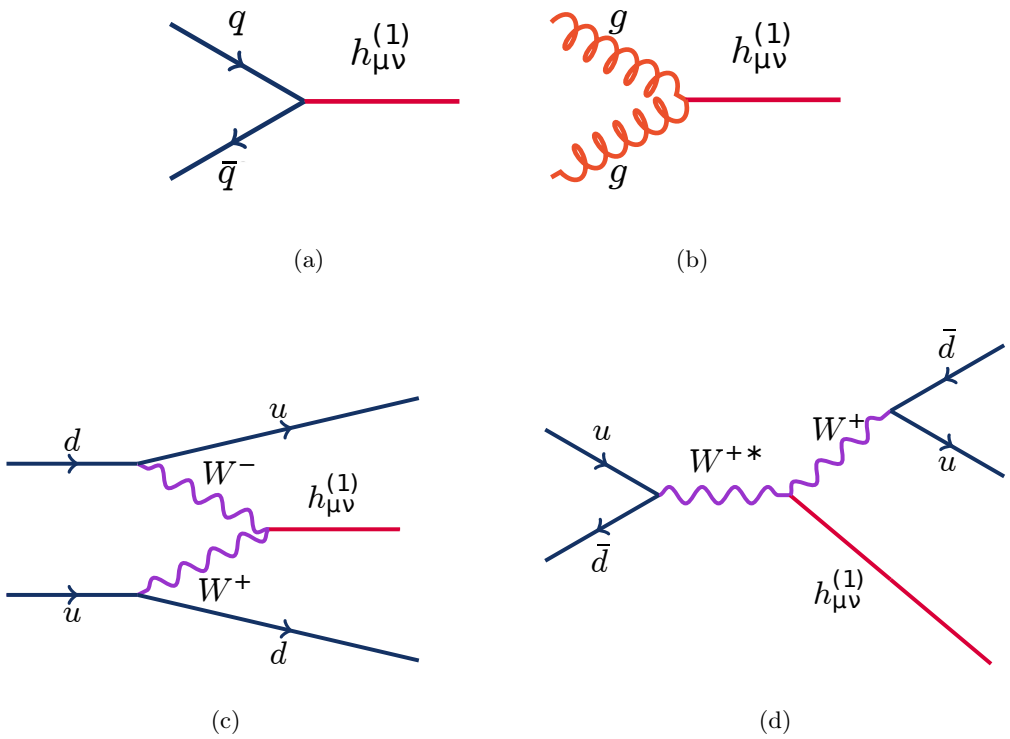

Figure 1.2.: The Feynman graphs for Drell-Yan (DY) (a) and gluon-gluon-fusion (ggF) (b) production of a hypothetical spin-2 resonance. The Feynman graphs for vector boson fusion (VBF) (c) and vector boson associated (VBA) production (d) are shown on the bottom. The Figure is taken from Reference [56].

spin-2 resonances (the gravitons) and the spin-0 radions. In the search presented in this thesis only gravitons are searched for. The reason for this is a prediction of a relatively high branching fraction of the radions to photons, which is a very clean discovery channel at the LHC and therefore radion resonances that could be examined with vector boson decays are already excluded.

Figure 1.2 shows the tree-level Feynman graphs for the production of a graviton. In Figure 1.3 (left) the expected cross sections for a bulk graviton at a center-of-mass energy of 13 TeV is shown as a function of the resonance mass. The dominant production mechanism below a resonance mass of 5 TeV is gluon-gluon fusion. Due to constraints from measurements of flavor-changing neutral currents a mass of ≈ 4 TeV of the first KK-graviton is favored by WED models. Figure 1.3 (right) shows the branching fraction of gravitons to SM particles, which shows large branching fractions to vector boson pairs (WW or ZZ) and top quark pairs ($t\bar{t}$). The polarization of the vector bosons from a decay to WW or ZZ can influence the detector acceptance and efficiency of later analysis selections. For the bulk graviton mostly longitudinally polarized V bosons are produced as can be seen from Figure 1.4.

1.3.2. Heavy Vector Triplet Models

The Heavy Vector Triplet (HVT) model is a simplified model approach, which restricts itself to modeling the directly measurable consequences of a more complicated model. For a more

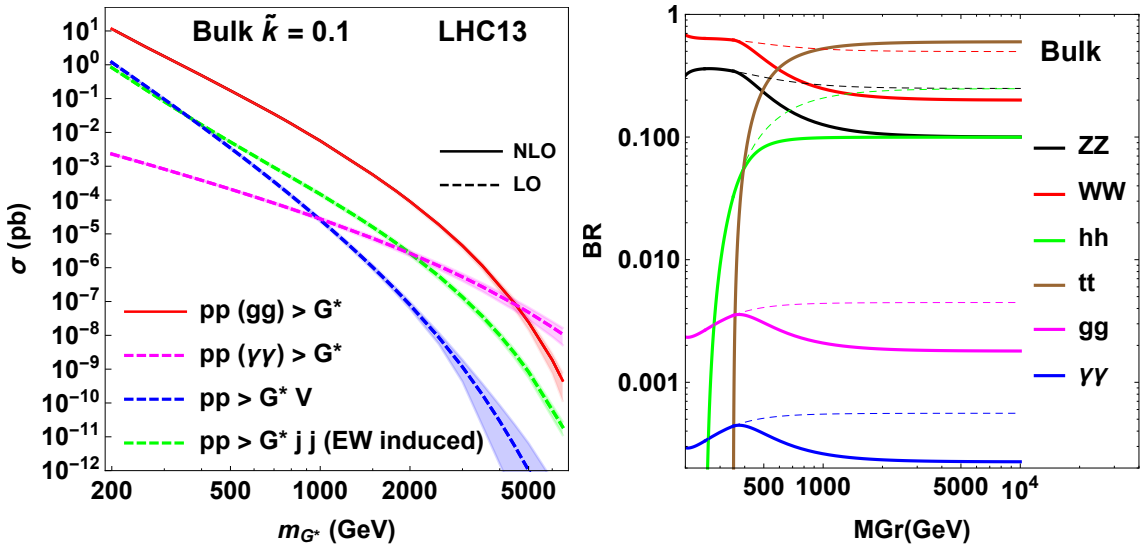

Figure 1.3.: The phenomenological characteristics of a bulk graviton from Randall-Sundrum WED models, figures taken from Ref. [56]. The left figure shows the production cross section as a function of the first KK-resonance mass for a value of $\tilde{\kappa} = 0.1$. The leading order cross section is proportional to $\tilde{\kappa}^2$. The right figure shows the branching fractions to different SM particles as a function of the mass of the first KK-resonance. The dashed lines correspond to a different fermion embedding scenario as described in Ref. [4]. The branching ratios are independent of the warp factor $\tilde{\kappa}$.

detailed discussion of the model see Ref. [13]. Such an approach is necessary because of the large number of theoretical models available, and feasable since a resonance search is usually not sensitive to all details and free parameters of a particular model. Therefore, it is sensible to describe a large number of theory models with a phenomenological Lagrangian containing only the couplings relevant to the production and decay of the new resonances. The HVT model describes heavy electroweak charged spin-1 resonances called Z′ or W′, which can arise from a number of composite Higgs models [6–8], technicolor models [58, 59], electroweak extensions of the SM [9, 10] or WED models [60, 61].

The HVT simplified model introduces a new electroweak sector analogous to the SM electroweak sector. This leads to very similar phenomenologies as for the SM vector bosons, but with larger expected resonance masses. One important feature that can be derived with this simplified model is that the expected masses of the new charged and uncharged heavy particles are expected to be very nearly degenerate. This means that the reach of a given search can be considerably improved when taking this fact into account and the search is performed for a W′ and Z′ resonance with the same mass simultaneously.

Couplings to Matter

Since the newly introduced sector mirrors the SM electroweak sector closely, three massive new bosons appear, the charged W′ and the neutral Z′ bosons. Of interest from a phenomenological perspective are their couplings to SM matter, which are parameterized by a scaling of order 1 to the couplings of W′ and Z′ with respect to the SM couplings of a W or Z boson,

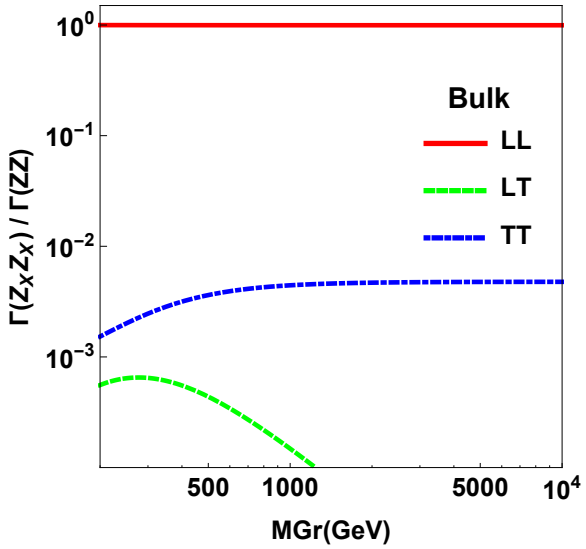

Figure 1.4.: Polarization of the decay products of a bulk graviton decaying to a Z boson pair taken from Reference [56]. Decays to WW show the same behavior. The red line (LL) shows the portion of decay to longitudinal gauge bosons, the blue dot-dashed line (TT) shows the portion of decay to pure transversal modes and the green dashed line (LT) shows decays to mixed transverse and longitudinal modes.

denoted with c_H, c_F and g_V, respectively. The parameter c_H scales the phenomenological relevant couplings to the SM Higgs boson, while c_F scales the couplings to fermions and the parameter g_V denotes the typical interaction strength with V bosons.

There are some further constraints on the possible coupling space coming from the fact that the SM couplings of W and Z bosons are measured with high accuracy and therefore no values for the new coupling can be allowed that would significantly change these couplings at more than percent level.

The new resonances couple mainly to left-handed fermions, just as their SM counterparts, with their coupling to fermions described by

$$g_F^N = \frac{c_F g^2}{2 g_V} , \tag{1.29}$$

$$g_F^C = \frac{c_F g^2}{\sqrt{2} g_V} , \tag{1.30}$$

for neutral g_F^N and charged g_F^C resonances and the SM electroweak coupling g. The parameters c_F control the relative branching ratios to fermions.

Similar to the WED models discussed in the previous sections, the couplings to vector bosons have to be considered separately for transversal and longitudinal polarization of the vector bosons. Due to the small expected mixing angles of the new resonances their couplings to transversely polarized SM vector bosons are highly suppressed and lead to negligible branching fractions. However, this is not the case for longitudinally polarized SM bosons. This coupling is proportional to

$$g_{VB} \approx \frac{g_V c_H}{2} , \tag{1.31}$$

for decays to VV or VH. Decays to HH, $\gamma\gamma$ and Wγ are either forbidden or strongly suppressed. For the generation of Monte Carlo (MC) simulation [62] two different models are typically used, where these coupling parameters are set to specific values. In the scenario denoted with HVT model A, which more closely resembles extended gauge theory models, the decay to vector bosons is suppressed. In the HVT model B scenario those couplings are larger, therefore this is the scenario used in this thesis. In this scenario the specific values $g_V = 3$, $c_H = -0.98$, and $c_F = 1.02$ are used for the generation of events. It is also important to note here that the approximation of narrow decay width is only valid in a regime of $g_V < 7$. Larger couplings lead to extremely broad resonances that cannot be constrained anymore by direct searches to narrow resonances.

Phenomenology at the Large Hadron Collider

The dominant production mechanism for heavy W′ and Z′ resonances at the LHC is via Drell-Yan processes. A production via ggF as in the case of WED models is possible only via loop processes and therefore suppressed. There is also a sizable production via vector boson fusion, which becomes more important for very high resonance masses. The corresponding leading-order Feynman diagrams are shown in Figure 1.5. In Figure 1.6, the expected production cross section for the HVT model B are shown. Both charged and uncharged resonances have comparable production rates at the LHC.

The branching ratios for a W′ and Z′ resonance decaying into SM particles are found in Figure 1.7. The branching ratio to SM vector bosons is significantly higher than into any other SM particles in the model B scenario.

1.4. Current Status of Diboson Resonance Searches at the LHC

There is a large program of searches for signatures of new particles at the LHC. Particularly, there is a large program searching for the most straightforward of those signatures–an s-channel resonance decaying to two SM particles–in numerous search channels such as diphoton, dilepton, or diboson both from the ATLAS and CMS collaborations [14–34]. In Figure 1.8 a summary of CMS results for 35.9 fb^{-1} of data collected in 2016 is shown for different final states of the diboson channel. There was no significant deviation above the SM background found by the ATLAS or CMS collaborations in any of the listed final states. Therefore the observed 95% confidence level upper exclusion limits on the production cross section times branching fraction for bulk graviton WED models (Figure 1.8 top) and HVT model B (Figure 1.8 bottom) are shown here. For all three models the limits achieved in the all jets final state VV $\rightarrow$ 4q and the ones with a semileptonic final state WV $\rightarrow$ lν2q are the most competitive at high resonance masses while the full leptonic final states are more competitive for small resonance masses. The CMS Collaboration can exclude the production of narrow spin-2 resonances below a mass of 0.9 TeV and charged (uncharged) spin-1 resonances below masses of 3.2 (2.8) TeV with the data recorded in 2016 alone. The ATLAS collaboration reports very

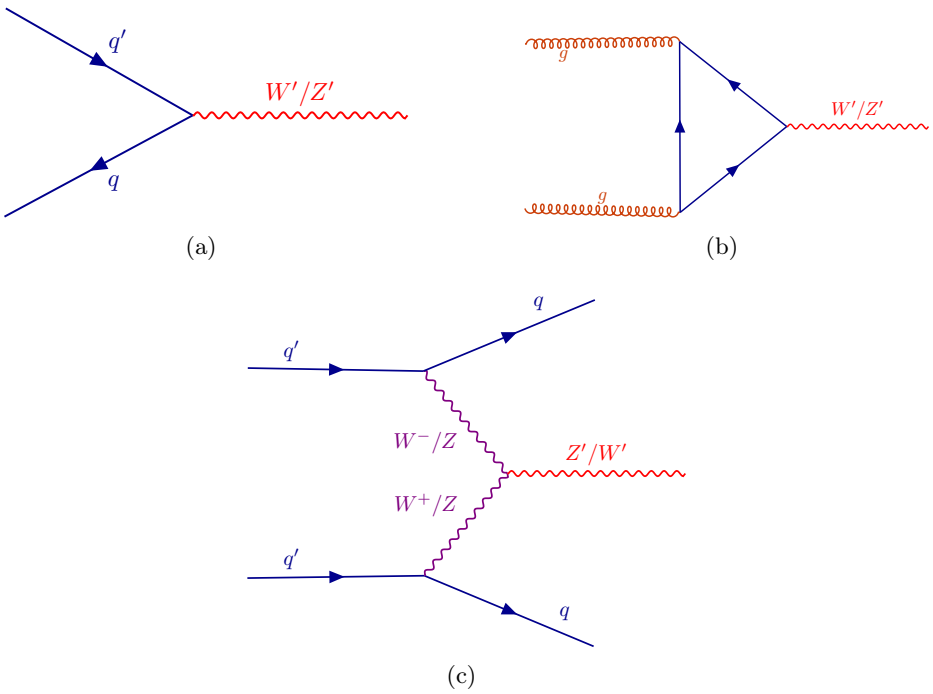

Figure 1.5.: The leading-order production Feynman diagrams for the HVT model at the LHC for DY production (a), ggF (b) and for VBF production (c).

similar results and exclusion bounds.

To enhance the reach of the individual analysis, combinations of diboson and dilepton final states are performed, the most recent ones combine analyses of the data collected in 2016. The results of this combination are shown in Figure 1.9 for the CMS experiment [11], however similar results exist also for the ATLAS Collaboration [66].

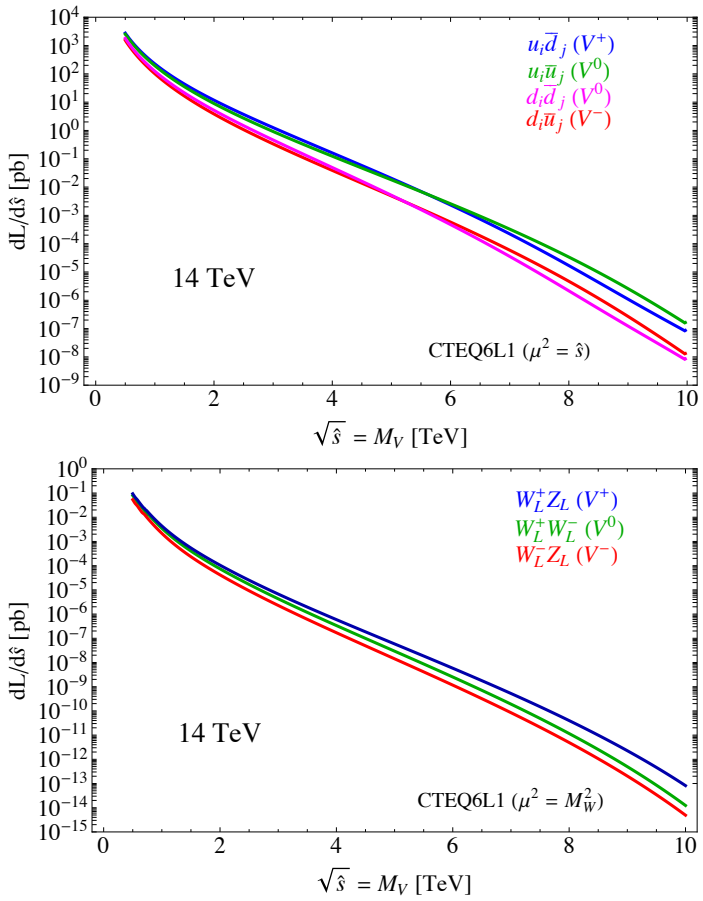

Figure 1.6.: The leading-order production cross sections of the HVT model for DY processes (top) and for VBF production (bottom) for charged and uncharged heavy vector bosons at a center-of-mass-energy of 14 TeV and for the model B scenario [13].

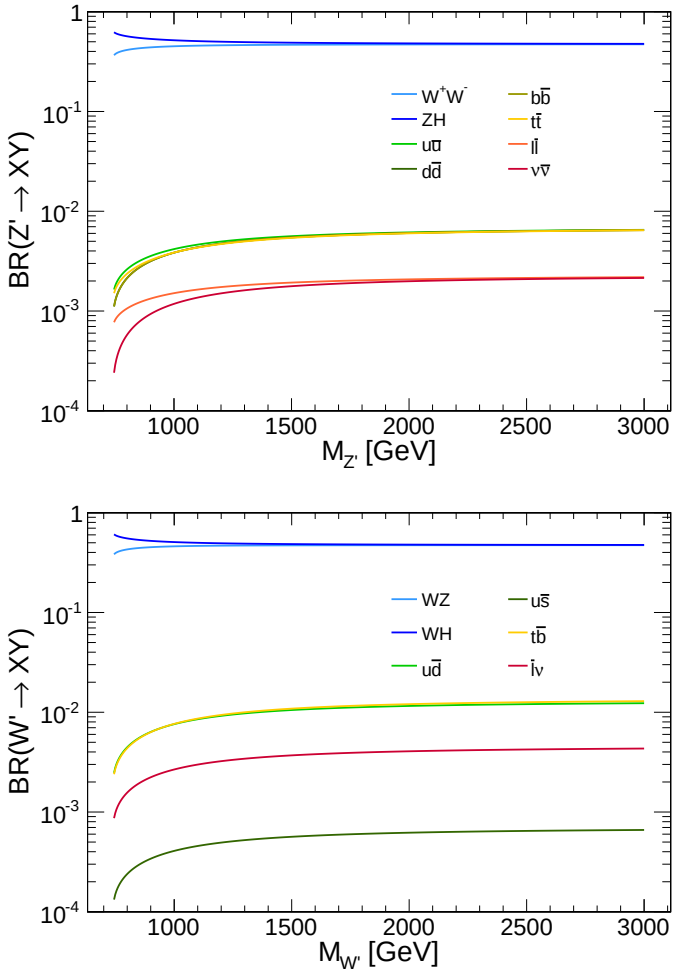

Figure 1.7.: Branching ratios for the HVT model B for a neutral spin-1 boson (top) and a charged spin-1 resonance (bottom), calculated using the tools documented in Ref. [63]. The figures are taken from Ref. [64].

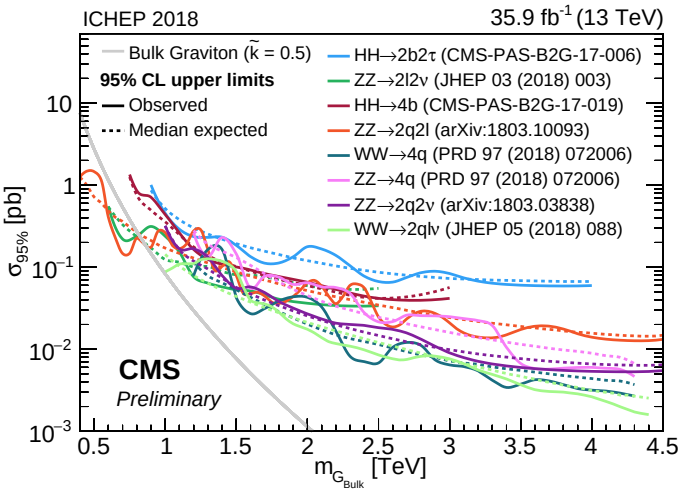

(a)

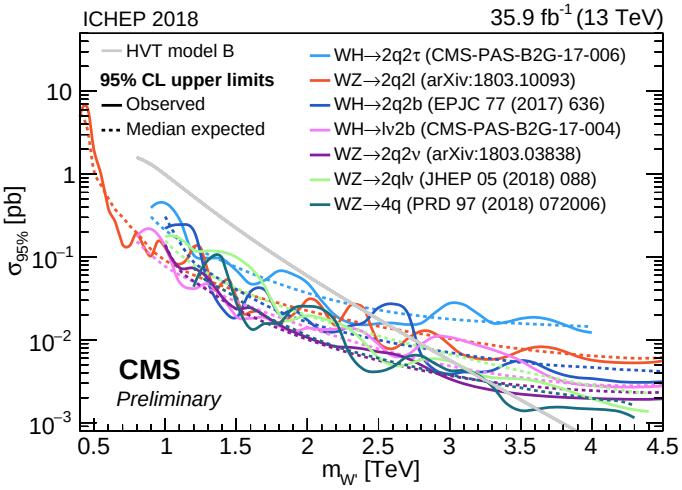

(b)

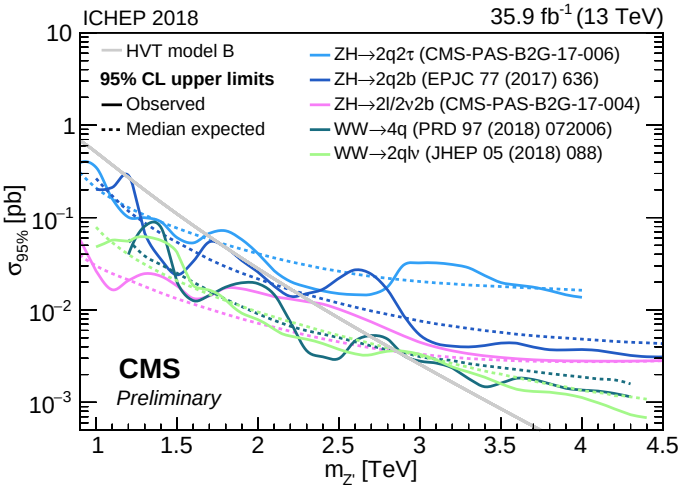

(c)

Figure 1.8.: Overview of CMS diboson searches in 2017 taken from Ref. [65]. Plot (a) shows upper 95% confidence limits on the production cross section of a bulk graviton. The plots (b) and (c) show the upper 95% confidence limits on the production cross section of a W′ and Z′.

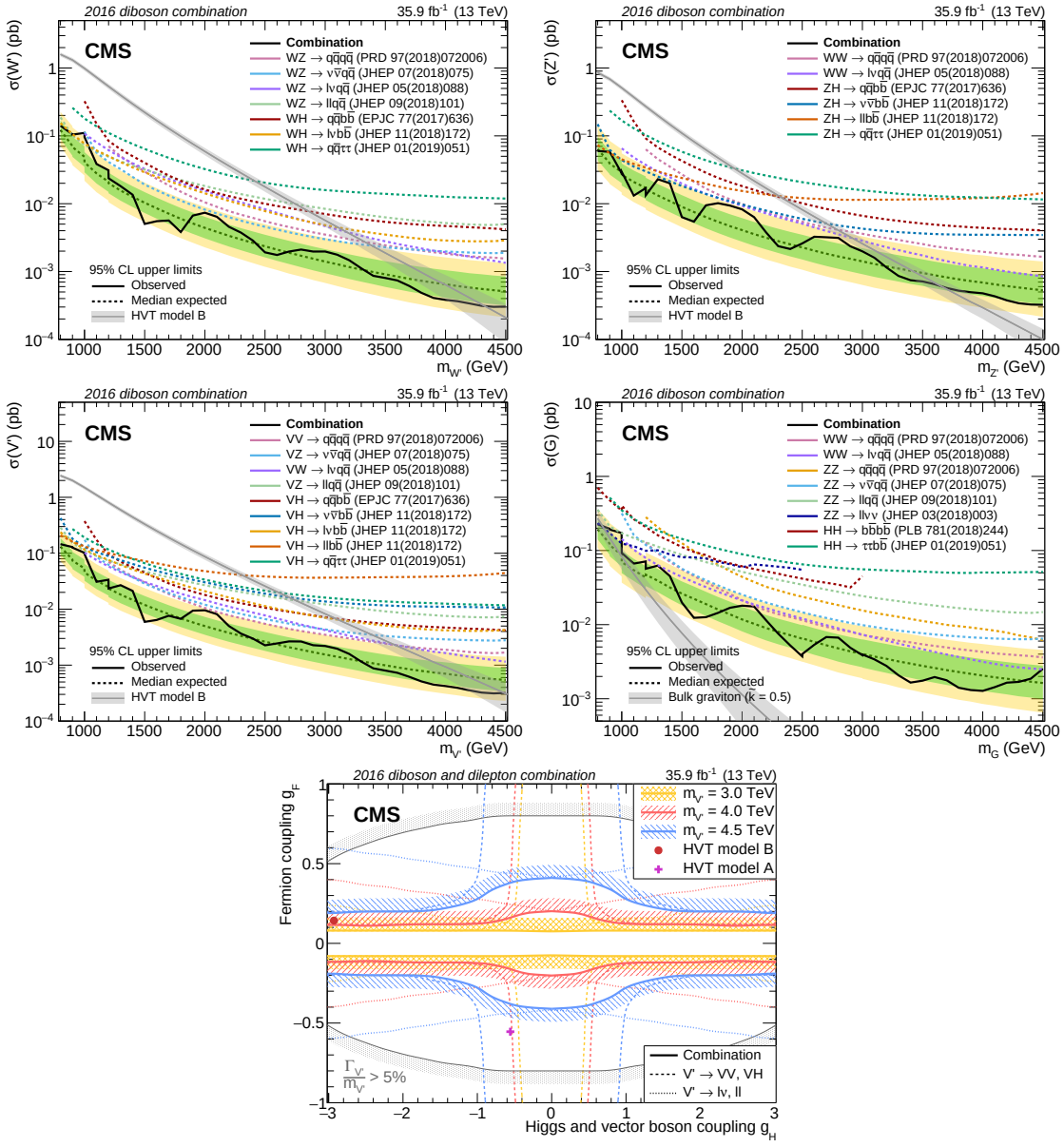

Figure 1.9.: Combination of diboson and dilepton searches for 35.9 fb^{-1} of data collected by CMS in 2016 [11]. Upper limits on the production cross section are shown for charged (uncharged) spin-1 resonances top left (top right), for a vector-triplet (middle left) and an uncharged spin-2 resonance (middle right). The lower figure shows the exclusion region in the HVT model coupling plane. The grey hashed area denotes the region where the narrow-width hypothesis breaks down.

2. Statistical Inference

Any search for new physical phenomena beyond the SM should reliably quantify the agreement or disagreement of the measured data with a prediction. In this Chapter, the statistical methods employed for deriving the results presented in Chapter 5.6 are introduced. First, the principles of maximum likelihood estimations and basic hypothesis tests are discussed. Then, the determination of upper limits with the CLs method is described, as well as the inclusion of uncertainties in the procedure. The Refs. [67–70] contain a more detailed description of these methods.

2.1. Basic Principles

The foundation of any hypothesis test is quantifying the prediction, i.e., null-hypothesis. In high energy physics a prediction of the number of events expected in bins of a particular variable, for example a mass, is ususally needed. For this a probability density function (pdf) is derived for each SM process considered as a background in the analysis and the assumed signal, thus leading to a prediction for the number of expected events N

$$N(\boldsymbol{x}) = N_{\text{exp}} \cdot P(\boldsymbol{x}|s + b_i, \theta) \tag{2.1}$$

$$N(\boldsymbol{x}) = N_{\text{bkg}}(\boldsymbol{x}) + N_{\text{sig}}(\boldsymbol{x}) = \sum_{i=1}^{k} P_i(\boldsymbol{x}, \theta_i) \cdot \sigma_i \epsilon_i \cdot \mathcal{L} + \mu P_{\text{S}}(\boldsymbol{x}, \theta_s) \cdot \sigma_s \epsilon_s \cdot \mathcal{L} \ , \tag{2.2}$$

where N is measured as a function of the parameters $\boldsymbol{x}$, P_i is the probability for the i-th background, which is parametrized by the set of parameters θ_i ,and μ is a factor scaling the signal strength. Since pdfs are per definition normalized to unity, the prediction has to be multiplied by the expected cross section of the process $\sigma_{i,s}$, the analysis efficiency and acceptance $\epsilon_{i,s}$ and the luminosity provided by the LHC integrated over the period of data taking $\mathcal{L}$. Equation (2.2) is not universal, since in case of interference the pdfs of signal and background processes cannot necesserily be split into two separate contributions. For large amounts of measured data the parameters $\boldsymbol{x}$ are typically binned variables, i.e., the distribution N is a binned histogram with each bin corresponding to an independent counting experiment, which means the probability of measuring n events in each bin is described by a Poisson distribution

$$\text{Poisson}(n|\lambda) = \frac{\lambda^n e^{-\lambda}}{n!} \ . \tag{2.3}$$

The measured value n of events per bin is therefore expected to be randomly drawn from a Poisson distribution with λ equal to the true number of events $\lambda = s + b$, with the number of background events b and the number of signal events s. Thus, each measured value has a Poisson error of $\sqrt{\lambda}$. However, since the true number of expected events is generally unknown the uncertainy of data is usually set to $\sqrt{n}$.

2.2. Maximum Likelihood Estimation

The binned shapes of kinematic distributions are commonly used in particle physics analyses. Often, no definitive prediction of the expected probability distributions exists, and if such a prediction exists, there are usually free parameters which need to be adjusted to data.

Regardless of whether a distribution is described by a well motivated prediction or an educated guess, a method determining the function parameters that best describe the measured data is crucial. A maximum likelihood parameter estimation is a method that accomplishes exactly that, i.e., finding the values of a parameter set θ that maximize the probability of measuring a given sample of data points x_i. Here the index i runs either over all measured data points, or in case of a binned distribution over the number of bins. The maximum of the likelihood l

$$l(\theta|\{x_i\}) = \prod_{i=1}^{n} P(x_i, \theta) \ , \tag{2.4}$$

or the logarithmic likelihood L

$$L = \ln(l) \ , \tag{2.5}$$

yields the parameterset $\hat{\theta}$ that maximizes the probability of measuring the given dataset $\{x_i\}$. The logarithmic likelihood is often used in computations instead of the likelihood function.

2.3. Template Morphing

In the event that the prediction of a data distribution is available in form of a set of binned shapes only, a smooth morphing between different histogram shapes is rendered possible by introducing a morphing parameter m that allows an interpolation between two different template shapes $f(x|m_i)$ given for a specific value m_i of the morphing parameter. The true dependency of the shapes on m is usually not known and difficult to obtain. However, the template shape for arbitrary morphing parameters can be interpolated using

$$f_{\text{pred}}(x|m) \approx \sum_{i,j=0}^{n-1} (m - m_0)^j M_{ij}^{-1} f(x|m_i) \ , \tag{2.6}$$

where m_i are values of the morphing parameter where the distribution $f(x|m_i)$ is known, and $M_{ij} = (m_i - m_0)^j$ is a transformation matrix for the morphing parameter. The parameter m_0 is the reference value of the morphing parameter that can be selected arbitrarily. The indices i, j are running from zero to the number of provided alternative shapes n minus one. Thus, the final prediction is a weighted sum of the provided input templates. This approach is known as moment morphing, and shows good computational performance and numerical stability. For more information see Ref. [71]. Using this template morphing technique a maximum likelihood estimation can be used to find the value of the morphing parameter that maximizes the probability of measuring the given dataset. Thus, a combination of template morphing and maximum likelihood estimation allows the adaption of binned predictions to a given data distribution.

2.4. Hypothesis Tests

A hypothesis test is designed to answer in a quantitative and reproducible way the basic question of whether a measured data set is compatible with a certain prediction or not. To this end, a measure needs to be constructed that quantifies differences between data distributions, which are subject to statistical uncertainties, and the prediction, in a way that a decision of agreement or disagreement can be made and the degree of certainty of this decision is understood. Three ingredients are needed for a hypothesis test: a set of measurements of the distribution that is to be tested, a so-called *null-hypothesis* H_0, which describes the expected distribution of the data, and an H_1 hypothesis which describes an alternative distribution. It is also possible to reject H_0 based on its agreement or disagreement with data alone. However, a positive outcome of this kind of test is not sufficient to decide that the data actually follows the null-hypothesis.

For the notation in this section it is assumed that the null-hypothesis is characterised by the lack of a signal contibution s, which is scaled by a signal strength parameter μ. Therefore, H_0 and H_1 hypothesis differ only in the strength of the signal contribution which is zero in case of the null-hypothesis. This case was chosen since it is used in this thesis, however, the expressions derived are not completely general anymore.

Another key ingredient for hypothesis tests is the so-called *test statistic (q_μ)*, which is a quantity chosen for each test with its most important property being different distributions $f(q_\mu|\mu = 0)$ for H_0 and $f(q_\mu|\mu)$ for the H_1 hypothesis. Figure 2.1 shows an example of the distributions $f(q_\mu|\mu = 0)$ and $f(q_\mu|\mu)$ for a test statistic q. For consistency a *level of significance* α for the test has to be chosen in advance. Typical values for α are for example 5%, 1% etc. The meaning of this significance is a quantization of the error of the first kind, i.e., the chosen significance level of α tells us that in α% of possible measurements the null-hypothesis is rejected although it is the true distribution of data. Note here that this approach cannot quantify errors of the second kind, i.e., the probability of accepting H_0 although it is false is unknown. Once a significance level is chosen, and the distribution of the test statistic is known, two *p-values*

$$p_{b+s} = \int_{q_\mu^{\text{obs}}}^{\infty} f(q_\mu|\mu) \ , \tag{2.7}$$

$$p_b = \int_{-\infty}^{q_\mu^{\text{obs}}} f(q_\mu|\mu = 0) \ , \tag{2.8}$$

can be calculated. Here q_μ^{obs} denotes the observed value of the test statistic given the measured data. The p-value quantifies the probability of observing a distribution with a variation between data and prediction as large, or larger than the observed variation given that the hypothesis is true. If only the disagreement between data and a H_0 hypothesis is tested the null-hypothesis is rejected if $p_b < \alpha$, i.e., the probability of measuring a disagrement as bad or worse as the one observed, although the null-hypothesis is true, is smaller than α%.

2.5. Goodness-of-Fit Tests

Goodness-of-fit (gof) tests are hypothesis tests that only test the level of agreement to a given null-hypothesis. They are mainly useful in determining the validity of a chosen model in describing a data distribution. The best-known gof test is the chi-square test which utilizes the

$$\chi^2 = \sum_i \frac{(d_i - f_i)^2}{\sigma_i^2} \ , \tag{2.9}$$

distribution, with the model prediction f_i, the data d_i and the root mean square (RMS) of the data σ_i. This test is applicable only when the measurements d_i are sampled from a Gaussian distribution with standard deviation σ_i. The index i denotes the i-th data point in the measured set. In most high energy physics cases, the compatibility of binned datasets and predicted histograms with Poissonian RMS are tested. In these cases, it is beneficial to use the following distribution as proposed by Baker and Cousins [72], based on a likelihood ratio

$$-2\ln(\lambda) = -2\ln l(f,d) + 2\ln l(m,d) \ , \tag{2.10}$$

with the likelihood function l and the predicted number of events in each bin f, and the measured number of events d. The variable m denotes the true, unknown values of the data distribution given that no uncertainties exist in the measurement. For Poission-distributed data, the unknown parameters m can be replaced by their bin-by-bin maximum likelihood estimation, which is equal to the measured number of events d. This approach is called the *saturated model*. Equation 2.10 can then be written as

$$-2\ln(\lambda) = 2\sum_i \left(f_i - d_i + d_i \ln(\frac{d_i}{f_i}) \right) \ , \tag{2.11}$$

for Poisson-distributed histograms.

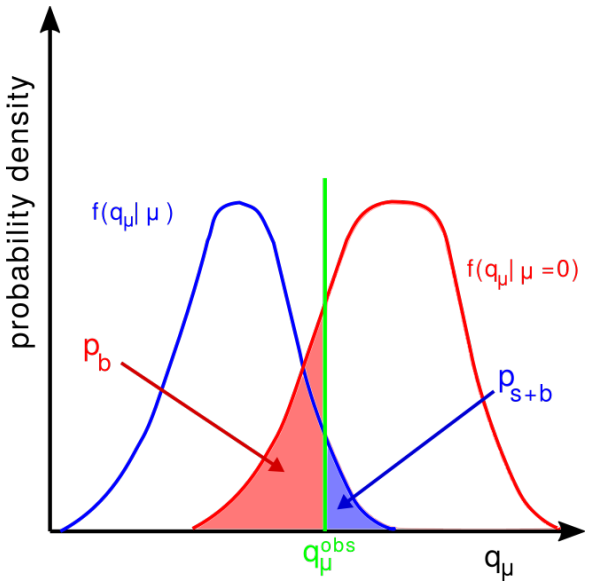

Figure 2.1.: Illustration of the distribution of a test statistic q_μ for the background only $f(q_\mu|\mu = 0)$ and signal-plus-background $f(q_\mu|\mu)$ hypothesis.

2.6. Systematic Uncertainties

In addition to statistical uncertainties, which are the result of stochastic fluctuations in the finite data, there are so-called *systematic uncertainties*, which arise from uncertainties associated with the measuring device and the model used for predicting the data distributions.

A way to treat these uncertainties is to introduce *nuisance parameters* (θ) to account for changes in the overall model due to a particular uncertainty. This change can affect the shapes of distributions, the overall event yield, or both. Each uncertainty source warrants the introduction of a new nuisance parameter that models the impact of the uncertainty on the prediction. In its simplest form, the introduction of an uncertainty on the number of background events b can be written as

$$L(n|s,b) = \text{Poisson}(n|s+b) \rightarrow L(n|s,b,\theta) = \text{Poisson}(n|s+b\cdot(1+\theta))\cdot P(\theta)\ , \tag{2.12}$$

assuming a Poisson distributed simple counting experiment. The likelihood function becomes dependent not only on the overall signal s and background b count, but also on the nuisance parameter θ. The pdf $P(\theta)$ is called a *prior probability function* or *constraint* and describes the probability distribution for the nuisance parameter θ, thus providing essentially a constraint on the size of the nuisance parameter. The exact form of $P(\theta)$ has to be provided from external sources such as for example secondary measurements. Following the approach highlighted in Ref. [73], the likelihood, built from the background and signal models and the nuisance parameters, is profiled with respect to the nuisance parameters θ, leading to a likelihood ratio λ, which only depends on the parameter of interest, the signal strength.

There is a second method available based on a more Bayesian-like approach called the Highland-Cousins method, see Ref. [74]. Here, the nuisance parameters are handled by integrating the likelihood over the parameter space of the uncertainty.

In a typical analysis in high energy physics much more than one uncertainty source needs to be taken into account. The form of the prior distributions then depends on the nature of each uncertainty. Some common choices are log-normal or Gaussian distributions, however, the choice of prior distribution is not always a priori clear and has to be determined on a case by case basis.

In addition to the prior function, correlations between different model component have to be considered. For example it might be the case that either multiple backgrounds or some backgrounds and the signal are affected by one uncertainty. The strength and direction of this effect can be different between contributions. If the impact of a nuisance is opposing between two components, they are called anti-correlated. Thus, a linear correlation can be incorporated into the simple counting experiment likelihood by

$$L(n|s,b) = \sum_i \text{Poisson}(n|s+b_i\cdot(1+f_i\theta))\cdot P(\theta)\ , \tag{2.13}$$

with the correlation coefficients f_i. Here i denotes the i-th background contribution.

2.7. Exclusion Limits

The goal of a particle physics analysis searching for new phenomena or particles is to either *discover* such a new particle, or to give exclusion limits. In the case of a discovery the background-only hypothesis has to be decisively rejected in favor of a signal-plus-background hypothesis. In case of exclusion limits, the signal strength μ must be determined for which the observed data does not exclude exotic phenomena with a signal strength less or equal to μ with a given confidence level $1 - \alpha$. Naturally, it is not a priori clear whether or not an analyses will lead to a discovery or exclusion limits until all of the calculations have been performd. Analyses searching for new particles are therefore performed *blind*, this means that the measurement in the kinematic regions where a new signal might be located is not considered at any point in the process of deciding on analysis methods or selections. This procedure tries to minimize any unintentional biases of the analyst that might otherwise lead to false discoveries. Since the aim of such analyses is to potentially find new particles all optimizations are performed with regards to discovery, i.e., analysis selections are chosen to optimize the significance of a possible discovery, not to give optimal exclusion limits.

2.7.1. The Test Statistic

So far it has not been discussed which quantity to use as the test statistic. This discussion has been postponed until now, since the choice of which quantity to use is ambiguous. A well-known example for a test statistics used in goodness-of-fit tests is the χ^2 value, defined as

$$\chi^2 = \sum_k \frac{(N_k - N_{0k})}{N_{0k}} \ , \tag{2.14}$$

here N_{0k} is the number of expected events and N_k the number of observed events. Another function commonly used as a test-statistic is the likelihood or logarithmic likelihood as defined in Section 2.2. For the calculation of the CLs limits a ratio of likelihoods is utilized

$$\lambda(\mu) = \frac{L(\mu, \hat{\theta}_\mu | \{x\})}{L(\hat{\mu}, \hat{\theta} | \{x\})} \ , \tag{2.15}$$

with the *profiled likelihood function* $L(\mu, \hat{\theta}_\mu | \{x\})$, where L is maximized for fixed μ with regard to all nuisance parameters θ, and the maximized likelihood function $L(\hat{\mu}, \hat{\theta} | \{x\})$. The values of μ and θ that globally maximize the likelihood function are denoted as $\hat{\mu}$ and $\hat{\theta}$. The final test statistic is then defined as

$$q_\mu = \begin{cases} -2 \ln (\lambda(\mu)) & , \hat{\mu} \leq \mu \\ 0 & , \hat{\mu} > \mu \end{cases} \ . \tag{2.16}$$

This choice of test statistic is driven by the *Neyman-Pearson lemma*, which states that the likelihood ratio λ provides the best separation power between background-only and signal-plus-background hypothesis when no nuisances are present. This lemma remains approximately true when constrained nuisances are present. The test statistic is set to zero for values of the signal strength smaller than $\hat{\mu}$. Thus, by disregarding these values of μ the test takes into account that these values do not represent a worse compatibility to the data and therefore should not contribute to the rejection region.

2.7.2. CLs Limits

In this thesis, the more complex case of rejecting the H_0 hypothesis in favor of a certain signal-plus-background hypothesis or vice versa is considered. In this case, it is prudent to choose a slightly different quantity than the p-value to account for the test's *sensitivity*, i.e., the distributions of q_μ might have a large overlap for both hypotheses which leads to a low sensitivity. This means that in case of low sensitivities the p-values for both hypotheses will be similar, and therefore no statements about the validity of either of the hypotheses can be made since rejecting the signal hypothesis in favor of the background-only hypothesis in such a case would be disingenuous. Therefore, the quantity CLs is defined as

$$\mathrm{CLs} = \frac{\mathrm{P}(\mathrm{q} \geq \mathrm{q}^{\mathrm{obs}}|\mathrm{s}+\mathrm{b})}{\mathrm{P}(\mathrm{q} \geq \mathrm{q}^{\mathrm{obs}}|\mathrm{b})} \coloneqq \frac{\mathrm{p_{s+b}}}{1-\mathrm{p_b}} \ . \tag{2.17}$$

This approach takes into account how well the signal-plus-background and background-only hypotheses can be separated. To set upper limits, for example on the production cross section of an exotic new particle, the value μ of the signal strength that satisfies

$$\mathrm{CL}_\mu = \frac{\mathrm{p}_\mu}{1-\mathrm{p}_{\mu=0}} = \alpha \tag{2.18}$$

has to be determined. In this analysis $\alpha = 5\%$ is set as is convention in high energy physics.

The distribution of the chosen test statistic is not a priori known for arbitrarily complex models. This means that in a typical use case, when calculating the CLs limits, this distribution is determined through a large number of toy experiments. MC methods are used to generate these toys by calculating the value of the test statistic for different sets of pseudo-data, which are generated using the background-only and signal-plus-background models for different values of the signal strength μ. The expected $(1-\alpha)-$ CLs limit is then defined as the median solution μ' to $\mathrm{CL}_\mu = \alpha$ with pseudo-data originating from the background-only hypothesis. The expected 1σ and 2σ uncertainty bands are the values of μ that mark the intervals containing 68 and 95% of toys distributed around μ'. The *observed* limit is calculated as the CLs value given the measurement instead of a toy experiment.

In this thesis, the *combine* tool is used for all limit calculations. More detailed descriptions of the methods employed in the tool can be found in References [75–77].

2.7.3. Asymptotic Approximation

The calculation of CLs upper limits is computing intensive since it requires the generation of a lot of toy data. The *asymptotic* CLs *method* is an approximation that drastically reduces the number of toys needed for the limit computation to zero. However, although the method often produces limits similar to the computationally expensive method even for small sample sizes, it is strictly mathematically valid only in the limit of large sample sizes and has to be used with some caution. See References [70, 78] for more information on the method. The approximation relies on the asymptotic behaviour of the profile likelihood ratio used as test statistic which is

$$-2\ln(\lambda(\mu)) \approx \frac{(\mu-\mu')^2}{\sigma^2} + O(1/\sqrt{N}) \ , \tag{2.19}$$

in the limit of a large sample ($N \to \infty$). The standard deviation σ of the distribution of signal strength parameters μ and mean μ' are then estimated using the covariance matrix of the estimators for all nuisance parameters. These quantities are calculated using an artificial data set called *Asimov data set*, which is the data set in which profiled estimators are equal to their true values for all parameters. Equivalently, this means that the values of all quantities in the Asimov data set are equal to their expectation values.

3. The Large Hadron Collider and the Compact Muon Solenoid Detector

To learn more about the matter in the universe and its interactions, particle interactions have to be probed at high energy scales, where the effects of new phenomena beyond the SM might become apparent. For this reason, scattering experiments with large center-of-mass energies are built, such as the Large Hadron Collider (LHC), which is the largest collider experiment to date. The LHC is able to reach energies of $\sqrt{s} = 13\,\text{TeV}$ in its collisions, which is an unprecedented energy threshold, leading to the discovery of the Higgs boson in 2012. So far the experiments surrounding the LHC ring have discovered very few and only minor deviations from the SM predictions. However, searches for new phenomenology remain one of the primary goals of the LHC.

In the following chapter, the experimental setup of the LHC as well as the setup and function of one of the major detectors, the Compact Muon Solenoid (CMS) detector, are explained.

3.1. The Large Hadron Collider

The LHC [79] is an annular particle accelerator with a circumference of 27 km. The accelerator is located 100 m beneath the border between France and Switzerland, at the compounds of the European Organization for Nuclear Research (CERN) in Geneva. The collider was built in a tunnel previously occupied by the Large Electron-Positron Collider (LEP) [80] but surpasses the center-of-mass energies previously reached by LEP by almost two orders of magnitude due to a reduced loss of energy through bremsstrahlung for protons compared to electrons. Figure 3.1 shows an overview of the complete ring structure of the LHC complex.

The LHC is a proton-proton (pp) accelerator designed to reach a peak center-of-mass energy of 14 TeV and an instantaneous luminosity of $10^{34}\ \text{cm}^{-2}\text{s}^{-1}$. Two proton beams are accelerated in opposite directions using two separate beam pipes to be brought to collision in one of the four major LHC experiments. A total of 1232 superconducting dipole magnets are used to force the proton beams on their circular orbit in the accelerator ring. The magnets are cooled to a temperature of 2 K using liquid helium and reach a stable magnetic field of 8 T. Furthermore, an additional 4800 corrector magnets, such as quadrupole magnets, are used to control the beam position, bunch localization and beam focus. The protons are accelerated and stored in the ring using high frequency (400 MHz) cavities.

Before the beam can be injected into the final accelerator, it has to undergo a process of pre-acceleration starting from the extraction of protons from a bottle of hydrogen. The protons

are then injected into the Linear Accelerator 2 (LINAC 2) which is in operation since 1978, where the beam is brought to an energy of 50 MeV through radio-frequency cavities. From there, the beam enters the Proton Synchrotron Booster (PSB), which brings the beam to a 1.4 GeV energy, and goes on to the Proton Synchrotron (PS). The PS is a synchrotron with a circumference of 628 m and is in operation since 1959 with conventional room temperature magnets to bend the beam. The protons leaving the PS have an energy of 25 GeV and enter the Super Proton Synchrotron (SPS), which has a circumference of nearly 7 km and is the last pre-accelerator before the LHC ring. The SPS itself was the site at which the Nobel-prize-winning discovery of the W and Z bosons were made in 1983 when the collider was run as a proton-antiproton collider. The protons leave the SPS and are injected into the main ring of the LHC, having an energy of 450 GeV.

The LHC complex is able to switch between accelerating protons and heavy ions such as lead nuclei, which are used in collisions in order to probe conditions in the early universe.

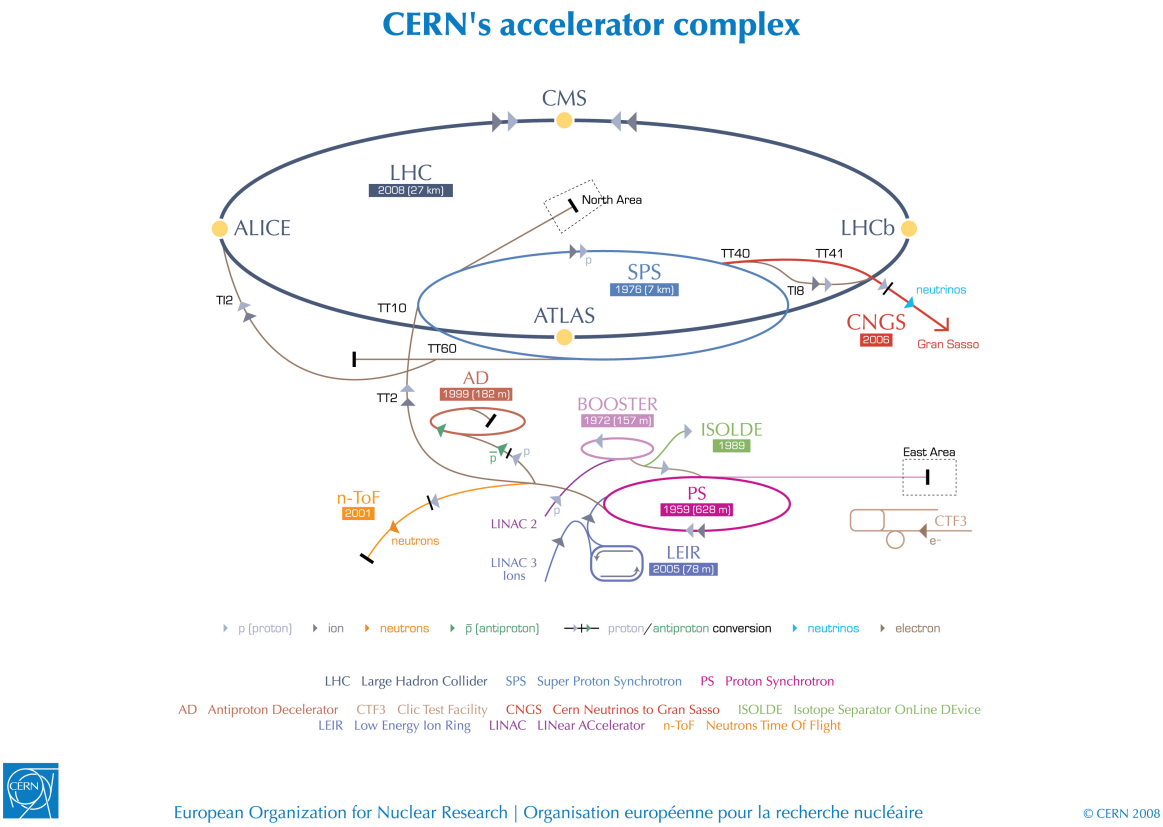

Figure 3.1.: Complete overview of the accelerator complex of the LHC at CERN. The figure shows the position of the four main experiments, as well as the schematic location of the multiple pre-accelerators [81].

In total, the LHC has four main experiments, each situated at one of the collision points.

- The CMS (Compact Muon Solenoid) detector is a multipurpose detector designed for the search of the Higgs boson, new phenomena and particles beyond the SM, as well as precision tests of the SM itself at high center-of-mass energies.

- The ATLAS detector [82] is built with the same goals as the CMS detector in mind, thus providing an independent check of all results achieved.

- ALICE (A Large Ion Collider Experiment) [83] is a detector dedicated entirely to measuring heavy ion collisions. The goal is to study strong interactions in quark-gluon plasma that model conditions of the early universe shortly after the big bang in the laboratory.

- The LHCb (Large Hadron Collider beauty) experiment [84, 85] is built asymmetrically around the beam axis in one forward direction and specializes in measurements involving B mesons and CP violation.

In addition to these four major experiments, there are also some smaller experiments piggybacking on the LHC beams. Such experiments include TOTEM [86], a precision proton spectrometer in the very forward region of the CMS detector, MoEDAL [87], an array of plastic nuclear track detectors in the LHCb cavern designed to search for magnetic monopoles, and the LHCf [88] experiment, situated in the ATLAS forward region and designed to help with the simulation and calibration of cosmic rays.

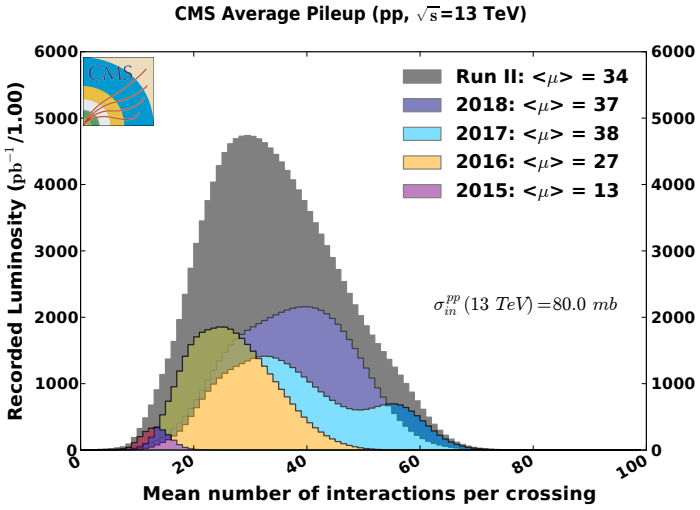

Figure 3.2.: Distribution of the average number of interactions per crossing (pileup) for pp collisions at 13 TeV for 2015 (purple), 2016 (yellow), 2017 (light blue), 2018 (dark blue) and all years combined (gray) [89].

The LHC reaches a total of 2808 bunches per proton beam with a bunch spacing of 25 ns and about 10^{11} protons per bunch. This resulted in an average of 27 (38) pp interactions per bunch crossing in 2016 (2017) see Figure 3.2. This forces experiments to put a focus on the removal of particles coming from a different proton interaction from the main event, called pileup. These specifications are planned to be significantly upgraded in order to push the luminosity provided by the machine to a factor of five more than the original design values [90]. The luminosity, which provides a measure for the number of particle collisions per time unit, depends on the number of bunches n_b, the frequency f with which they run around the accelerator, the number of particles N_b per bunch and the area of a bunch given by $\sigma_x \sigma_y$, since the bunches are nearly Gaussian, with $\sigma_{x,y,z}$ being the standard deviation of

the Gaussian beam profile in $x/y/z$ direction. The luminosity is given by

$$\mathcal{L} = \frac{N_\mathrm{b}^2 n_\mathrm{b} f \gamma_\mathrm{r}}{4\pi\sigma_x\sigma_y} F \ , \tag{3.1}$$

$$F = \left(1 - \left(\frac{\theta_\mathrm{c}\sigma_z}{2\sigma^*}\right)^2\right)^{-\frac{1}{2}} \ , \tag{3.2}$$

where F is a reduction factor caused by the crossing angle θ_c at the collision point. The relativistic gamma factor is denoted with γ_r and σ^* is the transverse beam size at the interaction point. The integrated luminosity L is

$$L = \int \mathcal{L} \, \mathrm{d}t \ . \tag{3.3}$$

The number of events N expected for a particular process with cross section σ are calculated as

$$N = L\sigma \ . \tag{3.4}$$

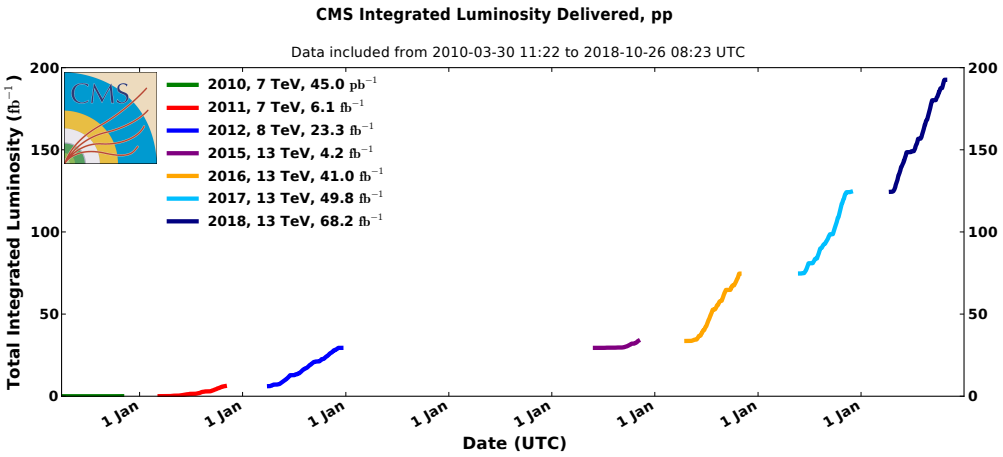

Figure 3.3.: Cumulative luminosity distribution versus time delivered to CMS during stable beams for pp collisions. Data taken in 2010 (green), 2011 (red), 2012 (blue), 2015 (purple) and 2016 (orange), 2017 (light blue) and 2018 (dark blue) are included in the figure [89].

The first LHC data was recorded in 2010 with a center-of-mass energy of 7 TeV, and later in 2012 with a center-of-mass energy of 8 TeV. From 2013 to 2014, the LHC was shut down for improvements of the accelerator and detectors to reach a higher center-of-mass energy. In the following years the center-of-mass energy was raised to 13 TeV and a total of 163 fb^{-1} of data were delivered until the end of 2018. An overview over the luminosity delivered by the LHC and recorded by the CMS experiment during its operation time up to the year 2018 is shown in Figure 3.3. This thesis is based on the 91 fb^{-1} data set delivered in 2016 and 2017.

3.2. The Compact Muon Solenoid Experiment

The Compact Muon Solenoid (CMS) experiment [91] is a multipurpose detector located at one of the interaction points at the LHC accelerator complex. The detector is arranged in multiple layers cylindrical around the beam axis and is in total 21.6 m long and has a diameter of 14.6 m. The whole detector weights about 14 000 Tons. At the heart of the CMS detector is a 3.8 T superconducting solenoid magnet large enough to contain both the inner tracker and the calorimeters. Starting from the interaction point and moving outward the CMS detector consists of an inner silicon tracker, the electromagnetic calorimeter, the hadronic calorimeter, the superconducting solenoid and the muon system. The muon system is situated both directly inside and on the outside of the iron return yoke designed to guide the magnetic field lines. A schematic view of the CMS detector can be found in Figure 3.4.

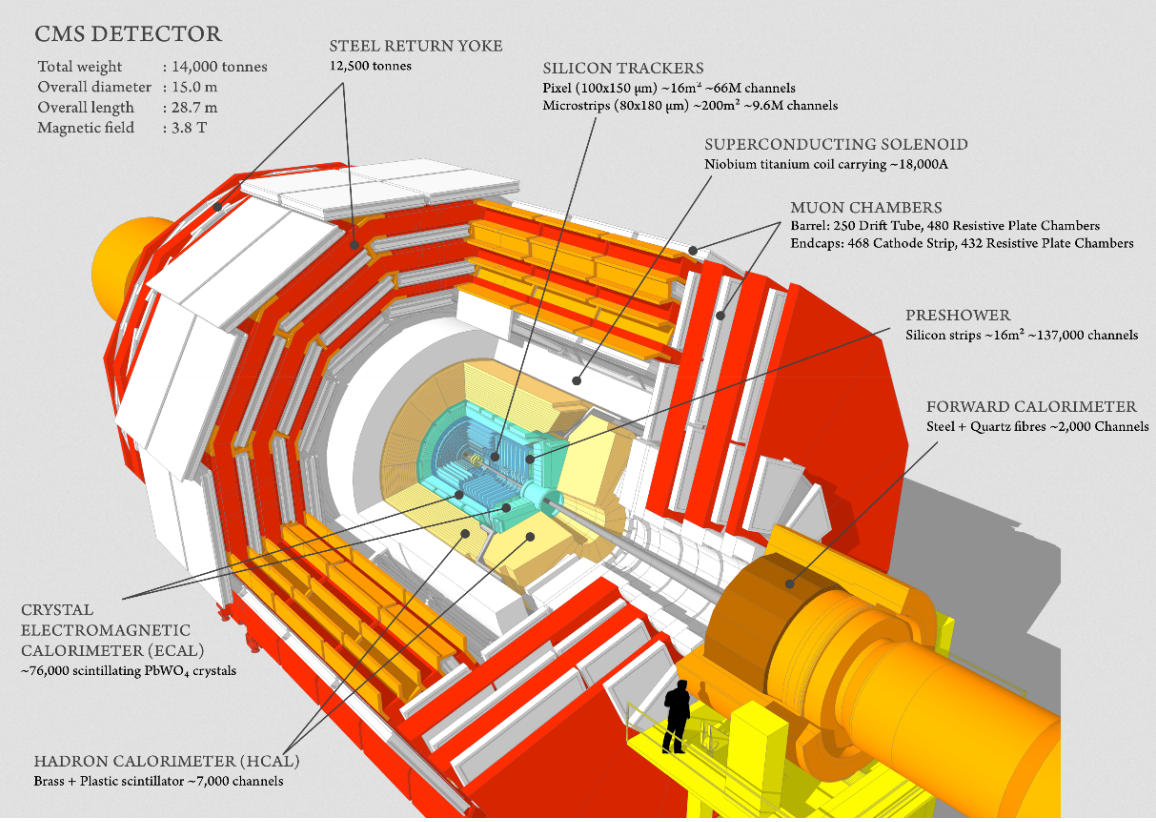

Figure 3.4.: A schematic view of the CMS detector [92] showing the location of all subdetectors.

In the following sections, a Cartesian coordinate system is used. It is defined by setting the origin at the collision point, the z-axis along the anti-clockwise beam direction, the x-axis pointing to the center of the LHC and the y-axis pointing upwards perpendicular to the plane of the LHC. A spherical coordinate system is defined in the following way: the angle θ is measured from the z-axis, the azimuthal angle ϕ is measured from the x-axis in the xy-plane, and r is the distance to the interaction point. Likewise important is the rapidity y, defined as the boost along the beam axis that transforms from the lab frame to a frame where the

particle moves only orthogonal to the beam axis

$$y = \frac{1}{2} \log \left(\frac{E + p_z}{E - p_z} \right) \ . \tag{3.5}$$

Here, E is the energy of a particle, while p_z is its momentum in z-direction. The pseudorapidity η

$$\eta = -\log \left(\tan(\frac{\theta}{2}) \right) \tag{3.6}$$

is often used in measurements, since it only depends on the polar angle of a particle and not its energy, which is used to describe the particle's absolute location in the detector system. Pseudorapidity values can range from 0 for a particle perpendicular to the beam axis to infinity for a particle parallel to the beam direction. For massless particles, η and y coincide. The quantity $\Delta R = \sqrt{(\Delta\eta)^2 + (\Delta\phi)^2}$ is used as a measure of the angular distance of two particles. The transverse momentum of a particle is defined as

$$p_{\mathrm{T}} = \sqrt{p_x^2 + p_y^2} \ . \tag{3.7}$$

In the following sections, the various components of the CMS detector are described in more detail starting from the innermost part closest to the beam pipe and therefore the interaction point.

3.2.1. Tracker

The idea of tracking is to pinpoint the whereabouts of a particle at a given time with high spatial resolution by measuring where the particle crossed a layer of detector material. Given sufficient detector layers, the trajectory of a particle through the tracking detector can be reconstructed from those hits.

The CMS tracker [93, 94] is situated closest to the interaction point, directly encasing the beam axis. The tracker of the CMS experiment is a silicon tracker with an active silicon area of 200 m^2. It consists of an inner layer of silicon pixel detectors surrounded by layers of silicon strip detectors. The tracker of the CMS experiment has a high spatial resolution and low response times, resulting in a very good track and momentum reconstruction. The detector material is kept as sparse as possible to avoid multiple scattering or bremsstrahlung losses inside the tracker. However, the tracker also needs a cooling system, since the high particle fluxes and the operation of the detector cause a substantial amount of heat. Therefor, the entire tracker is kept at a temperature of -20° C with a dedicated cooling system, which substantially prolongs the silicon lifetime. Since the inneremost pixel tracker is subject to the highest particle fluxes it has to be resistant to radiation damage. The tracker is an indispensable part of the CMS detector, able to precisely reconstruct charged particle tracks, which are used to measure the direction and the magnitude of the particle momenta as well as their charge. As such the CMS tracker is an essential part of almost all physics analyses. The momentum and charge measurement is only possible due to the deflection of particle tracks in the 3.8 T magnetic field of the solenoid magnet. A schematic layout of the CMS tracker is shown in Figure 3.5.

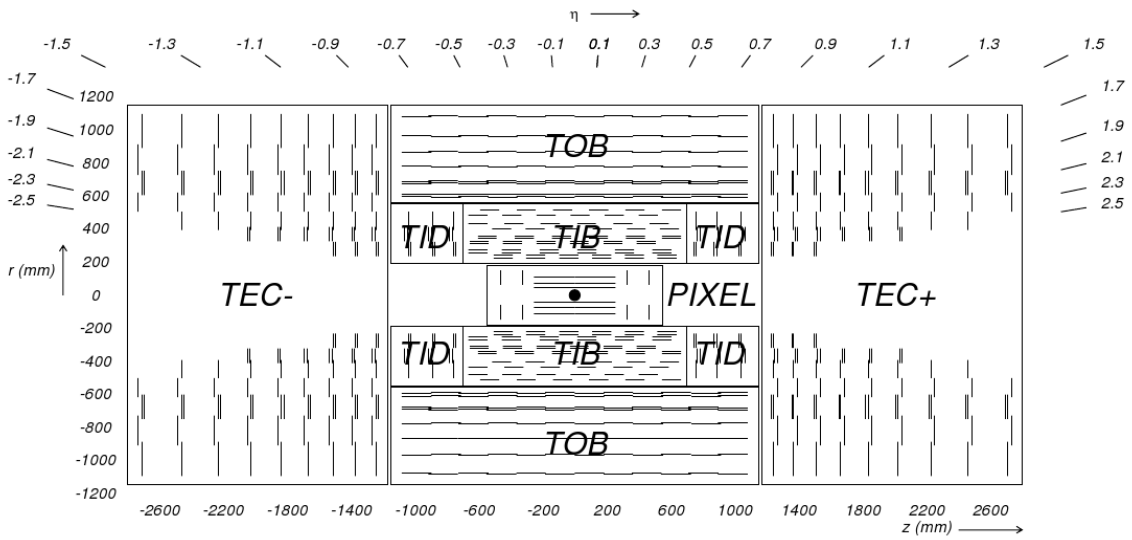

Figure 3.5.: Schematic layout of the CMS tracker before the Phase-1 upgrade [95]. The detector consists of the pixel detector (PIXEL) situated closest to the beam pipe, and the silicon strip tracker, which consists of the tracker inner barrel (TIB), tracker outer barrel (TOB), tracker inner disks (TID) and tracker endcap (TEC) region.

The silicon pixel detector, after its upgrade in 2017 [95], consists of four cylindrical layers around the beam axis, at the radii of 2.9, 6.8, 10.9 and 16.0 cm, as well as three disks in each of the forward regions. Overall around 65 million pixels made of 100×150 µm^2 silicon cells are used in the pixel detector. If a charged particle hits one of those pixels, it creates electron-hole pairs inside the semiconductor material giving rise to electrical signals, which are amplified and measured by readout chips mounted to the pixel chips. The silicon pixel detector reaches a resolution of 15-20 µm in all spatial directions and covers a range of $|\eta| < 2.5$. The readout of this subdetector is one important input to the fast three-dimensional reconstruction of the interaction vertices. In the end-of-year shutdown between 2016 and 2017, the pixel detector was replaced with the Phase-1 upgrade [96]. Improvements include an additional fourth layer in the barrel region and optimizations in cooling, readout electronics and powering of the readout chips. The increase in luminosity delivered by the LHC in 2017, thus increasing the mean number of primary vertices by a factor of 2, and the significant radiation damage of the old pixel detector made a replacement with improved technology necessary.

The silicon strip detector is situated in ten layers around the pixel detectors and is constructed to give a high spatial resolution in every direction when the measurements from two adjoining layers are combined. The physical principles behind the measurement are the same as for the silicon pixel detectors but the spatial resolution provided is lower – about 20 µm in the (r,ϕ)-plane and about 200 µm in the (r,z)-plane. The detector consists of the tracker inner barrel (TIB), tracker outer barrel (TOB), consisting of ten strip layers in total, which extend to a radius of 130 cm. In the endcap region additional modules called tracker endcap (TEC) and the tracker inner discs (TID) are installed. In total the strip detector consists of about 10 million detector strips. The tracker of the CMS detector reaches a momentum resolution

of about

$$\frac{\sigma}{p_{\mathrm{T}}} \approx 1.5 \cdot 10^{-5} p_{\mathrm{T}} \oplus 0.005 \ . \tag{3.8}$$

3.2.2. Calorimeters

The Electromagnetic Calorimeter (ECAL) [90,97] and the Hadron Calorimeter (HCAL) of the CMS detector are dedicated to energy measurements of electromagnetically interacting and hadronic particles. In contrast to the tracker discussed in the previous section, the calorimetry system is also able to detect uncharged particles such as neutral hadrons and photons. Since the goal of the calorimetry system is a measurement of the complete energy of the incoming particles, all particles should ideally be absorbed completely inside the detector material.

The basic principle of the energy measurement inside a calorimeter is the following: through interactions with the detector material, the incoming particle produces a shower of secondary particles with decreasing energies, which either deposit their energy in the detector by exciting or ionizing the atoms inside the detector material or produce new shower particles. The energy deposited by all shower particles is proportional to that of the incident particle.

Electromagnetic Calorimeter

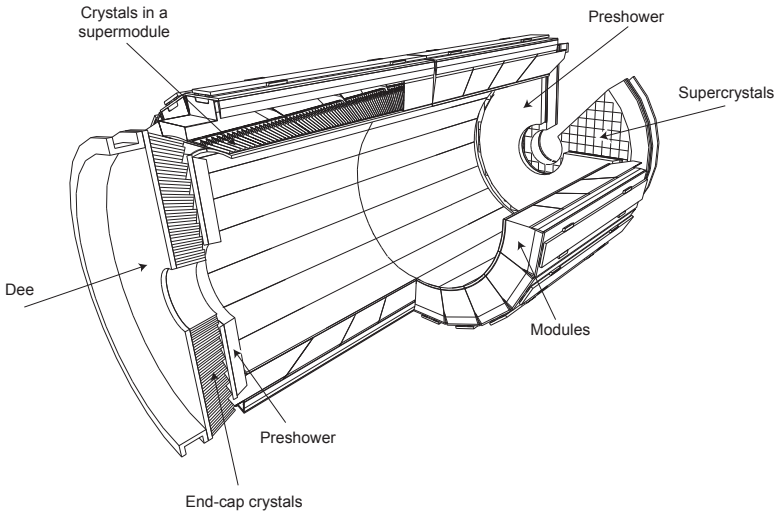

Figure 3.6.: The layout of the CMS ECAL, Figure taken from [98]. In the barrel region, the ECAL is made of modules comprised of lead tungstate crystals. In the endcap region, an additional material (the preshower) is installed in front of the main calorimeter to enable an improved identification of photons from π^0 meson decays. The schematic shows the location of the four ECAL endcap half-disks (Dee), the preshower, as well as the location of the super modules and the crystals they consist of.

The ECAL of the CMS experiment is situated directly around the tracker inside the magnetic

field and consists of around 76 000 lead tungstate ($PbWO_4$) crystals. A schematic layout of the CMS ECAL can be found in Figure 3.6. The ECAL's primary purpose is the energy measurement of particles interacting through electromagnetic processes such as electrons, positrons and photons. For energies larger than 10 MeV, electrons and positrons loose their energy mainly through bremsstrahlung, while photons degrade via pair production. This leads to the emergence of showers of secondary particles which themselves decay further through interactions with the detector material until the energy of the shower particles falls under a critical value. Once this critical value is reached, the remaining energy is deposited in the detector either through ionization or thermal excitation (in case of electrons and positrons) or through Compton scattering and the photoelectric effect (in case of photons). In case of scintillation detectors, these excitations lead to the emittance of photons of a specific wavelength for which the material is transparent. For the ECAL of the CMS detector, the $PbWO_4$ crystals serve as scintillator and absorber material. The total energy deposit is then measured by measuring the number of emitted photons using photomultipliers.

There are essentially two specific characteristics governing the properties of such showers. One is the mean free path in the detector material, called radiation length X_0. It is defined by measuring the length of material needed for an electron traveling through to reduce its energy by $1/e$. This radiation length is a material-specific constant governing the longitudinal shape of the shower and that in a rough approximation scales like $X_0 \approx 180A/Z^2$, where A is the number of protons and neutrons in a nucleus and Z the number of protons. The second important property is the critical energy ϵ below which the cross sections for bremsstrahlung and pair production are smaller than for other energy loss processes. The critical energy is also material-dependent and is approximately anti-proportional to Z.

For the CMS ECAL, a small radiation length of 0.89 cm was chosen in order to place the relatively compact calorimeter inside of the magnetic coil. The mean transverse spread of the shower is given by the Molière radius $R_\mathrm{M} \approx 21\ \mathrm{MeV}\frac{X_0}{\epsilon}$ which is approximately 2.2 cm for the CMS ECAL.

To ensure that the whole shower will be contained in the ECAL even for high-energy particles, the length of the lead tungstate crystals is about $26 \times X_0$. Similar to the tracker, the ECAL is divided in a barrel region and an endcap region providing a total coverage of $|\eta| < 3.0$. The crystals in the barrel are further arranged to 36 supermodules containing 1700 individual crystals each.

An experimentally very important quantity is the energy resolution of the calorimeter, since it essentially sets the maximal precision of the energy measurement. The energy resolution can be parametrized with the following terms

$$\frac{\sigma(E)}{E} = \sqrt{\left(\frac{a}{\sqrt{E}}\right)^2 + \left(\frac{b}{E}\right)^2 + c^2}\ . \tag{3.9}$$

The contributions in equation (3.9) have different sources, where the three constants a, b, c depend on the specific detector. The $1/\sqrt{E}$ dependence is due to statistical fluctuations in the showering process and fluctuations in the number of photons detected in the photomultipliers and therefore called the stochastic term. The second term is the noise term and is mainly due to electronic noise in the readout chain. The third term is related to imperfections in the readout, the detector geometry or the aging of detector units. For the CMS ECAL, these

contributions to the resolution have been measured in electron test beams to be

$$\frac{\sigma(E)}{E} = \sqrt{\left(\frac{2.8\%}{\sqrt{E[\text{GeV}]}}\right)^2 + \left(\frac{12\%}{E[\text{GeV}]}\right)^2 + (0.3\%)^2} \,. \tag{3.10}$$

Hadron Calorimeter

Similar to the processes in the ECAL, hadronic calorimeters are designed to measure energies, this time the detector material has to be chosen to facilitate interaction with particles that do not interact primarily through electromagnetic interactions. Here, the interactions taking place are often mediated by the strong interaction, which allow the detection of both charged and neutral hadrons. However, energy measurements with hadronic calorimeters have two large caveats compared to electromagnetic calorimeters. Firstly, due to the production of neutral pions in the cascade a significant portion of energy gets deposited by purely electromagnetic interactions. This is due to the fact that the pions usually decay into two photons before they can interact strongly. For example for a 10 GeV hadron, about 30% of the total energy will be deposited purely electromagnetically. The second caveat is that a considerable amount of energy is deposited in neutrons or protons emitted in the shower. This means that the binding energy of these nucleons is "robbed" from the energy of the cascade resulting in a decline of the average response of the calorimeter compared to electrons of the same energy. This effect has to be corrected either by choosing appropriate thickness relations between the readout material and the absorber in sampling calorimeters or in the reconstruction. Similarly to the radiation length in the electromagnetic calorimeter, an interaction length λ_0 can be defined for hadrons.

The central hadron calorimeter (HCAL) at CMS [99] is a sampling calorimeter consisting of an active material (plastic scintillator) inserted between absorber plates made of a non-magnetic copper alloy (brass) with an interaction length of $\lambda_0 = 15$ cm. A schematic layout of a quarter slice of the HCAL is shown in Figure 3.7. To ensure maximal coverage of phase space, which is necessary for accurate measurements of invisible particles such as neutrinos, the HCAL consists of a barrel region and an endcap region that cover $|\eta| < 3.0$ as well as a forward calorimeter (HF) that covers a pseudorapidity region up to $|\eta| < 5.2$.

The HF is a Cherenkov detector chosen due to harsh requirements on radiation hardness in the forward region. Cherenkov detectors utilize the effect of light radiation from charged particles that travel faster than the speed of light inside the material of the detector. This has the effect that only charged particles with sufficiently high velocities can be measured in the forward region. The HCAL energy resolution was measured in test beams consisting of charged pions, electrons and muons over a larger energy range ($\approx 20 - 300$ GeV) and found to be

$$\frac{\sigma(E)}{E} = \sqrt{\left(\frac{115\%}{\sqrt{E[\text{GeV}]}}\right)^2 + (5.5\%)^2} \tag{3.11}$$

according to Reference [100].

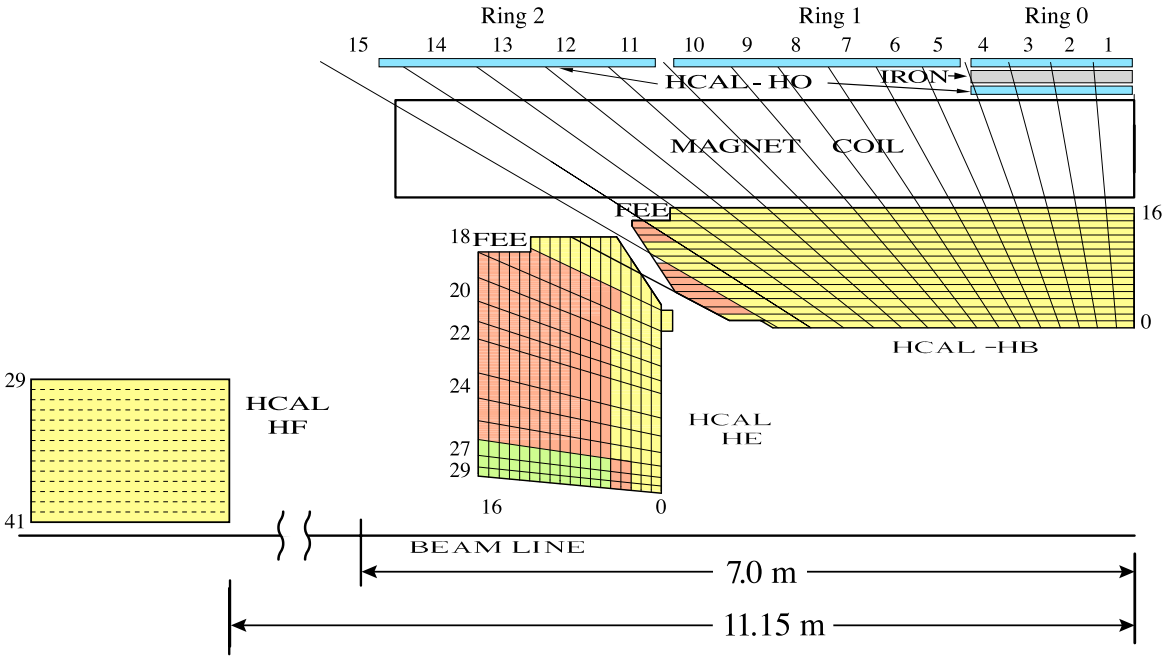

Figure 3.7.: The layout of the CMS HCAL (quarter slice), figure taken from [101]. The locations of the front end electronics is indicated by FEE, the rest of the calorimeter is split into the barrel region (HB), the endcap region (HE) and the forward region (HF). The outer detectors denoted with (HO) are located outside the magnet coil in order to catch the energy leakage from the HCAL barrel detectors.

3.2.3. Muon System

The muon detectors of the CMS experiment are situated outside of the superconducting solenoidal magnet forming the last layer of the detector. Muons, being approximately 200 times heavier than their first generation counterparts, have far smaller interactions with the detector material and therefore loose less energy because of bremsstrahlung. Muons are therefore the only particles that do not decay within the detector and do not get absorbed in the calorimeters. These properties are used by the CMS detector for muon identification and the precise measurement of muon energy and tracks by having the outer layer of the detector dedicated to muon identification and measurements. The muon detectors are in principle tracking detectors for muons passing through the whole detector thus providing an unambiguous method of muon identification and a very precise measurement of the muon properties with all subsystems of the CMS detector. The muon system consists of drift tubes (DT) in the barrel region, which are layered inside the iron return yoke, cathode strip chambers (CSC) in the endcap region and interleaved layers of resistive plate chambers (RPC) in both barrel and endcap regions. A schematic of the muon detectors is provided in Figure 3.8.

The DTs in the barrel region of the CMS detector achieve a spatial resolution of 100 µm in the (r,ϕ) plane and 150 µm in the (r,z) coordinate if at least three of the four layers can be used for track reconstruction. The RPCs provide a very good time resolution of about 3 ns but a poorer spatial resolution. These detectors are primarily used to provide a muon signal for the triggering of events.

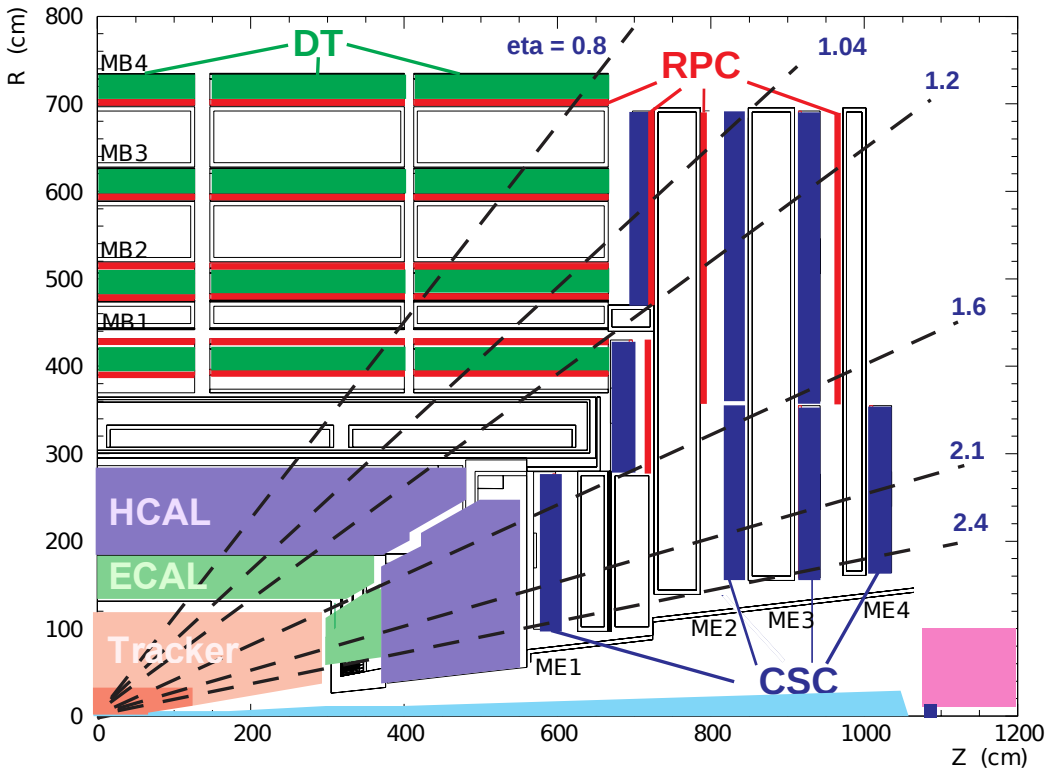

Figure 3.8.: A quarter slice layout of the CMS muon systems [102]. The situation of the components of the muon system are shown, namely the drift tubes (DT) in the barrel region, and the combination of cathode strip chambers (CSCs) and resistive plate chambers (RPCs) in the endcap regions.

3.2.4. Trigger and Data Acquisition

Since the LHC is usually operated with a bunch crossing every 25 ns, with around 20 collisions each, the amount of produced data exceeds the storage capabilities by far. Therefore, a system is needed that quickly distinguishes between interesting events, which should be kept for future analyses, and those that can be discarded. A decision on whether or not an event has an interesting signature which validates further analysis has to be made within milliseconds. For this purpose, the CMS detector has a two-level trigger system [104] consisting of the Level-1 (L1) trigger and the high-level trigger (HLT). An overview over the CMS data acquisition structure is shown in Figure 3.9. The L1 trigger is a hardware trigger implemented on custom hardware for example field programmable gate arrays (FPGA) which receive raw inputs from the subdetectors such as the calorimeters and the muon system, and additionally check for availability of subsystems. With the L1 triggers the data rate is reduced several orders of magnitude from 40 MHz to 100 kHz. For this, the L1 trigger thresholds are adjusted to the instantaneous luminosity of the LHC during data taking. The trigger decision to either keep or discard an event is done within 4 µs.

The HLT is software based and performs in a similar way as in offline data processing. Particles such as electrons, muons and jets are reconstructed with similar algorithms as used

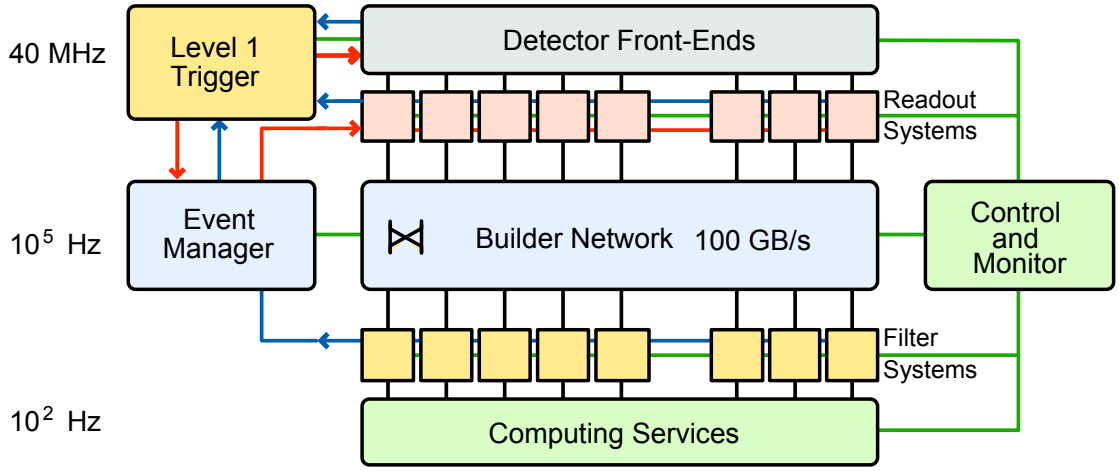

Figure 3.9.: Simplified schematic view of the CMS data acquisition system architecture taken from Ref. [103]. The data rate is reduced to 100 kHz by the Level-1 hardware triggers to search for events with interesting signatures. From there, standard computing farms are used for a simplified reconstruction and further reduction of events by high-level triggers. The event rate is reduced to a maximum of around 10^2 Hz (around 10^3 Hz for the data taking period of 2016-2018) of events being stored for the final analyses.

for the full event reconstruction with a per-event time budget of 175 ms. The reconstruction is based around trigger paths, which run a set of processing steps in a predefined order while simultaneously making selection cuts on the reconstructed objects in each step of the trigger path, thus reducing the processing time by reconstructing the event in increasing order of complexity.

3.2.5. Computing Infrastructure

After the final trigger decision is made, the selected events still have to be stored and processed for physics analyses. The computing requirements for the CMS experiment are enormous and very hard to fulfill with a single on-site computing center. Therefore, a distributed model consisting of a network of worldwide computing centers operated in a hierarchical structure is created. The so called Worldwide LHC Computing Grid (WLCG) [105, 106] distributes the collected data to analysis groups worldwide, thus ensuring a smooth operation.

The WLCG has a hierarchical structure with one Tier-0 center at the CERN laboratory, 13 Tier-1 centers around the world — one of them at the KIT — and many more Tier-2 and Tier-3 centers. In Figure 3.10, a schematic overview over the grid structure is provided.

The primary task of the Tier-0 center is the safekeeping of the raw detector data as well as a first pass at reconstructing the events. These data get distributed to the Tier-1 centers, via an optical-fiber network working at 10 Gbs^{-1}. The Tier-1 centers distribute data to Tier-2 centers, store raw and processed data from CERN and process the raw data further. Tier-2

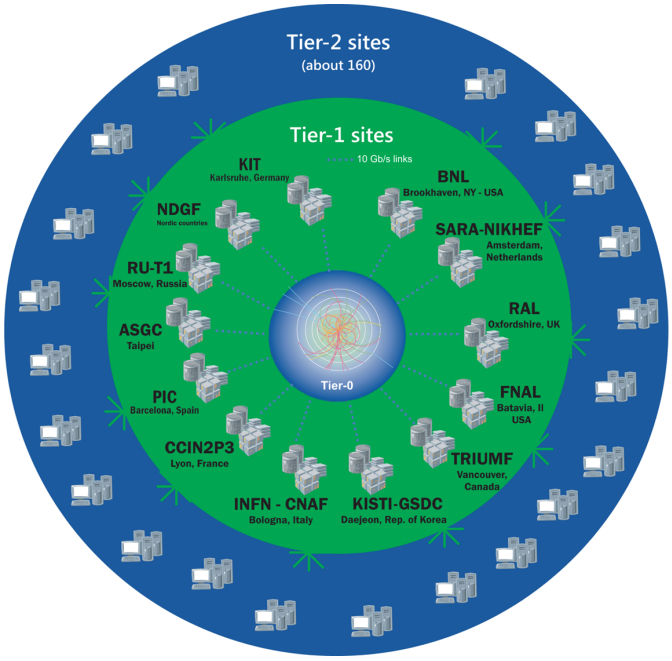

Figure 3.10.: Illustration of the computing infrastructure used by the CMS experiment, which is part of the Worldwide LHC Computing Grid (WLCG) as shown in Reference [105].

centers are usually university clusters capable of handling the production of simulated events. Scientists can also gain access to the grid infrastructure through local (Tier-3) computing resources.

4. Event Reconstruction and Simulation

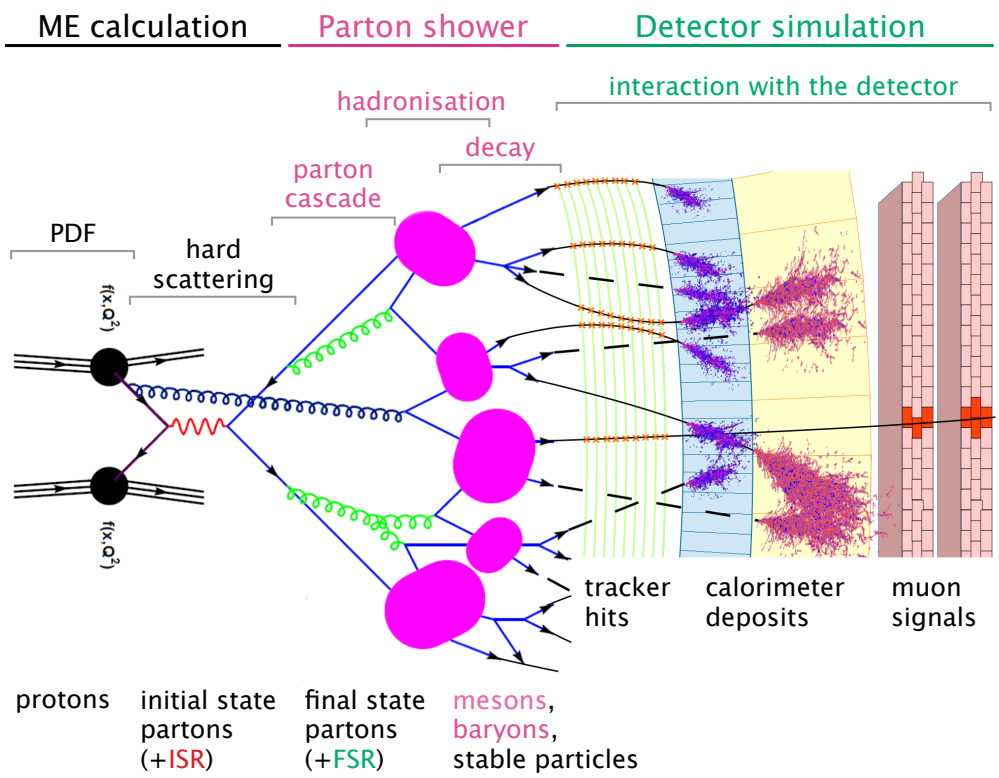

Figure 4.1.: A schematic view of the stages of MC event generation. Figure taken from Ref. [107].

Measurements of SM properties and searches for new particles alike depend on the ability to precisely predict SM interactions. In order to find differences with respect to the SM expectation, it is necessary to know what these expectations are and how exactly they manifest for the LHC. Generating these predictions is a complex involved process that takes a great deal of computational power. Since particle physics deals solely with quantum mechanical processes, a precise prediction of the outcome of an experiment on an event-by-event basis is not possible. Theory predictions therefore provide probability distributions to predict the result of a measurement (in this case a collision), from which a set of events is sampled using MC methods [62]. The final prediction has to be compared with results as measured in the detector, which requires the addition of a showering and hadronization step and a full detector simulation. This is described in detail in Section 4.1. From the detector response, both in data and simulation, actual physical particles like electrons and muons, are reconstructed, in order to analyze the measurements. The procedure of reconstructing events is described

in detail in Section 4.2 for the CMS detector. Figure 4.1 shows a schematic overview of the simulation stages needed for the MC simulation of LHC processes.

4.1. Characteristics of Proton-Proton Collisions

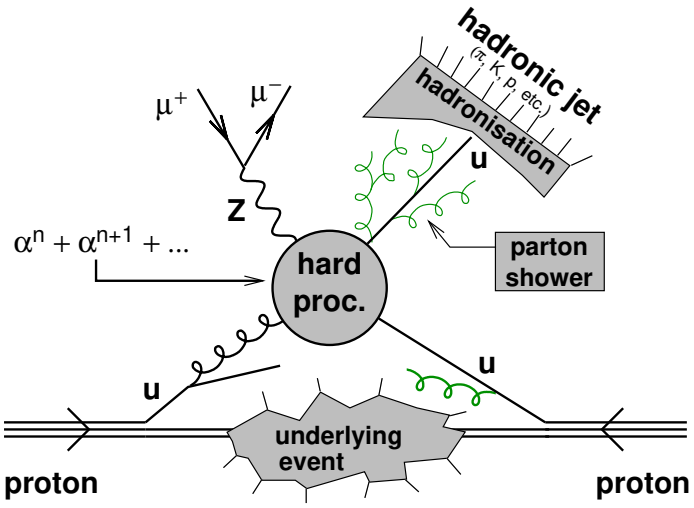

Figure 4.2.: A schematic representation of a proton-proton collision, taken from Ref. [108]. In addition to particles from the hard scattering process, initial- and final-state radiation and particles coming from the underlying event make up the full event.

The simulation and theoretical description of a proton-proton collision has a number of challenges some of which are not present at e^+e^- colliders such as LEP. For instance the choice of protons as particles accelerated in the collider means that the LHC is able to reach hitherto inaccessible center-of-mass energies, but on the other hand the description of the processes taking place in the collisions becomes harder. This is due to the composite nature of the proton, the partons, i.e., constituents of the proton, are the ones partaking in the theoretically predictable hard scattering. This makes it necessary to model the composite structure of the proton, in order to make accurate predictions. Once predictions exist for the parton structure of the proton and the hard scattering process, showering and hadronization models have to be applied and the decays of primary particles have to be taken into account in order to deduce a final state as is expected to manifest in the detector. Figure 4.2 shows a visualization of the subprocesses necessary for a precise simulation of proton-proton scattering events. The theoretical description of LHC physics relies on the fact that all the described steps can be factorized.

4.1.1. Hard Process

The parton interaction with the highest momentum transfer in an event is the so called *hard process*. It can be calculated theoretically in perturbation theory, starting from quantum field theories such as the SM. Due to asymptotic freedom, strong interactions can be calculated in

a perturbation series as well. Although the development of future MC generators goes in the direction of including more scattering particles and detailed theory calculations for a large number of processes, most MC generation is of the form of $2 \to \mathrm{X}$ scattering. The differential cross section of the hard scattering process of interest is then given by

$$\mathrm{d}\sigma\left(k_1, k_2 \to \sum_n p_n\right) = \frac{|\mathrm{ME}|^2}{4\sqrt{(k_1 \cdot k_2)^2 - m_1^2 \cdot m_2^2}}\mathrm{dLIPS}\ , \tag{4.1}$$

where LIPS denotes the Lorentz-invariant phase space, ME is the matrix element calculated at fixed order in perturbation theory, k_i are the momenta of the initial particles, m_i their masses, and p_i the momenta of the final particles. When the prediction of the differential cross section of a process is calculated only to first order in this perturbation series it is called a leading-order (LO) cross section. The perturbation series is an expansion in $\alpha \cdot \ln(\frac{Q^2}{\mu^2})$, with the running coupling constant α, the transfer energy scale Q of the scattering, and the renormalization scale μ. Increasing the number of terms in this series is called next-to-leading order (NLO) and next-to-next-to-leading order (NNLO) calculations. Adding more terms in this expansion series makes the computation more resource-expensive and theoretically challenging. Each order contains more terms of both real and virtual contributions with infrared divergences that have to be carefully cancelled between these two contributions and ultraviolet divergences that have to be handled in a renormalization scheme. In the LHC research program, LO (NLO) usually refers to QCD processes only, i.e., to the perturbation term reached for strong interactions. However, in principle there are corrections for higher order electroweak processes as well. The fact that only a finite number of diagrams in this perturbation series is considered for theoretical predictions is a source of systematic uncertainty of the prediction.

4.1.2. Underlying Event

Since the LHC deals with proton-proton collisions, there are partons present in the collision that do not directly take part in the hard scattering process. However, these partons are still capable of secondary interactions either by scattering among themselves or even by interacting with the final state particles of the hard scattering process. This can lead to secondary particles measured in the detector. The contributions to the event of the proton constituents not taking part in the hard scattering are called underlying event (UE) and have to be modeled in MC generators as well. Simulation models for the UE are phenomenological since the interactions taking place are mostly soft scatterings where a perturbative expansion might not be possible. The models are tuned to measurements from the ATLAS and CMS experiments [109] in order to provide accurate descriptions of UE physics.

The event generation also has to deal with *initial-* and *final-state radiation*, which denotes the possibility of the partons of the hard scattering event to emit real particles either before or after the hard interaction. Initial-state radiation decreases the energy available to the scattering, while final-state radiation influences the expected final state, therefore the overall topology of the event is subject to change. If this radiation would be considered in its enterity, the calculation of higher order corrections would be necessary. However, in practice the most important contributions to this radiation originate from collinear and soft emissions which are dealt with by using parton showers.

4.1.3. Parton Distribution Functions

Since the proton is a QCD bound state, its structure cannot be directly determined from theory calculations, since in this coupling regime perturbation theory is not applicable. However, for precise predictions of interaction processes at the LHC it is necessary to know the probability of a parton to carry a particular momentum fraction x of the proton momentum.

A set of distributions called the parton distribution functions (PDFs) are defined to bridge the aforementioned gap in the knowledge of proton-proton scattering processes. They depend on the momentum fraction x carried by the parton, the energy scale μ^2 at which the scattering process takes place and the parton flavor. These functions cannot be calculated from first principles but have to be determined using experimental data from deep inelastic scattering at colliders. Using that the full scattering cross sections are independent of the ultimately unphysical factorization scale μ, a set of differential equations can be derived called DGLAP equations[1], which can be used to extrapolate the PDFs to high energy scales.

The PDFs used for predictions of scattering events at the LHC are either a set of empirical functions or neural networks [110–112] which are determined using deep inelastic scattering cross section measurements. Figure 4.3 shows the NNPDF3.1 PDF set at an energy scale of $\mu^2 = 10\,\mathrm{GeV}^2$ (left) and $\mu^2 = 10^4\,\mathrm{GeV}^2$ (right). The MC simulation samples used in this thesis were either calculated using this PDF set or the slightly older version NNPDF3.0.

The cross sections are calculated using PDFs $f_i(x, \mu^2)$ as

$$\mathrm{d}\sigma(\mu^2, s) = \int f_{i_1}(x_1, \mu^2) f_{i_2}(x_2, \mu^2) \mathrm{d}\sigma\left((x_1 s), (x_2 s)\right) \mathrm{d}x_1 \mathrm{d}x_2 \ , \tag{4.2}$$

where $i_{1/2}$ denotes the quark or gluon flavor of the initial state particles, $x_{1/2}$ is the momentum fraction of particle 1/2 and σ is the hard scattering cross section from equation (4.1).

4.1.4. Pileup

In order to ensure a sizable collision cross section at the LHC, the protons are accelerated in so-called bunches, with one bunch containing of the order of 10^{11} protons. This leads to multiple proton-proton interactions during one bunch crossing, thus particles from secondary interactions are also measured in the detector. This additional noise source is called pileup. Pileup leads to tracks and energy deposits in the detector that do not come from the primary event and can therefore distort the measurement. Two different kinds of pileup can be distinguished. The first is in-time pileup, which originates from scattering processes happening at the same bunch-crossing as the primary process. The second is called out-of-time pileup and denotes events from a different bunch crossing that get associated with the primary event due to the finite temporal detector resolution and response time. In simulation, the contribution from pileup is modeled by adding total inelastic proton-proton collision events to the simulation. Additional differences in the amount of pileup between simulation and

[1] DGLAP stands for Dokshitzer, Gribow, Lipatow, Altarelli and Parisi, who derived these differential equations independently.

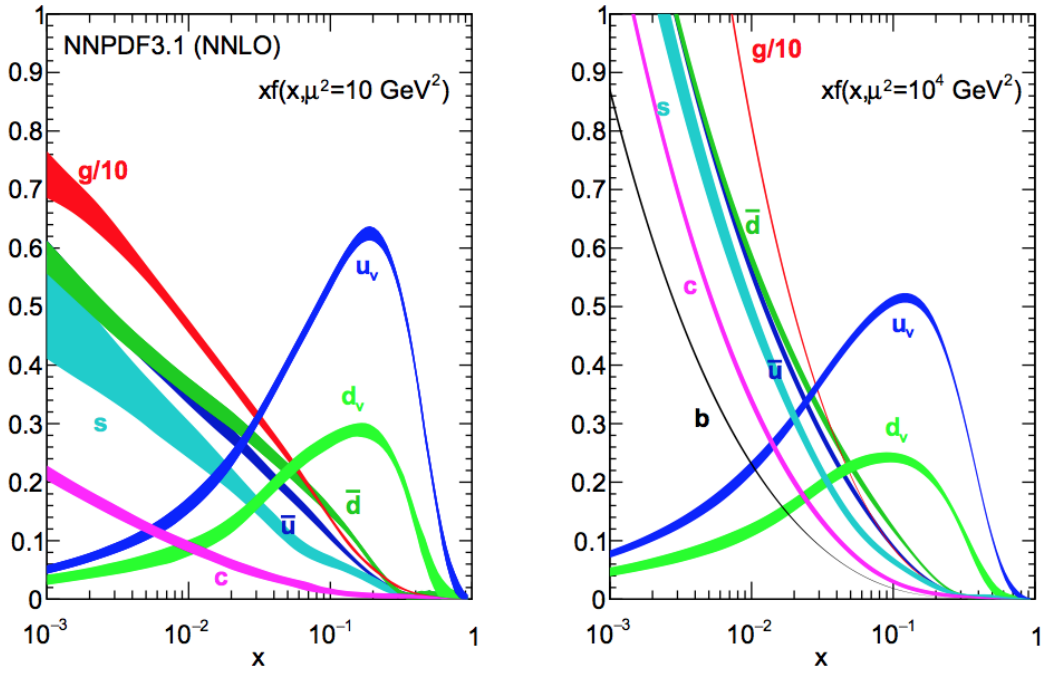

Figure 4.3.: The NNPDF3.1 parton distribution functions, taken from Ref. [112]. On the left hand side, the PDFs are shown at a low energy scale of $\mu^2 = 10$ GeV^2. On the right hand side, the PDFs are propagated to the higher energy scale of $\mu^2 = 10^4$ GeV^2.

data are corrected by reweighting the number of pileup events in simulation to the one found in data.

4.1.5. Parton Showers and Hadronization

Showering is added to the generated events in order to describe real final- or initial-state radiations, that are not included in the caculation of the matrix element itself. This process includes emissions mediated by all forces of the SM, however since an all-jet final state is considered here, parton showers and the formation of jets are of greater interest for this thesis.

Due to the phenomenon known as confinement, no color charged particles can exist on their own. Instead, an energetic color charged particle will generate new, mostly also color charged particles, in a process called showering until the individual particles in the shower have a low enough energy to start forming colorless hadrons. Such a shower of hadrons that reaches the detector is mostly contained in a cone around the original parton direction and is called a *jet*. The process of hadronization cannot be calculated from QCD directly since the energy scales involved here are in a regime where perturbation theory breaks down.

The parton shower describes the scale evolution from the initial high energies of the partons

produced in the hard scattering to an energy scale of around 1 GeV, where the confinement of the partons into hadrons begins. One of the most important aspects to note here is that this showering process factorizes from the hard scattering itself and can therefore be calculated separately from the matrix element calculation. As a consequence, the shower itself does not depend on the actual hard scattering taking place. It is also important to note that the number of particles emitted in the shower is ill-defined, i.e., there might be an infinitely high number of partons with infinitely low energies. However, the number of *measurable* partons above a certain energy threshold is well defined and finite. Similar to this, there is a second divergence in the emission of collinear partons, but also here the finite resolution of any real experiment comes into play, meaning that in order to calculate properties with physical meaning, it has to be taken into account that at some point two very collinear particles cannot be distinguished from each other anymore. Since these parton emissions are not only factorizing from the hard scattering, but are also independent of each other, a parton shower generator then iteratively creates new shower partons for each parton line according to the probability to emit a parton of a certain energy q from that line. This emission probability is large, both in the soft and collinear limits, which are used in the generation of such showers. Whenever a desired final state strongly depends on hard multijet final states, the hard scattering should therefore be calculated to higher orders. When using higher order calculations of the matrix element interfaced with a showering algorithm, the double counting of emissions has to be avoided and therefore a careful *matching* [113] has to be applied.

After the partons reach a certain energy threshold through the showering, hadronization, i.e., the clustering of partons into color-neutral hadrons, begins. There are two main models of hadronization that are commonly used: the Lund string model [114–116] and the cluster model [117]. The starting point for the Lund string model is the linear confinement expected at large distances between partons. In principle, this model assumes a linear potential between two quarks in the event, called a "string". Gluons have two attached "strings". When the distance between the partons grows larger than around 1 fm, the "string" breaks and creates a new quark-antiquark pair. These partons then form hadrons together with the initial partons in the event. This procedure is iterated until there are no "free" partons left in the event. A key feature of this model is its soft and collinear safety meaning that the results of hadronization do not depend on the choice of the energy cut-off in the shower generator. Cluster models are based on a universal property of the color structure of a shower, which can be used to find color singlet clusters with a computable mass distribution. These clusters, together with an enhanced splitting of gluons into quarks, are utilized to build final state hadrons. Here a large number of excited hadronic states are formed from the clusters and subsequently decayed into the final state hadrons. Both string and cluster models usually exhibit a number of parameters that can be adapted to more closely reproduce measured data, called tuning.

4.1.6. Monte Carlo Event Generators

There are many MC event generators distinct in their implementation, some, including POWHEG and MADGRAPH5_AMC@NLO are matrix element calculators; their output in the Les Houches (LHE) event format [118] is easily interfaced with parton shower generators such as PYTHIA8. Other generators are general-purpose event generators and can be used for the full event simulation including showering and hadronization. A more complete overview of existing MC event generators for high energy physics at the LHC and

their methods can be found in Ref. [119].

MadGraph5_aMC@NLO

The MadGraph5_aMC@NLO [120, 121] event generator is used to calculate LO or NLO matrix elements for SM processes, or for exotic models when interfaced with additional packages. MadGraph5_aMC@NLO is capable of simulating the phase space including PDFs and initial- and final-state radiation. In combination with MadEvent, it is also possible to calculate LO cross sections for the given process. In this thesis, the MadGraph5_aMC@NLO event generator is employed for the simulation of bulk graviton and HVT signals at LO [122, 123] as well as for the simulation of SM QCD multijet and V+jets production at LO.

Pythia8

Pythia8 [124] is a general-purpose event generator, but can also be utilized as a shower generator and interfaced with other matrix element calculators. Since Pythia8 can only calculate the matrix element at LO accuracy, it is often used in combination with generators such as MadGraph5_aMC@NLO or Powheg, that provide NLO accuracy, which is made possible by Pythia8's p_{T}-ordered showering. The hadronization in Pythia8 is performed based on the Lund string model. Pythia8 includes the calculation of the underlying event which is modeled using different tunes, i.e., adaption of a set of phenomenological parameters to data, such as the CUETP8M1 [125] and CP5 [126] tunes which are used in this analysis.

Powheg

The event generator Powheg [127, 128] provides NLO accuracy in QCD. Powheg calculates the hardest radiations with NLO accuracy, while soft radiation is calculated at LO. It can therefore be interfaced with any shower generator that provides either p_{T}-ordered showers or is capable of including a p_{T} veto. In this thesis, Powheg interfaced with Pythia8 is used for the generation of QCD multijet events with NLO accuracy.

Herwig++

Herwig++ [129] is another multipurpose event generator, i.e., capable of simulating the matrix element, the underlying event, and the showering and hadronization process. As opposed to Pythia8, this generator uses angular-ordered showers and makes use of the cluster hadronization model. In this thesis, Herwig++ is used to generate an independent sample of QCD multijet processes using the CUETHS1 tune [125].

Geant4

All MC event generators have to be interfaced with a detector simulation before their results can be compared to data. The CMS detector is simulated using the Geant4 software [130, 131]. Geant4 simulates the interactions of the collision particles obtained with MC event generators with matter, including ionization, bremsstrahlung losses, multiple scattering effects, and the hadronic and electromagnetic showering taking place in the calorimeters.

4.2. Event Reconstruction

Event reconstruction in the CMS experiment utilizes the so called *particle flow algorithm* (PF), which iteratively combines information from all subdetectors to form high-level physics objects such as muons, electrons or jet candidates. A more detailed description of the PF algorithm in CMS can be found in Ref. [132, 133]. The general idea of PF is as follows: starting from subdetectors, the algorithm reconstructs tracks, vertices, and clusters energy deposits into *PF elements*. The elements are then combined to *PF blocks* by testing for matches of different elements, for example tracks that lead to energy deposits. From this list of blocks, physical particles are reconstructed in sequence starting from the muons which are easiest to identify. The blocks corresponding to a reconstructed muon are then removed from further reconstruction steps. Following the muon reconstruction, electrons, photons and lastly neutral and charged hadrons are reconstructed each with dedicated algorithms and removing blocks used for the reconstruction of a physical object from the further processing chain. Lastly, the PF candidates are used in jet clustering. This approach to reconstruction allows for an outstanding performance for jet reconstruction, electron and muon identification and determination of missing transverse energy, as well as for a natural integration of efficient pileup mitigation methods. In the following sections, the principle of operation for the different reconstruction algorithms is explained in more detail.

4.2.1. Track Reconstruction

Reconstructing particle tracks from hits in layers of detector material has a very high combinatorial complexity. To tackle this task, the *Combinatorial Track Finder* (CTF) is applied to the detector data. The CTF uses a sequential reconstruction procedure, starting from high-p_{T} tracks with many associated hits which are subsequently removed from the reconstruction process. In detail, the track reconstruction starts from the innermost layers of the pixel detector. From there, seeds for the track reconstruction are identified which consist of at least three hits in the pixel detector. The algorithm then uses Kalman filters [134] to extrapolate the track to the next detector layer. Kalman filters provide a prediction of the most likely position of the next detector hit for the track belonging to the seed in question. When possible hits are found, they are added to the track and the prediction of the Kalman filter for the next hit can be updated, thus providing a better prediction for the next iteration of the filter. This method also allows a compensation of missing hits in detector layers. The track reconstruction stops either when the tracks leave the tracking detectors or the p_{T} of the track falls below a threshold value. After this first pass at reconstructing the trajectory, a second more refined Kalman filter is used to determine the most probable track for the given hits. These hits are then removed from the rest of the particle track reconstruction. In the end, only tracks are kept that pass a variety of quality criteria such as the χ^2 of the track fit, the quality of the track seeds or the compatibility of the track originating from the primary vertex. The overall track finding is optimized to have a high track reconstruction efficiency while keeping the misreconstruction rate low. There are also filters run with displaced tracks mostly to recover tracking efficiency for interactions of the primary particle with nucleons in the tracker material. Due to the increased energy loss caused by bremsstrahlung, there is an additional separate algorithm to reconstruct electron tracks.

4.2.2. Vertex Reconstruction

After all particle tracks are reconstructed, their points of origin, i.e., the position of the vertices where the tracks originate are reconstructed, see Ref. [135]. The first goal of vertex reconstruction is finding the primary vertex, the point in the beam pipe where the hardest interaction of the bunch crossing took place. Per definition, the primary vertex is the crossing point found in the reconstruction with the highest p_{T} sum of associated tracks, weighted with a goodness-of-fit value for each track. In addition to the primary vertex, it is important to reconstruct secondary vertices as well, since particles originating from a different interaction need to be removed from the event with various pileup removal techniques.

For the vertex reconstruction, only tracks fulfilling quality requirements are clustered based on their z-coordinates at the point of their closest approach to the center of the beam spot. This clustering uses a *deterministic annealing* (DA) [136] algorithm, which finds a global minimum for a problem with many degrees of freedom and therefore allows the reconstruction of any number of vertices. Starting from this assignment of tracks to vertices, the position of the vertex is then fitted using an *adaptive vertex fitter* [137] if there are at least two tracks associated with the vertex. According to their probability to genuinely originate from the vertex in question a weight derived from the DA clustering is assigned to each track.

4.2.3. Energy Reconstruction

In the ECAL and HCAL, energy clusters are formed separately starting from cells with a local maximum of deposited energy above an energy threshold. Surrounding cells are then combined into one cluster until the energy deposited in a cell falls below two times the resolution of the calorimeter. Starting from these clusters, the (η, ϕ) coordinates of the energy deposit are determined as accurately as possible. Here it is assumed that the energy in the clustered calorimeter cells is deposited as a Gaussian energy deposit by a number of particles equal to the number of initial seeds. The position of the Gaussian energy deposits is then fitted and the fit parameters are used as final cluster parameters. Later, this information is used again in the reconstruction of PF candidates, starting with charged particles, where traces in the tracker can be associated with the energy deposits found.

4.2.4. Long-Lived Leptons

Muons
Muons are the first kind of particles to be reconstructed by the PF algorithm because of their relatively clear signatures in the detector. The centerpiece of muon reconstruction is linking hits in the muon chambers to tracks in the inner tracker of the CMS detector. The hits in the muon system are used to reconstruct standalone trajectories for muon candidates which are then extrapolated to the tracker and matched with trajectories reconstructed there. If insufficient hits to reconstruct a standalone track in the muon system are present, a second reconstruction step can also match muon tracks starting from the inside out. This second method is mainly used for low-p_{T} muon candidates.

Electrons
The electron reconstruction aims not only to match trajectories in the tracker to energy deposits in the ECAL but also to properly match energy deposits from bremsstrahlung photons to the electron candidates. Since a considerable amount of energy can be lost due to bremsstrahlung, electron track reconstruction requires a second pass over tracker hits (using tracks with a too large χ^2 value of few registered hits) with a dedicated algorithm that takes this additional energy loss into account. For electrons with $p_{\mathrm{T}} < 5\,\mathrm{GeV}$, these recalculated tracks are then matched to energy deposits in the ECAL. For high-p_{T} electrons, the reconstruction starts from PF clusters in the ECAL that exhibit a spread of energy in ϕ as would be expected from the bremsstrahlung photons originating from the particle trajectory and are matched to a corresponding track.

4.2.5. Photons, Charged Hadrons and Neutral Hadrons

For neutral particles, no corresponding track in the tracker can be found, i.e., isolated photons are energy clusters with no matched particle trajectory, which also are not associated to an electron track as a bremsstrahlung photon and not in immediate vicinity of any other energy deposit or particle track. All remaining ECAL and HCAL clusters that cannot be linked to a trajectory are turned into candidates for neutral hadrons. For the position measurement of those particles, only information from the calorimeters can be used, therefore giving a worse resolution compared to charged particles. If an ECAL and HCAL cluster can be linked, the total energy deposited in both calorimeters is assumed to be caused by the same neutral hadron traveling through both detectors. Every HCAL cluster that can be linked to particle tracks is a candidate for a charged hadron, however if the energy deposited in the HCAL is much smaller than the energy calculated from the associated tracks, a second search for a muon associated to one of the high-p_{T} candidate tracks is started further increasing the muon identification efficiency.

4.2.6. Missing Transverse Momentum

In the last step, the missing transverse momentum ($p_{\mathrm{T}}^{\mathrm{miss}}$) is calculated as

$$p_{\mathrm{T}}^{\mathrm{miss}} = -\| \sum_{k} \vec{p}_{\mathrm{T},k} \| \ , \tag{4.3}$$

with the transverse momentum of the k-th particle $\vec{p}_{\mathrm{T},k}$ and summing over all reconstructed PF objects originating from the primary vertex. Especially muons coming from simultaneous cosmic muon events have to be cleared from the event to guarantee a correct calculation of the missing transverse momentum. The missing transverse momentum can be used in the reconstruction of neutrinos produced in the event or in searches for new particles like dark matter candidates that are not expected to interact with the detector. The general idea behind this quantity is that the transverse momentum of the partons in the hard interaction is negligibly small, since the protons in the collision have a negligible transverse momentum, thus the sum of all transverse particle momenta from the primary interaction add up to zero, barring either invisible particles or detection inefficiencies.

4.2.7. Jets

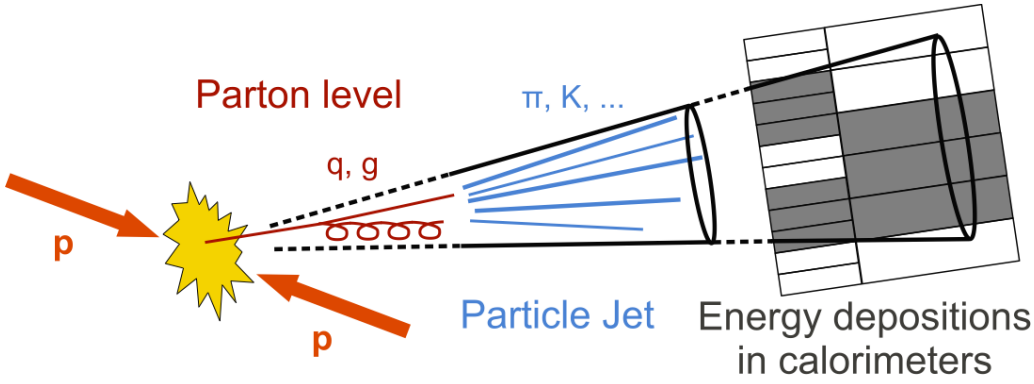

Figure 4.4.: A sketch of how the partons in a proton-proton interaction are clustered into a jet of secondary shower particles, taken from Ref. [138].

In the end, the quantities needed in the final analysis are the properties of the partons from the hard interaction. In case of long-lived particles like muons and electrons, this is a matter of simply reconstructing the particles. When the partons in the hard interaction are quarks or gluons, this is another matter entirely. Because of confinement, quarks and gluons are not the final state particles found in the detector, but rather the starting point of a shower of secondary particles that hadronize into color-neutral particles which are finally found in the detector. In order to reconstruct the momentum, energy, and direction of the initial parton, all secondary particles coming from its shower have to be found and clustered into one object. These objects are called jets and are used to infer the true parton properties, see Figure 4.4. There are a number of ways to consistently cluster the particles identified by the PF algorithm into jets but all algorithms should fulfill the requirements of collinear and infrared safety, i.e., the jet clustering should be robust against soft radiations and against a collinear splitting of their constituents. Some illustrative examples can be found in Figure 4.5.

Two classes of jet clustering algorithms can be distinguished: cone-based algorithms such as *Iterative Cone* or *SisCone* [140], and sequential clustering algorithms like *Cambridge-Aachen* (CA) [141] and anti-k_{T} [142]. The CMS Collaboration most prominently utilizes the anti-k_{T} and CA algorithms [143]. Although all of the aforementioned algorithms have their uses, in this thesis only the anti-k_{T} algorithm will be used and therefore discussed in detail.

The anti-k_{T} algorithm iteratively combines each PF object with its nearest neighbor into pseudo-jets using the distance measure given in equation (4.6). This procedure is repeated until the distance of the pseudo-jet to the nearest particle is greater than the distance to the beam $d_{i\mathrm{B}}$. In this algorithm the distance d_{ij} between objects is defined as

$$d_{ij} = \min(k_{\mathrm{T},i}^{2n} k_{\mathrm{T},j}^{2n}) \frac{\Delta_{ij}^2}{R^2} \ , \tag{4.4}$$

$$\Delta_{ij}^2 = ((y_i - y_j)^2 + (\phi_i - \phi_j)^2) \ , \tag{4.5}$$

$$d_{i\mathrm{B}} = k_{\mathrm{T}i}^{2n} \ , \tag{4.6}$$

where R is a radius parameter, and $k_{\mathrm{T},i}$ is the transverse momentum of object i. In the case of the anti-k_{T} algorithm, the parameter n is fixed to -1, while the CA algorithm uses a value

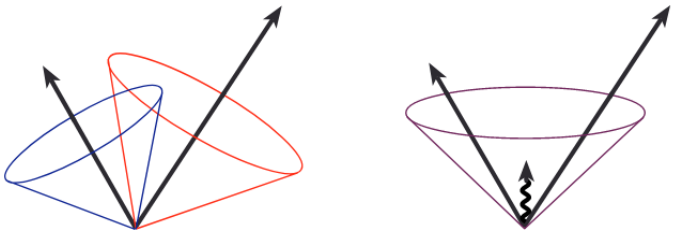

(a) An example of misclustering of jets due to the radiation of an additional soft particle which leads to the clustering of the contributions of two partons into one jet.

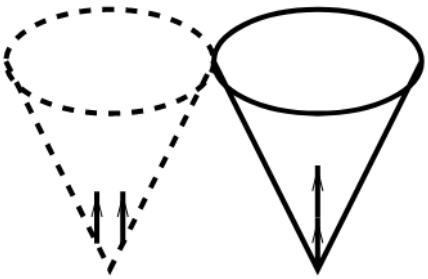

(b) Due to a collinear splitting, the jet energy is distributed into two detector cells and therefore the energy threshold for seed clustering are not met anymore.

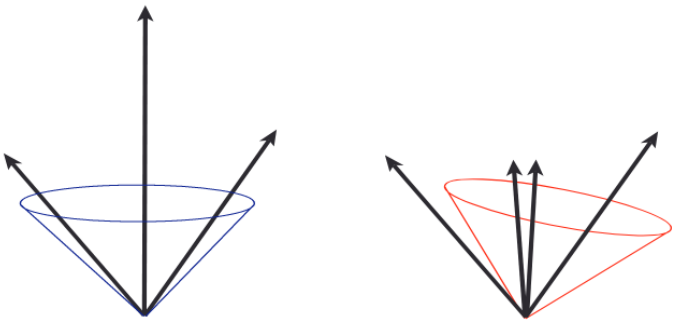

(c) The collinear radiation of an additional particle might lead to different jet outcomes by changing the particle with highest momentum.

Figure 4.5.: An illustration for the need of infrared and collinear safety in the clustering of jets, taken from Ref. [139].

of $n = 0$ but otherwise works in the same way. This clustering is per definition collinear- and infrared safe. The parameter R determines the size of the jets in the (y, ϕ) plane and is further on in this analysis chosen to be 0.8 in order to contain all constituents from highly boosted vector boson decays. Jets with such a large radius parameter for the clustering are called *fat jets*. Jet algorithms can in simulation also be applied to the generated particles after the showering and hadronization step, but before applying the detector simulation. Jets clustered in such a manner are called *generator jets*.

Jet Energy Corrections

Before the jets can be used in a final analysis, they need to be calibrated to the correct energy scale and residual dependencies of the measured energy on the p_{T} or η region of the jet need to be removed in order to relate the energy of reconstructed jets to the true particle level energy. This is carried out by a series of corrections for different effects, for a detailed description of these corrections used in the CMS experiment, see Ref. [144, 145]. The jet energy furthermore strongly dependend on the number of additional pileup interactions, which can result in particles being clustered into the reconstructed jets that did not originate from the primary vertex. The jet corrections also aim to remove this pileup dependence. In Figure 4.6, the stages of jet energy corrections as they are applied to jets in the CMS experiment are shown.

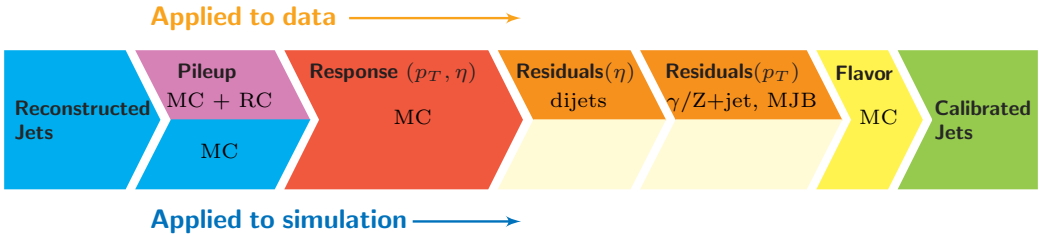

Figure 4.6.: Consecutive stages for jet energy corrections of the CMS collaboration as applied to MC simulation and data. As a first step, pileup corrections based on studies in MC are applied. Additional p_{T}- and η-dependent corrections to adjust the detector response to that simulated in MC events are applied. In the next step, residual corrections based on specific well-known processes in data are applied to the jets. If necessary, another set of flavor-dependent corrections can also be applied [144].

First, the *L1* corrections are applied, which subtract energy in the event evoked by pileup effects using a jet area approach, based on the calculation of the average p_{T} density ρ per unit area which characterizes the soft radiation activity in the event. The reconstructed jets are in a second step corrected to compensate for the non-linear response of the calorimeters as a function of p_{T} and η (*L2L3* corrections). These corrections are derived from simulation and the offset energy is compared to data in random total inelastic pp events using a random cone algorithm. Lastly, small residual corrections are derived based on measurements of the relative scale as a function of η from dijet events and in the detector central region the absolute scale is corrected from measurements of Z+jets events. These corrections are called *L2L3Residual*.

Pileup Removal

An important part of jet calibration is the removal of particles originating from pileup [146]. In the 2016 data taking period, an average number of 27 pileup vertices per event were observed. Here, a combination of an area based pileup subtraction for neutral hadrons as well as the PF based *Charged Hadron Subtraction* (CHS) technique [147] is used for pileup removal. CHS is based on PF objects for which the track reconstruction can be used to calculate

whether or not they originated from the primary vertex. PF objects clearly originating from a secondary vertex are removed from the event. For the data taking period of 2017, an average of 38 pileup events are measured in the CMS detector which makes the usage and application of better pileup removal methods necessary. To this purpose, *Pileup per Particle Identification* (PUPPI) [148] is used. PUPPI assigns a probability value to each particle in order to classify how pileup-like a particle is. This is calculated using the collinear versus soft radiation structure surrounding the particle. The weights derived from the PUPPI algorithm are used to scale the particle four momenta, thus reducing the influence of pileup-like particles on the jet. For each particle, the shape value α

$$\alpha_i = \log \sum_j \frac{p_{\mathrm{T},j}}{\Delta R_{ij}} \times \theta(\Delta R_{ij} - R_{\mathrm{min}}) \times \theta(R_0 - \Delta R_{ij}) \ , \tag{4.7}$$

where θ is the Heaviside step function, $p_{\mathrm{T},j}$ is the transverse momentum of the j-th particle which has to be closer than R_0 to the particle i but farther away than R_{min}, and ΔR_{ij} is the (η,ϕ) distance between particle i and j. The weight applied to the particle four-momenta is calculated as the squared difference between α_i and the mean of this shape variable calculated from charged pileup particles, divided by the squared RMS of the α distribution in pileup.

B tagging

The procedure to classify jets according to their probability of originating from a bottom quark is called b tagging. The technique uses the relatively long lifetime of B mesons. This long lifetime originates from the suppression of the decay to up and charm quarks, due to the small CKM matrix element, while the decay to the top quark is suppressed because the top quark mass is larger than the B meson mass. This results in a displaced secondary vertex inside of the jet, which can be resolved by the tracker if the distance between primary and secondary vertex is large enough. This analysis uses the Combined Secondary Vertex (CSV) algorithm [149,150] to obtain an orthogonal $\mathrm{t\bar{t}}$ enriched data set for scale factor measurements. The CSV algorithm combines information about track parameters and secondary vertices of the jets into a likelihood discriminant, thus providing a method to discriminate jets coming from a b quark, from those originating from a light quark, gluons, or charm quarks. There are different working points (WP) for the CSV algorithm, which are defined as the values of the b tagging discriminant that achieve a certain mistag rate. If a jet coming from light quarks is misidentified as a b jet, the jet is considered to be *mistagged*. In this thesis the CSVv2 medium working point [149] is used, which has a misidentification probability of about 1.5%. In Figure 4.7, a schematic of a jet containing a secondary vertex is shown.

Jet Grooming

In many analyses, especially if they deal with the identification of highly boosted particles that decay hadronically, such as hadronic top decays, W, Z, or H boson decays etc., it is beneficial to utilize jet substructure for background reduction. These techniques build on the fact that jets originating from such boosted decays are structurally different from jets originating from a light quark or gluon. In order to differentiate jets originating from massive particle decays from those originating from QCD, a number of algorithms can be applied.

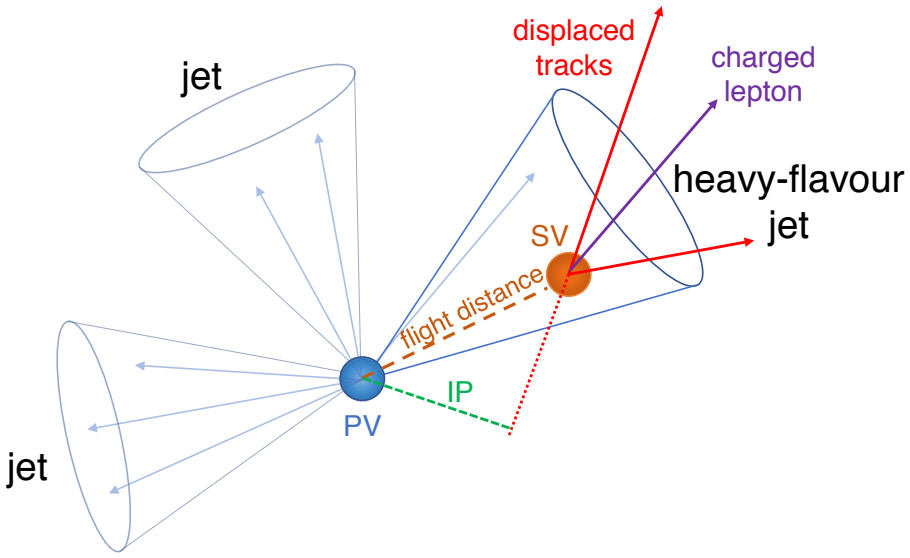

Figure 4.7.: An illustration of the principle of the CSV algorithm. The blue jet has a displaced secondary vertex coming from the decay of a B meson. The tracks originating from the B meson do not point to the primary vertex but are displaced by an impact parameter d_0. The displaced tracks can be used to reconstruct the secondary vertex at a distance from the primary event vertex. Figure taken from Ref. [150].

For example *grooming* algorithms such as *trimming* [151], *pruning* [152] and the *soft drop* algorithm [153], which aim at improving the mass resolution of large-radius jets. These various tagging and grooming algorithms aim to suppress or reshape backgrounds, i.e., QCD quark and gluon jets, while simultaneously retaining signal jets and enhancing their characteristics. This is achieved by different methods, however all methods in their core rely on the removal of soft and wide angle QCD radiation from the jets, thus reducing the dependence of the jet characteristics on soft divergences of QCD. They also further remove dependence of jet quantities on the UE and pileup. In this analysis two jet grooming algorithms are utilized, the trimming algorithm is applied online for the triggers based on jet substructure, while the soft drop algorithm, which is based on the modified mass drop algorithm [154] is used for the more detailed offline analysis of data. The trimming algorithm [151] works by reclustering a large-radius jet into subjets of a fixed cone-size $R_{\text{sub}} = 0.2$ using the k_T algorithm. Each subjet is removed from the large-radius jet if it fails the criteria

$$\frac{p_{\text{T},i}}{p_{\text{T,jet}}} > 0.03 \ . \tag{4.8}$$

The remaining subjets are clustered into the final trimmed jet. The trimming algorithm is used on trigger level, since it provides a fast discrimination between jets originating from QCD multijet processes and V boson jets.

Like any grooming method, the soft drop algorithm declusters the jets with the aim to remove effects from initial state radiation, UE and pileup. The soft drop algorithm starts from a CA jet, which has been clustered from the constituents of the anti-k_{T} jets used in the event and

starts by breaking it into two subjets. If the subjets both pass the soft drop condition

$$\frac{\min(p_{\mathrm{T}1}, p_{\mathrm{T}2})}{p_{\mathrm{T}1} + p_{\mathrm{T}2}} \geq z_{\mathrm{cut}} \left(\frac{\Delta R_{12}}{R_0} \right)^{\beta} , \tag{4.9}$$

the jet is considered the final soft drop jet, if not, the procedure is repeated on the subjet with the largest p_{T}, removing the other jet from the calculation. The procedure is repeated until the soft drop condition is met. The parameter z_{cut} can be tuned to achieve optimal results, for this analysis $z_{\mathrm{cut}} = 0.1$ is set, while R_0 is the radius of the jet. The exponent β can be chosen according to how much soft and soft-collinear radation should be removed. The most commonly used setting within the CMS Collaboration is setting $\beta = 0$, which provides the best discrimination between signal and background processes, while maintaining a good resolution of the signal mass peak. This setting has been used in this analysis as well. For exponents $\beta > 0$ soft-collinear radiation is per definition not removed from the jet, while setting $\beta <= 0$ removes soft and soft-collinear emissions.

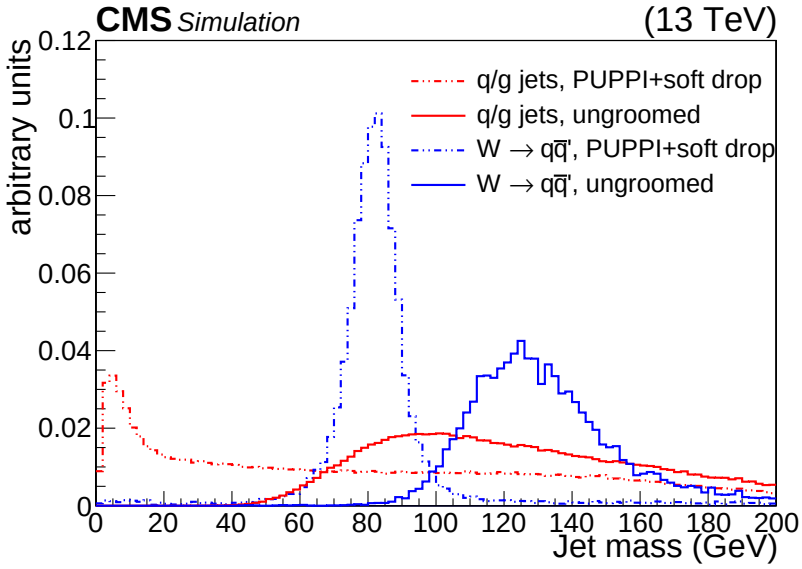

Figure 4.8.: The mass distribution of jets origination from QCD multijet (red lines) and signal (blue lines) processes groomed with the soft drop algorithm (dashed lines) and ungroomed (solid lines).

Although jets cleaned with the soft drop algorithm can be used to calculate different jet quantities, it is mainly used to calculate a corrected jet mass. Figure 4.8 shows the jet mass distribution for a jet mass, calculated using the sum of four-vectors of all particles inside the jet, as well as the mass distribution reached when the jet has been groomed using the soft drop algorithm before calculating the jet mass. The distributions are shown for QCD jets and jets originating from a W boson.

At first glance the fact that the invariant mass of jets originating from QCD processes is much larger than zero, might be confusing. This can be explained by the IR divergences in the limit of soft radiation, which lead to the appearance of logarithmic divergences in jet quantities such as the mass. This dependence on divergent terms increases with the radius of the jet, thus necessitating the removal of soft radiation from fat jets.

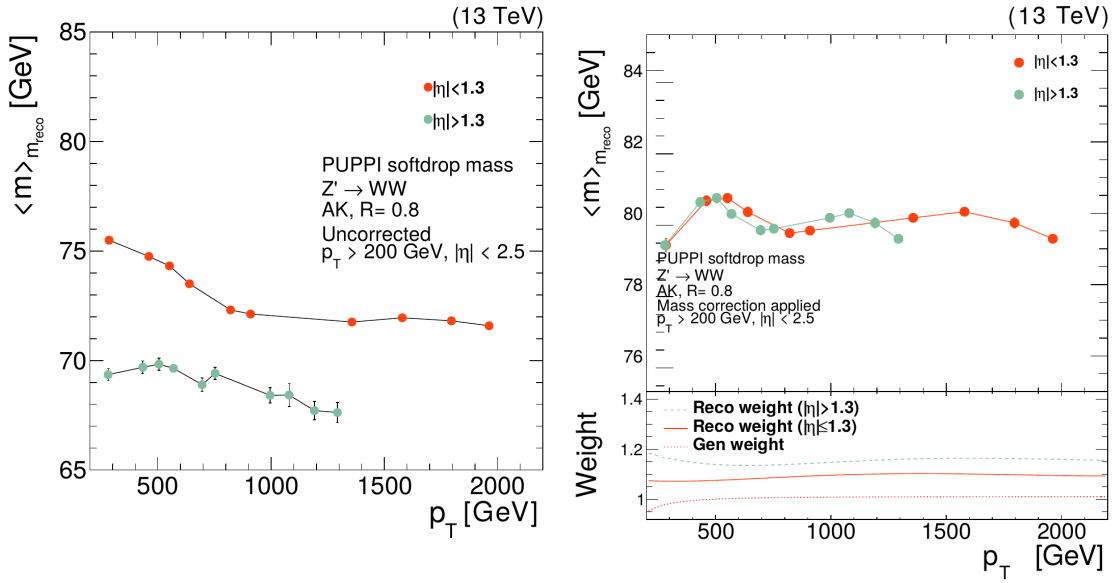

Figure 4.9.: The uncorrected soft drop jet mass for a Z′ signal as a function of the signal p_{T} for two regions in η (left) and the corrected soft drop mass as a function of p_{T} in two η bins (right).

To ensure an optimal performance of the soft drop algorithm in recovering the true parton mass for V jets, the algorithm is applied to uncorrected jets, i.e., before the jet energy corrections are applied. A set of separate corrections of detector nonlinearities and a residual p_{T} dependence of the algorithm are derived for the barrel and endcap detector regions separately. In Figure 4.9, the distribution of the soft drop mass calculated from uncorrected jets is shown in two η bins for the barrel and endcap region of the CMS HCAL. The Figure shows a residual p_{T} dependence as well as the mass of the jet being lower than the expected W boson mass.

To mitigate these effects, a set of corrections are derived based on the MC simulation of a high mass resonance decaying into two highly boosted W bosons. Two kinds of corrections are derived. One correction for generated jets, to adjust their soft drop mass to the real W boson mass peak. These corrections are applied to all MC simulations. The second kind of corrections are derived for the reconstructed soft drop jet mass for the barrel and endcap region separately.

These corrections are applied to both MC simulation and data as a function of p_{T}. The corrections are shown in Figure 4.10 while the resulting stable distribution after applying the corrections is displayed in Figure 4.9 on the right hand side.

It is interesting to note that pruning techniques such as the one applied in this analysis, can have different efficiencies depending on the polarization of the V bosons. These differences stem from the higher asymmetry in the transverse momenta of the two quarks from the decay of transverse polarized W bosons. This leads to the higher possiblity of rejecting particles from the softer of the two quarks, when grooming algorithms that are designed to eliminate soft radiation, are applied. In turn this might lead to lower jet masses, and thus a worsening of the jet mass resolution.

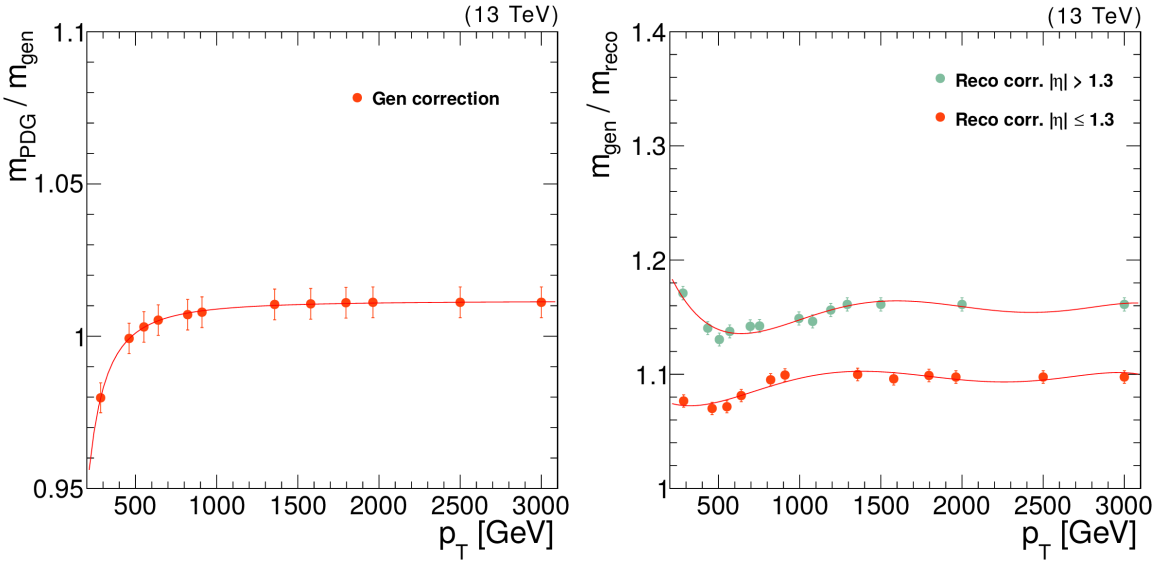

Figure 4.10.: The corrections derived for the soft drop mass, the generator level correction (left), and the reconstruction level correction (right).

Substructure Techniques

The substructure of jets becomes important in the regime of highly energetic decays, where a decaying particle such as a SM vector boson, cannot be reconstructed from two distinct jets anymore since its decay products can no longer be resolved from each other, see Figure 4.11 (left). In these cases the fact is utilized that there is a difference in the number of energy axes in the jet and in the jet mass depending on which SM particle is the origin of the jet. A schematic view of this is shown in Figure 4.11 (right).

These properties can be used in order to further discriminate between jets from SM background and jets coming from a boosted vector boson decay. The quantity called n-subjettiness [156] is a good discriminant between one-prong and two-prong fat jets, thus allowing a discrimination between quark (gluon) jets and jets coming from a V boson decay. Descriptively the n-subjettiness value quantifies the likelihood of the jet to have n subjet axes with small n-subjettiness values corresponding to a larger likelihood of the jet radiation to be aligned with n subjets. For this, the jet is reclustered into N subjets using the anti-k_T algorithm. The n-subjettiness is then defined as

$$\tau_n = \frac{1}{d_0} \sum_k (p_{T,k} \min(\Delta R_{k1} \Delta R_{k2} \dots \Delta R_{kN})) \ , \tag{4.10}$$

The index k runs over all particles in the original jet, $d_0 = \sum_k p_{T,k} R_0$ and R_{ki} is the distance of particle k to the candidate subjet axis i. The candidate subjet axes have to be chosen appropriately in order for the algorithm to deliver reasonable results. In the ideal case they would be determined by minimizing τ_N over all possible candidate subjet directions, in practice, however, the subjet axis are chosen by forcing the anti-k_T clustering algorithm to return N subjets. Jets coming from a V boson decay are characterized by lower values of τ_{21} compared to the SM background [15,156,157]. Figure 4.12 shows a schematic of the difference between a fat QCD jet and a jet coming from a boosted W decay.

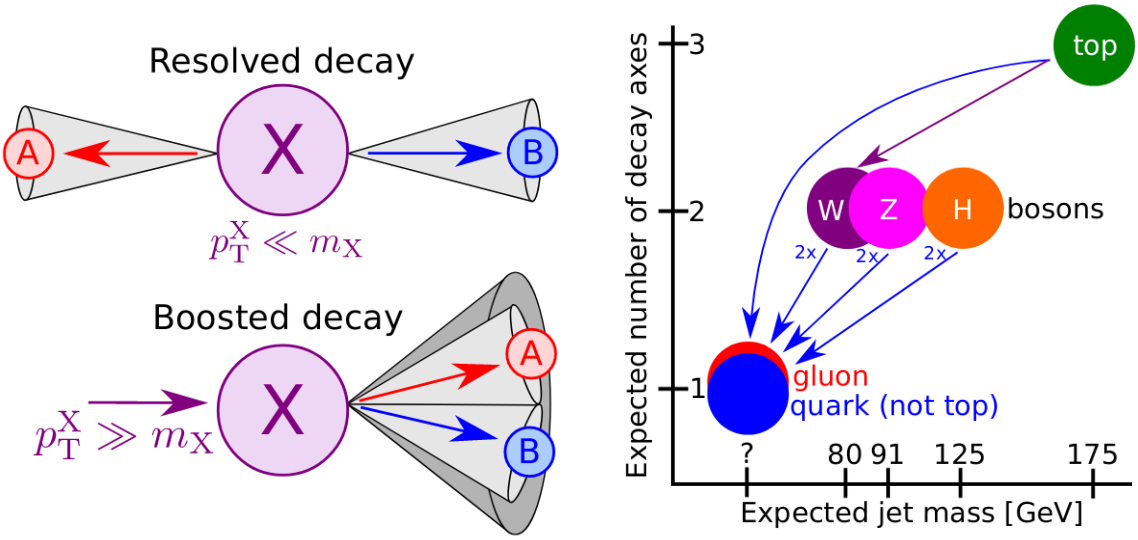

Figure 4.11.: A schematic view of boosted and resolved vector boson decays (left) and the number of expected energy axes in a boosted jet for different jet origins (right). Figures taken from Ref. [155].

Figure 4.13 show a comparison of the variables τ_1 and τ_2 for jets originating from a W boson, and jets originating from QCD multijet processes. By themselves the variables τ_N do not offer much discriminating power, since QCD-jets can also exhibit small values of τ_2. Similarly, QCD-jets can also have large values of τ_1 indicating that a large fraction of their energy is distributed away from the subjet candidate axis. However, QCD-jets with large τ_1 values are more likely to also exhibit large τ_2 values, while W-jets are more likely to have small τ_2 and large τ_1 values.

Therefore, the quantity 2-1-subjettiness

$$\tau_{21} = \frac{\tau_2}{\tau_1} \tag{4.11}$$

is used to identify jets clustered from two subjets. The use of the τ_{21} ratio to discriminate between QCD jets and jets coming from a boosted vector boson decay by applying a selection cut on this variable is called *V-tagging*.

For this analysis, the τ_{21} variable is further refined by decorrelating the variable from the jet p_T and the jet mass to first order, as outlined in Ref. [158]. This decorrelation procedure is designed to decrease the scale dependence of τ_{21} using a linear decorrelation. The procedure and its results are shown in Figure 4.14 which shows a clear scale dependence of the τ_{21} variable (left) while this dependence has largely vanished for the decorrelated variable τ_{21}^{DDT} (right), where DDT stands for *designed decorrelated tagger*. The decorrelation itself is performed by flattening the τ_{21} profile in $\rho' = \ln(m_{\mathrm{jet}}^2/(p_T \mu))$, where $\mu = 1\,\mathrm{GeV}$, in simulated QCD multijet events. This leads to the definition of τ_{21}^{DDT} as

$$\tau_{21}^{\mathrm{DDT}} = \tau_{21} - M \times \rho' \,, \tag{4.12}$$

where M is the slope extracted from a linear fit to the τ_{21} distribution as a function of ρ'. A value of $M = -0.08$ is determined for this analysis. Since the decorrelation is only done to

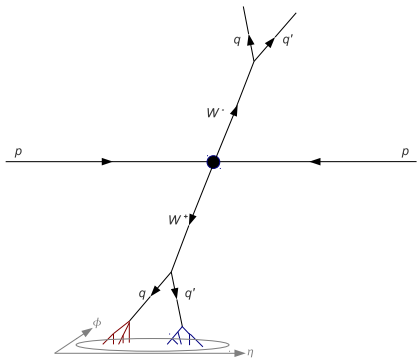

(a)

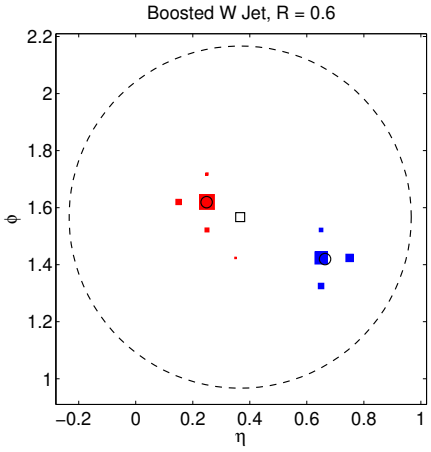

(b)

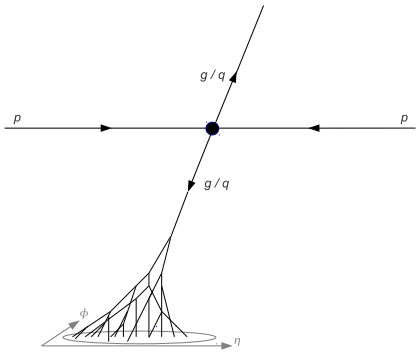

(c)

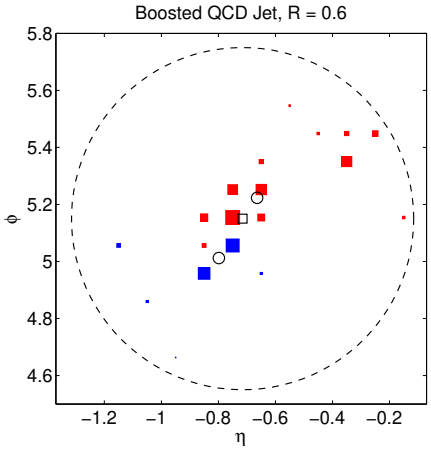

(d)

Figure 4.12.: Figure (a) shows an event with boosted W^+ W^--production. Figure (b) shows the typical substructure of a fat jet coming from such events; as is illustrated two distinct subjets can be distinguished. Figure (c) shows a typical QCD dijet event and (d) the corresponding event display. All jets were clustered using the anti-k_T algorithm. Figure taken from [156].

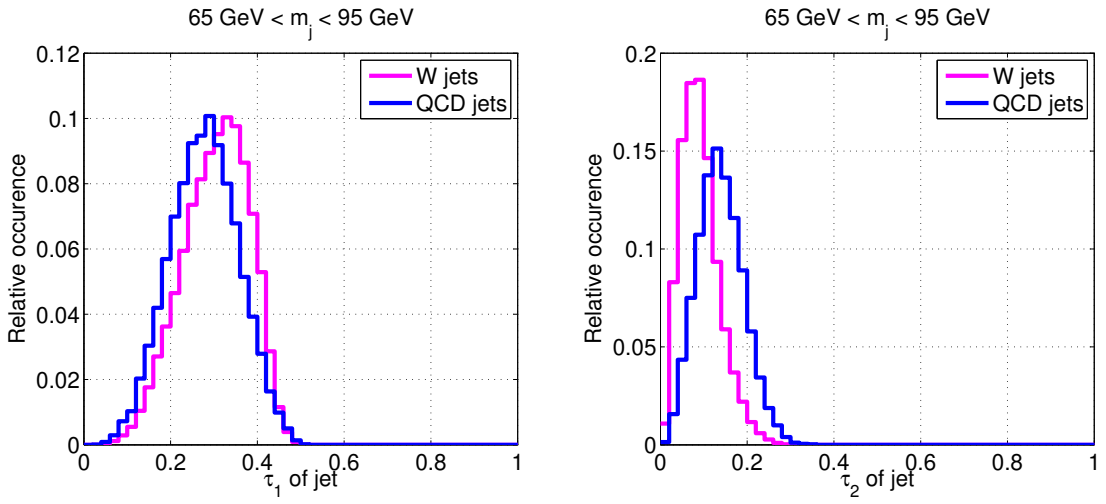

Figure 4.13.: The distributions of τ_1 (left) and τ_2 (right) for W-jets and QCD-jets that pass a cut on the invariant jet mass of 65 GeV$< m_{\text{jet}} <$95 GeV. The figure was derived for jets with a radius parameter of $R = 0.6$, $p_{\text{T}} > 300$GeV and $|\eta| < 1.3$. Figure taken from [156].

first approximation, there is still a residual difference between p_{T} bins, however this has a negligible impact on the overall analysis. There is a linear dependence of $\langle\tau_{21}\rangle$ on ρ' for all p_{T} bins in the interval from one to about 4.2. In the regime of ρ' larger than 4.2 a decorrelation is not possible anymore, here, increasingly less radiation is clustered into the large-radius jets, leading to a larger impact of higher order or UE effects. The outlier for $p_{\text{T}} \in [1000, 1100]$ is a statistical fluctuation and edge effect due to the jet mass and dijet invariant mass selection.

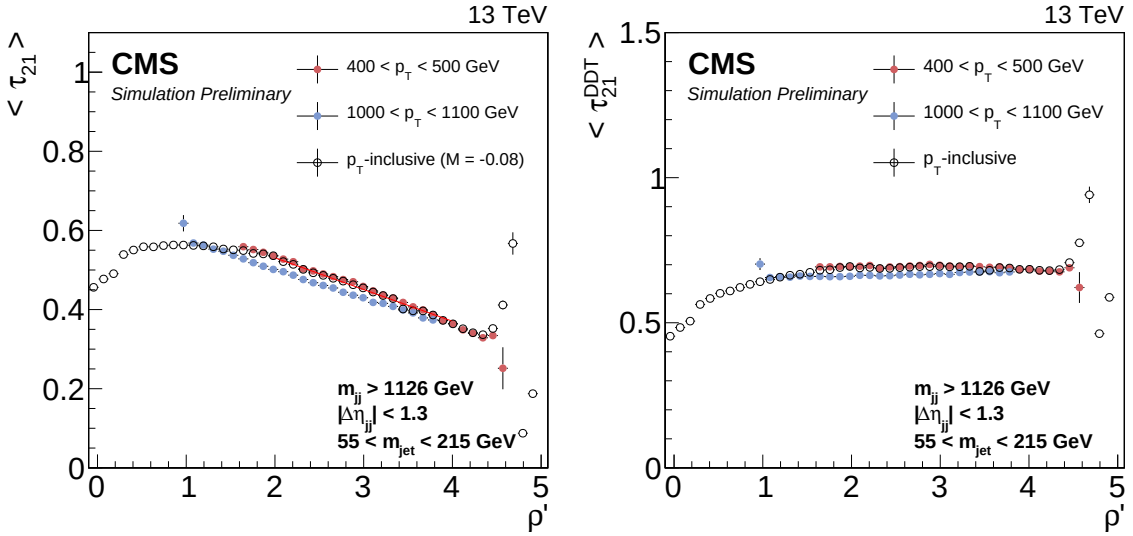

Figure 4.14.: Profile distribution of τ_{21} (left) and of τ_{21}^{DDT} (right) as a function of ρ'. The distribution is shown inclusively and for two different p_{T} ranges, showing a slight residual dependence of the τ_{21}^{DDT} distribution on the jet p_{T}.

5. Search for Diboson Resonances in the Full-Hadronic Final State

Searches for diboson resonances are one of the most interesting and sensitive discovery channels for new particles, which are predicted by many exotic theory models. The full-hadronic decay channel, where both vector bosons in the event decay into quarks, is the decay channel with the highest branching fraction and provides the possibility to discover or set limits on heavy new particles with masses at the TeV scale. This decay channel in particular is suited for the search for resonances at the multi-TeV scale, as opposed to leptonic or semileptonic decay channels, that are typically more limited in their reach. Searching for high mass resonances entails that the decay products of the potential new particle are highly boosted. Thus, the two quarks originating from a V boson decay cannot be resolved anymore as individual objects in the jet clustering. The constituents of a single V boson are therefore clustered into one large-radius jet, which leads to a final state of two fat jets for a full-hadronic search for diboson resonances. The search presented in this thesis is based on public results in the process of being published (in peer review), see Ref. [159] as well as results presented in Ref. [35] and earlier work detailed in Ref. [160–162].

A downside of utilizing full-hadronic final states is the relative complexity of correctly estimating and reducing contributions from background processes, which originate primarily from QCD multijet events. This analysis implements a new data-driven background estimation, which still allows the employment of knowledge relating to the full event topology. Furthermore, jet substructure methods are utilized to distinguish jets stemming from V boson decays from those originating from QCD multijet processes. In this thesis the data set recorded by the CMS experiment in 2016, corresponding to an integrated luminosity of 35.9 fb^{-1}, and the data set recorded in 2017, corresponding to an integrated luminosity 41.4 fb^{-1}, are studied.

The overall analysis strategy including the event selection and reconstruction is discussed in Section 5.1. In Section 5.2 and 5.3, the modeling of signal and background processes employed in this analysis are described. Section 5.4 discusses the systematic uncertainties influencing the results of the search and their inclusion in the statistical inference. In Section 5.5 the extensive tests employed to verify the validity and accuracy of the modeling are described, while the final results are presented in Section 5.6.

5.1. Analysis Strategy

There are several theoretical models that predict heavy particles, which decay into pairs of vector bosons. Usually, these theory models aim to solve open challenges of the SM, such

as incorporating gravity. This analysis aims to test the existence of such resonances in data, collected with the CMS experiment at the LHC in 2016 and 2017, utilizing a data set of 77.3 fb^{-1} in total. The analysis described here is an improvement of earlier searches performed in the same final state, such as results found in Ref. [35]. This search was conducted by the author of this thesis as well. However, this search is only briefly summarized in Appendix E, since the results achieved in this earlier work are surpassed by the methods employed and described in this thesis.

The aim of the search is to produce largely model independent results, that test a wide variety of different models and model parameters. Two theoretical frameworks are tested and used to produce exclusion limits in this analysis in particular: the HVT model, and the bulk graviton model. However, the limits produced are valid for any theory model, provided the new particle predicted is either a spin-1 or spin-2 particle and the couplings to longitudinally polarized and transversely polarized vector bosons are similar as in the theory models used for event generation. The limits are furthermore set in the narrow-width approximation, i.e., the natural decay width of the resonance is required to be smaller than the detector resolution. As a consequence of narrow resonances, the production can be factorized into its production cross section σ and the branching fraction to vector boson final states.

The all-hadronic decay has the highest branching fraction of W (Z) boson decays with 67.4% (69.9%) [1], which makes this analysis channel one of the most powerful in the search for new diboson resonances. However, it also presents unique challenges such as the reconstruction of the vector bosons from their highly energetic decay products. This necessitates the reconstruction of the boosted decay products in one large-radius jet, utilizing dedicated jet substructure based techniques (*V-tagging*) for background rejection. Another challenge in this decay channel is the background modeling. Since the theoretical prediction of QCD multijet processes and the modeling of the jet substructure in MC simulation, are difficult tasks that depend on the showering and hadronization models, largely data-driven background estimation techniques have to be employed. The events are reconstructed by choosing two large-radius jets in an event and calculating the invariant mass of the dijet system m_{jj}. If a new particle exists, a resonant structure is expected to appear in the m_{jj} spectrum around the mass of the new particle. In previous versions of analyses performed in the same decay channel, this invariant dijet mass was utilized to fit resonant signals above a continuously falling SM background, modeled by fitting an analytic function to the spectrum in data. This analysis implements a new method based on a three-dimensional maximum likelihood fit in the space, spanned by the dijet invariant mass and the individual masses of the two jets used to reconstruct the event. While all background processes are expected to show a monotonically falling distribution in the dijet invariant mass and similar behaviors in the distributions of the jet masses, an expected signal would show a resonant structure in all three mass dimensions. This can be utilized in a three dimensional resonance search where signal and background contributions can be fitted simultaneously, while the background contributions can be well constrained by the phase space sideband regions, where no signal is expected. A schematic picture of this approach is shown in Figure 5.1. Furthermore, the real V bosons originating from SM V+jets backgrounds can be used to constrain uncertainties that affect the signal as well as this subdominant background at the same time.

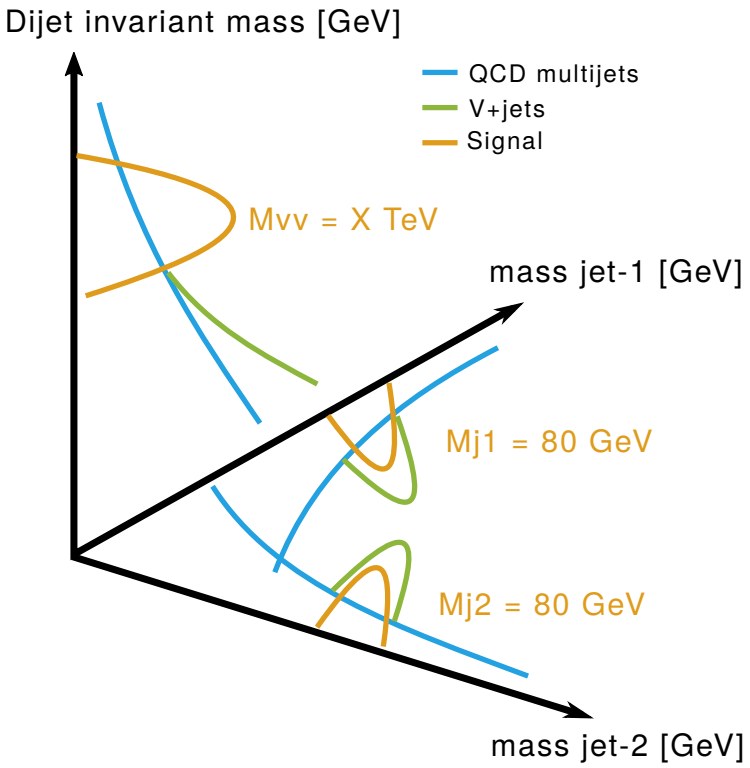

Figure 5.1.: A schematic representation of the topology of signal and background distributions in a three dimensional fit in the m_{jj}-m_{jet1}-m_{jet2} space. The orange lines correspond to a hypothetical signal contribution, while the light blue and green lines show the background contributions from QCD multijet and V+jets SM processes, respectively.

5.1.1. Event Topology

Since the expected signal cross sections are orders of magnitude smaller than the cross section of SM QCD multijet events, an important part of the analysis is the selection of a phase space that is enriched in signal events, while simultaneously reducing the number of background events. In order to successfully select such a kinematic region, a careful understanding of the topology of signal and background events is necessary. A full list of all utilized MC simulation samples can be found in Appendix A.

Signal Processes

The signal processes of interest for this analysis are the s-channel production of a new heavy particle, which in turn decays into two vector bosons. The LO Feynman graphs for this process are shown in Figure 5.2.

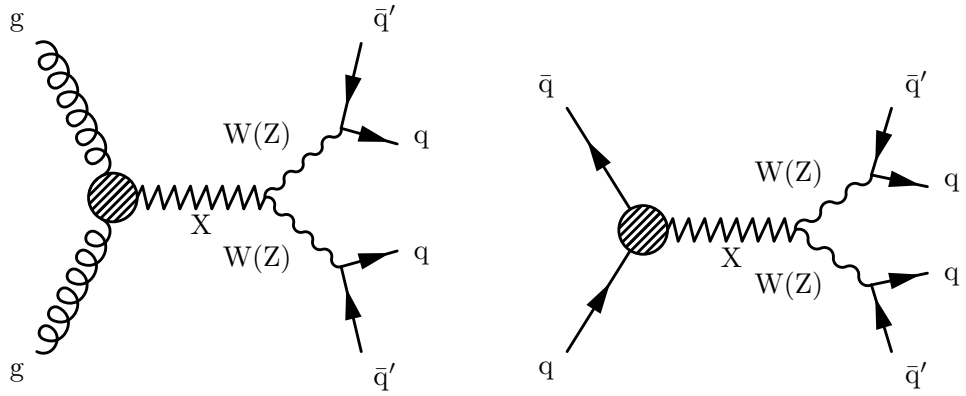

Figure 5.2.: The Feynman graphs for the considered signal processes. The production diagram of a heavy resonance through ggF is shown on the left, while the DY process is shown on the right. The hatched circle represents the model independent coupling of an exotic resonance to gluons or quarks.

Since the new particle is expected to have a large mass, the resulting two jets in the final state are expected to have high transverse momenta. For small boosts, i.e., small resonance masses, not all decay products of the V bosons might be clustered into the same fat jet. Therefore, this analysis only searches for new particles with resonance masses above $\approx 1\,\text{TeV}$. The two jets originating from signal events are furthermore expected to possess a back-to-back topology, with a wide angular separation between the two jets.

QCD Multijet Processes

QCD multijet processes are the main contribution to all background processes of this analysis. This background category comprises all SM processes that lead to two or more jets in the final state. Figure 5.3 shows some selected Feynman graphs of QCD dijet processes. This background shows smoothly falling distributions in both the dijet invariant mass and the mass distribution of the two individual jets comprising the event. These processes can be further suppressed by applying requirements on the jet substructure to only select jets, that have a two-pronged energy pattern, as expected to arise from boosted V boson decays.

V+jets Production

The cross section for SM V+jets processes is much smaller than for the QCD multijet production. However, this background is still important for the analysis presented here since it contains contributions from real V bosons. Utilizing jet substructure selections enhances the contribution of this background compared to QCD multijet events. The presence of a real V boson in this background also entails the appearance of a resonance around the V boson mass in the jet mass distribution. This resonance originating from the V+jets background can be used to constrain major uncertainties of the analysis, which are related to the V-tagging efficiency and the scale and resolution of the jet mass. Figure 5.4 shows Feynman graphs for

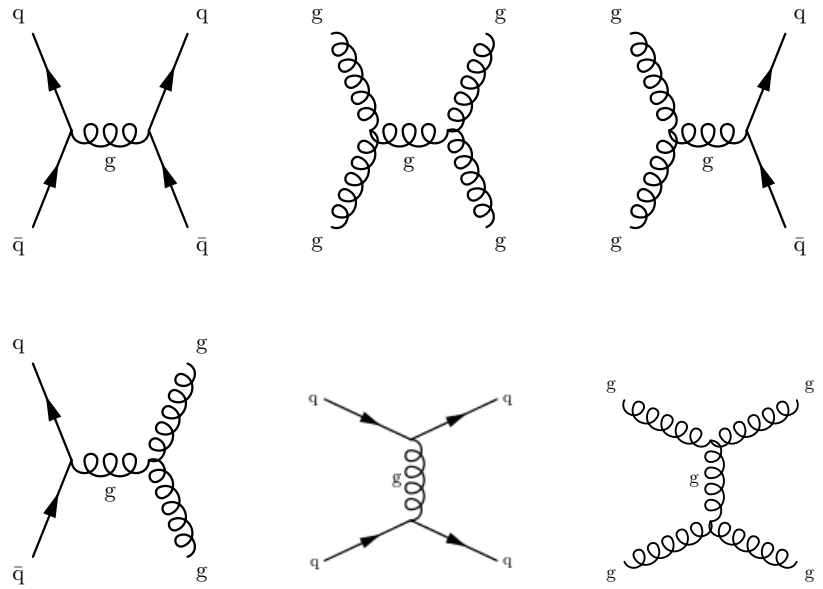

Figure 5.3.: Selected LO Feynman graphs contributing to the QCD multijet background.

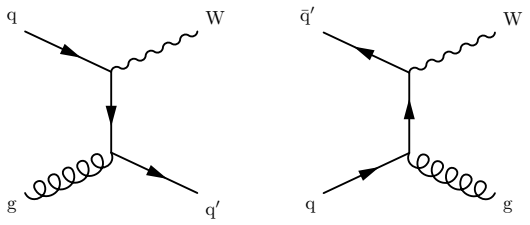

Figure 5.4.: Representative Feynman graphs for SM W+jets processes.

the production of a real W boson in association with a jet. Similar processes for Z bosons are considered in this analysis as well.

Top Quark Pair Production

Top quarks decay almost always into a W boson and a bottom (b) quark. Events from top-antitop quark ($t\bar{t}$) production processes are therefore another background for this analysis. Two possibilities can be distinguished: either the W boson and b quark from the top quark decay are clustered into a single, large-radius jet, which leads to a resonance in the jet mass spectrum around the top quark mass, or the W boson decay products are clustered into one jet while the b quark is separated enough to be clustered into a separate jet. This second topology leads to a similar behavior as for the V+jets backgrounds, with a resonant contribution around the W boson mass. Due to the selection of a highly boosted phase space, the overall contribution of $t\bar{t}$ events is small compared to both the QCD multijet production and the V+jets processes. Figure 5.5 shows the LO diagrams for the production of $t\bar{t}$ processes.

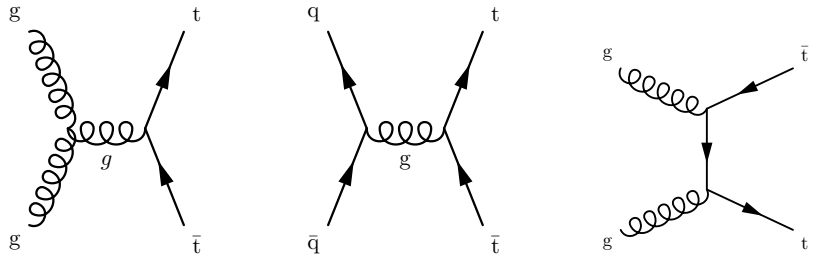

Figure 5.5.: The LO Feynman diagrams for $t\bar{t}$ production.

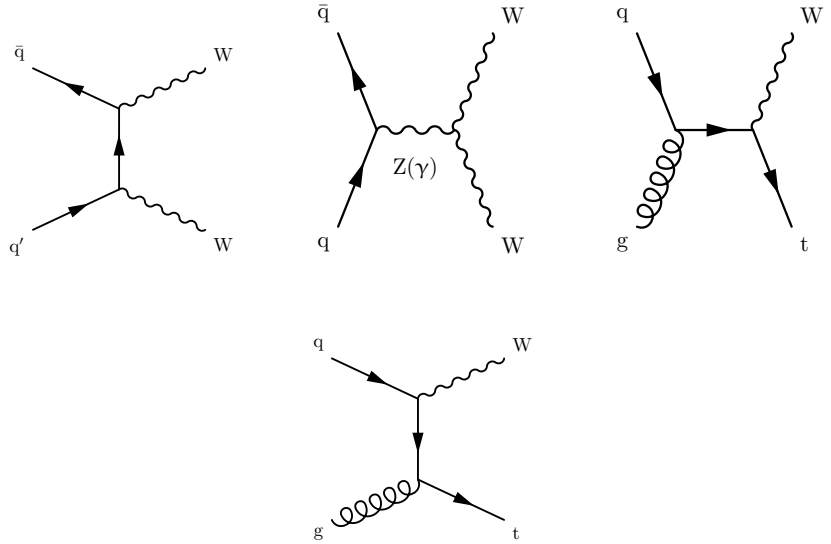

Figure 5.6.: The LO Feynman graphs for SM processes with two W bosons in the final state. These diagrams picture contributions to background processes for diboson resonance searches.

SM VV Boson and Single Top Quark Production

The selected final state signature also includes events originating from either SM VV boson production, or the production of a single top quark. The LO Feynman graphs for these processes can be found in Figure 5.6. However, in the phase spaces selected in this analysis the SM cross section for these processes are very small, leading to a number of expected events for both process types that is smaller than 3% of the selected events. The overall number of expected events is therefore smaller than the statistical uncertainties of V+jets background processes. Note here, that these processes do not only have small cross section, but their distributions in the m_{jet1}-m_{jet2}-m_{jj} hyperspace are indistinguishable from how the V+jets contribution is modeled. The contributions from these processes are therefore negligible for this analysis, since in the current modeling of backgrounds the small contributions from SM VV production processes and single top quark production can be absorbed in the modeling of the much larger V+jets background processes.

5.1.2. Selection and Reconstruction of Events

Based on the topologies discussed in the previous sections and MC samples generated at LO in QCD for signal and LO or NLO for background processes, a set of selection criteria designed to enhance the relative contributions of signal to background processes is derived. In the following Section, the selection criteria and event reconstruction are discussed. A complete list of MC samples used in the analysis, as well as their generator conditions, can be be found in Appendix A.

Trigger Selections

Events are selected online utilizing a mixture of triggers, based either on the highest jet p_{T} in the event, the sum of all jet p_{T} in the event (H_{T}), or utilizing additional requirements on the trimmed jet mass. The H_{T}-triggers are based on a standard jet collection of anti-k_{T} jets, with a distance parameter of $R = 0.4$ and an H_{T} threshold larger than 750–800 GeV, depending on data taking conditions, for the data taken in 2016 and larger than 1050 GeV for 2017 data.

The triggers utilizing the trimmed jet mass and jet p_{T} operate on AK8 jets, and require either at least one jet with $p_{\mathrm{T}} > 400(500)$ GeV or at least one jet with $p_{\mathrm{T}} > 200(360)$ GeV, and a trimmed jet mass larger than 30 GeV for data taken in 2016 (2017).

A second set of trimmed mass triggers requires $H_{\mathrm{T}} > 650(750)$ GeV, and at least one jet with a trimmed mass larger than 50 GeV, for data taking conditions in 2016 (2017). Adding these trimmed mass triggers to the event allows the lowering of the trigger thresholds, where the combined triggers reach an efficiency of larger than 99%. The trigger requirements in the year 2017 are slightly larger than those applied in 2016, in order to maintain the same trigger rate despite a higher instantaneous luminosity.

Figure 5.7 shows the event selection efficiency of the trimmed mass triggers as a function of the jet mass for the leading p_{T} jet. Since an event selection efficiency is shown, the efficiency as a function of the jet mass of the second leading jet is very similar. The trimmed mass trigger reach full efficiency for jet masses larger than 52 GeV. During the first 4.8 fb^{-1} of data taking in 2017, the trimmed mass triggers were not applied. This leads to a slight loss in efficiency for the full 2017 data recorded using substructure triggers. Figure 5.8 shows the event selection efficiency for a combination of all triggers utilized in the analysis as a function of the dijet invariant mass. The event selection efficiency is evaluated on a single muon data set orthogonal to the events used in the analysis. The combination of triggers is chosen to optimize the value of the dijet invariant mass, m_{jj}, above which the triggers are highly efficient. The trigger selection reaches an efficiency of at least 99% for events in which m_{jj} is greater than 1126 GeV. Since the selection criteria ensure that only data above the trigger threshold is used in the analysis, no uncertainty due to trigger turn on effects is applied.

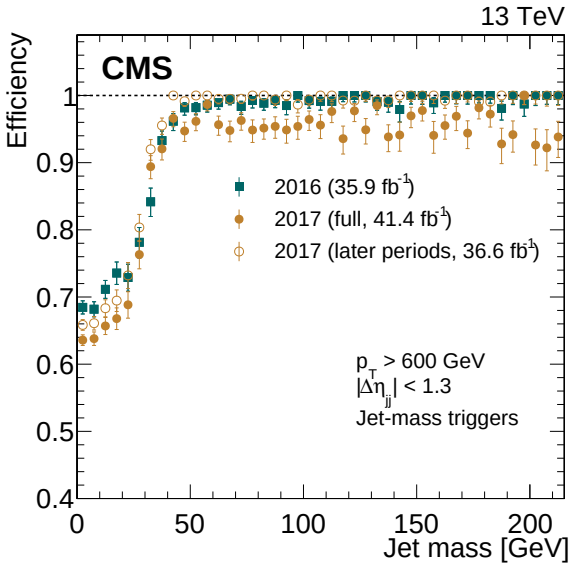

Figure 5.7.: The event selection efficiency as a function of the jet mass for triggers requiring an online trimmed mass of at least 30 GeV. The solid yellow circles correspond to the event selection efficiency for the full 2017 data set, and do not reach 100% efficiency because the jet mass based triggers were unavailable for a period at the beginning of data taking (corresponding to $4.8\,\mathrm{fb}^{-1}$). The open yellow circles are the corresponding efficiencies excluding this period. The uncertainties shown are statistical only. The efficiency is depicted as a function of the mass of the jet with the largest p_T in the event, denoted here as jet mass.

Noise Filters and Primary Vertex Selection

All events are required to contain at least one primary vertex, which is reconstructed within a 24 cm long cylinder along the beam axis, with a transverse distance from the nominal pp interaction region of less than 2 cm [163]. In the presence of more than one vertex complying with the primary vertex criteria, the vertex with the highest total ${p_\mathrm{T}}^2$, summed over all associated physics objects, is chosen as the primary vertex. Here, physics objects are tracks assigned to the candidate vertex, as well as missing transverse momentum, calculated as the negative vector sum of the p_T of the associated tracks. Furthermore, events affected by misreconstructed $p_\mathrm{T}^\mathrm{miss}$ due to instrumental effects such as anomalous energy deposits in the HCAL or ECAL, are removed from the reconstruction by applying noise filters following the recommendation of the MET POG [164].

Preselection

The events are reconstructed using the PF algorithm. In order to mitigate the effects of pileup, two methods are used separately for 2016 and 2017 data. For data recorded in 2016, the standard CHS pileup subtraction method is utilized to reduce the dependence of event properties on pileup. For data collected in 2017, where the average number of interactions was about 30% higher than in 2016, a new pileup subtraction method, PUPPI [148], is used.

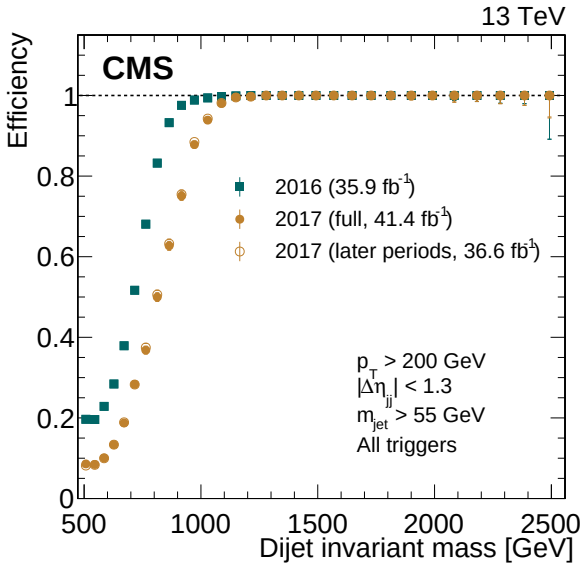

Figure 5.8.: The event selection efficiency as a function of the dijet invariant mass for a combination of all triggers used in this analysis. The solid yellow circles correspond to the event selection efficiency for the full 2017 data set, while the hollow yellow circles correspond to the efficiency excluding the first 4.8 fb^{-}1 collected. The green squares show the event selection efficiency for the 2016 data set. The uncertainties shown are statistical only.

For both years, jet substructure quantities, such as the jet mass and the n-subjettiness, are calculated utilizing the PUPPI method. Jets are clustered with the anti-k_{T} jet clustering algorithm, with a clustering parameter of $R = 0.8$ using the FastJet package [165].

Two different pileup subtraction methods are used for the jet four-vectors, and consequently to calculate the dijet invariant mass in 2016 and 2017, because an increase in the dijet mass resolution was observed when using the PUPPI algorithm. Figure 5.9 shows the difference in resolution between 2017 and 2016 signals in MC simulation. Here, for the sake of comparison the same jet energy corrections were applied in 2016 and 2017 thus showing the difference in resolution of around 10% due to the pileup subtraction methods. This issue is caused by the PUPPI algorithm removing too many charged and neutral particles from jets with high transverse momenta. This happens due to the track-vertex association which deteriorates with increasing p_{T}, leading the PUPPI algorithm to reject too many particles. This in turn leads to larger low-mass tails and an increase in the resolution. A new tune for the PUPPI algorithm is in development, in order to increase the performance of PUPPI for high-p_{T} jets. However, since this tune wa not available at the time of writing, the CHS method was used to retain a better dijet mass resolution for 2016 data. For 2017 data, where the mean number of interactions per bunch crossing is about 1.3 times larger than in 2016, the PUPPI algorithm was used in order to take advantage of the greater stability of jet variables with respect to pileup.

This is also the reason why all jet substructure variables such as the jet mass and the τ_{21}^{DDT} variable are calculated using PUPPI pileup subtraction. Figure 5.10 shows the dependence of τ_{21} to pileup, comparing the variables calculated using the CHS method and the PUPPI

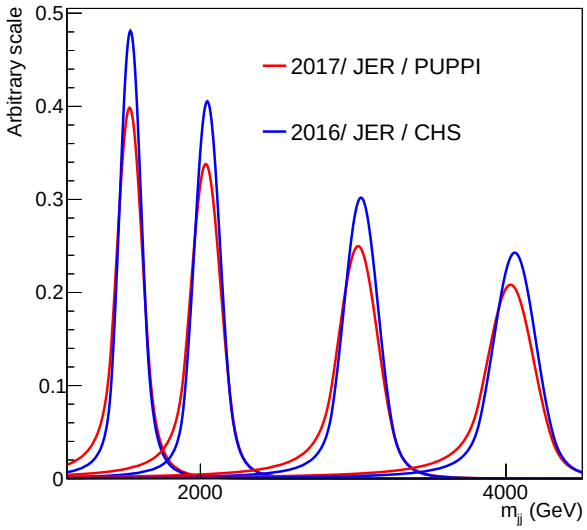

Figure 5.9.: A comparison between the dijet invariant mass resolution achieved in 2016 using the CHS pileup subtraction method and 2017 using PUPPI as pileup subtraction method. The dijet invariant mass shapes for a $G_{bulk} \rightarrow WW$ signal are compared for different mass points, showing that the resolution achieved in 2017 is about 10% larger compared to 2016.

algorithm for pileup subtraction. The PUPPI algorithm shows a clear reduction of the dependence of the tagging efficiency on pileup.

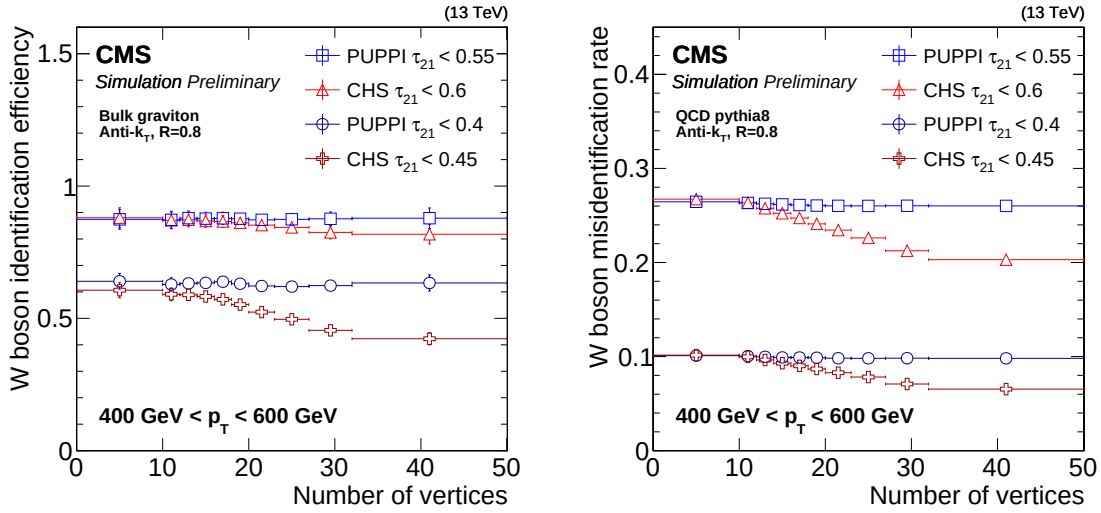

Figure 5.10.: The boson tagging efficiency (left) and misidentification rate (right) for two working points as a function of the number of vertices in the event comparing two different pileup subtraction methods used by the CMS Collaboration. Figure published in Ref. [166].

Table 5.1.: The requirements on jet quality for all jets used in the subsequent steps of the analysis. In case of differences between the two years of data taking, the differing value for the year 2017 is added in parenthesis.

	requirement	region
number of constituents	> 1	-
neutral hadron energy fraction	< 0.90	-
neutral EM energy fraction	< 0.90	-
charged hadron fraction	> 0	$\lvert\eta\rvert \leq 2.4$
charged hadron multiplicity	> 0	$\lvert\eta\rvert \leq 2.4$
charged EM energy fraction	< 0.99 (< 0.80)	$\lvert\eta\rvert \leq 2.4$

All jets considered for the reconstruction are furthermore required to pass the quality requirements shown in Table 5.1. The jets are corrected for nonlinearities of the detector response in p_{T} and η using standard jet energy corrections, as described in Section 4.2. Events are required to contain at least two jets, that satisfy the jet quality criteria in Table 5.1, have a p_{T} larger than 200 GeV and $|\eta| < 2.5$. The two jets in the event with the highest transverse momenta, satisfying these criteria, are selected as the boosted vector boson candidates.

Furthermore, the two jets are required to have a separation $|\Delta\eta_{\mathrm{jj}}| < 1.3$ to reduce the QCD multijets background and to satisfy $\rho = \ln({m_{\mathrm{jet}}}^2/{p_{\mathrm{T}}}^2) < -1.8$ to veto events with high jet masses, but low jet p_{T}. In these cases, the selected cone size of the jet is too small to contain the full jet, which affects both the jet mass resolution and the τ_{21}^{DDT} tagging efficiency. This selection has a negligible effect on signal events and only cleans the sample of poorly modeled background events. Finally, the jet mass is required to be within 55 to 215 GeV.

Jets originating from the misreconstruction of a high momentum lepton, are rejected by requiring an angular separation of $\Delta R > 0.8$ to muons (electrons) in the event, with a p_{T} greater than 20 (35) GeV, and satisfying criteria optimized for high momentum lepton identification [167, 168].

Figure 5.11 shows a comparison between data and MC simulation after these preselections have been applied. The contributions from minor backgrounds such as V+jets processes, and $\mathrm{t\bar{t}}$ processes are scaled to their SM expectation, while the QCD multijet simulation is scaled to the data, after the expected events from minor backgrounds have been subtracted. Thus the normalization of MC to data is correct by definition. For the QCD multijet sample simulated with PYTHIA 8 enough events have been simulated to provide an oversampling of 20%. In Figure 5.11 two spikes in the PYTHIA 8 MC simulation distribution are visible. These spikes are unphysical and originate in very few events with low-p_{T}, and therefore high event weights, that are misreconstructed with too large transverse momenta.

Figure 5.11 (top right) shows large differences between the τ_{21}^{DDT} distribution in data and QCD multijet MC simulation, as well as large differences between MC generators. The difficulties in modeling jet substructure variables in QCD multijet processes is well-known, and leads to the adaption of data-driven methods for QCD multijet processes.

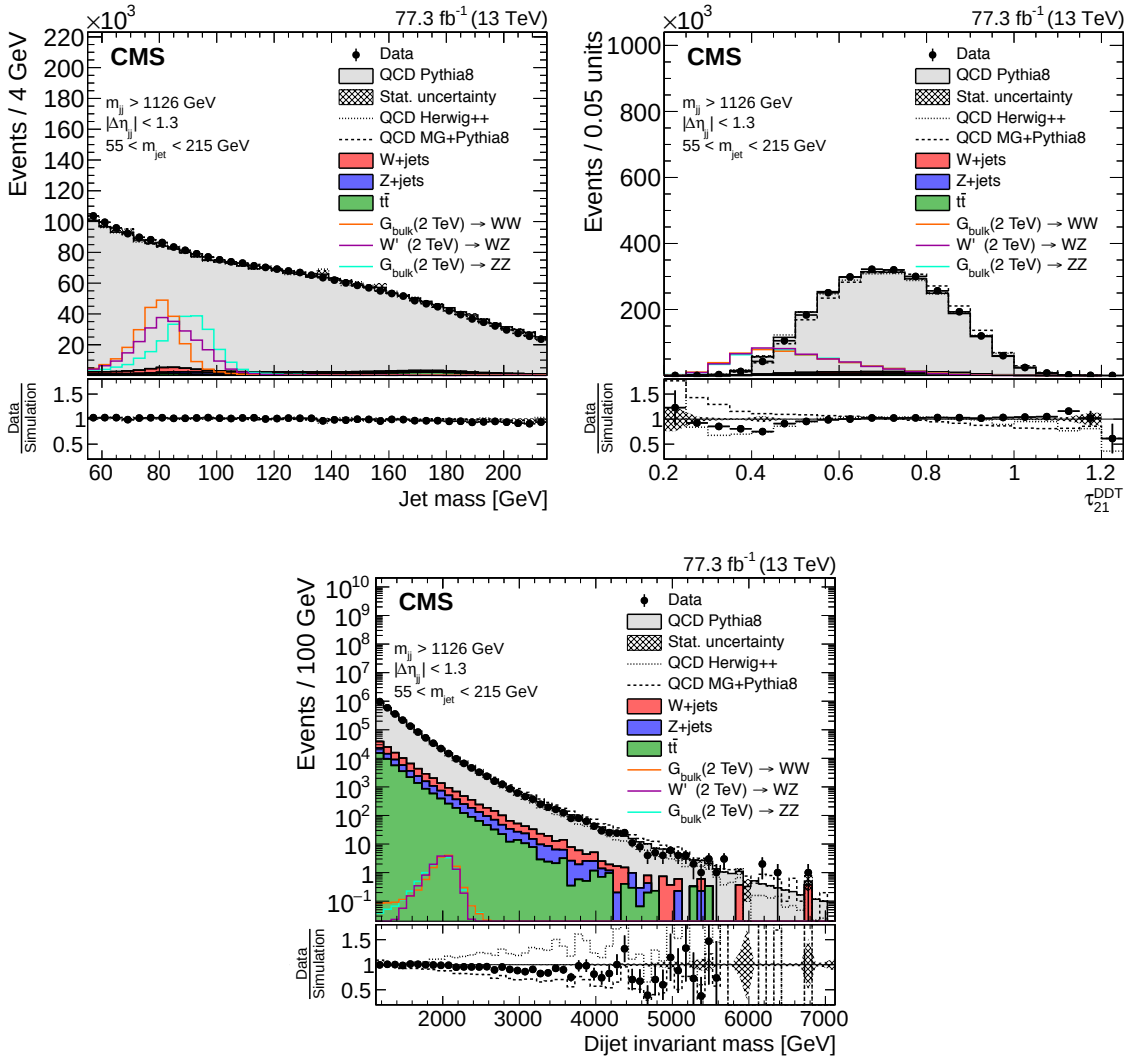

Figure 5.11.: The jet mass (upper left) and τ_{21}^{DDT} (upper right) distributions for selected jets (one random jet per event), and dijet invariant mass distribution (lower), for events with a jet mass between 55 and 215 GeV. For the QCD multijet simulation, several alternative predictions are shown, each scaled to the data minus the other background processes, which are scaled to their SM expectation. The different signal contributions shown are scaled to be visible in the plot. The ratio plots show the fraction of data over QCD multijet simulation for PYTHIA8 (black marker), HERWIG++ (dotted line) and MADGRAPH5_AMC@NLO interfaced with PYTHIA8 (dashed line).

Jet Substructure Selections

Jet substructure methods are utilized to further improve the signal to background ratio of the analysis. As mentioned before, a selection on the jet mass calculated with the soft drop algorithm of 55 GeV$< m_{\mathrm{jet}} <$ 215 GeV is applied on both jets in the event. This mass window is selected to remove QCD multijet events, which tend to have a lower soft drop jet mass

while fully containing the V boson, H boson and top quark masses, since future extensions of this analysis could include any of these final state particles in the same framework. This loose mass cut has the additional benefit of an improved selection efficiency for the signal, compared to previous analyses that applied a tight cut around the V boson masses.

In addition to the jet mass selection, two pure signal categories are defined, based on selection cuts on the substructure variable τ_{21}^{DDT}. The main reason for using the decorrelated substructure variable τ_{21}^{DDT} instead of τ_{21}, is shown in Figure 5.12. Here, the jet mass distribution for one randomly chosen jet is shown for different intervals of the dijet invariant mass in QCD multijet MC simulation. It can be seen that the sculpting of the jet mass distribution is reduced when using τ_{21}^{DDT}. This reduces correlations between the jet masses and the dijet invariant mass in the three dimensional modeling adapted in this analysis, thus leading to a simpler and more accurate background model.

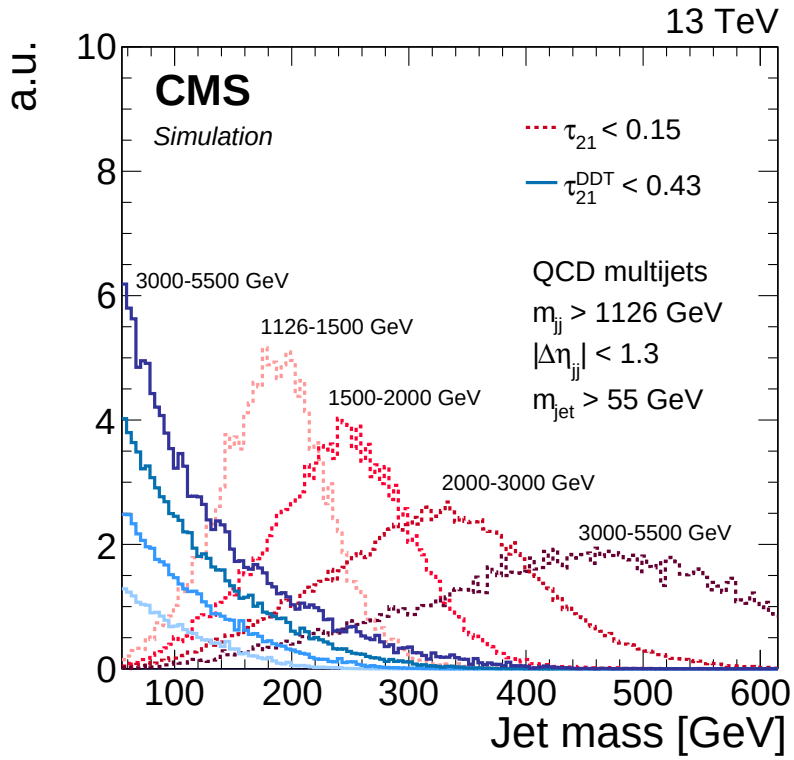

Figure 5.12.: The mass sculpting of the jet mass in QCD multijet simulation using τ_{21} and τ_{21}^{DDT} as a tagging variable. The jet mass distribution for different intervals in the dijet invariant mass are shown for a cut on $\tau_{21}^{\mathrm{DDT}} < 0.43$ (blue lines) as well as for τ_{21} (red lines) with a cut of $\tau_{21} < 0.15$, which corresponds to the same mistagging probability in QCD multijet processes as the cut used for τ_{21}^{DDT}. Figure published in Ref. [159].

Using the τ_{21}^{DDT} variable as opposed to τ_{21} has an addional benefit, namely it posses additional discrimination power due to the different distributions of $\rho' = \ln(m_{\mathrm{jet}}{}^2/(p_{\mathrm{T}} \cdot 1\,\mathrm{GeV}))$ between quark or gluon jets and jets originating from real V boson decays. This is shown in Figure 5.13, which shows the ρ' distribution in simulation for signal and background from QCD multijets. This leads to an improvement in performance, which can be seen in Figure 5.14

(left), showing the performance of τ_{21} and τ_{21}^{DDT} in the background-signal efficiency plane, after the preselections have been applied, i.e., after applying the selections detailed in the previous section. The mistagging efficiency is calculated in QCD multijet simulation, as the efficiency of misidentifying a jet as coming from a vector boson decay, while the tagging efficiency is the rate of correctly identified vector boson jets, evaluated using MC truth information in signal simulations of $\mathrm{G_{bulk}} \rightarrow \mathrm{WW}$. Figure 5.14 (right) shows a comparison of the τ_{21} and τ_{21}^{DDT} distributions in QCD multijet events and signal events.

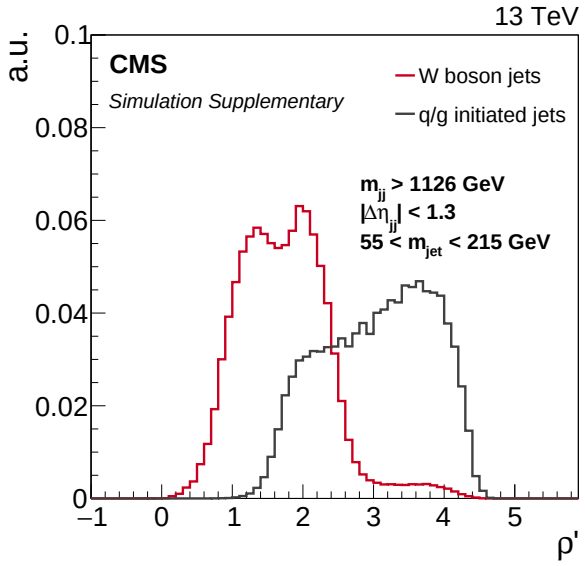

Figure 5.13.: Comparison of $\rho' = \log(m^2/(p_T \cdot 1\ \mathrm{GeV}))$ for jets originating from QCD multijet events and jets from vector boson decays, using MC simulations for the bulk graviton model as an example. Figure published in Ref. [159].

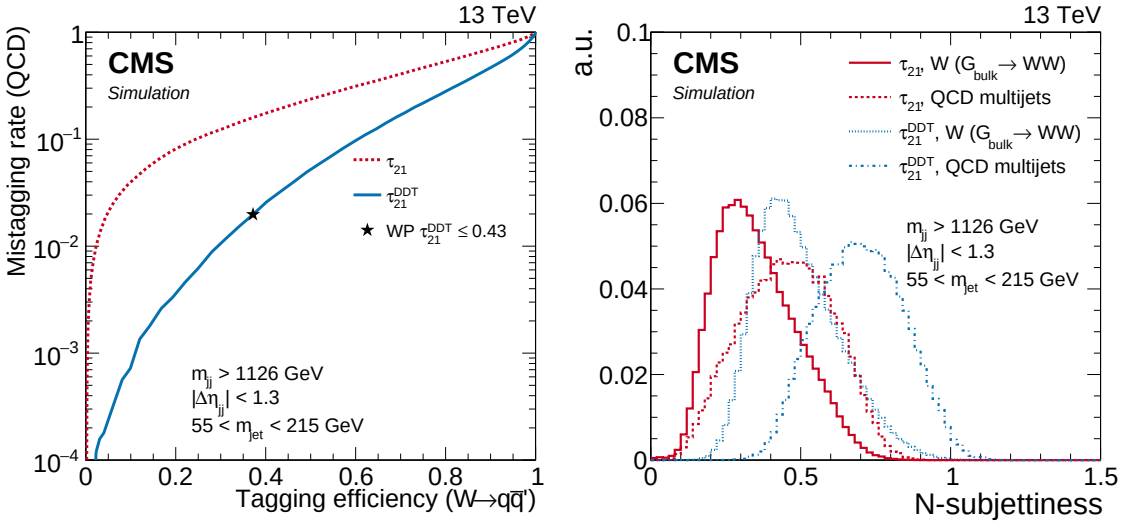

Figure 5.14.: The mistag efficiency over the tagging efficiency for τ_{21} and τ_{21}^{DDT} (left) and a comparison of the distributions of τ_{21} and τ_{21}^{DDT} (right). Figures published in Ref. [159].

The high purity category (HPHP) is defined by requiring both jets in the event to satisfy $\tau_{21}^{\mathrm{DDT}} \leq 0.43$, where the selection cut has been chosen to provide an optimal signal over background ratio for low mass signal processes. The low purity category (HPLP) is defined to contain at least 95% of signal events combined with the events already selected for the HPHP category. This purity region is designed to enhance the sensitivity of the analysis in phase space regions, where the number of expected background events is low. An event is classified as being in the HPLP category if one of the jets passes the HPHP requirements while the second jet satisfies $0.43 < \tau_{21}^{\mathrm{DDT}} \leq 0.79$. Further, an LPLP control region in data is defined by requiring both jets to pass the $0.43 < \tau_{21}^{\mathrm{DDT}} \leq 0.79$ selections. This region includes some signal, however, the signal to background ratio is very low, and the region can therefore be considered signal free for all practical purposes.

The optimal selection cut for the HPHP category was identified using a bulk graviton signal hypotheses, and a 20% window around the signal mass. The Punzi significance [169]

$$s_p = \frac{\epsilon}{a/2 + \sqrt{B}} \,, \tag{5.1}$$

is then calculated, where ϵ is the expected signal efficiency using the chosen selections of the analysis, a is the number of standard deviations of a normal distribution corresponding to the chosen confidence level of the search, and B is the expected number of background events. Although this expression is an approximation of the expected significance of the search, it is easier to compute than the full limit setting procedure, but still provides a good estimate of the expected significance that can be used to optimize analysis selections and to achieve a close to optimal sensitivity of the full search.

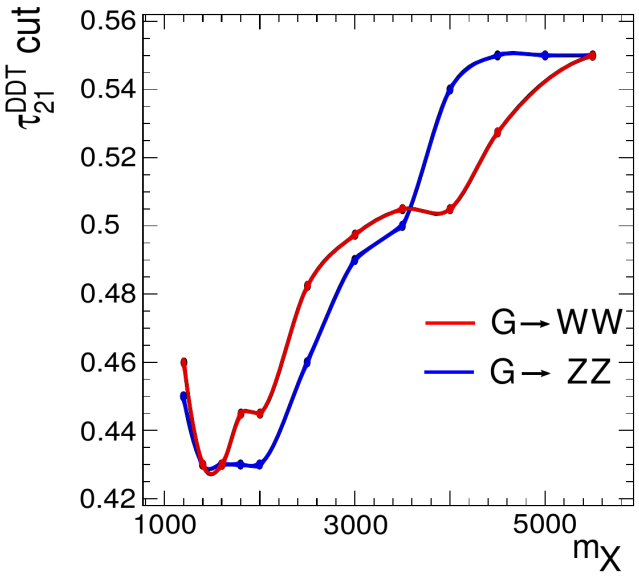

Figure 5.15.: The τ_{21}^{DDT} selection that maximizes the Punzi significance as a function of the resonance mass for a bulk graviton to WW signal (red line) and a bulk graviton to ZZ signal (blue line).

Figure 5.15 shows the τ_{21}^{DDT} cut, which maximizes the Punzi significance as a function of the resonance mass. In the optimization procedure two opposing trends are visible: on the one

hand both the signal selection efficiency and the number of background events increase with a looser τ_{21}^{DDT} cut, while the number of background events decreases exponentially with higher dijet invariant masses. This leads to an increase in the optimal τ_{21}^{DDT} cut for higher signal masses. Since the relation of the number of background events selected by an increasing τ_{21}^{DDT} cut is non-linear, the observed optimal selection cut as a function of the dijet invariant mass is non-linear as well. The overall trend that with decreasing background contribution, i.e., for higher signal masses, less stringent cuts on τ_{21}^{DDT} are favorable, while smaller values are more favorable for small masses can clearly be seen in Fig. 5.15. To mitigate this effect, the analysis uses two categories, one HPHP category where the τ_{21}^{DDT} value has been chosen as being around the optimal for small signal masses around 2 TeV, and a HPLP category, which reclaims significance for high signal masses.

In order to minimize any correlations in the jet mass distributions and simplify the modeling procedure, the two jets in the event selected for reconstruction are labeled at random, so that the mass distributions of the first (m_{jet1}) and second selected jet (m_{jet2}) have the same shape.

5.1.3. V-tagging

The modeling of jets and their substructure is very challenging since it relies on showering and hadronization models and their respective tuning to data. As explained in previous sections those models cannot be derived from first principles and are therefore phenomenological. This leads sometimes to large discrepancies between simulation and data. These differences need to be estimated and corrected, however, these procedures are still subject to rather large uncertainties. References [143, 170, 171] discuss the methods used to derive scale factors in order to correct observed differences between simulation and data in more detail. To estimate a scale factor, the procedure detailed in Ref. [143] is followed, by isolating a control sample of merged W-jets in high p_{T} $\mathrm{t\bar{t}}$ processes. The sample contains a $\mathrm{t\bar{t}}$-enriched control region, derived by identifying a leptonically decaying W boson, as well as at least one b-tagged jet. For this measurement the $\mathrm{t\bar{t}}$-enriched control region is split into a pass and fail category, passing the $\tau_{21}^{\mathrm{DDT}} \leq 0.43$ cut and failing it, respectively. A scale factor is extracted from both regions utilizing the peak originating in W boson decays in the soft drop jet mass distribution. Since the goal of the procedure is to extract a scale factor for real W bosons, the jet mass distribution is fitted using two analytic functions, a Gaussian modeling real W bosons, which are matched to the generated W bosons in simulation, and an Error function, which models the combinatorial background from unmerged ($\mathrm{t\bar{t}}$) jets. This model is fitted to both MC simulation and data, in order to extract the scale factors. The efficiency scale factors are calculated as the ratio of tagging efficiencies for W bosons in data over the same efficiency in simulation.

The results of the fits are shown in Figure 5.16 for 2016 and 2017 data respectively, while the resulting scale factors are listed in Table 5.2. The same scale factor measurement is also used to extract a scale factor for the jet mass scale and resolution, utilizing the fitted mean and width of the W boson peak in data and MC simulation. These scale factors and uncertainties are listed in Table 5.2 as well. In Figure 5.16 a mismodeling of the data spectrum for small jet masses can be seen, especially for 2017 simulation. In this region the contribution from unmerged and partially merged W bosons is largest. The modeling of these contributions in

MC simulation is challenging, and depends on radiation corrections as well as the UE, thus the difference between the years originates in the different tunes used in the MC generation. Note, that the corrections derived with this method are used to correct jets originating from W bosons to their measurement in data, differences in the modeling of unmerged $t\bar{t}$ jets are not corrected.

In addition to uncertainties arising from the fitting procedure itself and statistical uncertainties of the data in the control region, the uncertainties listed in Table 5.2 include systematic uncertainties due to the choice of the fit function, as well as uncertainties of the modeling of $t\bar{t}$ processes. The former uncertainty is estimated from a change of the function used to fit the W boson peak. For the latter, two systematic uncertainties are included: one due to differences in MC generation and modeling of the parton shower and one due to the impact of higher order corrections. Parton shower and MC generation uncertainties are evaluated by comparing the resulting scale factors when using $t\bar{t}$ simulation produced with different generators. The impact of higher order correction on the top quark p_T spectrum is evaluated by comparing the extracted efficiencies with and without reweighting according to the top quark p_T, where the reweighting is derived from data in order to better describe the observed p_T distribution in $t\bar{t}$ events, as derived in Ref. [171].

Table 5.2.: The W boson jet mass peak position (m) and resolution (σ), and the W-tagging efficiencies, as extracted from $t\bar{t}$-enriched data and from simulation, together with the corresponding data-to-simulation scale factors.

	m [GeV]	σ [GeV]	W-tagging efficiency
2016			
$\tau_{21}^{DDT} \leq 0.43$			
Data	82.0 ± 0.5 (stat)	7.1 ± 0.5 (stat)	0.080 ± 0.008 (stat)
Simulation	80.9 ± 0.2 (stat)	6.6 ± 0.2 (stat)	0.085 ± 0.003 (stat)
Data/simulation	1.014 ± 0.007 (stat+syst)	1.09 ± 0.09 (stat+syst)	0.94 ± 0.10 (stat+syst)
$0.43 < \tau_{21}^{DDT} < 0.79$			
Data			0.920 ± 0.008 (stat)
Simulation			0.915 ± 0.003 (stat)
Data/simulation			1.006 ± 0.009 (stat+syst)
2017			
$\tau_{21}^{DDT} \leq 0.43$			
Data	80.8 ± 0.4 (stat)	7.7 ± 0.4 (stat)	0.065 ± 0.006 (stat)
Simulation	82.2 ± 0.3 (stat)	7.1 ± 0.3 (stat)	0.068 ± 0.005 (stat)
Data/simulation	0.983 ± 0.007 (stat+syst)	1.08 ± 0.08 (stat+syst)	0.96 ± 0.12 (stat+syst)
$0.43 < \tau_{21}^{DDT} < 0.79$			
Data			0.935 ± 0.006 (stat)
Simulation			0.932 ± 0.005 (stat)
Data/simulation			1.003 ± 0.008 (stat+syst)

The W boson tagging efficiency in the selected $t\bar{t}$ events of around 7% is relatively low, since these events are dominated by W boson jets with a transverse momentum of around 200 GeV, just at the threshold where the decay products of the W boson merge into a single jet. However, V boson jets originating from signal processes mostly have a p_T above 600 GeV, and the tagging efficiency of τ_{21}^{DDT} increases with the jet p_T to an efficiency of around 35%. The tagging efficiency for the background stays constant as a function of p_T as shown in Ref. [170].

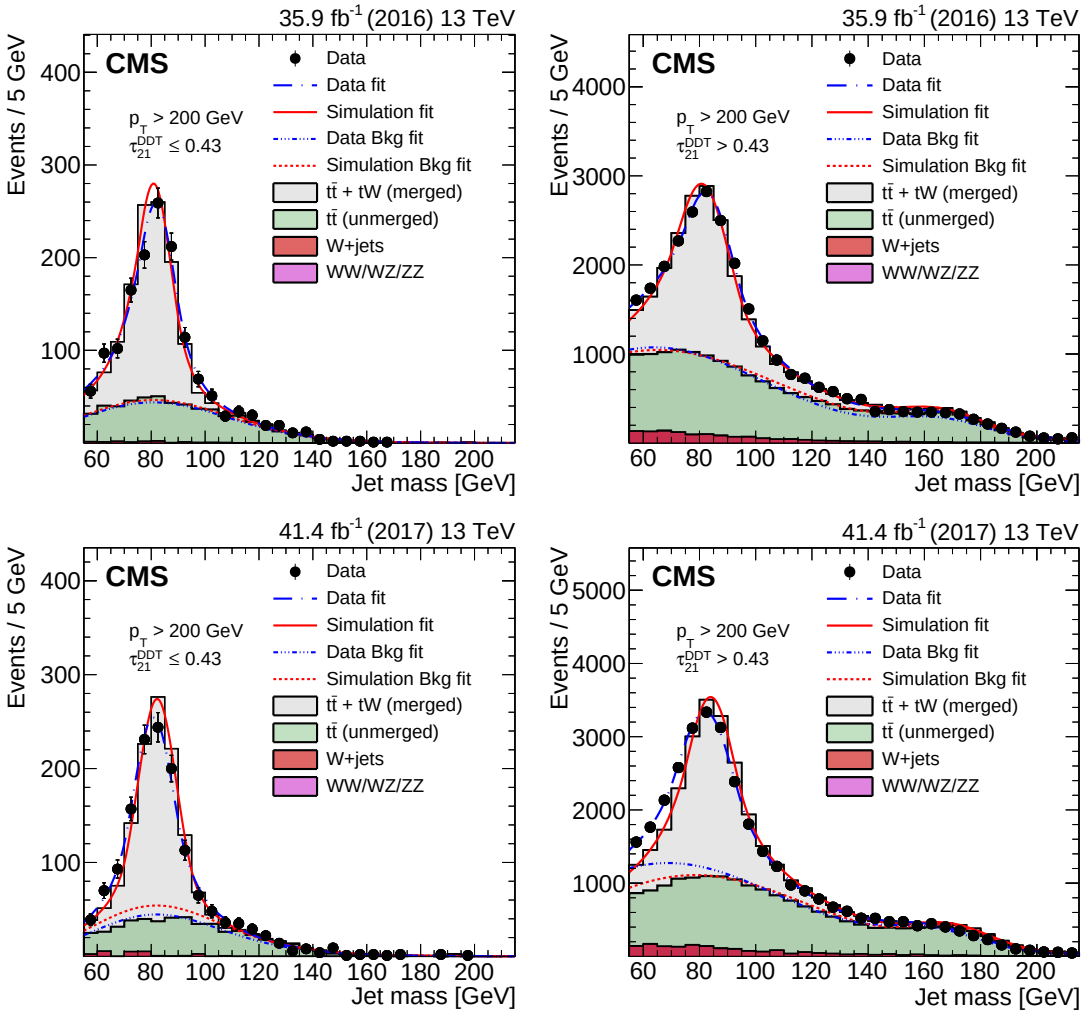

Figure 5.16.: PUPPI soft drop jet mass distribution that pass (left) and fail (right) the τ_{21}^{DDT} selection in a $t\bar{t}$ enriched control sample. The results are shown for the 2016 data taking period (top) and the 2017 data taking period (bottom). The result of the fit to data (blue line) and simulation (red line) are shown as well as the background components of the fit which are shown as dashed-dotted lines. Figure published in Ref. [159].

An additional uncertainty on the scale factor is applied, which estimates the uncertainty on the p_{T} dependence of the scale factor, when applying the measured scale factors to higher momenta jets outside of the range of the $t\bar{t}$ control region. Uncertainties in the p_{T} extrapolation of the W-tagging scale factors are expected to originate mostly from differences in the showering and hadronization of particles in the jets between data and simulations. This uncertainty is therefore estimated by parametrizing the difference between PYTHIA8 and HERWIG++ simulation relative to their difference at low transverse momenta. Therefore, the difference in tagging efficiency between the two samples at low-p_{T} is compared to the same difference in tagging efficiency at high-p_{T}. The quantity

$$\sigma_{p_{\mathrm{T}},i} = \frac{\epsilon_{\mathrm{H++}}}{\epsilon_{\mathrm{P8}}}\bigg|_{p_{\mathrm{T}},i} \div \frac{\epsilon_{\mathrm{H++}}}{\epsilon_{\mathrm{P8}}}\bigg|_{p_{\mathrm{T}}=300\,\mathrm{GeV}} - 1\ , \tag{5.2}$$

is calculated, where $\sigma_{p_{\mathrm{T}},i}$ is the p_{T}-dependent uncertainty on the scale factor, with the interval in p_{T} denoted as i, while the tagging efficiency in a HERWIG++ (PYTHIA8) sample is given by $\epsilon_{\mathrm{H++}}(\epsilon_{\mathrm{P8}})$.

The result of this uncertainty estimation is parametrized using

$$u_{\mathrm{HPHP}} = 0.06 \cdot \log\left(\frac{p_{\mathrm{T}}}{300\ \mathrm{GeV}}\right) \tag{5.3}$$

$$u_{\mathrm{HPLP}} = 0.07 \cdot \log\left(\frac{p_{\mathrm{T}}}{300\ \mathrm{GeV}}\right)\ , \tag{5.4}$$

for the HPHP (HPLP) category, respectively.

5.2. Signal Modeling

In order to apply the new multi-dimensional fit method, the signal has to be parametrized in three dimensions. Because of the simple confined peak structure of the signal in all three dimensions, it is possible to define the signal pdf as a product of the shape of the resonance mass and the jet masses:

$$\begin{aligned} P_{\mathrm{sig}}(m_{\mathrm{jj}}, m_{\mathrm{jet1}}, m_{\mathrm{jet2}}|\overline{\theta}^{\mathrm{s}}(m_{\mathrm{X}})) = P_{\mathrm{VV}}(m_{\mathrm{jj}}|\overline{\theta}^{\mathrm{s}}_1(m_{\mathrm{X}}))\times \\ P_{\mathrm{j1}}(m_{\mathrm{jet1}}|\overline{\theta}^{\mathrm{s}}_2(m_{\mathrm{X}}))\ \times P_{\mathrm{j2}}(m_{\mathrm{jet2}}|\overline{\theta}^{\mathrm{s}}_3(m_{\mathrm{X}})). \end{aligned} \tag{5.5}$$

Here, the shapes for m_{jj}, m_{jet1} and m_{jet2} denoted as P_{VV}, P_{j1} and P_{j2}, respectively, are parametrized with double-sided Crystal Ball (dCB) [172] functions for each signal mass m_{X}. A dCB function is commonly used to describe detector resolutions and defined as

$$\mathrm{dCB}(x) = \begin{cases} e^{\frac{-(x-\bar{x})^2}{2\sigma^2}} & \text{for } -\alpha_1 < \frac{x-\bar{x}}{\sigma} < \alpha_2 \\ \left(\frac{n_1}{|\alpha_1|}\right)^{n_1} \cdot e^{-\alpha_1^2/2} \cdot \left(\frac{n_1}{|\alpha_1|} - |\alpha_1| - \frac{x-\bar{x}}{\sigma}\right)^{-n_1} & \text{for } \frac{x-\bar{x}}{\sigma} < -\alpha_1 \\ \left(\frac{n_2}{|\alpha_2|}\right)^{n_2} \cdot e^{-\alpha_2^2/2} \cdot \left(\frac{n_2}{|\alpha_2|} - |\alpha_2| - \frac{x-\bar{x}}{\sigma}\right)^{-n_2} & \text{for } \frac{x-\bar{x}}{\sigma} > \alpha_2 \end{cases}, \tag{5.6}$$

with the parameters n_1, n_2, α_1 and α_2 as free parameters governing two power-law tails, while σ and $\bar{x}$ are the standard deviation and mean of the Gaussian core function, respectively. In equation (5.5), the parameters $\overline{\theta}^{\mathrm{s}} = (\overline{\theta}^{\mathrm{s}}_1, \overline{\theta}^{\mathrm{s}}_2, \overline{\theta}^{\mathrm{s}}_3)$ denote the free parameters of the dCB functions. Due to the resonant, and therefore, localized distributions of signal processes in all considered mass dimensions, the m_{jj} and m_{jet} distributions can be considered uncorrelated and can therefore be fitted separately from each other.

In order to parametrize signals with arbitrary resonance masses m_{X}, each dCB parameter is considered to be a function of m_{X}. Each dCB parameter is then interpolated between generated signal masses. This interpolation is based on fitting the dCB parameters as a function of the resonance mass m_{X}, with a polynomial of sufficient degree to ensure smooth shapes for each interpolated mass point, as can be seen in Figure 5.17. The resulting signal shapes are shown in Figure 5.18 for the dijet invariant mass (left), and the jet mass of jet-1 (right). The distribution for jet-2 is omitted since it is effectively identical to that shown for jet-1, because of the random jet labeling. The shapes describing the invariant dijet mass show a clear increase of their widths for large m_{X}. This is directly linked with the detector

resolution, that deteriorates with increasing energy. A similar increase in widths for high m_X can also be observed in the jet mass shapes. Here, three different shapes are observed depending on the signal model under consideration: both $G_{bulk} \to WW$ and $Z' \to WW$ result in very similar W boson mass shapes, while the $G_{bulk} \to ZZ$ signal model leads to a pure parametrization of the Z boson mass peak. The third observed shape for a $W' \to WZ$ is a mixture between the W and Z boson mass distributions, since each jet mass contains about 50% W bosons and 50% Z bosons, due to the random labeling of jets in the event. This, as well as the large overlap between the W boson and Z boson mass distributions, leads to difficulties to clearly distinguish between signal models in the case that an excess should be observed. However, even using the previously established method of splitting the jet mass into windows for the W, Z and Higgs boson the distinction between different signal models is not more reliable due to the large jet mass resolution.

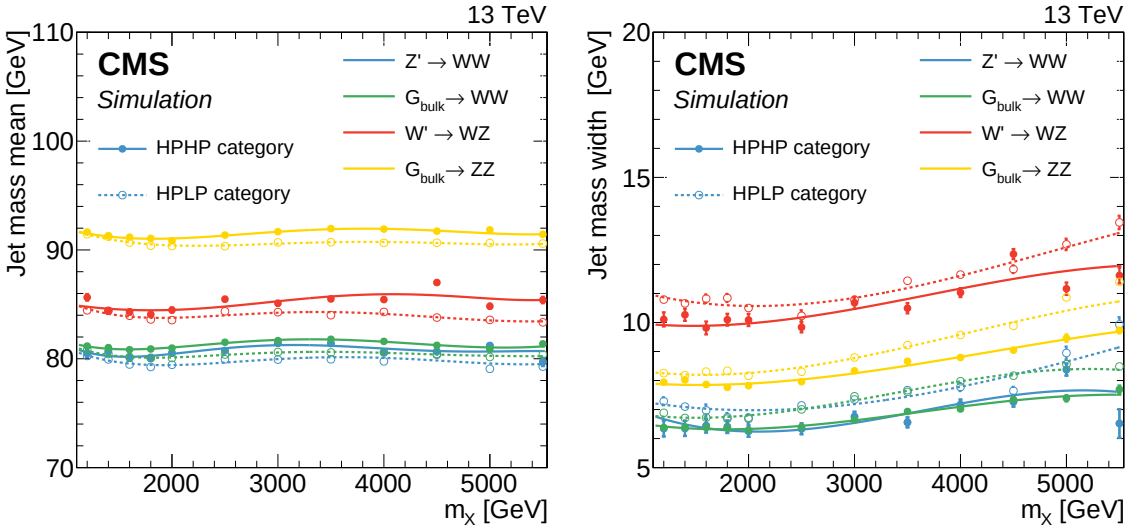

Figure 5.17.: The mass scale (left) and resolution (right) of the jet as a function of m_X, as they are obtained from the mean and width of the dCB function fitted to the spectrum. The HPHP (solid line) and HPLP (dotted line) categories are shown for different signal models. The distributions are only shown for one of the two jets in the event, since the distributions for the second jet are essentially the same due to the random labeling of jets utilized by the analysis. Figure published in Ref. [159].

Figure 5.17 shows the polynomial fit to two dCB parameters for P_{j1}, i.e., the jet mass scale and resolution as a function of m_X, after the full HPHP (HPLP) analysis selections have been applied. The jet mass mean is stable as a function of the resonance mass, while the width increases with m_X. In general the jet mass width of W bosons is around 7-8 GeV, while the jet mass distribution of a Z boson shows widths around 10 GeV. These apparent differences originate in the higher production rate of B-mesons in Z decays than in W decays, due to the rate of $Z \to b\bar{b}$ decays being about 15%. The branching ratio of $W \to bq'$ on the other hand is much smaller, due to the small phase-space of bt decays because of the top quark mass and the small branching fractions to other flavors because of the small CKM-mixing. Since B-mesons have about a 20% probability to decay semileptonically there is a non-negligible energy loss due to the production of neutrinos for Z bosons, which leads to the decrease in resolution and a larger tail of the distribution to low jet masses.

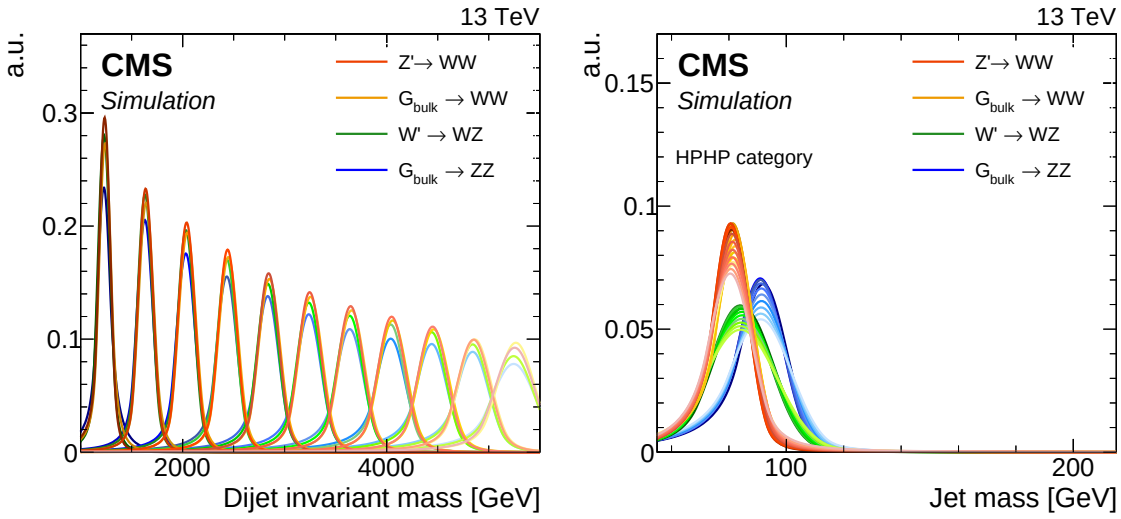

Figure 5.18.: The final m_{jj} (left) and m_{jet1} (right) signal shapes extracted from the parametrization of the dCB function. The same m_{jj} shapes are used for both purity categories. The jet mass distributions are shown for a range of resonance masses between 1.2 and 5.2 TeV for one of the two jets in the event in the HPHP category. Since the jets are labeled randomly, the jet mass distributions for the second jet are essentially the same and not shown here. The distributions for a bulk graviton decaying to WW have the same shapes as those for the Z′ signal and are therefore not visible. Figure published in Ref. [159].

For each mass point m_X and each purity category the signal efficiency is calculated and shown in Figure 5.19. The total signal yield after passing all analysis selections is divided by the number of generated events and parametrized as a function of m_X. To extract the expected signal yields for arbitrary resonance masses, the resulting spectrum is again fitted with a polynomial. Since a cut of m_{jj} <5.5 TeV is applied to the analysis, the signal efficiency drops for very large resonance masses. This selection cut on high resonance masses is applied to the whole analysis for technical reasons: to set limits for masses that are higher than can be generated in a reasonable amount at the LHC would be disingenuous, for this reason the analysis is stopped at 5.5 TeV, which is approximately 400 GeV above the event with the highest dijet invariant mass in data. Since the modeling of both background and signal processes is stopped at this point, this has to be taken into account when modeling the expected signal yields.

To cross check the validity of the signal modeling, the shapes derived by the methods described in this section, are compared to toy MC samples following the distributions expected from MC simulation for 1000 signal events. The results of this test are shown for a $G_{bulk} \rightarrow WW$ sample in Figure 5.20, 5.21 and 5.22 for m_{jj}, m_{jet1} with HPHP selections and m_{jet1} with HPLP selections, respectively. The tests show a good agreement between the signal modeling and the MC simulation. The same tests for the remaining signal models can be found in Appendix B.

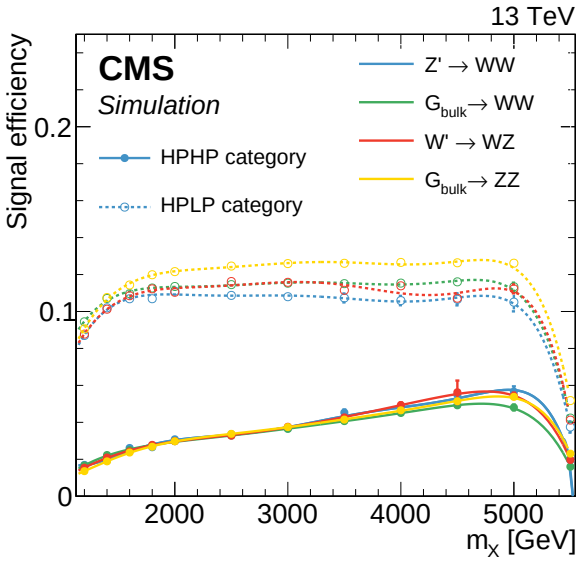

Figure 5.19.: The total signal efficiency as a function of m_X after all selections are applied, for different signal models. The denominator is the number of generated events. The solid and dashed lines show the signal efficiencies for the HPHP and HPLP categories, respectively. Figure published in Ref. [159].

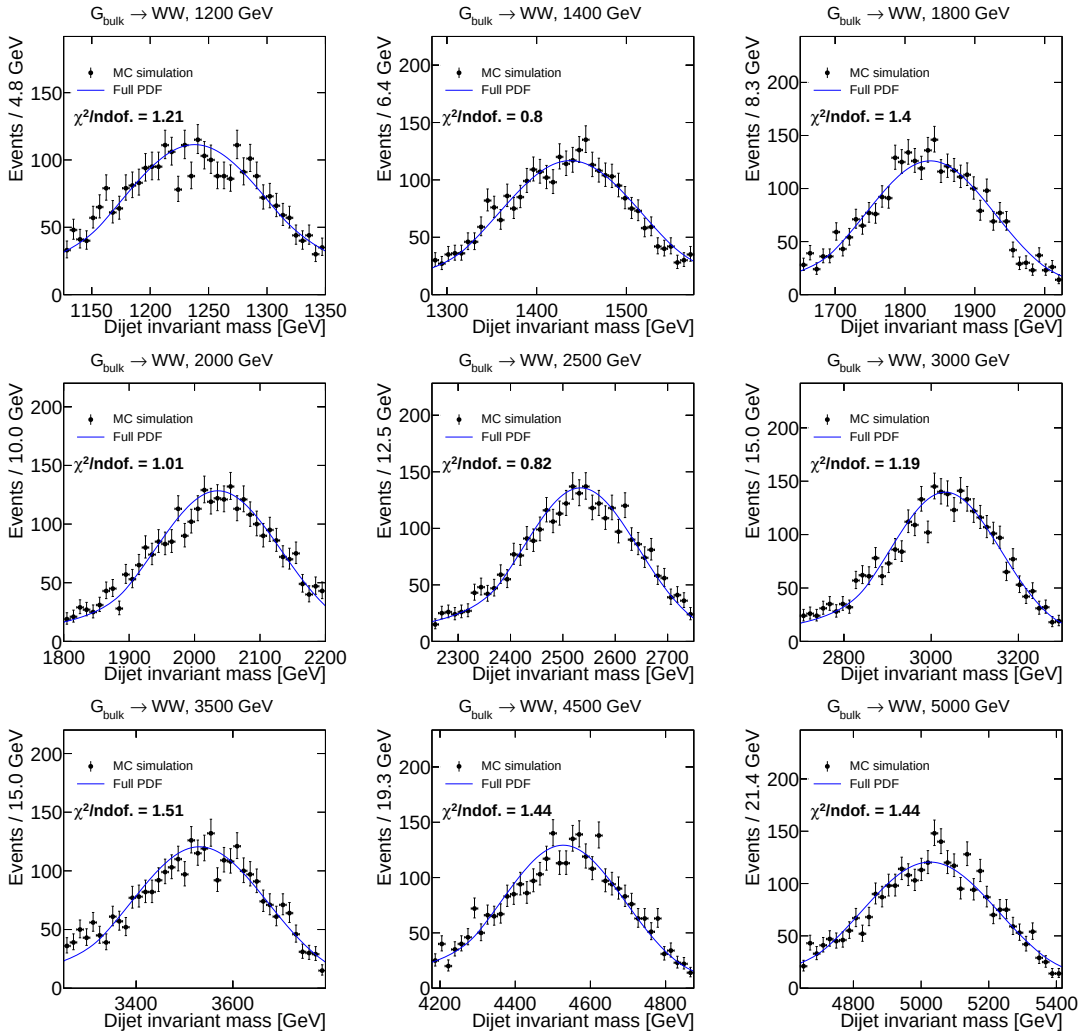

Figure 5.20.: Comparison between the final signal model and the dijet invariant mass distribution from MC simulation for 1000 signal events. Note that no additional fit is carried out for this comparison.

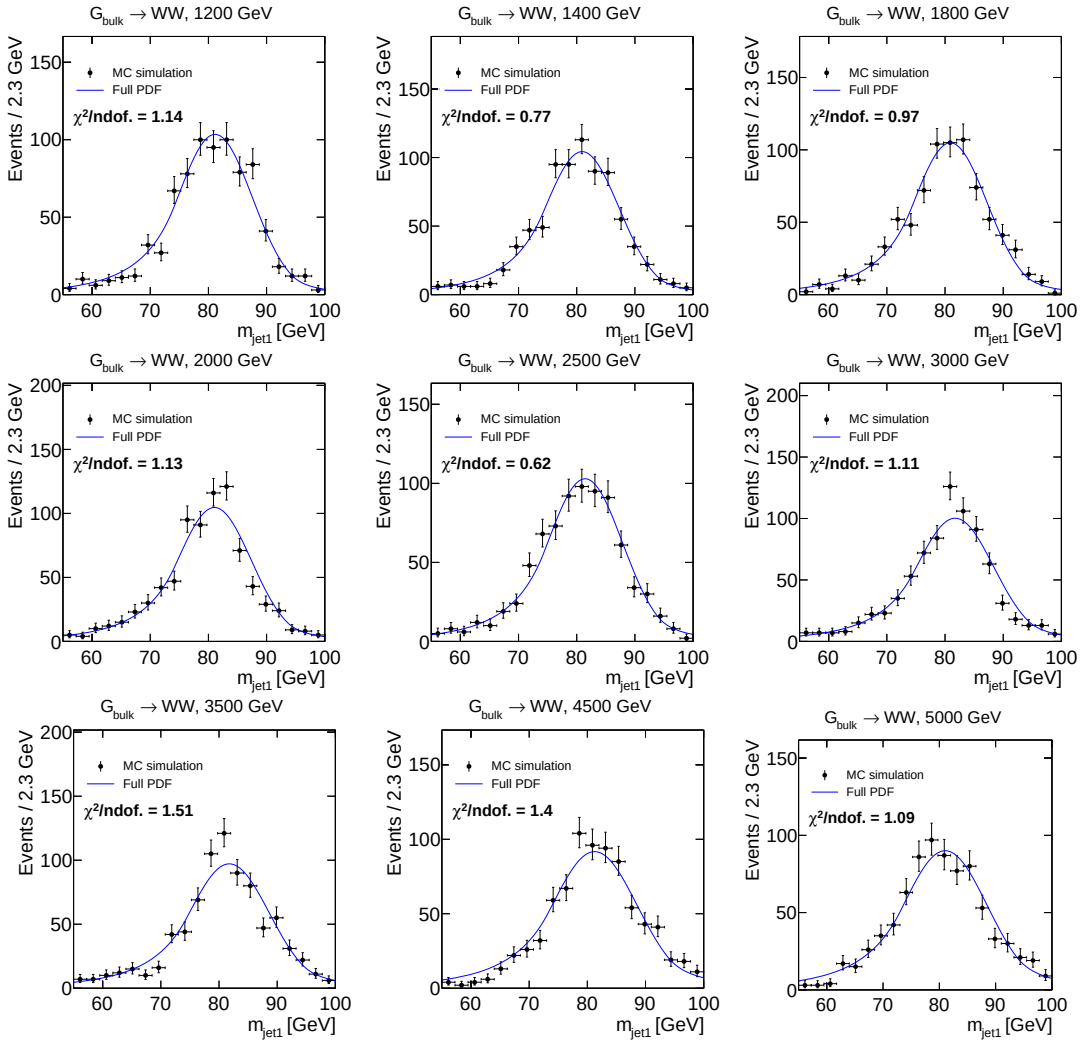

Figure 5.21.: Comparison between the final signal model and the jet mass distribution from MC simulation for 1000 signal events in the HPHP category. Note that no additional fit is carried out for this comparison.

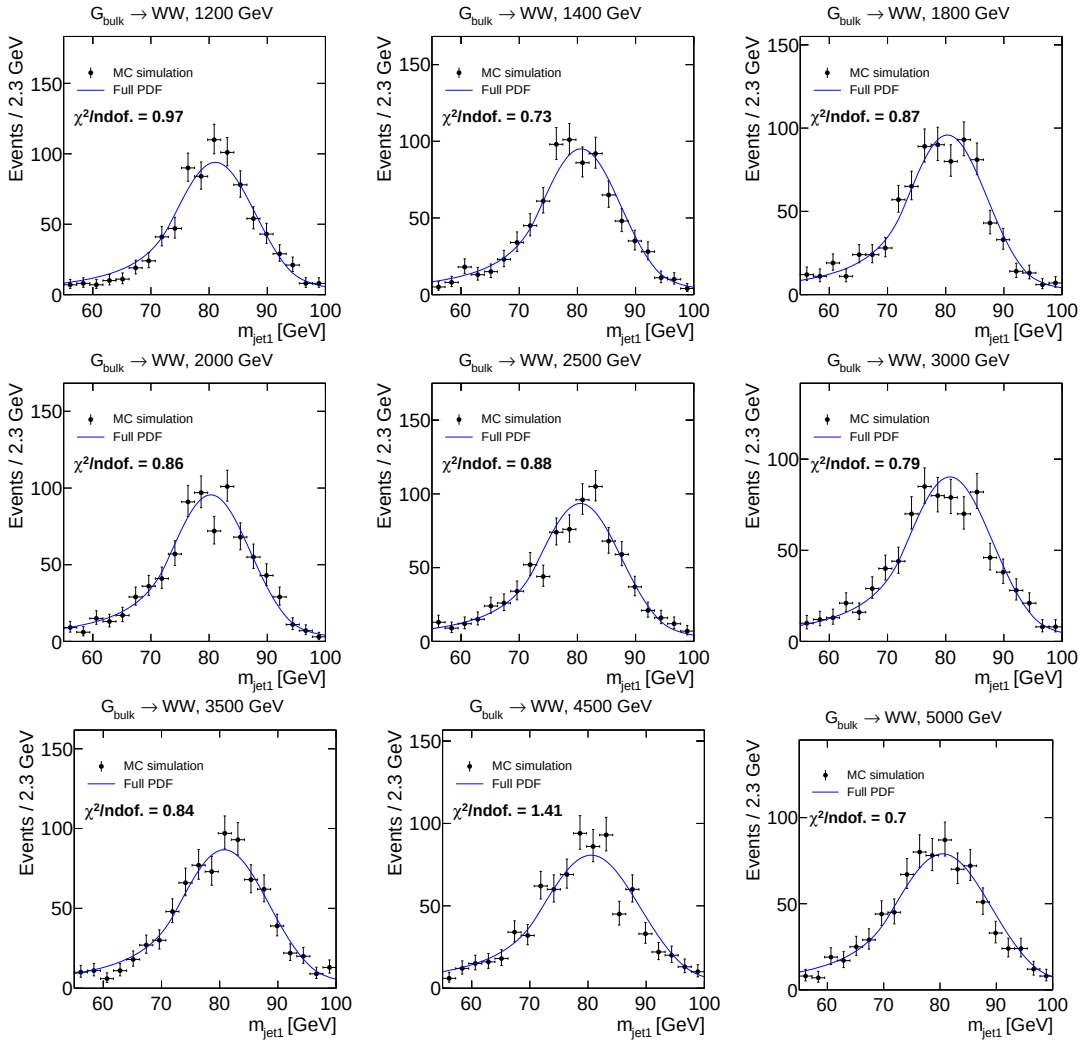

Figure 5.22.: Comparison between the final signal model and the jet mass distribution from MC simulation for 1000 signal events in the HPLP category. Note that no additional fit is carried out for this comparison.

5.3. Background Modeling

The background modeling in previous iterations of all-hadronic diboson resonance searches [35,173] relies on a one-dimensional fit of a monotonically falling function to the dijet invariant mass spectrum of the signal region, around a soft drop mass of 65 GeV $\leq m_{\text{jet}} \leq$ 105 GeV. This approach is a relatively simple and robust method to derive a completely data driven background estimation, but also has some downsides, e.g. that valuable information, such as the correlations between variables, are not utilized. Therefore, a new method utilizing a three-dimensional fit of the m_{jet1}-m_{jet2}-m_{jj} hyperspace is implemented for the analysis of the data sets recorded in 2016 and 2017 by the CMS experiment comprising a total luminosity of 77.3 fb^{-1}. The new method can take advantage of the fact that the signal processes show a resonant behaviour not only in the dijet invariant mass but the masses of the two jets are also resonant around the W (Z) boson mass, while the main background is smoothly falling in all three-dimensions. It also opens the possibility of using a larger soft drop mass spectrum for the fit (55 GeV-215 GeV), which increases the yield of the available signal as well as permitting the future use of a single analysis framework for all VV, VH and HH signal searches. This method allows the incorporation of correlations between the jet masses and the dijet invariant mass for SM background processes, adding information to the multi-dimensional fit, which has not been exhaustively utilized in the past. For future developments the generality of the approach also allows for an easy extension to more exotic searches, for example signals decaying into a vector boson and a non-SM particle, or for wide resonances.

The main background of the analysis originates from QCD multijet events (see Figure 5.23), while there are other backgrounds mostly coming from processes with one vector boson and associated jets, which will be discussed in section 5.3.3.

5.3.1. Modeling of the QCD Multijet Background

To model the background from QCD multijet events, three-dimensional binned template shapes are built. These shapes are required to be smooth, without empty bins and describing the complex three-dimensional phase space of the analysis, including all important correlations between the mass observables.

The following fit range and binning is used for the three axes: m_{jet1} and m_{jet2} are fitted from 55 to 215 GeV using bins with a width of 2 GeV, leading to 80 bins in each jet mass, and a binning corresponding to the dijet resolution for m_{jj} leading to 36 bins with variable bin widths in the dijet invariant mass for m_{jj} between 1126 to 5500 GeV. The lower bound is chosen to avoid complications in the fitting procedure due to trigger turn-on effects, while the upper bound is chosen considering the highest dijet invariant mass found in data. The lower range of the jet mass was chosen to exclude a jet mass region that is not very well modelled in MC simulations, since in this phase-space regions NLO effects gain importance, while the upper bound on the jet mass was chosen to fully include a potential top quark mass peak. In addition to a nominal shape describing this background process, a number of alternative shapes corresponding to different jet energy scale and resolution variations and hadronization scenarios are built and used to allow the templates to be fitted to the data distribution. The generation of alternative shapes for the background prediction will be discussed in detail

in Section 5.3.2. This method allows a data-driven background estimation, which absorbs mismodeling in the QCD simulation. It further allows the determination of the shapes for QCD multijet distributions in the same fit in which the signal is determined by utilizing all available information from data sideband regions. Here, the term data sideband denotes a region in phase space, which contains no or only a small contribution from signal processes.

In order to model the QCD multijet background in the three-dimensional m_{jet1}-m_{jet2}-m_{jj} plane the following conditional product is used

$$\begin{aligned} P_{\text{QCD}}(m_{\text{jj}}, m_{\text{jet1}}, m_{\text{jet2}}|\overline{\theta}^{\text{QCD}}) = P_{\text{VV}}(m_{\text{jj}}|\overline{\theta}_1^{\text{QCD}}) \\ \cdot P_{\text{cond,1}}(m_{\text{jet1}}|m_{\text{jj}}, \overline{\theta}_2^{\text{QCD}})\, P_{\text{cond,2}}(m_{\text{jet2}}|m_{\text{jj}}, \overline{\theta}_3^{\text{QCD}})\,, \end{aligned} \tag{5.7}$$

with the two-dimensional templates $P_{\text{cond,1}}$ and $P_{\text{cond,2}}$ containing different jet mass shapes in intervals of m_{jj}, and the one-dimensional template P_{VV}, describing the dijet invariant mass distribution for QCD multijets. The templates $P_{\text{cond,1}}$ and $P_{\text{cond,2}}$ are essentially the same, except for statistical fluctuations, the choice to generate two templates is purely technical. The parameters $\overline{\theta}^{\text{QCD}} = (\overline{\theta}_1^{\text{QCD}}, \overline{\theta}_2^{\text{QCD}}, \overline{\theta}_3^{\text{QCD}})$ denote free parameters of the background fit. These parameters are included in the limit setting as nuisance parameters, that govern the template morphing between the up and down variations of an alternative shape and thus include shape variations for the three-dimensional QCD multijet spectrum. Which alternative shapes and corresponding nuisance parameters are included in the fit is discussed further in Section 5.3.2 and Section 5.4, while the following Section describes how the necessary templates are generated.

Using the probability density in equation (5.7) the problem of deriving a smooth three-dimensional shape describing the QCD multijet spectrum is reduced to computing the conditional two-dimensional shapes of m_{jet1} or m_{jet2} for a given interval in m_{jj}, as well as a one-dimensional shape of the m_{jj} distribution. Contrary to the signal, where correlations between $m_{\text{jet},i}$ and m_{jj} were negligible due to its small localization in the the three-dimensional space, these correlations have to be modeled for the QCD multijet background.

Due to the large phase-space that needs to be modeled and the limited number of available simulated events, the MC simulation cannot be used directly as a background model. A parametric description of the spectrum is complicated due to the need to parametrize three dimensions. Moreover, studies with the functional parametrization of the dijet spectrum, see Appendix E, have shown that a fit of the full dijet spectrum is not possible with a simple parametric function when no selection cut on the jet mass window is applied. The fitting procedure with a parametric function brings additional problems as well, such as the potential for large biases for signals beyond the narrow-width approximation as long as the function parameters are not sufficiently restricted. Thus, the templates are built using a forward-folding approach, which is described in more detail in the following sections 5.3.1 and 5.3.1.

Modeling of the Non-Resonant m_{jet} Spectrum

For the generation of the two-dimensional conditional templates of m_{jet} for a given m_{jj}, a forward-folding approach is used as follows: instead of filling a two-dimensional histogram

with reconstructed events, the important quantities of each event are calculated on generator level. This entails a full jet clustering on generator level particles. The generator quantities of each simulated event are then smeared with a Gaussian distribution, parametrizing the mass scale and resolution, resulting in smoothed histograms of reconstructed quantities.

For this approach the mass scale and resolution are parametrized using the ratio of $m_{\text{jet}}^{\text{reco}}$ and $m_{\text{jet}}^{\text{gen}}$, as a function of the generated transverse momentum of the jet. Since a random labeling of the two jets in the event is used for reconstruction, only one such parametrization is derived. The final scale and resolution used in the smearing of each event is derived by fitting a Gaussian function to the histogram containing $m_{\text{jet}}^{\text{reco}}/m_{\text{jet}}^{\text{gen}}$ for different regions in the generated jet p_{T}. Figure 5.24 shows the mass scale and resolution for an inclusive p_{T} selection. Figure 5.25 shows the final scale and resolution of the mass extracted as a function of the generated p_{T}. The same procedure is used to parametrize the mass scale and resolution for m_{jj}, as shown in Figure 5.24 and 5.25 (right). The features observed at a p_{T} of 400 GeV in the jet mass scale and resolution of m_{jj} are statistically significant, and can be observed for all MC generators tested in this analysis. Since the feature exists for CHS and PUPPI pileup subtraction and in both the barrel and endcap region of the detector, it most likely originates from the jet energy corrections, however, the true source has not been unambiguously identified. The differences between the two years originate from changes in the detector conditions, as well as the different pileup subtraction methods used in the two years.

The final Gaussian kernel used for the smearing is defined as

$$k_i(m_{\text{jet}}^{\text{gen}}, m_{\text{jj}}^{\text{gen}}, p_{\text{T}}^{\text{gen}}) = \frac{w_i}{\sqrt{2\pi} r_{p_{\text{T}}^{\text{gen}},i} \cdot R_{p_{\text{T}}^{\text{gen}},i}} \exp\left(-\frac{1}{2}\left(\frac{m_{\text{jj}}^{\text{gen}}(1 - S_{p_{\text{T}}^{\text{gen}},i})}{R_{p_{\text{T}}^{\text{gen}},i}} \right)^2 - \frac{1}{2}\left(\frac{m_{\text{jet}}^{\text{gen}}(1 - s_{p_{\text{T}}^{\text{gen}},i})}{r_{p_{\text{T}}^{\text{gen}},i}} \right)^2 \right) , \tag{5.8}$$

where $S_{p_{\text{T}}^{\text{gen}}}(s_{p_{\text{T}}^{\text{gen}}})$ and $R_{p_{\text{T}}^{\text{gen}}}(r_{p_{\text{T}}^{\text{gen}}})$ denote the scale and resolution of the mass for $m_{\text{jj}}^{\text{gen}}$ ($m_{\text{jet}}^{\text{gen}}$) for a given momentum $p_{\text{T}}^{\text{gen}}$, w_i is the event weight and the index i denotes the event.

Each event in MC simulation is then smeared with the kernel function from equation (5.8) and used to generate two two-dimensional histograms containing the conditional binned pdfs $P_{\text{cond},1}$ and $P_{\text{cond},2}$. In Figure 5.26, the resulting two-dimensional conditional probabilities are shown for m_{jet1} (left) and m_{jet2} (right).

In order to avoid producing an artificial turn-on caused by the smoothing procedure, the analysis cuts applied on generator level are less stringent than the preselection on data. Instead all events with jet masses between 20-300 GeV and a generated dijet invariant mass between 800-6000 GeV are used in the forward-folding method.

Modeling of the Non-Resonant m_{jj} Spectrum

The modeling of the non-resonant m_{jj} spectrum uses the same technique as the m_{jet} conditional kernels, with the slight difference that this time only a one-dimensional kernel is built

from the smoothed simulated events. In Figure 5.27 the kernels derived from this procedure are compared to the reconstructed events taken from simulation.

Full Background Model

The one-dimensional shape P_{VV} and the two dimensional shapes $P_{\mathrm{cond,1}}$ and $P_{\mathrm{cond,2}}$ derived in the previous sections are convoluted into a full three-dimensional pdf, describing the whole phase-space of the analysis, following equation (5.7). Because of the forward-folding approach employed to create smooth 2D or 1D templates, each event in the simulated MC sample is smeared three times, once for each template. The goal of this approach is to fabricate smooth three dimensional pdfs that are able to reproduce the observed distributions in MC simulation in all three dimensions. However, this is only a part of the final background model, since large differences between data and MC simulation for substructure observable such as the PUPPI soft drop jet mass or the distribution of τ_{21}^{DDT} are observed, a data-driven approach is pursued. Consequently, the shapes derived in the previous sections are not the final background model, but rather an ensemble of alternative pdfs, corresponding to fluctuations of known uncertainties of the QCD multijet spectrum, are generated. These different pdf shapes are then fitted to data using vertical template morphing. This approach allows the incorporation of the jet energy scale and resolution uncertainties, as well as differences of the mass spectra due to different MC generators and showering algorithms. The final tests of the validity of this approach are described in detail in Section 5.5. Nonetheless, as a first sanity check of the template generation method, Figure 5.28 shows the comparison of the three-dimensional pdf to simulated events projected on m_{jj}, m_{jet1} and m_{jet2}. It is important to note, that the projections in Figure 5.28 are not used to decide if the pdfs derived in this Section are truly able to describe the spectrum from MC simulation, this decision is based on the gof tests described in Section 5.5, however, the projections already give a good indication that the derived pdfs are able to accurately reproduce the spectra and the correlation in MC simulation. The method shows a good compatiblity between the kernels derived from generator quantities and the reconstructed events from MC simulation, thus accomplishing a binned description of the QCD multijet background that is smooth over the whole covered phase space. The conditional projections on m_{jet} also show the correlations between m_{jj} and the two jet masses, which lead to a change in slope of the m_{jet} spectra depending on the interval in m_{jj}.

5.3.2. Alternative Background Shapes

The theoretical modeling of QCD multijet processes entails a multitude of challenges that makes the accurate description of such processes unreliable. For example, showering and hadronization are modeled empirically, which differs between generators such as PYTHIA8 and HERWIG++. Additionally, the MC simulation samples used to build the nominal kernels for the background estimation are generated at LO, meaning that there might be sizable differences between the distributions in simulation and in data. In order to account for such differences a number of alternative shapes are built in addition to the nominal kernel shapes, which are used in a fit to data in the limit setting using vertical template morphing. With this method, the data sideband region can be used to constrain the shape of the QCD

multijet background.
Since a simultanous fit of the background shapes and the signal is carried out in the limit setting procedure one has to be careful to not add background shapes that could potentially mask a signal. To ensure that there is no such bias for the shapes utilized in this analysis signal injection tests have been conducted, see Section 5.5, finding that the procedure does not introduce a bias on the number of fitted signal events.

At the same time the alternative shapes must provide enough flexibility for the fit to adapt to the QCD multijet distribution in data, which might be significantly different from the nominal shape for this background process extracted from PYTHIA8 simulation. Ten alternative shapes are created, which are up- and down-variations of a systematic uncertainty in the spectrum. Each pair of up- and down-variations introduces a new nuisance parameter, that is allowed to vary during the fitting procedure. In the end five nuisance parameters for shape variations of the QCD multijet background are introduced.

Two alternative shapes are built by varying m_{jet} and m_{jj} by a factor of

$$\alpha = 1 + 3 \cdot 10^{-4} \times m \tag{5.9}$$

or by a factor of

$$\beta = 1 + 1.2 \cdot 10^{3} \times m^{-1} \ , \tag{5.10}$$

where m is either m_{jj} or m_{jet}. The corresponding down-variations are built by varying the nominal template by $1/\alpha$ or $1/\beta$. The factors α and β are chosen to simulate the variation in the slope of the m_{jet} and m_{jj} spectra as expected from a variation of the underlying p_{T} spectrum. Such a change in the p_{T} spectrum might arise from a change in the jet energy scale or resolution. The alternative shapes derived using the variation with α are called "$\propto m_{\text{jj}}$ up/down" in the following, while the variation with β are called "$\propto 1/m_{\text{jj}}$ up/down".

There are four alternative shapes derived from building templates with MC simulation using different generators and parton showers. These shapes are generated by applying the procedure described in Section 5.3.1 to a HERWIG++ (MADGRAPH5_AMC@NLO) MC sample. The resulting templates are added to the fit as an "up-"variation following the spectrum from a different MC generator. The "down-"variations are created by scaling the nominal PYTHIA8 template with the ratio of the nominal and new shape, effectively mirroring the new shape along the nominal template.

The last set of alternative shapes are introduced to allow a larger slope variation in the range of $m_{\text{jet}} > 200\,\text{GeV}$ and $m_{\text{jj}} < 1300\,\text{GeV}$. These shapes were added since a fit test of the background model in a LPLP control-region showed a mismodling in this region, which could not be reproduced with the existing alternative shapes. These shapes are built by varying the three-dimensional nominal kernels up (down) with a sigmoid function

$$s = 1/(1 + e^{((m_{\text{jet1}}-235)/10)+((m_{\text{jet2}}-235)/10)+(-(m_{\text{jj}}-2000)/100)}) \ .$$

Note here, that the signal region is not affected by this shape, which only modifies a small part of the phase-space of the analysis.

Figure 5.29 shows projections on m_{jet} and m_{jj} for the nominal kernels and alternative shapes discussed here for the HPLP category. The shapes are normalized and compared to the

normalized distribution from a QCD multijet MC simulation derived with the PYTHIA8 MC generator. Since all shapes are normalized in this representation, the area covered by uncertainties are not represented in their entirety, i.e., the crossing point of the templates for alternative shapes at around 105 GeV (1.2 TeV) are due to the normalization and do not represent that this point in the spectrum is not covered by uncertainties. The simulation shown has many points below the template, however, this is mostly due to outliers in simulation because of the small event numbers, that result in the simulation moving below the template, when the same normalization is applied. In the final fitting procedure such differences are fully covered by the 50% normalization uncertainty assigned to the QCD multijet background.

The procedure described above is only used to derive templates for the HPLP category since the tight cuts for the HPHP category lead to poorly populated histograms that cannot be smoothed even with the used forward-folding approach. Instead, the templates for the HPLP category are used to fit the HPHP MC simulation, and the resulting post-fit templates are used to model the HPHP category. This procedure is possible since the sculpting of the jet mass distribution is minimal for different τ_{21}^{DDT} cuts, owing to the decorrelation of τ_{21}^{DDT} from the jet mass. The templates are shown in Fig. 5.30 compared to simulation from a PYTHIA8 MC sample for the HPHP category. There are some differences between the simulation and templates, however, these originate mostly in statistic outliers in the MC simulation, which lead the distribution to move below the templates when the same normalization is applied. However, in the final fit such differences are fully covered by the normalization uncertainty applied to QCD multijet processes, as well as by the alternative shapes added to the fit.

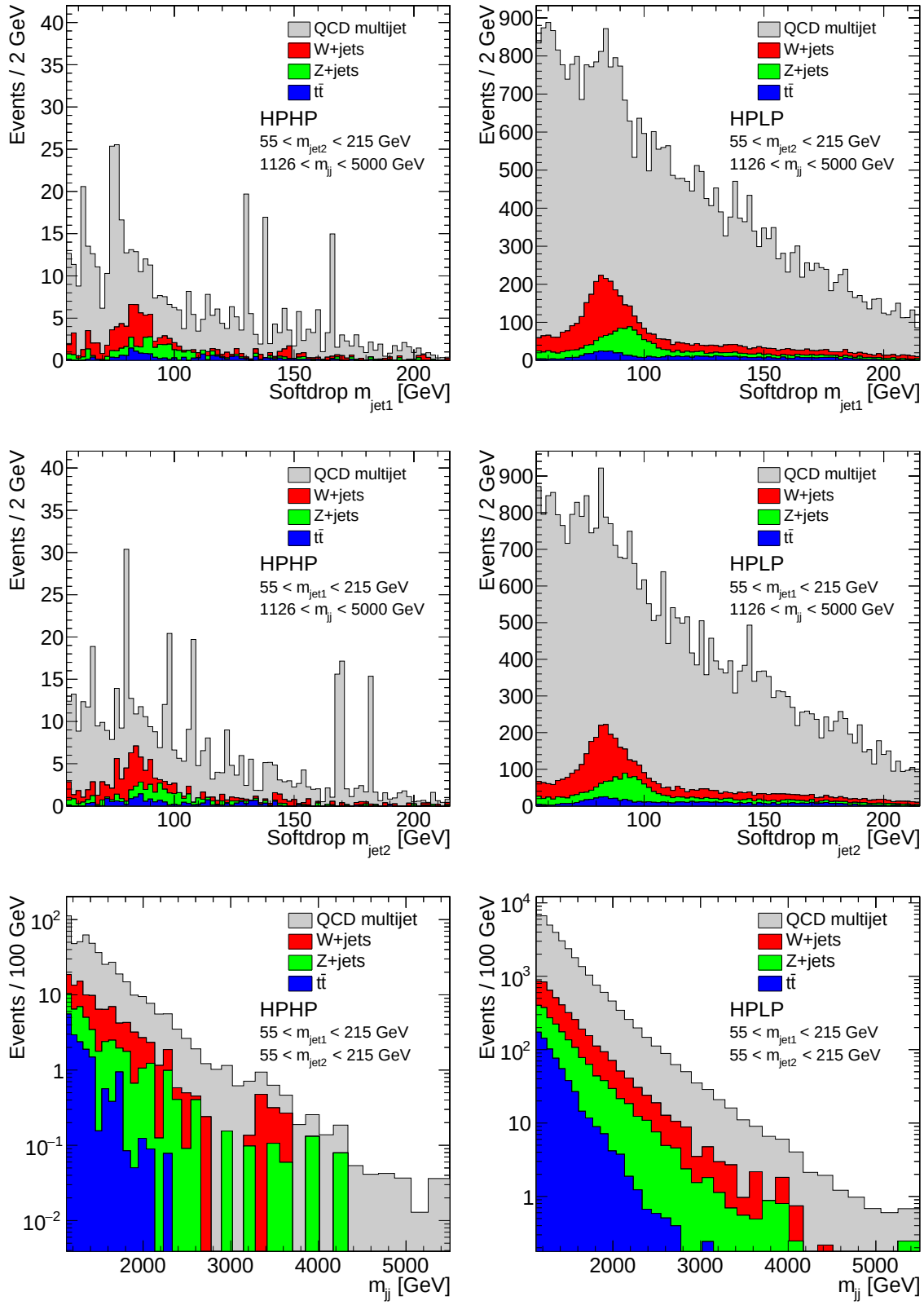

Figure 5.23.: Distributions of the different background processes in m_{jet1} (top), m_{jet2} (middle) and m_{jj} (bottom) for the HPHP category (left) and HPLP category (right).

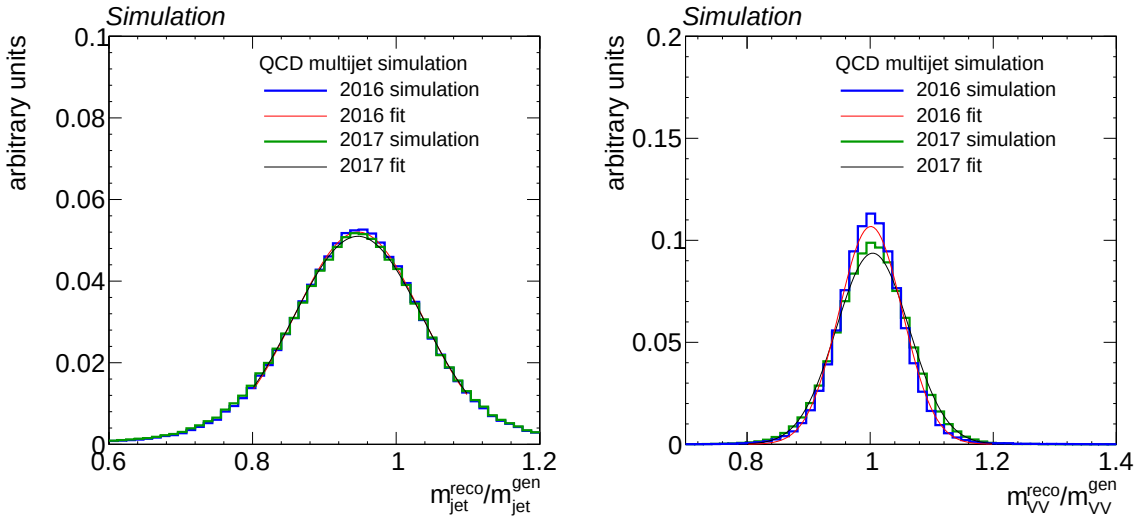

Figure 5.24.: The mass scale and resolution for all generated jet momenta for m_{jet} (left) and m_{jj} (right). To extract the scale and resolution, the spectrum is fitted with a Gaussian function for different intervals of the generated jet momenta.

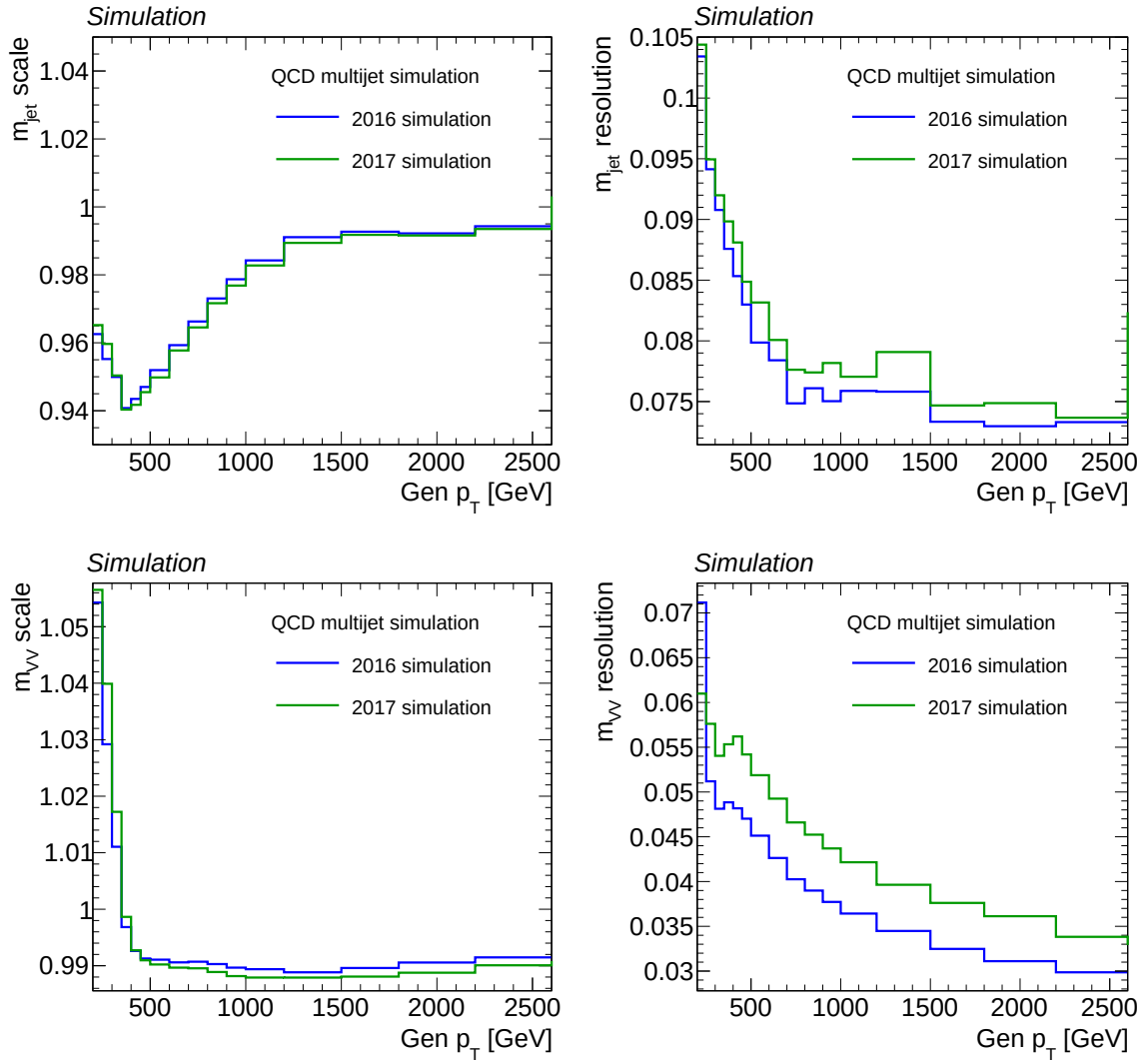

Figure 5.25.: The parametrization of the mass scale (left) and resolution (right) as a function of the generated jet p_{T} for m_{jet} (top) and m_{jj} (bottom).

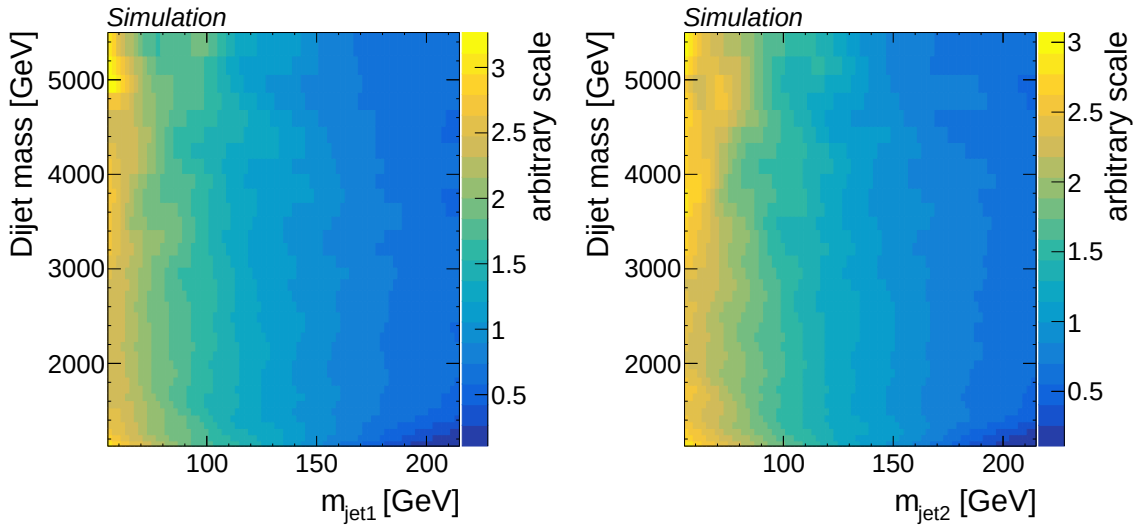

Figure 5.26.: The conditional pdfs of m_{jet} for a given interval in m_{jj} for the main QCD multijet background processes. The left histogram shows the pdf for m_{jet1} and the right for m_{jet2}. Since the two jets in the event receive random labels these distributions are essentially the same barring effects from statistical fluctuations.

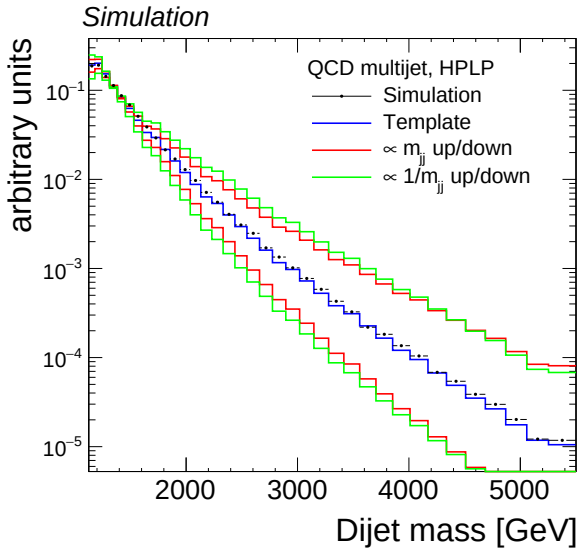

Figure 5.27.: The one-dimensional m_{jj} kernels derived from the forward-folding procedure compared to reconstructed events taken from a simulated sample for the QCD multijet background. The green and red lines show alternative shapes derived by varying the m_{jj} spectrum proportional to m_{jj} or to $1/m_{\text{jj}}$.

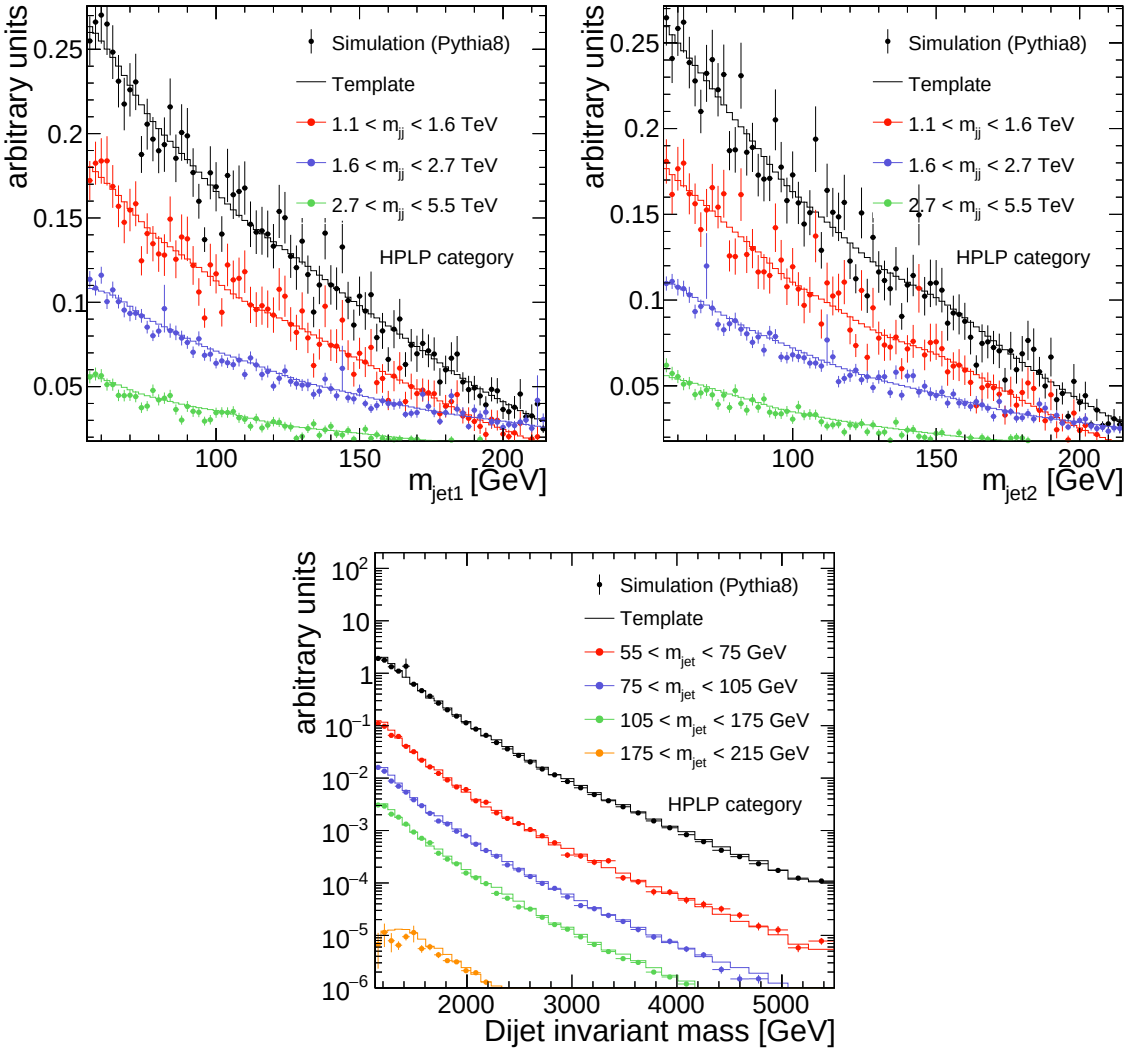

Figure 5.28.: Projections of the three-dimensional kernels (lines) on m_{jet1} and m_{jet2} (top) and m_{jj} (bottom) compared to QCD multijet events taken from simulation (markers) for the HPLP category. The black line (markers) show the projections of the whole phase-space for the pdf (simulation), while the colored lines (markers) show conditional projections.

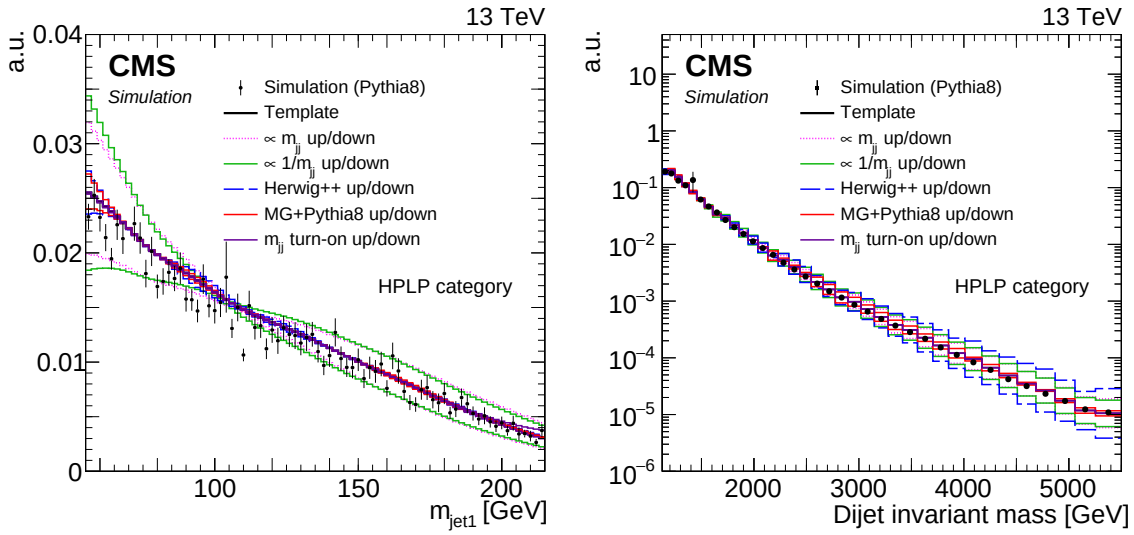

Figure 5.29.: Projections of the three-dimensional kernels (lines) on m_{jet1} (left) and m_{jj} (right) for the nominal template (black line) and the alternative shapes (colored lines) for the HPLP category. The projection on m_{jet2} is omitted since it is the same as the one shown for m_{jet1}, as a result of the random labeling of jets in the event. Both simulation and pdfs are normalized to unity. Figure published in Ref. [159].

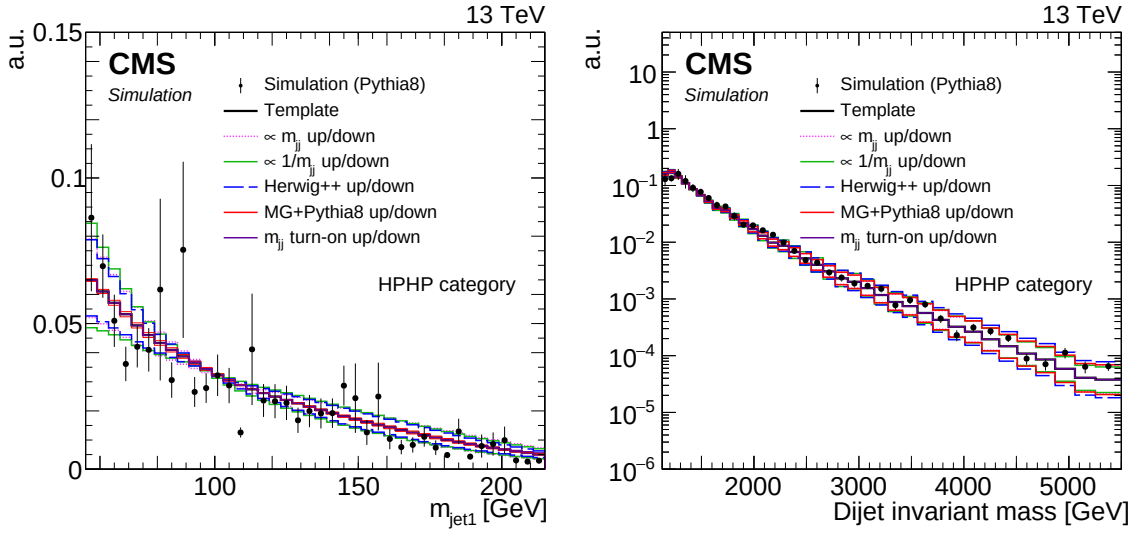

Figure 5.30.: Projections of the three-dimensional kernels (lines) on m_{jet1} and m_{jet2} (top) and m_{jj} (bottom) compared to QCD multijet events taken from simulation (markers) after the fit to the HPHP category. The projection on m_{jet2} is omitted since it is essentially the same as the one shown for m_{jet1}, as a result of the random labeling of jets in the event. Both simulation and pdfs are normalized to unity. Figure published in Ref. [159].

5.3.3. Modeling of the Subdominant Backgrounds

In addition to the main background from QCD multijet processes there are a few subdominant backgrounds to consider, mainly events from processes containing one real vector boson and at least one additional jet. These processes constitute around 28% (15%) of background events for the HPHP (HPLP) category, consisting of events from W+jets, Z+jets and $t\bar{t}$ production processes. In principle, a contribution from SM double boson production and single top quark production exists, but the contribution of such processes is negligibly small compared to the other backgrounds and is therefore neglected.

The treatment of these subdominant processes is fundamentally different compared to that of the main multijet background, since these events contain a real vector boson, which leads to a peak around the W (Z) boson mass for the two jet mass dimensions, while the dijet invariant mass has a monotonically falling distribution similar to the one from QCD multijet processes. Figure 5.31 shows the projections on all mass dimensions of the three subdominant background contributions. Since the jets in this analysis are randomly sorted, each jet mass contains two contributions: the resonant part, which denotes real V-jets and shows a clear peak around the V boson mass and the non-resonant part, which is composed of jets originating from a quark or gluon and shows a distribution similar to the one seen for QCD multijets. These two parts are modeled separately for each jet mass.

Full Background Model

The three-dimensional probability density function for the subdominant backgrounds is built as a product of one-dimensional pdfs as follows:

$$\begin{aligned} P_{\text{V+jets}}\left(m_{\text{jet1}}, m_{\text{jet2}}, m_{\text{jj}}|\bar{\theta}\right) = f \cdot \left(P_{\text{VV}}(m_{\text{jj}}|\bar{\theta}_1)\, P_{\text{res}}(m_{\text{jet1}}|\bar{\theta}_2)\, P_{\text{nonres}}(m_{\text{jet2}}|\bar{\theta}_3)\right) \\ + f \cdot \left(P_{\text{VV}}(m_{\text{jj}}|\bar{\theta}_1)\, P_{\text{res}}(m_{\text{jet2}}|\bar{\theta}_2)\, P_{\text{nonres}}(m_{\text{jet1}}|\bar{\theta}_3)\right) \ . \end{aligned} \tag{5.11}$$

The contribution for the resonant part P_{res} and non-resonant part P_{nonres} of the m_{jet} distributions is modeled separately in order to be able to correlate systematic uncertainties between real vector bosons in these backgrounds and the potential signal. The parameter f is set to $f = 0.5$, which is the mean value expected for two jets coming from V+jets events.

The contribution of the $t\bar{t}$ background is much smaller than the one originating from W+jets events, but shows the same resonant structure around the W boson mass. It will therefore be modeled together with the W+jets contribution. All in all two different pdfs are built, one for the combined W+jets and $t\bar{t}$ background processes, and one for the Z+jets background process. This treatment allows the estimation of the normalization for real W-jets and real Z-jets in data, separately. Since the number of events available from MC simulation after applying the HPHP selections is very low, the parametrization of this background is derived only for the HPLP category. The pdfs derived in the HPLP category are then applied for the modeling of both purity categories. The uncertainties for the different categories are included as separate nuisance parameters in the final fit.

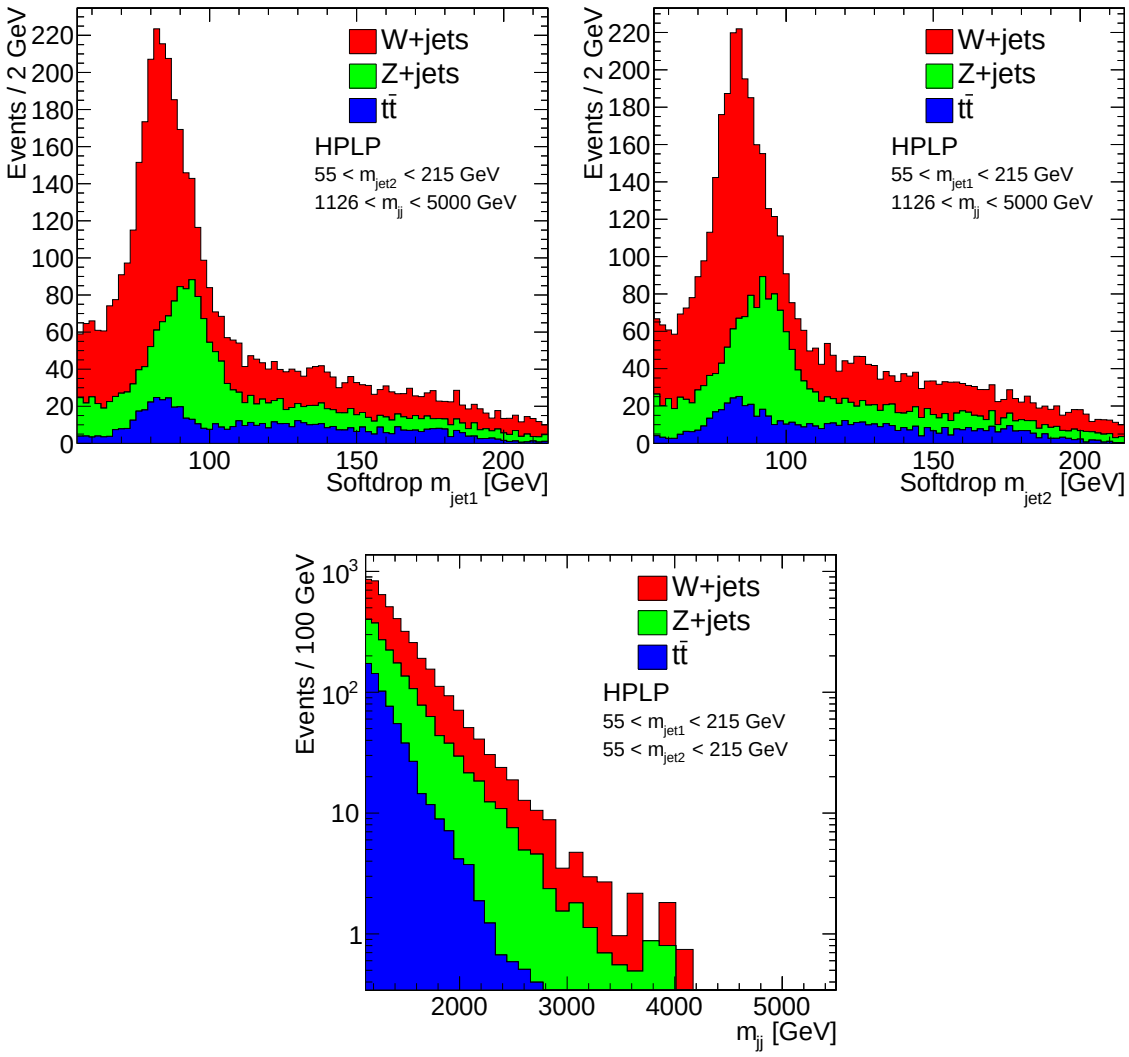

Figure 5.31.: Distributions of the subdominant backgrounds for m_{jet1} (top left) and jet mass m_{jet2} (top right), as well as the distribution of the dijet invariant mass m_{jj} (bottom) for the HPLP category.

Modeling of the m_{jj} Spectrum

For the dijet invariant mass shape, the same kernel approach as for the QCD multijet background is used. Since the MC simulation for these minor background processes contain fewer events than it is the case for the QCD multijet backgrounds, the final shapes for high masses are not smooth enough and have to be corrected with an additional smoothing procedure. This consists of fitting the tail of the m_{jj} distribution with a three parameter dijet function

$$\frac{\mathrm{d}N}{\mathrm{d}m} = \frac{P_0 \cdot (1 - m/s)^{P_1}}{(m/s)^{P_2}} \ , \tag{5.12}$$

where s is the center-of-mass energy and $P_{0/1/2}$ are free parameters. The function is fitted to the spectrum starting from a dijet mass of 1.1 (2.1) TeV for the HPHP (HPLP) category,

respectively. This procedure is applied in order to ensure a good description of the tails, where the kernel is sparse, while keeping the kernel approach for small dijet invariant masses. The number of events in the final kernel is taken from the dijet function rather than from the smoothing starting from a mass of ≈ 1.4 (3.5) TeV for the HPHP (HPLP) category. In order to avoid the appearance of discontinuities in the kernel due to the added dijet fit, the additional smoothing is added starting from a dijet bin where the difference between kernel and the fit function is smaller than 10^{-5}. The final 1D kernels are shown in Figure 5.32 compared to MC simulation. As can be seen in Figure 5.32 this procedure underestimates the event number in case of a limited number of events, as ist the case in the tail of the dijet invariant mass spectrum, by construction. The kernel procedure smears the limited number of events into a larger number of bins, thus leading to the template estimating less events in the tails as were present in the sample. This known effect is counteracted by the alternative shapes allowing for a variation in the slope of the template.

The dijet shapes derived for the V+jets background processes are similar than the ones derived for QCD multijet processes, however, they show a steeper slope to high dijet masses. Alternative dijet invariant mass shapes are derived using the same method as for the QCD multijet background and added in the final fitting procedure to accommodate mismodeling of the distribution, for example due to higher order QCD and electroweak corrections, which are not considered in the MC simulation samples.

Two corrections are applied on the V+jets backgrounds. First a NLO k-factor is applied that reweights the p_{T} spectrum of the LO MC simulation to one of NLO in QCD. This adds a substantial correction to the slope of the dijet invariant mass spectrum for both W+jets and Z+jets, since the correction are up to 40% (60%) depending on the p_{T} of the W (Z) boson. The second correction applied is a NLO electroweak correction, which is applied in bins of p_{T} of the generated vector boson, following the procedure detailed in Refs. [174–176]. The electroweak corrections are smaller than 25% for both W and Z bosons. The change in the slope of the dijet invariant mass distribution due to the application of the NLO k-factor and EWK corrections can be seen in Figure 5.33 for W+jets and Z+jets. To ensure a large number of events for this comparison, no τ_{21}^{DDT} selection has been applied in this Figure.

Modeling of the m_{jet} spectrum

The m_{jet} spectrum is split into two parts for the modeling, the resonant and non-resonant part of the spectrum. The resonant events are separated from the non-resonant ones by requiring that there is a generated V boson in a cone of $\Delta R = 0.8$ around the reconstructed merged jet. A dCB function, which is also used for the modeling of the signal m_{jet} shapes, is then fitted to the resonant spectrum for W+jets and Z+jets separately. This treatment allows to fully correlate the uncertainties on the mean and width of the m_{jet} distribution with the signal, since these uncertainties affect all jets originating from real vector bosons in the same way.

In Figure 5.34 the final fit of the dCB function to the resonant part of the V+jets spectrum is shown. The resonant W+jets jet mass spectrum clearly shows a small peak of merged top quarks at a mass of about 175 GeV. This small contribution is negligible for the current analysis, and therefore not modeled separately. The ratio of W+jets to $\mathrm{t\bar{t}}$ background is fixed

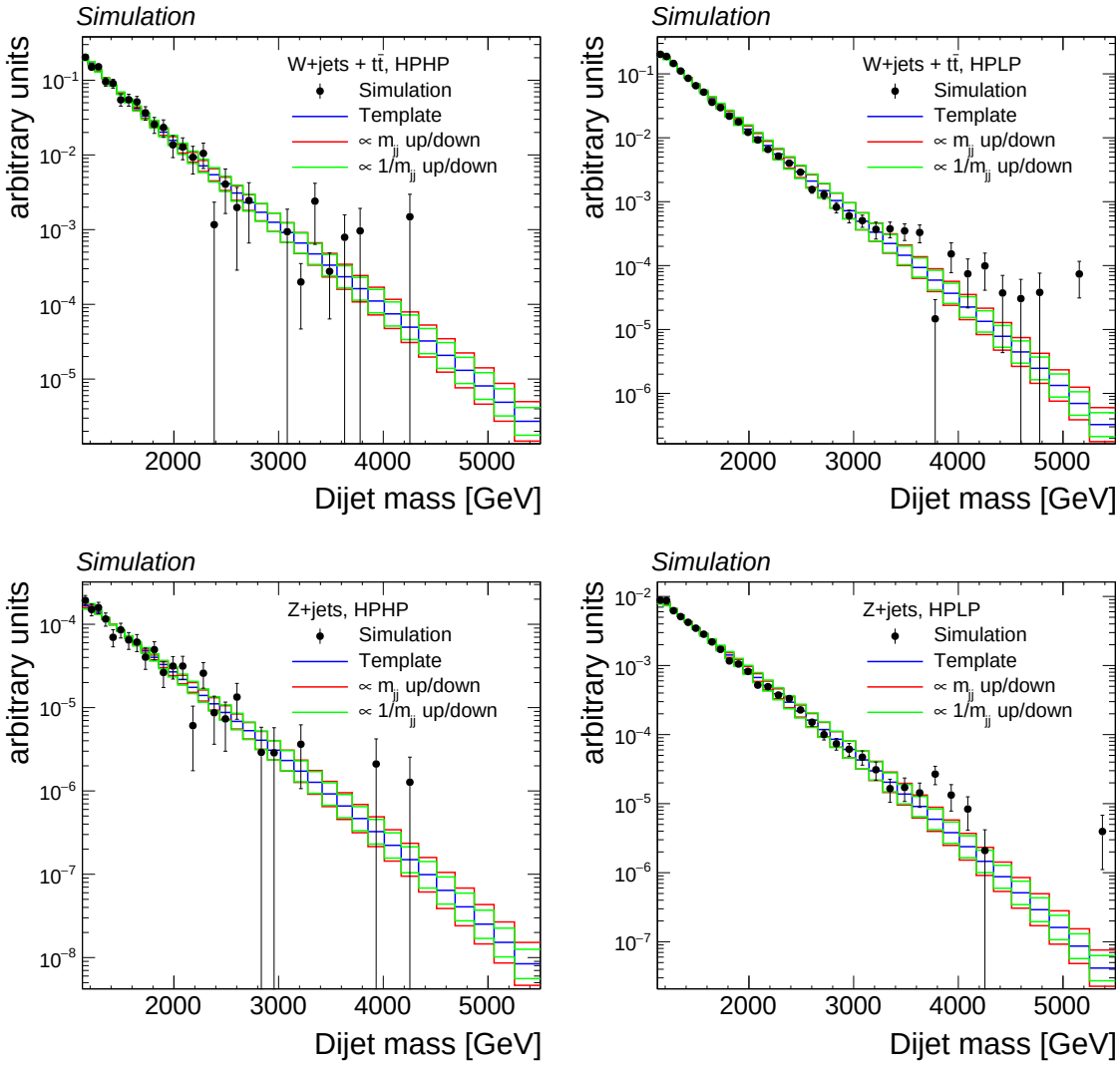

Figure 5.32.: Final one-dimensional kernels for the non-resonant background compared to MC simulation for the HPHP (left) and HPLP category (right). The nominal shape derived from the smoothing procedure can be seen as a blue line, alternative shapes derived from varying the slope of the m_{jj} spectrum are shown in green and red. The m_{jj} kernels for W+jets are shown on top, while the ones for Z+jets are on the bottom. The green and red lines show alternative shapes derived by varying the m_{jj} spectrum proportional to m_{jj} or to $1/m_{jj}$.

to its predicted value from MC simulation, while the overall contribution of W+jets plus $t\bar{t}$ has a normalization uncertainty of 20% in the final fit. The W and Z peak are both modeled with dCB functions that differ mostly in their mean of around 80 and 91 GeV as well as their resolution, which is around 7 and 8-9 GeV, respectively.

Figure 5.35 shows a comparison between the final jet mass shapes extracted from the modeling for the V+jets background processes and the signal processes. The shapes are similar, i.e., 3-7% difference in the mean and width of the dCB functions. These residual differences originate in misreconstruction effects, that are not considered in the fit for the background

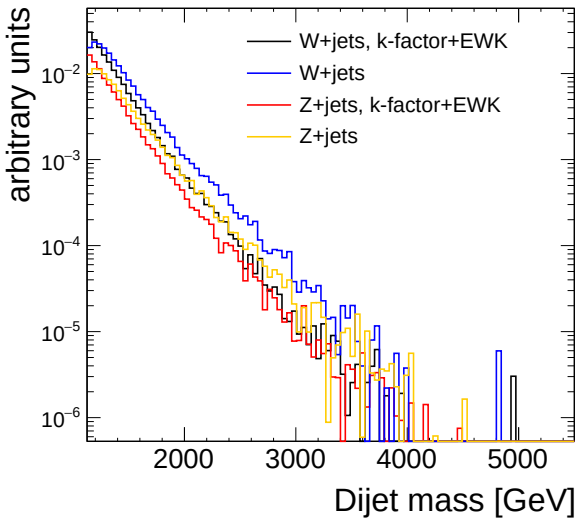

Figure 5.33.: Comparison of the dijet invariant mass spectrum with a NLO k-factor and EWK correction applied to the spectrum without corrections. The comparison is shown for W+jets and Z+jets background processes. To ensure a sufficient number of events, no τ_{21}^{DDT} selections have been applied.

processes, since here the jet used for reconstruction has to be within a cone of R=0.8 of the generated V boson. A second effect contributing to the larger width of the jet mass shape for signal processes is the higher transverse momentum expected for signal events, which leads to a decrease in resolution.

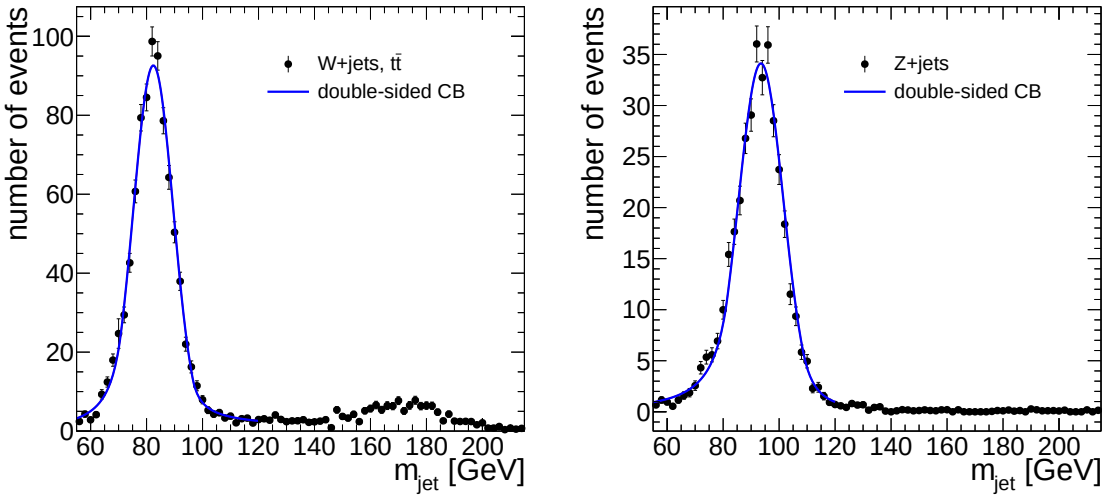

Figure 5.34.: The final fits of a dCB function (blue line) to the resonant part of the V+jets spectrum (black markers) for W+jets and $\mathrm{t\bar{t}}$ (left) and Z+jets (right) processes. Only one of the two jet masses m_{jet1} is shown since the projection on m_{jet2} is equivalent except for statistical fluctuations.

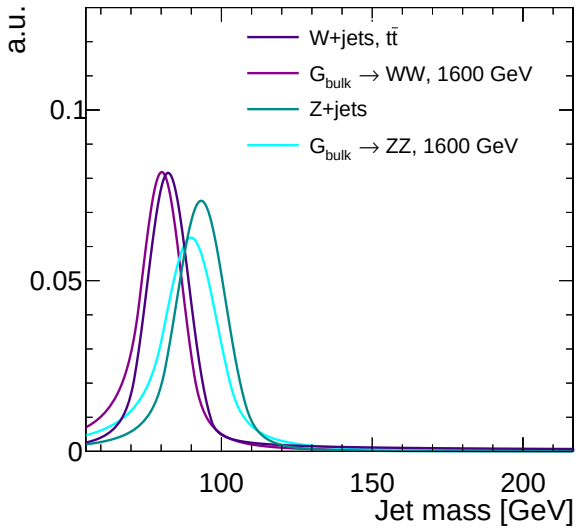

Figure 5.35.: Comparison between the fitted shapes of the jet mass, here the mass of jet-1 is shown as an example. The shapes for W+jets background processes are shown (purple line) compared to the shapes for a $G_{bulk} \rightarrow WW$ signal (magenta line) with a resonance mass of 1600 GeV. Additionally the shape for the Z+jets background process (dark blue line) is compared to the shape extracted from a $G_{bulk} \rightarrow ZZ$ signal with a resonance mass of 1600 GeV (light blue line).

The modeling of the non-resonant part is less critical since this part of the spectrum is very similar to the shapes observed in QCD and can therefore be in parts absorbed into the extensive modeling of the QCD non-resonant backgrounds. For the sake of a better fit stability, the non-resonant part of the V+jets backgrounds is modeled nonetheless using a simple fit with a Gaussian to the non-resonant part of the spectrum as shown in Figure 5.36. Note here, that the non-resonant jet mass spectrum shown on the left contains $t\bar{t}$ as well asW+jets processes leading to the difference in shape when compared to the spectrum for Z+jets processes.

Correlations between m_{jet1}, m_{jet2} and m_{jj} and Closure Tests

Two tests were conducted to shows that correlations between m_{jet} and the dijet invariant mass are small enough to be neglected in the modeling of these backgrounds, i.e., the shape of the jet mass spectrum does not significantly depend on the momentum of the jets. Firstly the resonant and non-resonant part of the m_{jet} spectra were fitted in four intervals of m_{jj} ($m_{\text{jj}} \in [[1126, 1400], [1400, 1600], [1600, 2000], [2000, 5500]]$) showing that the change of the parameters of the fit function is within the uncertainties of the fit to the whole jet mass spectrum. Secondly χ^2 tests were performed using the full model derived for these subdominant backgrounds and fitting this to the MC simulation of W+jets, Z+jets and $t\bar{t}$ in both HPHP and HPLP categories. The results of this fit can be seen in Figure 5.37 as well as Appendix D for different slices of m_{jet} and m_{jj} projected onto all three jet dimensions. Figure 5.37 shows a good agreement between the background model and the MC simulation for

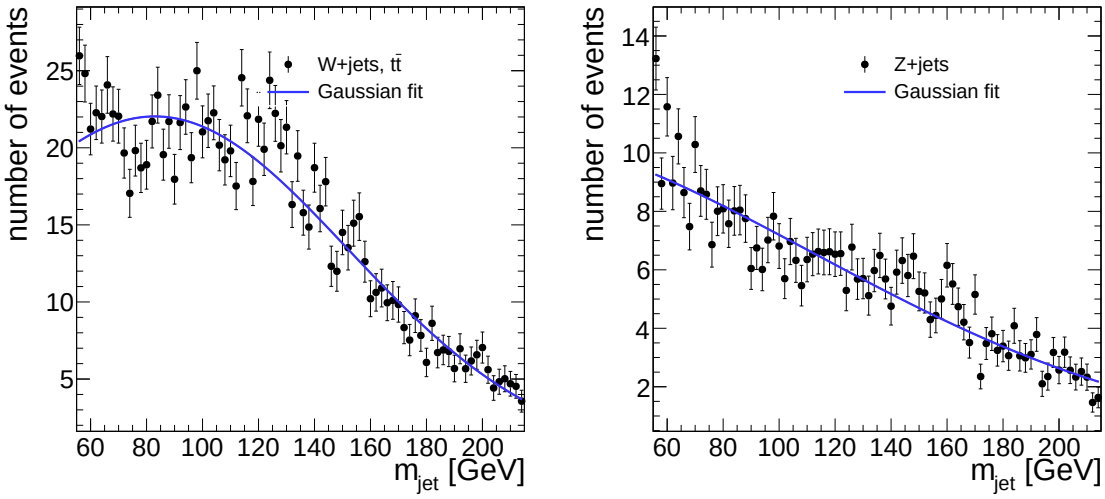

Figure 5.36.: The final fits for a Gaussian function (blue line) to the non-resonant part of the V+jets spectrum (markers) for W+jets and $t\bar{t}$ (left) and Z+jets (right) processes. Only one of the two jet masses m_{jet1} is shown since the projection on m_{jet2} is equivalent except for statistical fluctuations.

minor backgrounds in the HPLP (HPHP) category. The χ^2, and p-values were calculated for the full projection shown in Figure 5.37 as well as the conditional projections shown in Appendix D. The results show a good agreement between the model and the MC simulation for the important phase-space region between $65 < m_{\text{jet1}}(m_{\text{jet2}}) < 105\,\text{GeV}$ as well as a reasonable agreement for the remaining tested projections, for further details see Appendix D. Note here, that there is some discrepancy between the model and the MC simulation for jet masses between 140 to 190 GeV, due to the small resonance of merged top quarks. Due to the top quark contribution being small compared to the remaining background processes, this peak was not included in the modeling. For future analyses planning to include signal processes decaying to VH or HH this background will play a larger role and will be modeled as a separate background contribution. This will be neccesary as soon as b-tag categories are added to the analysis, which enhances the fraction of selected $t\bar{t}$ events. The tests conclude that correlations between m_{jet} and the dijet invariant mass can be neglected for the modeling of V+jets background processes. There is, however, a correlation between the two jet masses. This correlation stems from the fact that for the V+jets backgrounds one of the two jets in the final state originates from a real boson, while the second is a quark jet. Both of these jets have different distributions which means that depending on the fraction of real boson jets in m_{jet1} the fraction of such jets in m_{jet2} will change. Consequently these backgrounds are modeled as if there were two different contributions: one where the first jet is resonant and the second non-resonant, and one where the second jet is resonant and the first non-resonant. Both of these contributions are in the end added with a fraction of 0.5 because of the random labeling of jets, see equation 5.11.

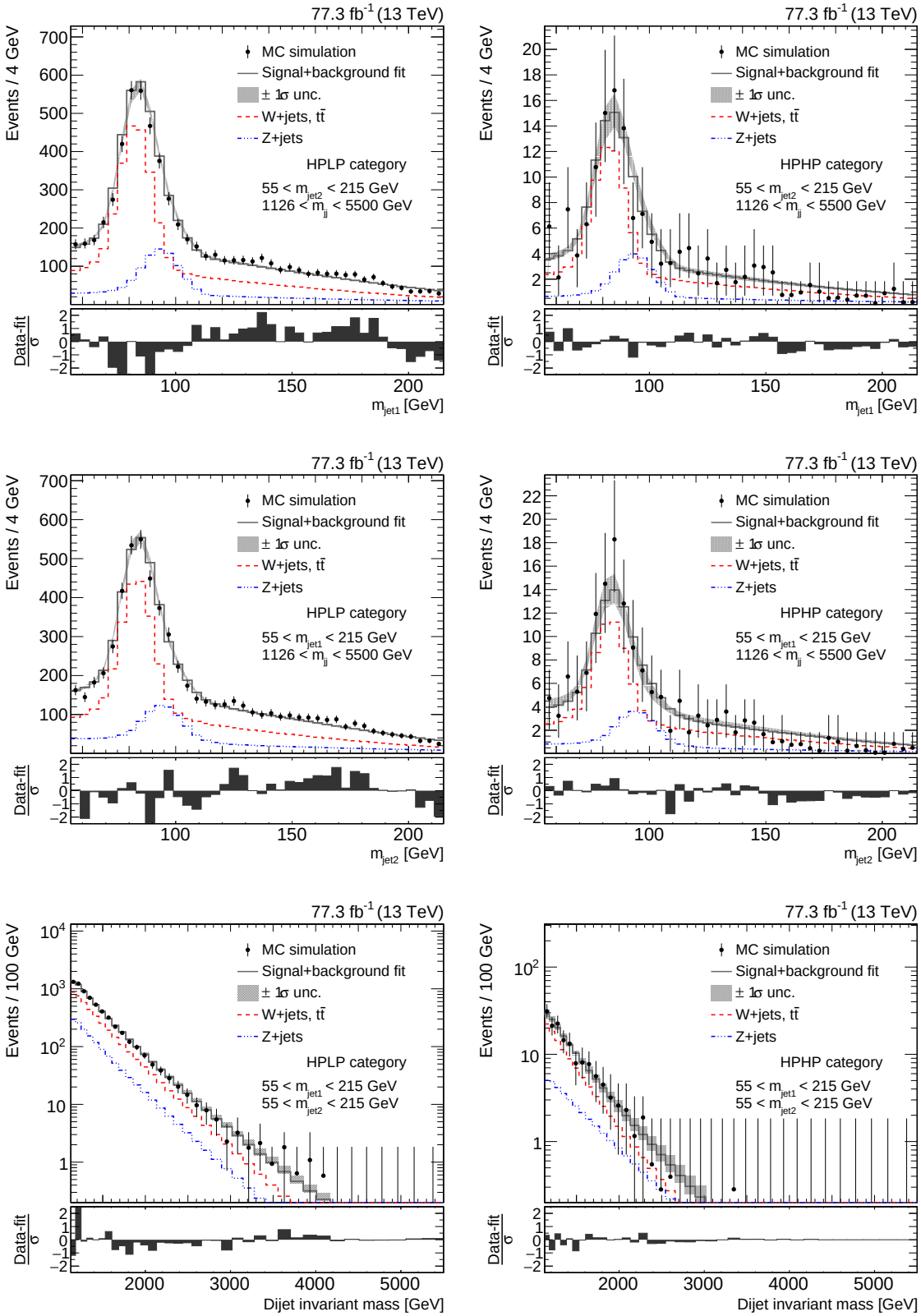

Figure 5.37.: The results of a fit of the complete background model (gray line) to the MC simulation of the V+jets background processes (black markers) as projections on m_{jet1} (top), m_{jet2} (middle) and m_{jj} (bottom) for the HPLP (left) and HPHP (right) category, respectively. For this Figure a binning of 4 GeV has been used for the jet mass, to ensure a better legibility.

5.4. Systematic Uncertainties

The distributions and yields of both background and signal models are subject to a number of systematic uncertainties, which in turn influence the shapes and yields of the model. In this Section, the systematic uncertainties considered in this analysis are discussed in detail. Due to the nature of the data-driven method employed to adapt the background model to data, some uncertainties have to be applied only to the signal model. Each systematic uncertainty is included in the final model as a nuisance parameter. The nuisance parameters for each uncertainty source are profiled in the statistical interpretation using log-normal constraints for normalization uncertainties and Gaussian constraints for shape uncertainties. A summary of all systematic uncertainties is provided in Table 5.3, while a detailed discussion of the individual uncertainties follows later in the section.

Table 5.3.: Summary of the systematic uncertainties and the quantities they affect. The numbers in parenthesis correspond to uncertainties for the 2017 analysis when these differ from those in 2016. Table published in Ref. [159].

Source	Relevant quantity	HPHP (%)	HPLP (%)
Integrated luminosity	Signal + V+jets yield	2.6 (2.3)	
W-tagging efficiency	Signal + V+jets yield	21 (25)	11 (13)
W-tagging p_{T}-dependence	Signal + V+jets yield	5-30	5-20
PDFs and $\mu_{\mathrm{F/R}}$	Signal yield	3	
QCD normalization	Background yield	50	
V+jets normalization	Background yield	10	
V+jets ratio	Migration	10	
PDFs	Signal $m_{\mathrm{jj}}/m_{\mathrm{jet}}$ shape	< 1	
Jet energy scale	Signal m_{jj} shape	2	
Jet energy resolution	Signal m_{jj} shape	5	
Jet mass scale	Signal + V+jets m_{jet} shape	1	
Jet mass resolution	Signal + V+jets m_{jet} shape	8	
QCD Herwig++	QCD shape	33	
QCD Madgraph+Pythia	QCD shape	33	
p_{T}-variations	QCD shape	33	
Scale-variations	QCD shape	33	
High-m_{jet} turn-on	QCD shape	33	
p_{T}-variations	V+jets m_{jj} shape	10	

5.4.1. Normalization Uncertainties

Signal Normalization Uncertainties

Since the contributions for the QCD multijet background are data driven, major systematic uncertainties affect only the signal and the subdominant background processes from V+jets events. Here, all systematic uncertainties affecting the signal yield are listed, however, the W-tagging efficiency uncertainty as well as the luminosity uncertainty, discussed in this Section, are applied to the V+jets background processes as well, assuming a full correlation.

- **luminosity uncertainty:** The integrated luminosity of recorded data is measured by the CMS Collaboration with an uncertainty of 2.6% and 2.3% for the 2016 and 2017 data sets, respectively.

- **W-tagging efficiency uncertainty:** The uncertainty of the scale factor correcting the efficiency of the τ_{21}^{DDT} selection in simulation to that measured in a data control region is anticorrelated between the HPHP and HPLP categories and affects both jets in the event. Overall an uncerainty of 21% (25%) is applied for 2016 (2017) data in the HPHP category, and of 11% (13%) is applied for 2016 (2017) data in the HPLP category.

- **W-tagging p_{T}-dependence uncertainty:** An additional uncertainty arises from the extrapolation of the W-tagging efficiency scale factors, which are estimated in $\mathrm{t\bar{t}}$ events, towards higher transverse momenta. This uncertainty is treated as correlated between the τ_{21}^{DDT} categories and is estimated to be between 5-30% and 5-20% for the HPLP and HPHP selections, respectively.

- **PDF and factorization (μ_{F}) and renormalization (μ_{R}) scale uncertainty:** The influence of uncertainties in the PDFs and of the choice of factorization and renormalization scales on the expected signal cross section and acceptance is evaluated by considering differences in the predicted kinematics of the resonance. Acceptance effects are added as nuisance parameters to the analysis, while effects on the predicted signal cross section are not taken into account, since the signal yield is extracted from the fit to data. Nonetheless, these uncertainties are evaluated and added as an uncertainty in the expected cross section from theory prediction that is utilized to interpret the results. Since the signal MC simulation samples are generated at LO in QCD, the NNPDF 3.1 LO set of PDFs is used to estimate PDF uncertainties. Following Refs. [177, 178], the uncertainties in the signal prediction due to missing higher order calculations are evaluated by varying the default choice of scales in the following six combinations of factors: $(\mu_{\mathrm{F}}, \mu_{\mathrm{R}})\times$(0.5,0.5) , (0.5,1), (1,0.5), (2,2), (2,1), and (1,2). The resulting cross section uncertainties vary from 4 to 72% and from 2 to 23%, respectively, depending on the resonance mass, particle type, and its production mechanism. These large uncertainties are highly model-dependent and therefore not considered in the statistical analysis. The uncertainty in the signal acceptance from the choice of PDFs, and of factorization and renormalization scales, ranges from 0.1 to 3% and < 0.1%, respectively. An overall uncertainty in the signal yield of 3% is therefore applied to cover this uncertainty source.

Background Normalization Uncertainties

In the final fit the background normalization is allowed to float around 50% of its predicted SM value for the QCD multijet background and around 20% of the SM prediction for the smaller V+jets background processes. This normalization is then constrained through the final fit to data. Normalization uncertainties, such as the W-tagging efficiency and luminosity uncertainties, are applied to the V+jets backgrounds and are considered to be fully correlated with the corresponding uncertainty in the singal processes. The normalization uncertainties are uncorrelated between purity categories and backgrounds, since different τ_{21}^{DDT} selections might lead to differences in the tagging efficiencies. The uncertainties affecting the background

normalization are also correlated between the years.

5.4.2. Shape Uncertainties

The shape uncertainties discussed in the following either affect the shape of the signal or background processes. For the background processes artificially large uncertainties are presumed and constrained through the multi-dimensional fitting procedure. The shape uncertainties for the background model are correlated between the years. It was tested that this choice does not significantly impact the gof or result of the fit or sensitivity of the search, however, it allows a significant speedup of the fit. Shape uncertainties for the signal processes are correlated between 2016 and 2017, with the exception of the uncertainties derived in the W-tagging scale factor measurement, such as the W-tagging efficiency and the jet mass scale and resolution uncertainties.

Shape Uncertainties for the Signal

Systematic uncertainties affecting the signal shapes are the jet energy scale and resolution, as well as jet mass scale and resolution uncertainties. They either impact the mean or standard deviation of the dCB functions parametrizing the dijet invariant mass and jet mass spectra. The uncertainties are assumed to affect both of the two jet masses in the same way. The jet energy scale and resolution uncertainties do not affect the PUPPI soft drop mass of the individual jets, since the soft drop algorithm is applied to uncorrected jet, with separate correction derived for this quantity, as explained in Section 4.2.7. Conversely, the uncertainties in the jet mass, that are derived as described in Section 5.1.3, do not affect the dijet invariant mass shape. Scale factors for the jet mass scale (resolution) are extracted from data and applied to the signal shapes before the fit in order to start from distributions corrected to data.

The dijet invariant mass scale and resolution uncertainties are derived by reweighting the transverse momentum of the jets in the event according to the centrally measured jet energy scale (resolution) uncertainties. The change in the dijet invariant mass spectrum due to these systematic uncertainty sources are then estimated by extracting the mean and standard deviation of the dijet invariant mass spectrum from a Gaussian fitted to the reweighted spectrum. This procedure is iterated over all available signal samples and mass points and the uncertainty is calculated as the standard deviation of the results of the reweighting. This approach is possible since the resulting uncerainties due to the jet energy scale and resolution are not dependent on the type of signal. The signal shapes used in the final limit setting are corrected to resemble the actual jet energy (resolution) measured in data. This leads to a broadening of the dijet invariant mass peak of around 5% as opposed to the width derived from simulation.

The impacts of PDF uncertainties on the dijet invariant mass and jet masses are tested in the same way, only this time the events are reweighted according to different PDF uncertainties of the NNPDF3.1 LO pdfset using the *lhapdf* package [179]. The shape variations due to

PDF uncertainties are evaluated to be neglibigly small compared to jet energy scale and resolution uncertainties and therefore no additional shape uncertainties are applied.

Shape Uncertainties for the Minor Backgrounds

The resonant part of the m_{jet} spectra are affected by the same uncertainties as the signal, namely jet mass scale and resolution uncertainties. These are assumed to be fully correlated between signal and the V+jets backgrounds since they affect all real V bosons in the same way. This treatment allows a constraining of these uncertainties due to the fit to the W (Z) boson peak in the jet mass spectrum.

To include uncertainties in the modeling of the dijet invariant mass spectrum, four alternative templates are incorporated in the fit, corresponding to an up (down) variations of the p_{T} spectrum proportional to m_{jj} ($1/m_{\text{jj}}$). Each set of alternative shapes is attached to a nuisance parameter with a Gaussian constraint, allowing the fit to adapt to the spectrum in data.

Shape Uncertainties for the QCD Multijet Modeling

Uncertainties in the QCD multijet background shape are included in the fit using alternative pdfs derived with the template-building method described earlier. Five nuisance parameters that vary the shape are defined, each of the parameters corresponding to an upward and a downward variation of alternative shapes that simultaneously affect all three dimensions.

The first nuisance parameter accounts for a variation of the underlying p_{T} spectrum, and the two corresponding mirrored templates are obtained by applying up and down variations of the expected yields to each bin along the two jet masses and m_{jj} by a quantity proportional to m_{jet} and m_{jj}.

The second nuisance parameter is a variation of the mass scale, and is taken into account through two mirrored alternative shapes obtained by applying up and down variations of each bin content along the two jet masses and m_{jj} by a quantity proportional to $1/m_{\text{jet}}$ and $1/m_{\text{jj}}$.

Two additional alternative shapes that simultaneously affect the resonance mass and the groomed jet mass are also added in order to take into account differences in MC generation and modeling of the parton shower. These alternative templates are derived using the HERWIG++ and MADGRAPH5_AMC@NLO QCD multijet simulation.

This method allows the inclusion of all known background variations into the fit. The final selection of templates included in the fit is based on goodness-of-fit tests using different combinations of alternative shapes in pseudodata, derived using the four available MC samples, as well as the LPLP data control-region, see Section 5.5. The chosen alternative shapes allow the fit to adapt to different variations of the background distributions while at the same time keeping the number of alternative shapes as low as possible, in order to keep the fitting procedure stable.

For events with a large jet mass ($m_{\text{jet}} > 175\,\text{GeV}$) and small dijet invariant mass ($m_{\text{jj}} < 1200\,\text{GeV}$), an expected turn-on due to the trigger thresholds exists. Therefore, an additional shape uncertainty parameterizing any discrepancy between the 3D template and the QCD multijet simulation is added to the fit. Note that this shape uncertainty only affects this particular region, which is far from where a signal is expected. The nuisance parameters associated with these alternative shapes are constrained using Gaussian pdfs in the fit, with the pre-fit values chosen in order to cover any differences between data and simulation observed in the control regions.

5.5. Closure and Bias Tests

To test the validity of the background and signal extraction method a number of closure and bias tests are performed. These tests are discussed in this chapter, starting with a test of the model in the LPLP data control region, discussed in section 5.5.1, a fit test of different variations of the QCD multijet prediction in the Section 5.5.2, and a signal injection test, which is discussed in Section 5.5.3.

5.5.1. Tests in a Data Control Region

The fit procedure is tested in a data control region where both jets are required to satisfy $0.43 < \tau_{21}^{\mathrm{DDT}} \leq 0.79$. With these selections the contribution of the resonant backgrounds is less than 0.5% and thus expected to be negligible with respect to the main QCD multijet background and their contribution is therefore removed from the fit. As for the HPLP analysis selections, the QCD background templates for this control region are built using the procedure described in Subsection 5.3.1. The post-fit distributions of data in this control region are shown in Figure 5.38 and conditional projections of the fit result are shown in Appendix C. Additionally, a gof test is performed by generating toy data sets using different predictions around the post-fit background-only model and comparing the likelihood distribution of these toys to the likelihood in data using a saturated model [72]. The result of the test is shown in Figure 5.39 for the nominal background model, i.e., including all alternative shapes discussed in Section 5.4. The p-value reported on the figure quantifies the agreement of the observed value with the toy distribution, where a p-value smaller than a preset value of 0.05 is considered the threshold for rejecting the background-only hypothesis. The obtained test statistics are Gaussian-distributed and the data is in good agreement with the background-only hypothesis. This control-region is also used to quantify which alternative shapes are needed to describe the data. For this test the alternative shapes are added to the fit one-by-one, checking the improvement in the goodness-of-fit. The p-values obtained with the nominal model are compared with the values for some alternative models in Table 5.4. As a conclusion all shapes included in the nominal model are utilized in the fit.

Table 5.4.: The observed p-values obtained from gof tests using a saturated model with different combinations of kernel shapes modeling the background components. The observed p-value is calculated for data in the LPLP control-region.

model	HERWIG++ shape	MADGRAPH shape	$\propto (1/m_{\mathrm{jj}}, 1/m_{\mathrm{jet}})$ shape	$\propto (m_{\mathrm{jj}}, m_{\mathrm{jet}})$ shape	p-value
nominal	yes	yes	yes	yes	0.30
model 1	yes	yes	yes	no	0.28
model 2	yes	yes	no	yes	0.27
model 3	yes	yes	no	no	0.26
model 4	no	yes	yes	yes	0.16
model 5	yes	no	yes	yes	0.13
model 6	no	no	yes	yes	0.09
model 7	no	no	no	yes	0.03

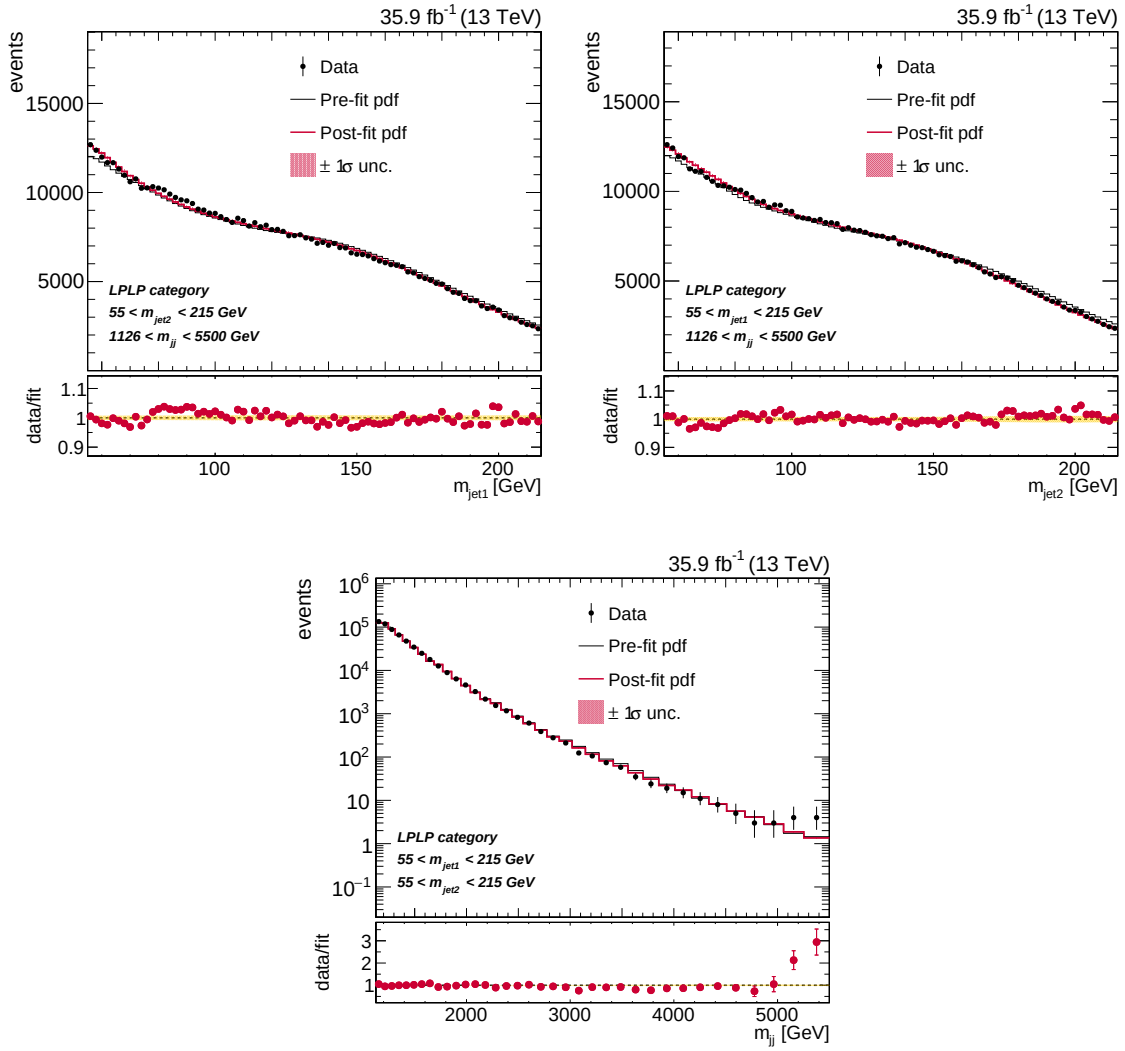

Figure 5.38.: Distributions obtained from a fit to 2016 data in a low purity control region. Projections are shown of m_{jet1} (top), m_{jet2} (middle) and m_{jj} (bottom).

5.5.2. Variations of the QCD Multijet Prediction

The alternative shapes described in section 5.4 are chosen such that the fit is able to adapt to all known variations in the QCD multijet prediction. Namely, to describe different parton showers, NLO predictions, as well as the data in a control-region. The number and form of alternative shapes included in the fitting procedure has been determined in the LPLP data control-region based on the resulting change in the p-value of the fit when including or excluding the alternative shape.

To test the validity of the fitting method employed in the analysis, i.e., the adaptivity of the final fitting procedure, background predictions from different MC generators PYTHIA8, HERWIG++, MADGRAPH5_AMC@NLO and POWHEG are fitted with the final background model to confirm that the procedure is able to capture differences in MC simulation

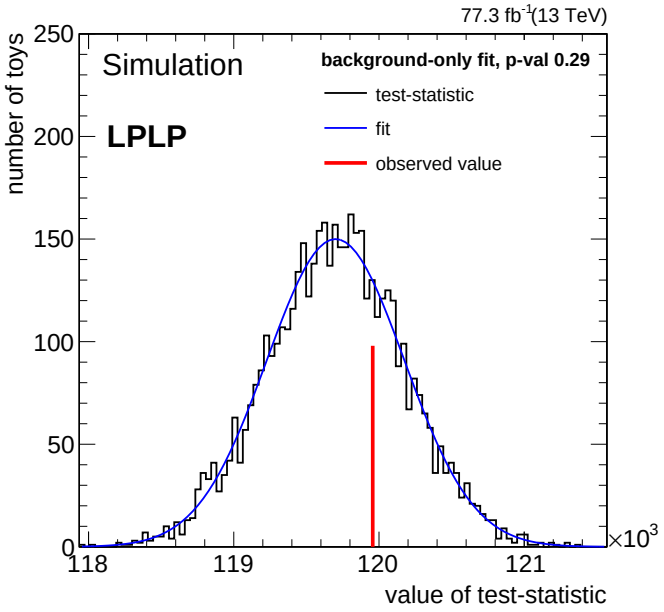

Figure 5.39.: Distribution of the likelihood for toys generated around the background-only fit in the LPLP control-region compared to the likelihood on data. The data is in good agreement with the background-only hypothesis.

from various generators and the modeling of parton showers. The toy data set is generated following the distributions of three different QCD multijet MC simulation samples: PYTHIA8 (nominal), HERWIG++, MADGRAPH5_AMC@NLO and POWHEG. Each toy data set is the sum of the data sets generated separately from the 2016 and 2017 background templates. In case of a sample being only available for one of the two years, which is the case for the POWHEG simulation, the available sample is used to generate the distributions for both years. In addition the predicted number of events for the V+jets background processes is generated following the model for the V+jets backgrounds. The post-fit distributions resulting from the combined fit of one toy data set generated in this way are shown in appendix D, separately, for the HPHP and HPLP category.

Additionally, a gof test is performed by generating toy data sets using different predictions around the post-fit background-only model and comparing the likelihood distribution of these toys to the likelihood in pseudo-data using a saturated model. The pseudo-data is generated from each of the different simulation samples. In this context the toy data sets are generated by random sampling following a given pdf distribution as derived using various simulated samples of QCD multijet processes. The results are shown in Figure 5.40. The gof tests are based on 1000 toys, utilizing the full model and combining both purity categories and years. All different QCD multijet predictions tested show good compatibility with the background-only hypothesis (p-values $> 5\%$), thus confirming that the fit is able to sufficiently adapt to different background distributions.

To illustrate how the multidimensional fit adapts to different QCD multijet distributions, toy data sets sampled following the distributions from different MC generators, the V+jets

background model, as well as signal events injected following the distribution from the signal modeling and corresponding to a significance of approximatly two standard deviations, are fitted using the multidimensional fit procedure. Approximatly 900 toy data sets are generated for each different background shape for the QCD multijet background with a $G_{bulk} \rightarrow WW$ model as injected signal. The pull distribution for each nuisance parameter, defined as $(\theta - \theta_{in})/\sigma_{\theta,in}$, with the post-fit value of the fitted parameter θ and its pre-fit value θ_{in} as well as its pre-fit uncertainty $\sigma_{\theta,in}$, is examined for different toy data sets. The values represent the shift of the nuisance parameter θ with respect to its pre-fit value relative to its pre-fit uncertainty, as well as the extent to which the nuisance parameter is constrained by the fit to pseudo-data. The pulls are extracted as the mean of the distribution $(\theta - \theta_{in})/\sigma_{\theta,in}$ for all toys, while the uncertainty on the parameters corresponds to the standard deviation of the pull distribution in toys. The results of this test for all nuisance parameters affecting the background shape for QCD multijet processes is shown in Figure 5.41. Note that the pre-fit value for each toy example was set to the nominal expectation following the PYTHIA8 simulation. This results in the pulls for the toy data sets following the distributions from other MC generators to be large. However, in doing so it is possible to demonstrate how the multidimensional fit to data pulls the provided shape parameters to adjust the background shape to the observed distribution. The fits to HERWIG++ and MADGRAPH5_AMC@NLO pseudo-data show that the fit favors a shape closer to the distribution from the HERWIG++ or MADGRAPH5_AMC@NLO generator, represented by the alternative shapes derived using HERWIG++ and MADGRAPH5_AMC@NLO MC simulation, while the other background shapes are only marginally pulled from their pre-fit values. A positive pull of the nuisance parameter for the HERWIG++ alternative shape of three means that the true shape of the pseudo-data is closer to the shape found in the HERWIG++ MC simulation, so much so, that the corresponding nuisance parameter gets pulled to three times of the pre-fit uncertainty on this shape. For the fit to toy data generated under the nominal (PYTHIA8) hypothesis, all nuisance parameters are centered around their pre-fit values, showing that the pre-fit assumption already describes the observed shape. The pulls for pseudo-data generated around the prediction from the POWHEG MC simulation show that a mixture of the alternative shapes is necessary to adapt to the observed distribution. In addition to the alternative shapes corresponding to the MADGRAPH5_AMC@NLO and HERWIG++ generators, the alternative shape derived by a variation of the spectrum proportional to the mass is pulled to positive values, indicating that the distribution generated with powheg has a steeper slope in the jet mass spectrum than the distribution generated with pythia.

Figure 5.42 show the pulls for all nuisance parameters affecting the shape of the V+jets production. With the exception of the pseudo-data generated following the distribution from POWHEG MC simulation, these shape nuisance parameters are only marginally different from their pre-fit values. In the case of a QCD multijet background shape following the distribution generated with POWHEG, slightly larger pulls are observed. The most likely reason for this behavior is the relatively small number of events available for this MC sample, leading to an overall less smooth distribution used for the generation of toy data. This might lead to the V+jets background processes being partly concealed by an unphysical dip in the QCD multijet distribution, which in turn affects the fit of its shape parameters as well as the fit of its normalization.

In Figure 5.43 the pulls are shown for all parameters affecting the signal shape. It is important to note here, that although the background-only fit is able to constrain the jet mass scale

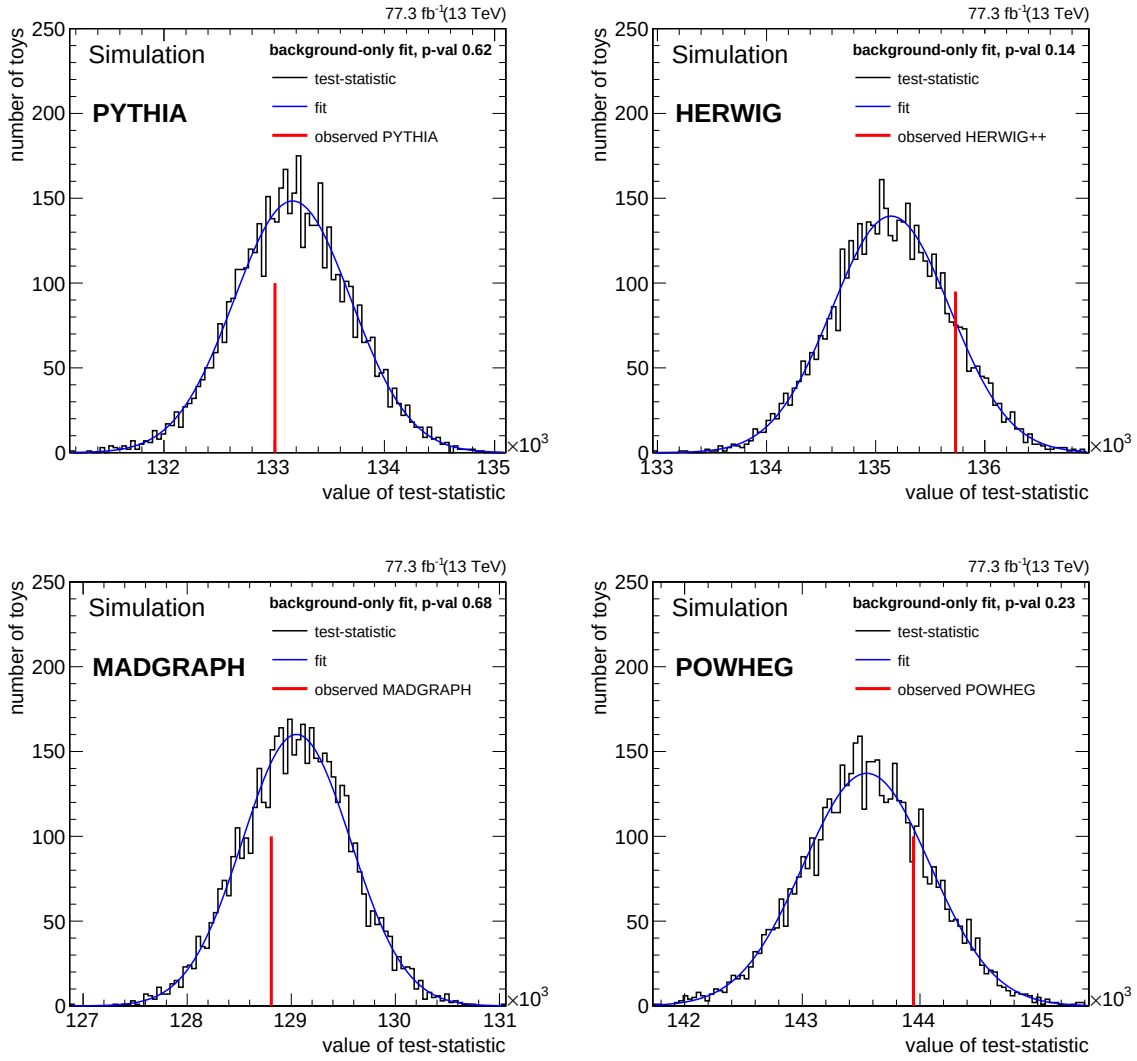

Figure 5.40.: Distribution of the likelihood for toys generated around the background-only hypothesis compared to the background-only fit to a toy following MC simulation of the nominal PYTHIA8 sample (top left), HERWIG++ (top right), MADGRAPH5_AMC@NLO (bottom left) and POWHEG (bottom right).

and jet mass resolution nuisance parameters utilizing the V+jets background processes, the constraints seen here for other nuisance parameters are only possible since a signal has been injected in the toy data sets. Figure 5.43 shows that the nuisance parameter constraint for the dijet mass resolution increases with the mass of the injected signal. The reason for this behavior is the increase in signal width as well as the decreasing number of background events for higher resonance masses. Due to the decreasing HCAL resolution for high dijet masses, the dijet mass scale cannot be constrained further.

Figure 5.44 and 5.45 show the nuisance parameters affecting the normalization of background and signal processes. They show very small deviations from their pre-fit values, and are highly constrained. The fit procedure is able to determine the number of expected events from each

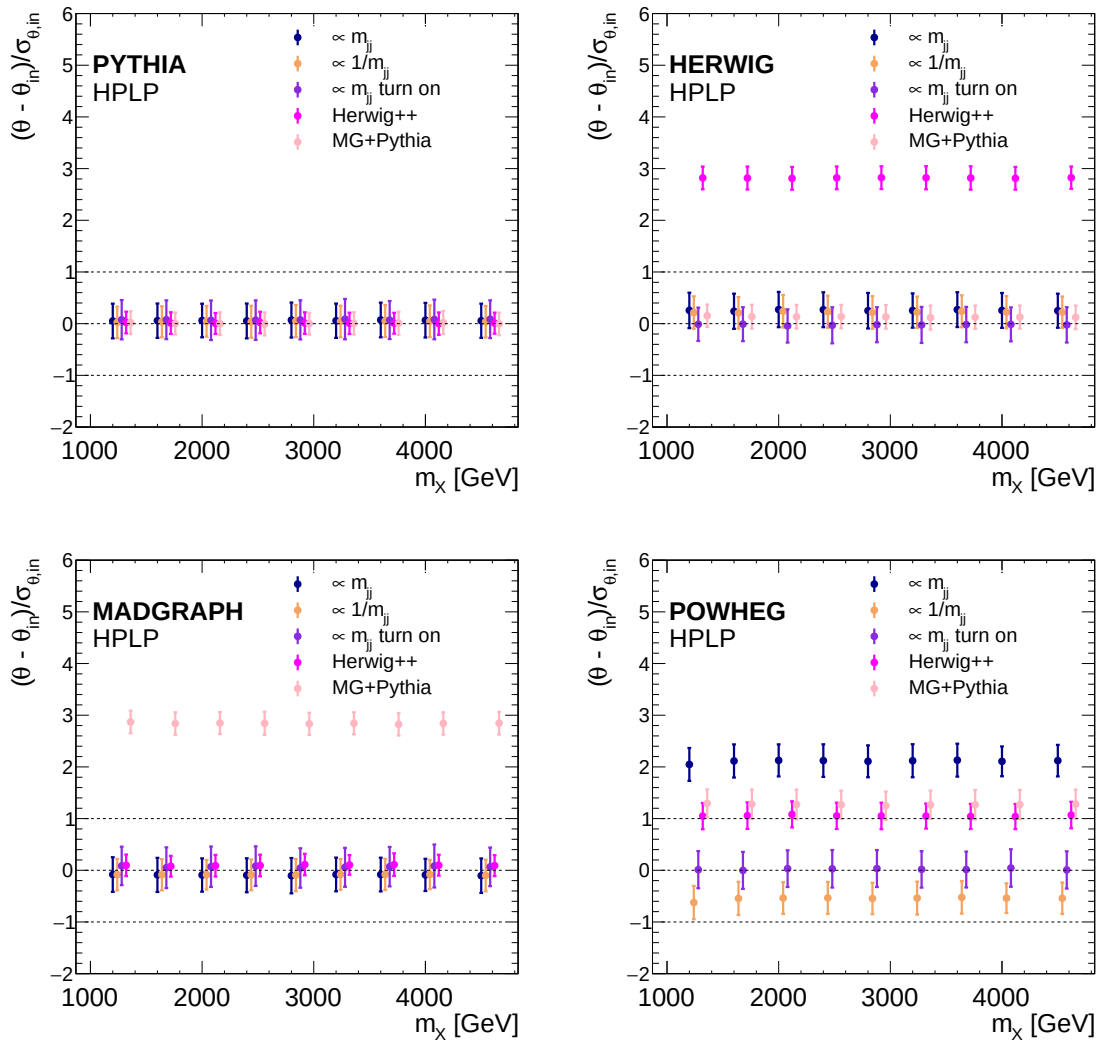

Figure 5.41.: The pull $(\theta - \theta_{\text{in}})/\sigma_{\theta,\text{in}}$ for nuisance parameters affecting the shape of the QCD multijet background for different toy data sets generated under the signal+background hypothesis for different signal masses and QCD multijet background predictions. The nuisance parameters are plotted 40 GeV displaced from each other for legibility. Note that for these fits the pre-fit nuisance parameters for all toy data sets are centered around the prediction from Pythia8, in order to show the differences between the toy data sets.

process with high precision. Note here, that again the constraints concerning the normalization parameters affecting the signal are due to the signal contribution in pseudo data. The nuisance parameters describing the τ_{21}^{DDT} p_{T}-dependence as well as the PDF uncertainty only affect the signal and can consequently only be constrained by a signal. The τ_{21}^{DDT} p_{T}-dependence uncertainty is between 5-30% and increases with the p_{T} of the resonance, making the large constraint of this nuisance parameter possible, provided that a signal resonance is present. The pull distributions for the nuisance parameters affecting the normalization are shown for toys generated following a Pythia8, Herwig++, MadGraph5_aMC@NLO and Powheg simulation. They are very similar for most of the generators, showing the

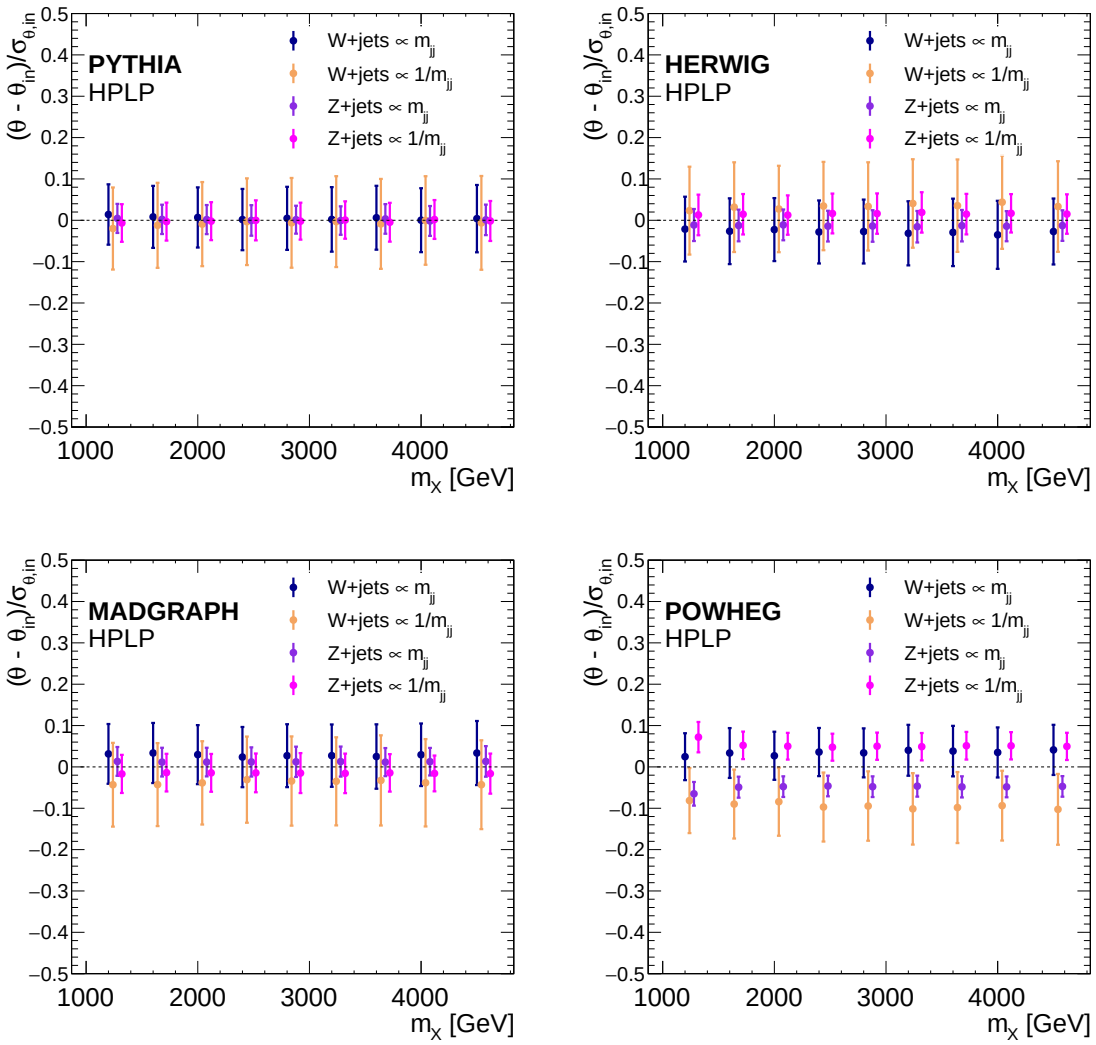

Figure 5.42.: The pull $(\theta - \theta_{\text{in}})/\sigma_{\theta,\text{in}}$ for nuisance parameters affecting the shape of the background originating from V+jets production for different toy data sets generated under the signal+background hypothesis for different signal masses and QCD multijet background predictions. The nuisance parameters are plotted 40 GeV displaced from each other for legibility.

very stringent constraint of the normalization uncertainty for the QCD multijet backgrounds. There is a pull observed for the normalization of the Z+jets background processes, for toys following a distribution for the QCD multijet backgrounds using the POWHEG generator. This is most likely again caused by the features introduced in the shape of this background component due to a low event number. Note however, that the signal injection test detailed Section 5.5.3 shows that the fit is still able to recover the number of injected signal events with sufficient accuracy.

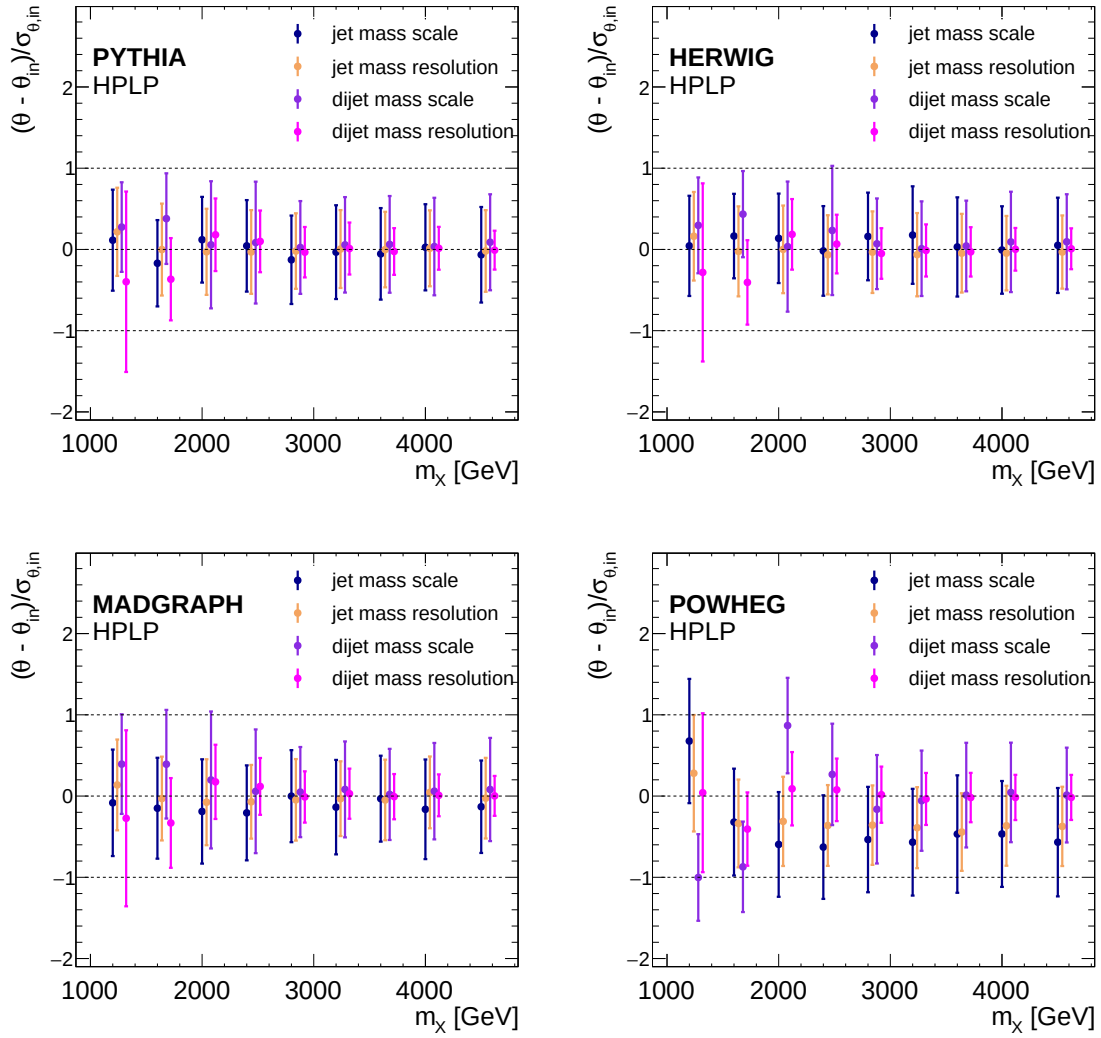

Figure 5.43.: The pull $(\theta - \theta_{\text{in}})/\sigma_{\theta,\text{in}}$ for nuisance parameters affecting the shape of a $G_{\text{bulk}} \rightarrow WW$ signal process for different toy data sets generated under the signal+background hypothesis for different signal masses and QCD multijet background predictions. The nuisance parameters are plotted 40 GeV displaced from each other for legibility.

5.5.3. Bias Tests in Pseudo-data

If the background models were inaccurate, or able to adapt in a manner that could fake the appearance of a signal, this could result in a biased measurement of the signal rate in data. To study the accuracy of the background model, and the capability of the fitting procedure to extract the correct number of signal events, if a signal is present, extensive bias tests are performed. The tests shown here are performed by injecting a $Z' \rightarrow WW$ signal with different masses and a signal strength corresponding to a significance of about 2 standard deviations for each signal mass. Thus, for each mass point tested 1000 pseudo-data distributions are created consisting of toys generated from different QCD multijet background predictions, as in the

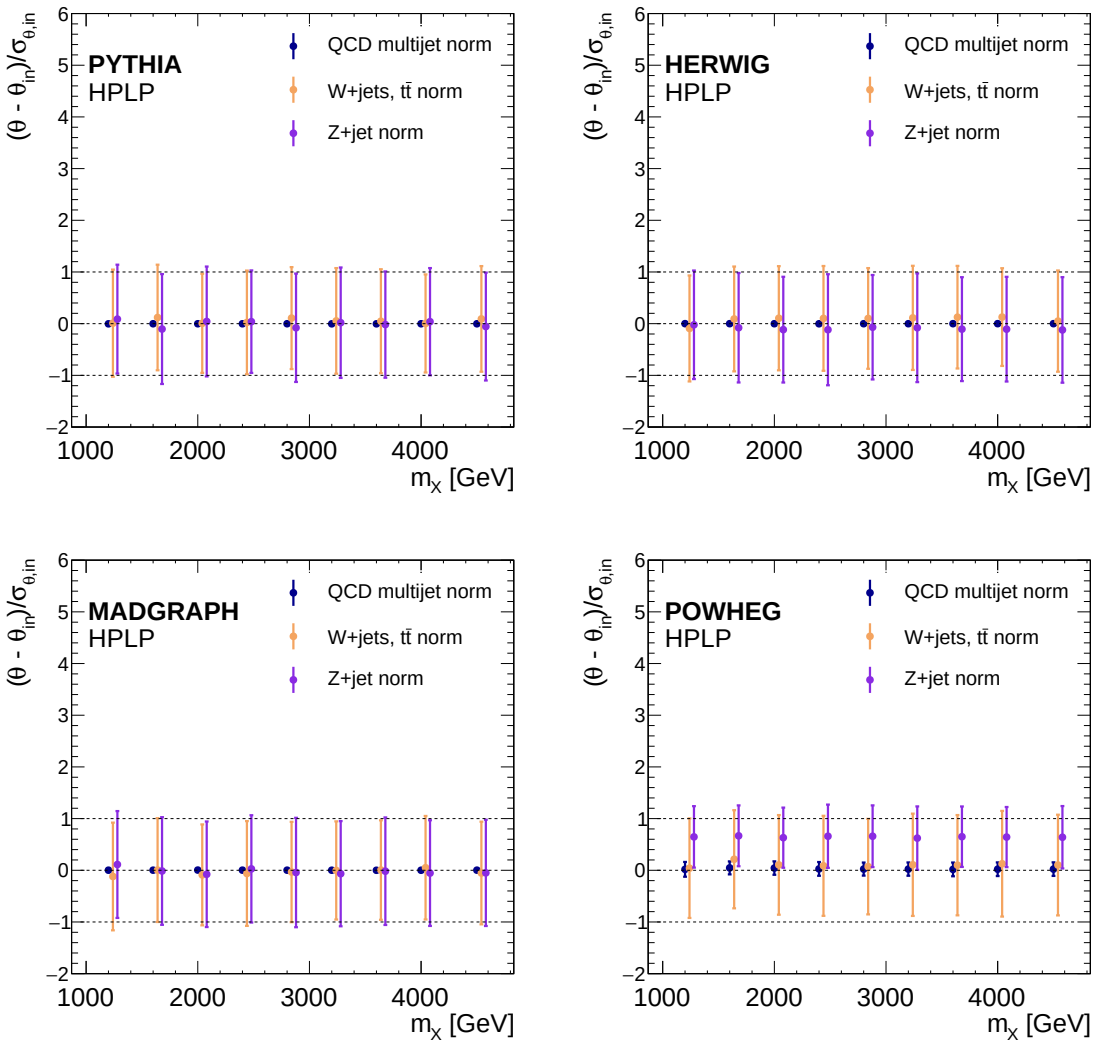

Figure 5.44.: The pull $(\theta - \theta_{\text{in}})/\sigma_{\theta,\text{in}}$ for nuisance parameters affecting the normalization of the background processes for different toy data sets generated under the signal+background hypothesis for different signal masses and QCD multijet background predictions. The nuisance parameters are plotted 40 GeV displaced from each other for legibility.

last section described. Additionally, toys generated from the V+jets background prediction corresponding to the number of events expected in data, as well as a number of random signal events, corresponding to the chosen signal strength, are included in the pseudo-data. For each toy a signal+background fit is performed and the number of background and signal events are extracted from the fit. The bias of the procedure is quantified using the mean and variance of the distribution of $(s_{\text{fit}} - s_{\text{in}})/s_{\text{in}}$ extracted from a Gaussian fit. Here, s_{in} is the number of signal events injected in the toy and s_{fit} is the number of signal events recovered from the fit to the pseudo-data. The results of these tests are shown in Figure 5.46, where these fits have been performed for the HPHP and HPLP categories separately, and using the MC predictions and luminosity corresponding to the 2016 data set.

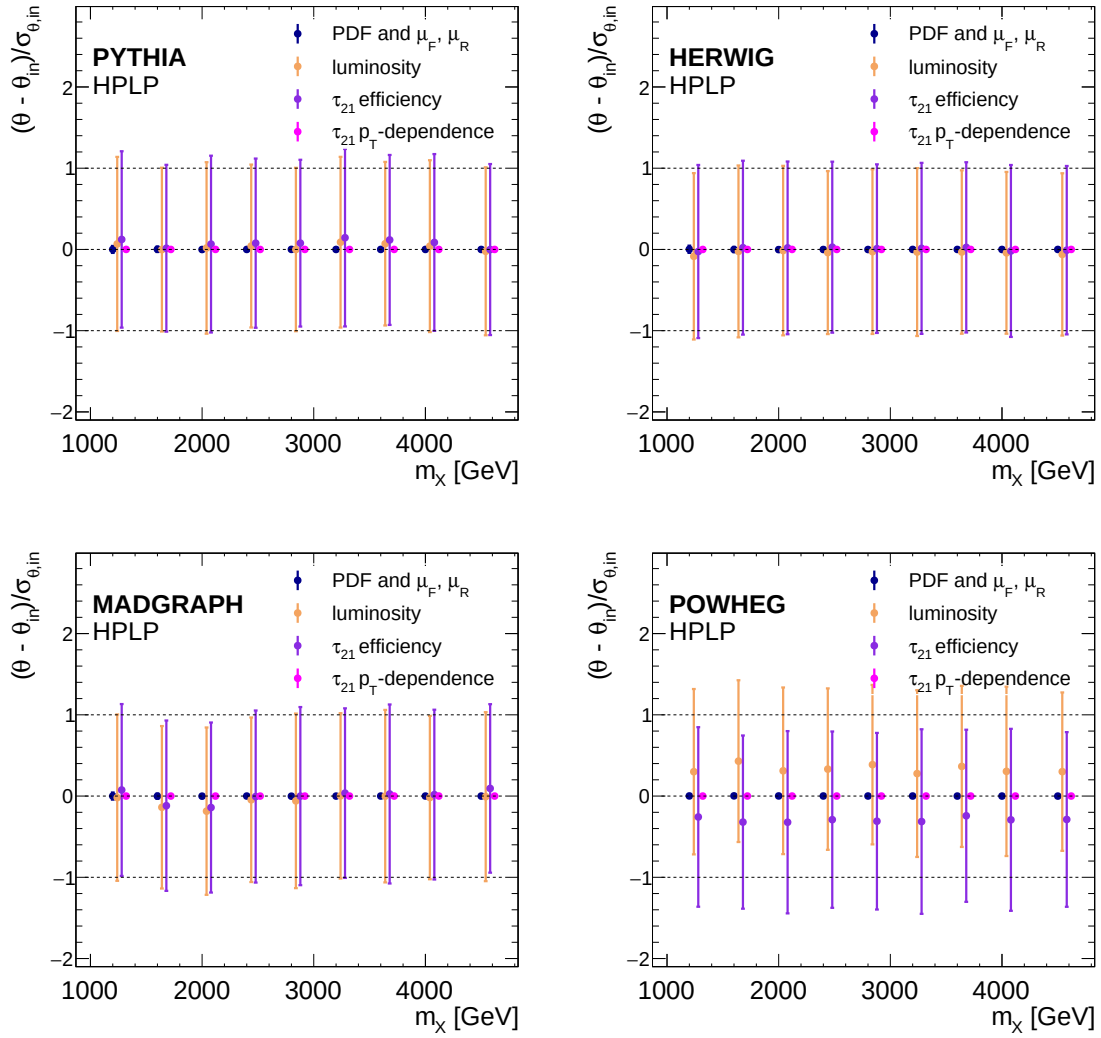

Figure 5.45.: The pull $(\theta - \theta_{\text{in}})/\sigma_{\theta,\text{in}}$ for nuisance parameters affecting the normalization of a $G_{\text{bulk}} \to WW$ signal process for different toy data sets generated under the signal+background hypothesis for different signal masses and QCD multijet background predictions. The nuisance parameters are plotted 40 GeV displaced from each other for legibility.

The tests show that the fit is able to recover the number of injected signal events within an accuracy of 10% of the number of injected events. The spread in variance is larger for the HPHP category, since this category contains much less events overall, which means the fit is less constrained in this category. However, in the limit setting, the fits to the HPHP and HPLP category are performed simultaneously, with some nuisances correlated or anti-correlated between categories. This allows a better constraining of the fit parameters for the HPHP category. There is also a notably larger fluctuation for the POWHEG simulation sample, especially in the HPHP category. This sample has the smallest number of generated event, and therefore exhibits the largest statistical fluctuations, which are transferred to the toy data sets.

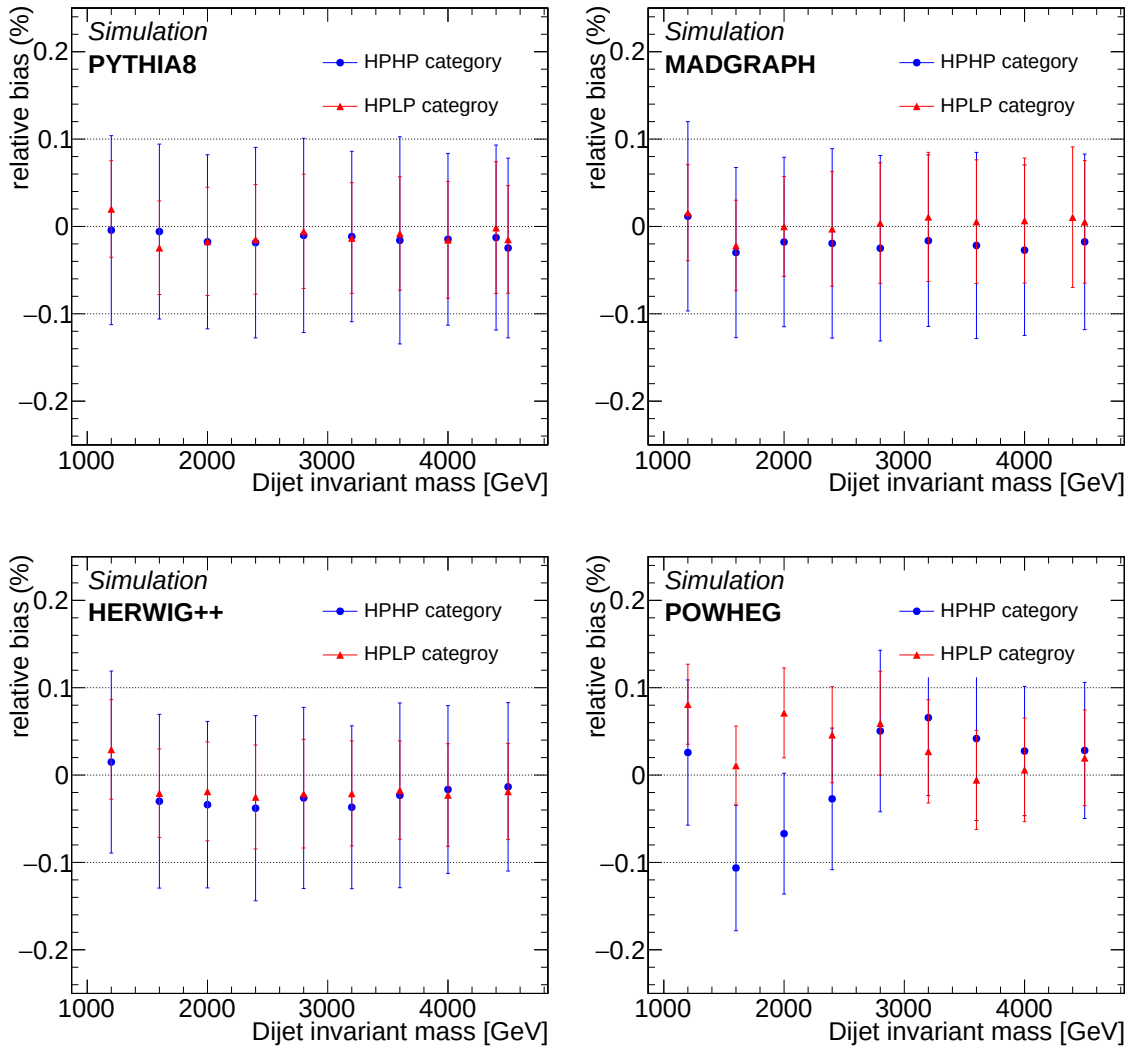

Figure 5.46.: The relative bias $(s_{\text{fit}} - s_{\text{in}})/s_{\text{in}}$ when injecting signal events equivalent to a significance of $2\,\sigma$ using 1000 toys per mass point and different MC simulation samples for the QCD multijet background. The injected signal follows the Z′ to WW model. The bias for a toy data set following predictions derived by PYTHIA8 is shown on the top left, while the same test is shown using MADGRAPH5_AMC@NLO (top right), HERWIG++ (bottom left) and POWHEG (bottom right).

5.6. Results

The results presented in this Section are based on the event selections and the modeling of signal and background derived in the previously. In Section 5.6.1 the final post-fit distributions on data are discussed. Since no significant deviation from SM backgrounds is observed, the upper 95% CL limits on the production cross section times branching fraction of new spin-1 and spin-2 particles in the full-hadronic diboson decay channel are presented.

5.6.1. Statistical Interpretation

The signal extraction procedure is based on a multidimensional fit of the signal and background pdfs to data, where the pdfs are allowed to vary within the systematic uncertainties by modifying the corresponding nuisance parameters. Figs. 5.47 and 5.48 show the projections of the resulting post-fit distributions on m_{jet1}, m_{jet2} and m_{jj} for the two purity categories, while Fig. 5.49 shows the projection of the signal region on the dijet invariant mass distributions. The post-fit distributions shown here are extracted from a simultaneous signal plus background fit to the data with an assumed signal mass of 2 TeV.

In Table 5.5, the background yields extracted from a background-only fit, together with their post-fit uncertainties, are summarized and compared with observations. The yields are given separately for the two purity categories. The extracted cross sections for V+jets are found to be compatible with the SM expectations obtained from MC simulation. As can be seen from the extracted numbers of events, the fit is able to very accurately reproduce the number of events in data, due to the large pre-fit uncertainties applied to the normalizations of the backround processes, particularly the 50% pre-fit uncertainty on the normalization for QCD multijet processes.

The associated systematic uncertainties to all nuisance parameters concerning the QCD multijet backgrounds are intentionally chosen very large in order to give the fit the capability to adapt to the a priori unknown shape of the QCD multijet spectrum in data. The nuisances associated with this background are then constrained by the fit. For example the normalization of the QCD multijet background is allowed to vary by 50% around its SM expectation. This nuisance is then severely constrained, to about 1%, through the multidimensional fit process. Another important aspect to note here is that through the fit of the V+jets background, especially in the m_{jet} spectrum the nuisance parameters associated with the largest uncertainty sources, namely the efficiency of the τ_{21}^{DDT} selection and the jet mass scale and resolution uncertainties, can be constrained notably. The corresponding pull distributions for the nuisance parameters defined as $p_\theta = (\theta - \theta_{\text{in}})/\sigma_\theta$ are shown for the two data taking years separately in Fig. 5.50. Here, θ is the post-fit value of the nuisance parameter, θ_{in} its pre-fit value and σ_θ the 1σ pre-fit standard deviation of the nuisance parameter θ. As can be seen in the Figure, the nuisance parameters affecting the QCD multijet shapes exhibit a difference between their pre-fit and post-fit values. This is insofar unsurprising as we do not a priori expect the data distribution to follow the nominal distribution from the fit, which was extracted from Pythia8 MC simulation. A pull in this shape parameters means for example, that the distribution in data, follows a mixture between the shapes extracted from Pythia8, Herwig++ and MadGraph5_aMC@NLO MC simulation, as was

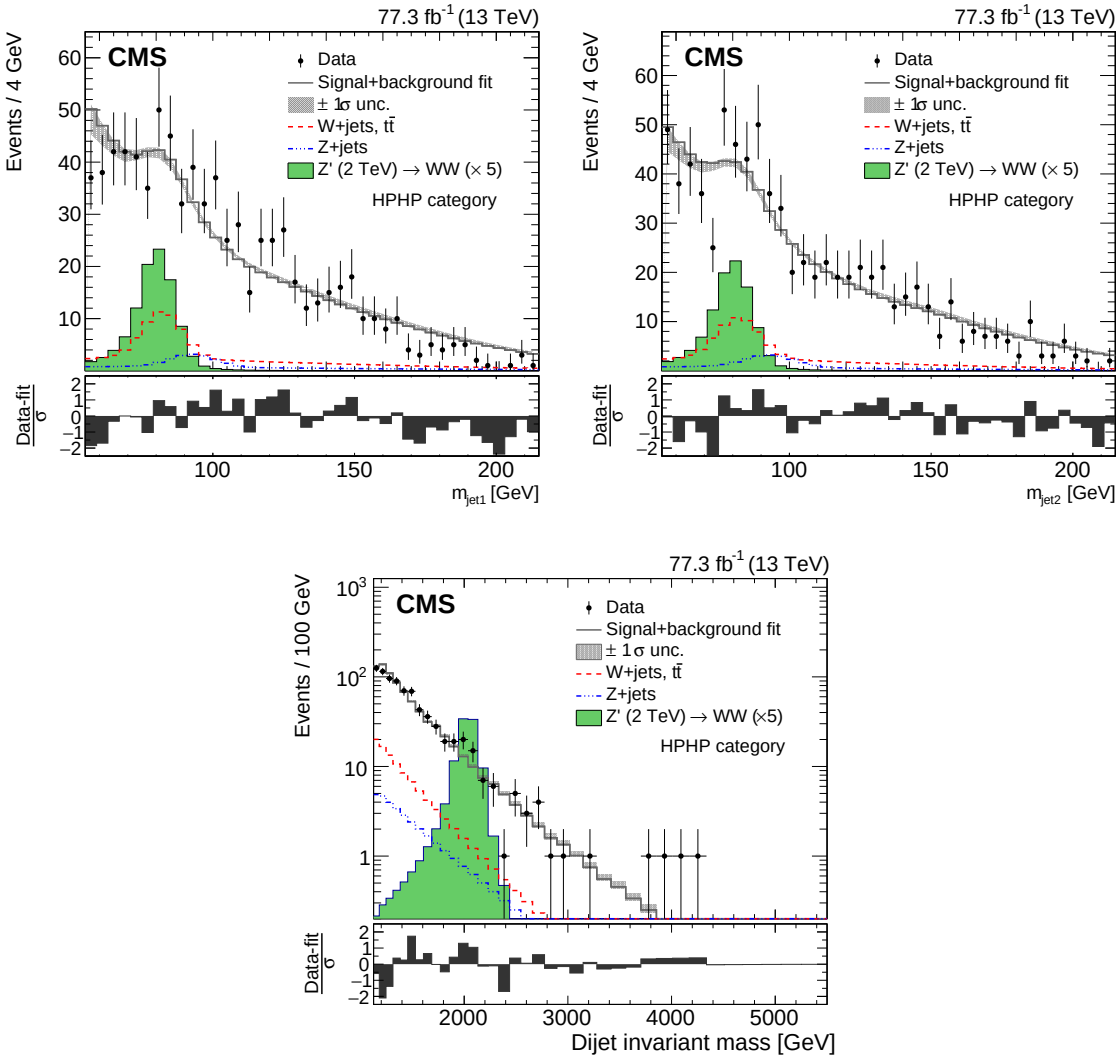

Figure 5.47.: For the HPHP category: comparison between the signal+background fit and the data distributions of m_{jet1} (upper left), m_{jet2} (upper right), and m_{jj} (lower). The background shape uncertainty is shown as a gray shaded band, and the statistical uncertainties of the data are shown as vertical bars. An example of a signal distribution is overlaid, where the number of expected events is scaled by a factor of 5. The corresponding pull distribution (Data-fit)/σ is shown below each mass distribution, where $\sigma = \sqrt{\sigma^2_{\text{data}} - \sigma^2_{\text{fit}}}$ for each bin to ensure a Gaussian pull-distribution, as defined in Ref. [180]. Figure published in Ref. [159].

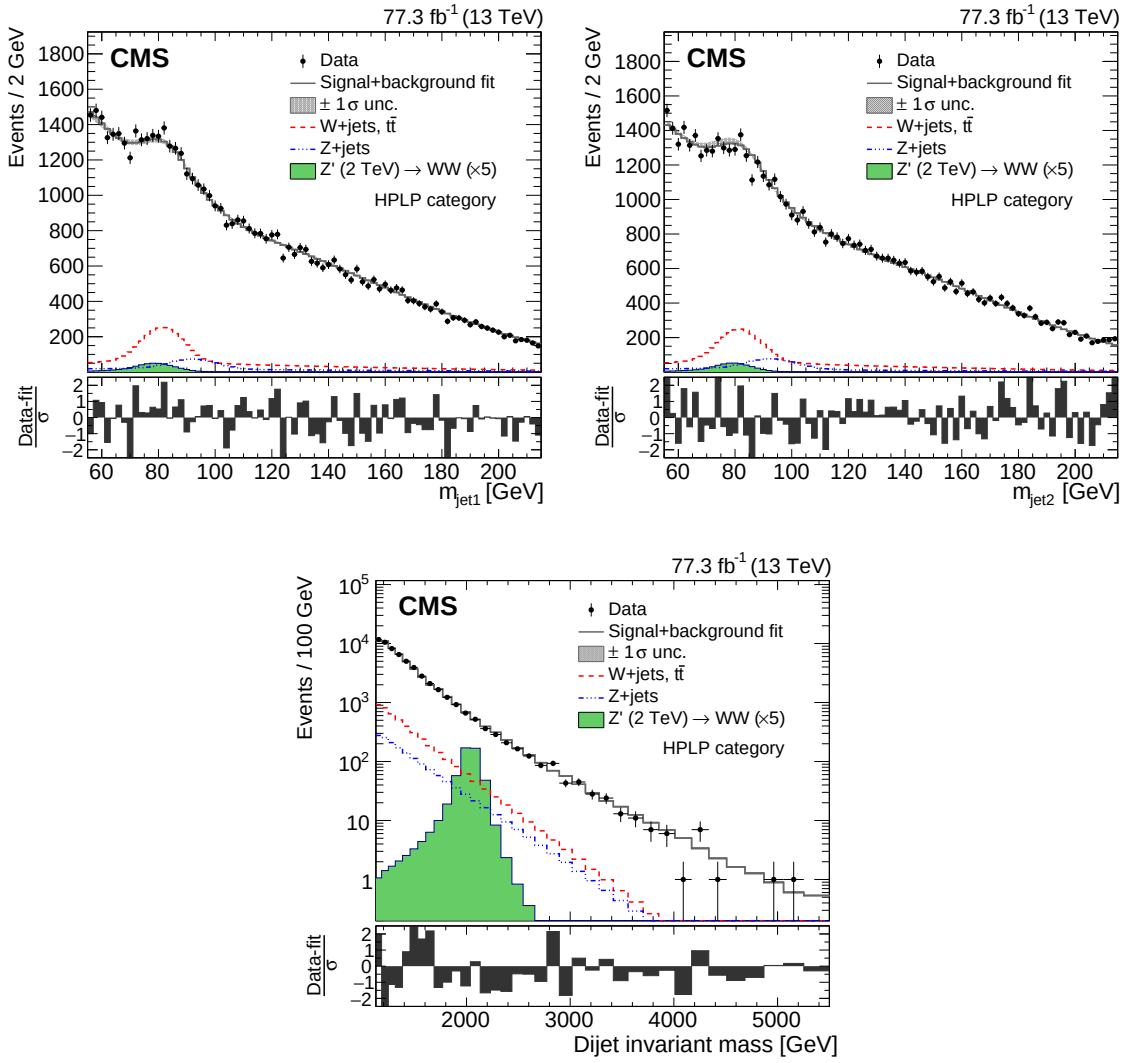

Figure 5.48.: For the HPLP category: comparison between the signal+background fit and the data distributions of m_{jet1} (upper left), m_{jet2} (upper right), and m_{jj} (lower). The background shape uncertainty is shown as a gray shaded band, and the statistical uncertainties of the data are shown as vertical bars. An example of a signal distribution is overlaid, where the number of expected events is scaled by a factor of 5. The corresponding pull distribution (Data-fit)/σ is shown below each mass distribution, where $\sigma = \sqrt{\sigma^2_{\mathrm{data}} - \sigma^2_{\mathrm{fit}}}$ for each bin to ensure a Gaussian pull-distribution, as defined in Ref. [180]. Figure published in Ref. [159].

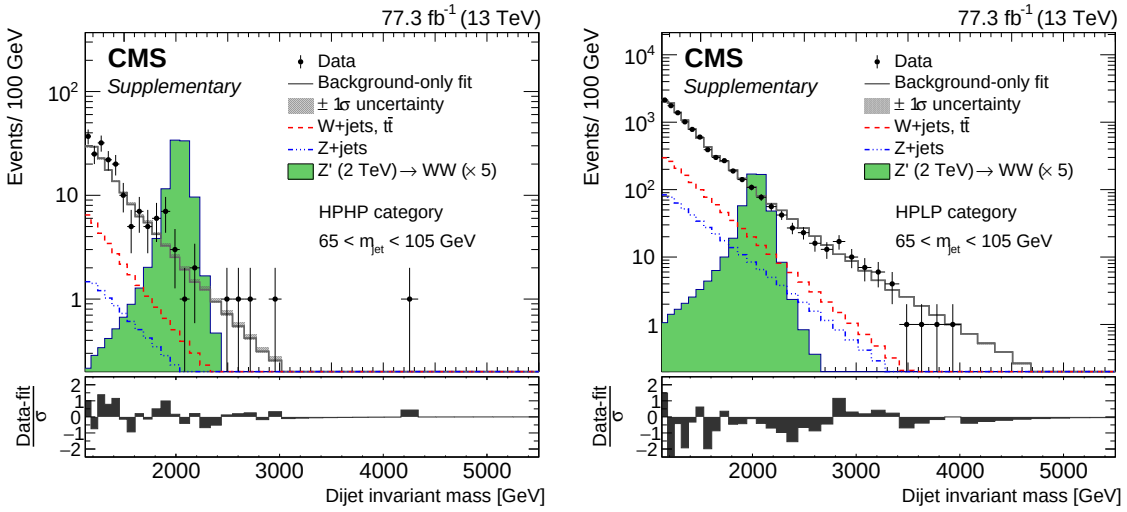

Figure 5.49.: Comparison between the background-only fit and the data distributions in the HPHP category (left) and HPLP category (right). The projections on m_{jj} are shown for events in which the masses of each jet are found in the range between 65 and 105 GeV where the bulk of the signal is expected. The background shape uncertainty is shown as a gray shaded band, and the statistical uncertainties of the data are shown as vertical bars. An example of a signal distribution is overlaid (green filled area), where the number of expected events is scaled by a factor of 5. The corresponding pull distribution (Data-fit)/σ is shown below each mass distribution, where $\sigma = \sqrt{\sigma^2_{\mathrm{data}} - \sigma^2_{\mathrm{fit}}}$ for each bin to ensure a Gaussian pull-distribution. Figure published in Ref. [159].

already shown for the shapes following the NLO POWHEG simulation. The distributions in 2016 and 2017 data are not exactly the same, due to differences in the jet energy corrections and the utilization of different pileup subtraction methods, which leads to differences in the fit of the QCD multijet background shape, when both years are fitted separately.

To asses how well the background-only hypothesis and its uncertainty model corresponds to the data, a gof test with a saturated model is performed. The gof test is performed using 1000 toys sampled from the background-only model with nuisances parameters constrained through a fit to data. The results of the test show good agreement of the background-only hypothesis with data and are shown in Fig. 5.51.

5.6.2. Exclusion Limits

To test for the presence of narrow resonances decaying into two vector bosons or, in absence of a resonance, to set upper limits on the production cross section times branching fraction, the CLs prescription evaluated using the asymptotic approximation as described in Section 2.7.3 is followed. No significant deviation from the SM expectation is found and upper limits on the product of the production cross section and branching fraction are set at 95% CL. The limits are interpreted in the context of a bulk graviton model and the HVT model B scenario. The

limits are computed using a shape analysis of the three-dimensional m_{jj}-m_{jet1}-m_{jet2} spectrum, where the three-dimensional signal and background pdfs discussed in the previous chapters are fitted to data simultaneously, for each mass point and purity category. The signal and background yields are both determined from this fit. The limits for a bulk graviton model are shown in Fig. 5.52 and for the HVT model B in Fig. 5.53. For the bulk graviton model, upper limits on the production cross section for $G_{\mathrm{bulk}} \to \mathrm{WW(ZZ)}$ are set in the range from 20 (27) fb for a resonance mass of 1.2 TeV to 0.2 fb for a resonance mass of 5.2 TeV. For the HVT model B, W′ and Z′ spin-1 resonances with masses below 3.8 and 3.5 TeV are excluded, respectively.

The combined upper limits on a $G_{\mathrm{bulk}} \to \mathrm{VV}$ are shown in Fig. 5.54 and the combined upper limits for the full HVT model B are shown in Fig. 5.55. Note that the limits on the full model cannot be interpreted under generic spin-1 or spin-2 models anymore since this calculation assumes the relative branching fractions and production probabilities of the two models used for interpretation. In Fig. 5.56, the limits on the HVT model B are translated into an exclusion region in the coupling plane $(g^2 c_{\mathrm{F}}/g_{\mathrm{V}}, g_{\mathrm{V}} c_{\mathrm{H}})$ of the model. Here c_{H} and c_{F} denote a factor scaling the coupling strength to the Higgs boson and fermions, while g_V denotes the interaction strength with SM V bosons and g is the weak coupling strength of the SM. The gray hashed region indicates a region of coupling parameters that lead to a larger decay width of the resonance, thus in this region the narrow-width approximation assumed in this analysis is no longer true, and the limits derived here are therefore not applicable.

In Fig. 5.57 (5.58), the results obtained using the new multidimensional fit method discussed in this thesis are compared to limits obtained in a previous search (see Appendix E) on the same data set for a $\mathrm{G_{bulk}} \to \mathrm{WW}$ ($\mathrm{W}' \to \mathrm{WZ}$) signal hypothesis. A gain in sensitivity due to the new method of 20–30% is observed. This gain originates from the higher signal efficiency due to the larger jet mass window, as well as the additional constraints placed on systematic uncertainties affecting the signal by measuring the standard model background from W or Z production with associated jets.

The limits presented here are the best to date in the dijet final state, and reach a similar sensitivity as the combination of different VV, VH, and HH decay channels using the 2016 data set.

Table 5.5.: Observed number of events and background yields extracted from the background-only fit together with post-fit uncertainties, in the two purity categories.

Category	HPHP			HPLP		
W+jets	100	±	11	4600	±	200
Z+jets	33	±	4	1580	±	160
QCD multijets	650	±	4	51100	±	300
Predicted total background	783	±	12	57200	±	400
Observed yield	780	±	30	57230	±	240

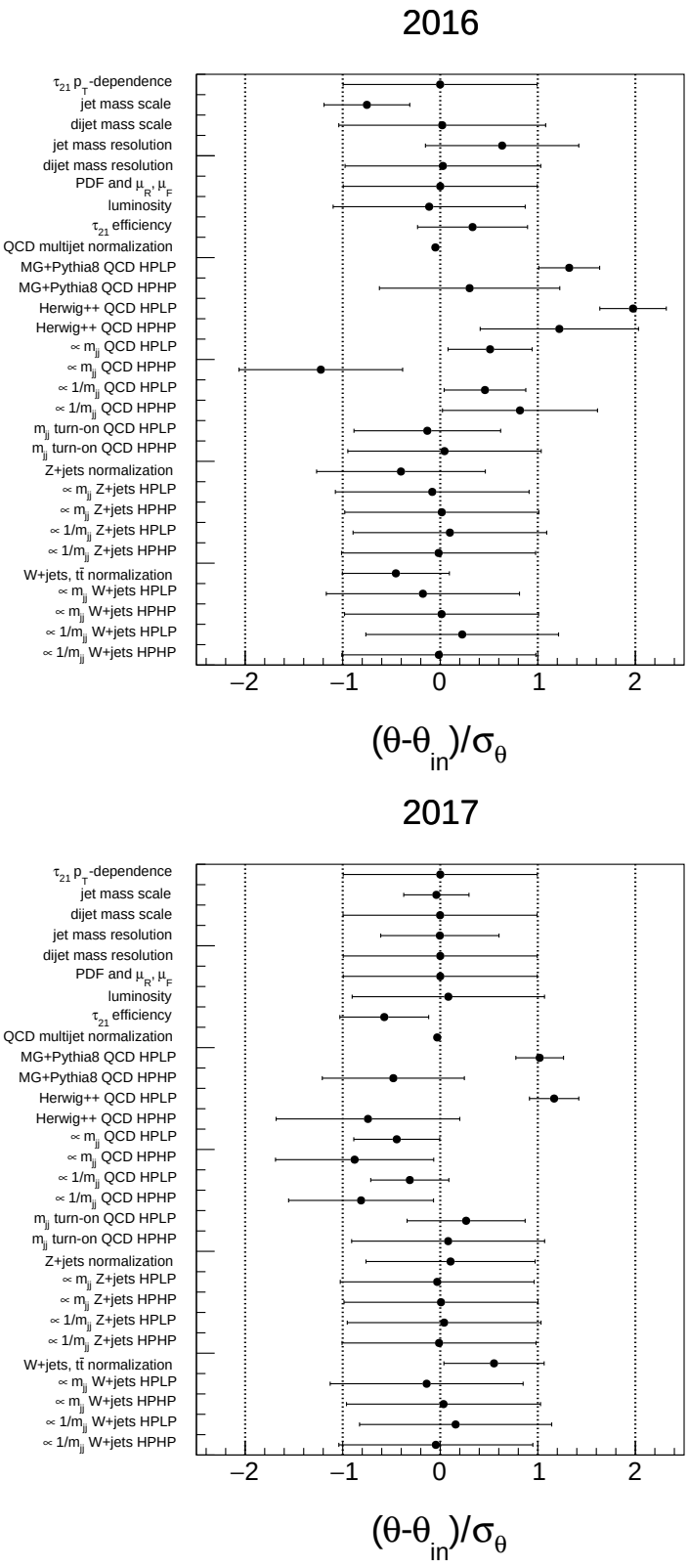

Figure 5.50.: The pulls for the signal + background fit to the two data sets 2016 (top) and 2017 (bottom) for both purities using a Z′ signal model with a mass of 2000 GeV. The pulls are shown for all nuisance parameters of the analysis.

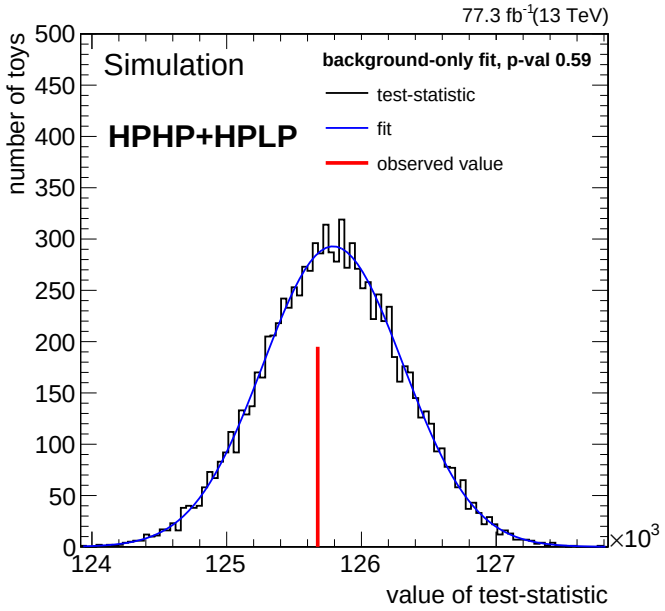

Figure 5.51.: Distribution of the likelihood for toys generated around the background-only fit in the signal region compared to the likelihood on data for a background-only fit and for the full combination of 2016 and 2017 data.

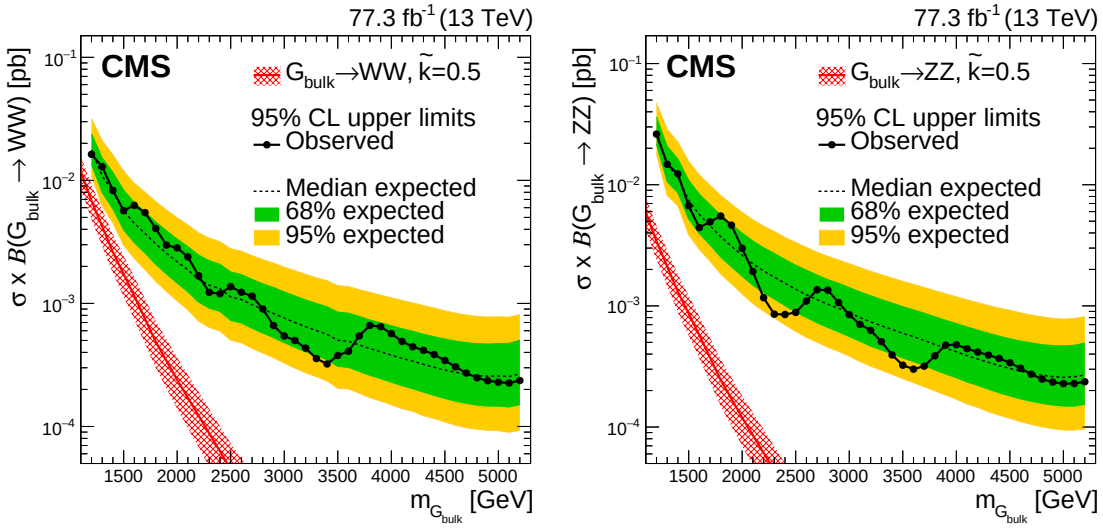

Figure 5.52.: The observed and expected 95% CL upper limits on the product of the production cross section (σ) and the branching fraction B, obtained after combining categories of all purities with 77.3 fb^{-1} of 13 TeV data. The limits are shown for a $G_{\text{bulk}} \to \text{WW}$ (left) and $G_{\text{bulk}} \to \text{ZZ}$ (right) model. For each signal scenario the theoretical prediction (red line) and its associated uncertainty due to the proton PDFs (red hashed band) is shown. The theory cross sections are calculated at LO in QCD [13, 56]. Figure published in Ref. [159].

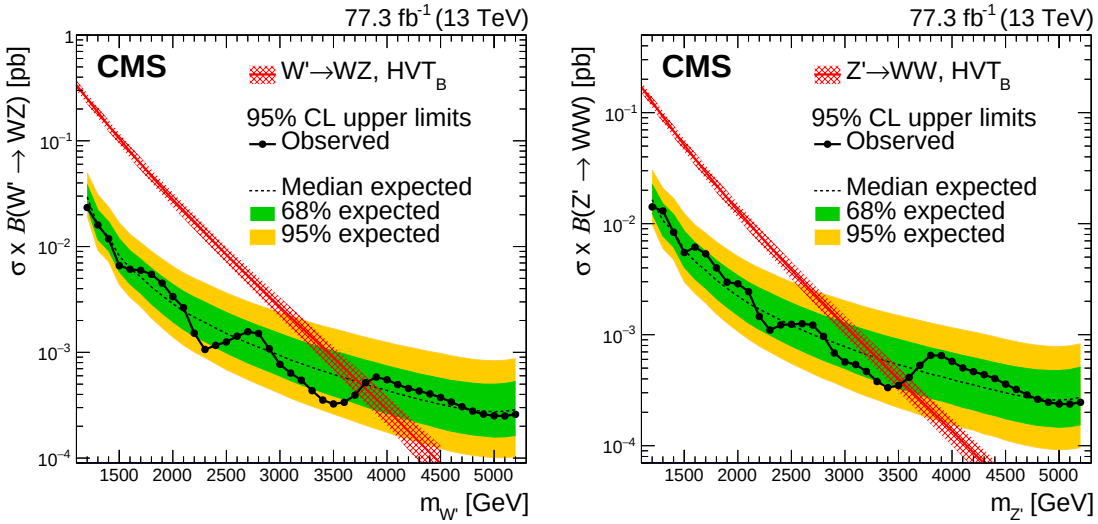

Figure 5.53.: The observed and expected 95% CL upper limits on the product of the production cross section (σ) and the branching fraction B, obtained after combining categories of all purities with 77.3 fb^{-1} of 13 TeV data. The limits are shown for a W$'$ $\rightarrow$ WZ (left) and Z$'$ $\rightarrow$ WW (right) model. For each signal scenario the theoretical prediction (red line) and its associated uncertainty due to the proton PDFs (red hashed band) is shown. The theory cross sections are calculated at LO in QCD [13, 56]. Figure published in Ref. [159].

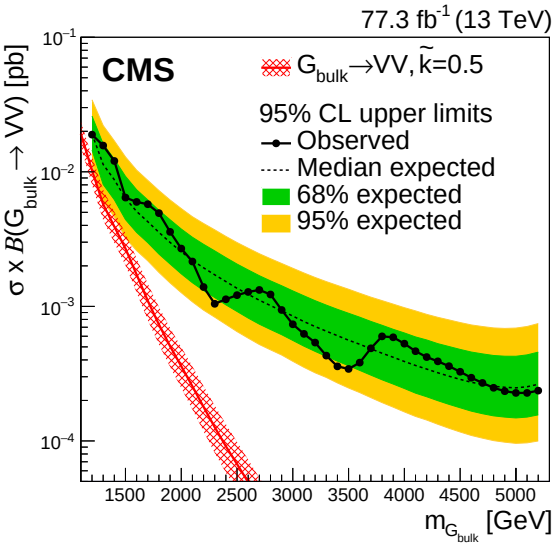

Figure 5.54.: Observed and expected 95% CL upper limits on the product of the production cross section (σ) and the branching fraction B, obtained after combining categories of all purities with 77.3 fb^{-1} of 13 TeV data, for a spin-2 bulk graviton decaying to WW or ZZ. The theoretical prediction (red line) and its uncertainty associated with the choice of the PDF set (red hashed band) is shown. The theory cross sections (red line) are calculated at LO in QCD. Figure published in Ref. [159].

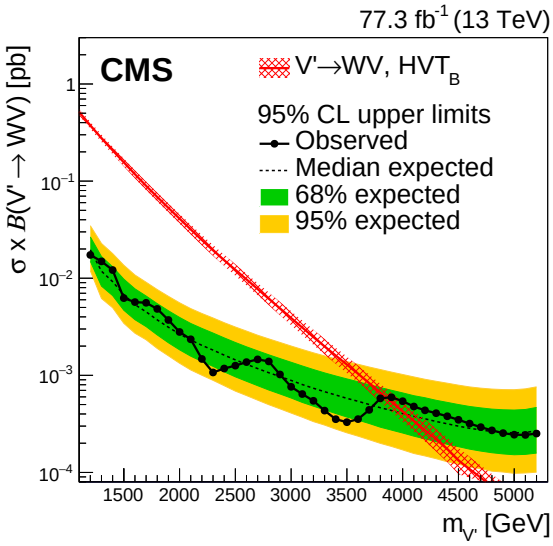

Figure 5.55.: Observed and expected 95% CL upper limits on the product of the production cross section (σ) and the branching fraction, obtained after combining categories of all purities with 77.3 fb^{-1} of 13 TeV data, for a spin-1 heavy vector triplet W′ and Z′ decaying to WZ and WW, respectively. The theoretical prediction (red line) and its uncertainty associated with the choice of the PDF set (red hashed band) is shown. The theory cross sections (red line) are calculated at LO in QCD. Figure published in Ref. [159].

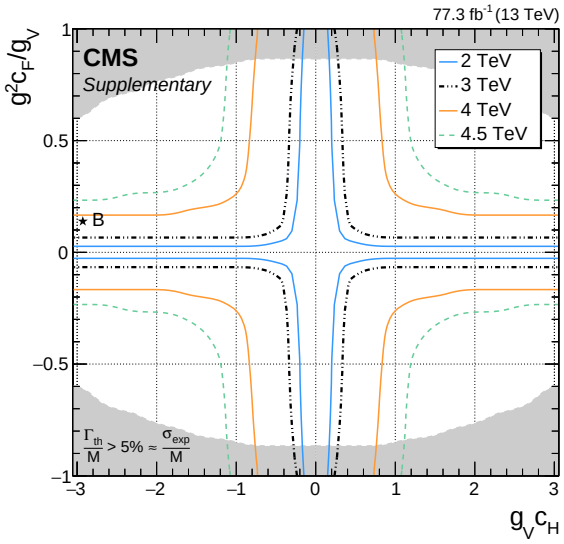

Figure 5.56.: Exclusion regions in the plane of the HVT couplings ($g^2 c_F/g_V, g_V c_H$) for four resonance masses, 2.0, 3.0, 4.0 and 4.5 TeV. The solid, dashed, and dashed-dotted lines represent the boundaries of the regions excluded by this search for different resonance masses (the region outside these lines is excluded). The areas indicated by the solid shading correspond to regions where the resonance width is predicted to be more than 5% of the resonance mass and the narrow-resonance assumption is not satisfied. The black star marks the point in the coupling plane corresponding to the HVT model B. Figure published in Ref. [159].

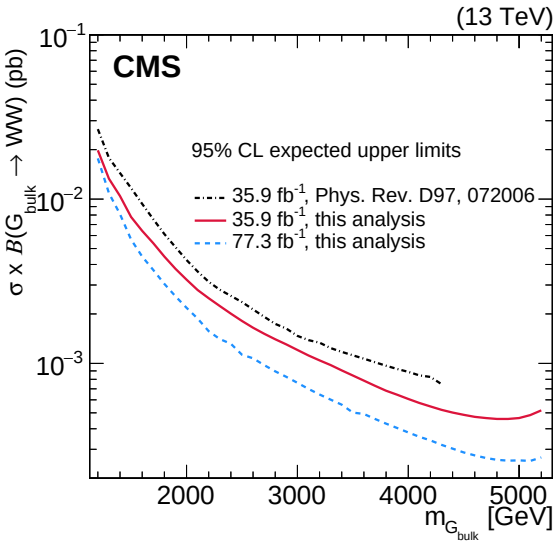

Figure 5.57.: The expected 95% CL upper limits on the product of the production cross section (σ) and the branching fraction B for a $G_{\text{bulk}} \rightarrow \text{WW}$ signal using 35.9 fb^{-1} of data collected in 2016 obtained using the multidimensional fit method presented in this thesis (red solid line), compared to the result obtained with previous methods (black dash-dotted line) with the approach discussed in Appendix E. The final limit obtained in this thesis with 77.3 fb^{-1} of data collected in 2016 and 2017 is also shown (blue dashed line). Figure published in Ref. [159].

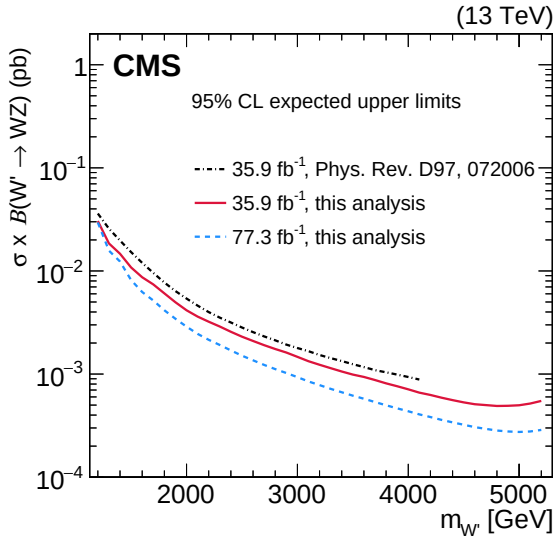

Figure 5.58.: The expected 95% CL upper limits on the product of the production cross section (σ) and the branching fraction B for a $\text{W}' \rightarrow \text{WZ}$ signal using 35.9 fb^{-1} of data collected in 2016 obtained using the multidimensional fit method presented in this thesis (red solid line), compared to the result obtained with previous methods (black dash-dotted line) with the approach discussed in Appendix E. The final limit obtained in this thesis with 77.3 fb^{-1} of data collected in 2016 and 2017 is also shown (blue dashed line).

6. Conclusion and Outlook

In this thesis an improved search for new diboson resonances with masses above 1.2 TeV that decay to WW, WZ or ZZ boson pairs in the all-hadronic final state, has been presented. Each of the two bosons decays into one large-radius jet, yielding dijet final states. The search utilizes substructure methods to distinguish jets originating from V boson decays from jets originating from single quarks or gluons. The analysis utilizes a total integrated luminosity of 77.3 fb^{-1}, recorded by the CMS detector at a center-of-mass energy of $\sqrt{s} = 13\,\text{TeV}$. The analysis presented is in the process of being published, with public results found in Ref. [159]. Similar exclusion limits as the ones presented here, have also been obtained by the ATLAS Collaboration for the 2016 and 2017 data set [181] and for 2016, 2017 and 2018 data combined [182]. Figure 6.1 shows a comparison between the expected limits obtained in this analysis and results obtained by the ATLAS Collaboration in a similar search for VV resonances decaying in the all-jet final state [181] on the data set recorded in 2016 and 2017 by the ATLAS detector. The results achieved in this analysis are similar or better by up to 35%.

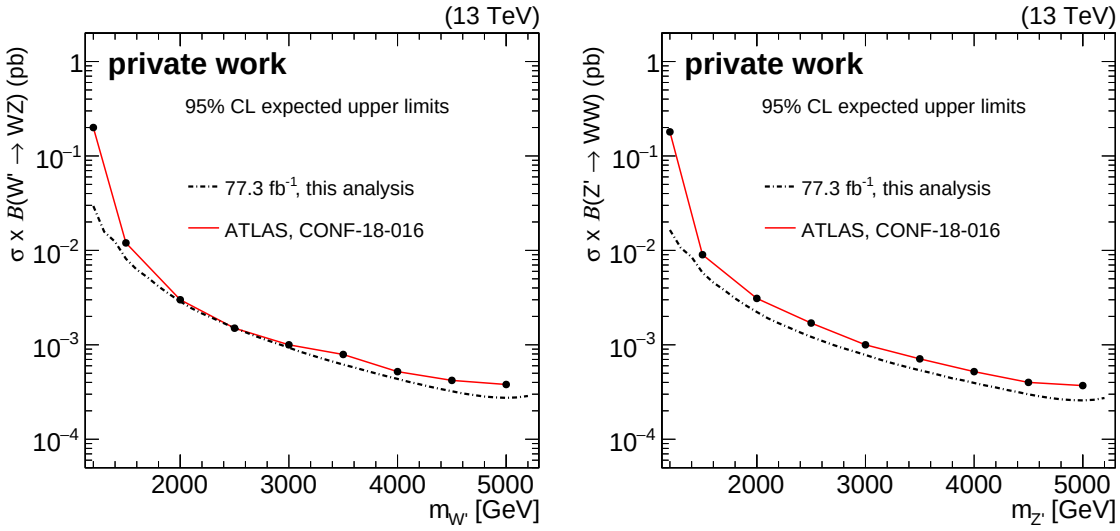

Figure 6.1.: Comparison of the expected limits obtained by this analysis on 77.3 fb^{-1} of data (black dash-dotted line), to the expected limits obtained by the ATLAS Collaboration in a similar search for a VV resonance decaying into hadrons, see Ref. [181]. The expected limits are shown for a W′ resonance (left) and a Z′ resonance (right).

This analysis introduces a new data-driven background and signal extraction based on a multidimensional maximum likelihood fit of the m_{jj}-m_{jet1}-m_{jet2} spectrum, thus taking advantage of the fact that the expected signal is resonant in all three mass dimensions. The

method yields an improvement of up to 30% relative to the previous search methods, and places additional constraints on systematic uncertainties affecting the signal by measuring the SM background from W or Z boson production in association with jets.

No significant deviation above the SM expectation was found, and exclusion limits on the production cross section times branching fraction of new particles decaying into two vector bosons have been set at the 95% CL as a function of the mass of the potential resonance. The limits presented here are the best to date in the all-hadronic diboson decay channel. Limits for spin-1 and spin-2 resonances are presented and interpreted in light of a bulk graviton model and the HVT model B scenario. For the HVT model B, W' and Z' resonances with masses below 3.8 and 3.5 TeV are excluded, respectively. For the bulk graviton model, upper limits on the production cross section for $G_{\text{bulk}} \to \text{WW}$ (ZZ) are set in the range of 20 (27) fb to 0.2 fb for resonance masses between 1.2 and 5.2 TeV.

The new multidimensional fit method also opens the possibility of combining a number of previously disjunctive searches into one common framework. Namely, all searches for resonances decaying into secondary particles φ that further decay hadronically, can potentially be carried out using this framework. This is particularly interesting in light of the increasingly more likely possibility that signatures of new processes beyond the SM are not appearing as initially expected. The new method presented here not only allows the inclusion of VH, HH or final states with top quarks, it also allows to start new searches for more exotic triboson signals, see Refs. [183, 184], but would also provide the possibility to incorporate generic hadronic searches of the form of $X \to \varphi_1\varphi_2$.

An additional benefit of the new analysis strategy is that this more sophisticated shape analysis allows an easier expansion of the searches to larger signal widths. So far most analyses searching for new resonances utilize the narrow-width approximation, as does the analysis presented in this thesis, a notable exception is Ref. [15], meaning the considered signals are expected to have an intrinsic width smaller than the detector resolution. This approximation, though beneficial to the straightforwardness of the search, should perhaps be abandoned in future searches, since theory models predict wider signal width with increasing frequency. Thus future analysis may greatly profit from these improvements.

Even though the only new particle found at the LHC at the time of writing remains the Higgs boson, decay channels such as the one probed in this analysis, provide a very promising window into potential physics beyond the SM. Further analysis of data recorded at the LHC complex in 2018 as well as future data from the next data taking period starting in 2021 (Run III), and the data that will be collected during the runtime of the High-Luminosity LHC project, might still unveil previously undiscovered phenomena or particles. Figure 6.2 shows a comparison of the expected sensitivity of the analysis presented in this thesis when the integrated luminosity of available data is increased. This study assumes no further improvements in the analysis strategy and that the systematic uncertainties are the same as for data recorded in 2016. Despite these conservative estimates the sensitivity of the analysis with the full Run III data set would reach the cross sections for bulk gravitons with masses smaller than 1.4 TeV. With the planned increase in collision energy to 14 TeV in Run III, the search will also be able to extend to resonance masses beyond 5.2 TeV. With new boson tagging methods using deep neural networks and additional improvements in the analysis strategy, or the determination of systematic uncertainties, such as the tagging efficiency scale

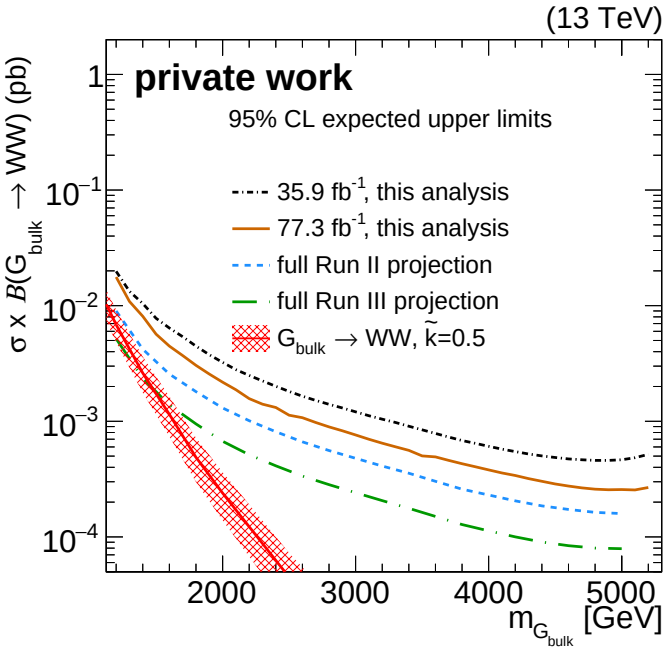

Figure 6.2.: The 95% expected upper limits obtained with this analysis for different expected luminosities. The black dash-dotted line corresponds to the data set recorded in 2016, while the orange line corresponds to the 2016 and 2017 recorded data set, that are analyzed in this analysis. The blue dashed line corresponds to the expected limit assuming 142 fb^{-1} of data as was recorded in the years 2016, 2017 and 2018 combined. The green dash-dotted line corresponds to the expected limits obtained assuming an integrated luminosity of 300 fb^{-1}, as is expected at the end of Run III. For these projections no further improvements of the analysis strategy and systematic uncertainties were assumed. The expected limits are compared with the theoretical prediction (red line) for a $\text{G}_{\text{bulk}} \rightarrow \text{WW}$ model.

factors, an even greater sensitivity will be reached in the coming years.

SM precision measurements, as well as searches for new particles with masses beyond the TeV scale, utilizing effective field theories, have become a very important pillar of the physics program at the LHC, especially in light of the so far unsuccessful direct searches for physics beyond the SM. However, until the full data set recorded during the operation of the LHC is thoroughly analyzed, so far undiscovered particles can still exist at the TeV scale. The discovery of a new particle would provide unique insights into the nature of particle physics. It is therefore important to carefully analyze the data provided by the LHC, as well as to develop innovative search methods, that might uncover new signatures in regions of phase space that were previously not considered by direct searches. The methods developed and described in this thesis can provide a key ingredient on the way to uncover beyond the SM physics, by greatly improving the sensitivity of conventional diboson searches, as well as providing a new framework which can potentially be used for highly sensitive searches of a generic resonance anywhere in the jet mass spectrum.

Table A.1.: A list of data sets used for the analysis. The latest recommended jet energy corrections (Spring16_23Sep2016_v3 for 2016, Fall17_17Nov2017_V6 for 2017) have been applied.

Sample name
/JetHT/Run2016B-03Feb2017_ver2-v2/MINIAOD
/JetHT/Run2016C-03Feb2017-v1/MINIAOD
/JetHT/Run2016D-03Feb2017-v1/MINIAOD
/JetHT/Run2016E-03Feb2017-v1/MINIAOD
/JetHT/Run2016F-03Feb2017-v1/MINIAOD
/JetHT/Run2016G-03Feb2017-v1/MINIAOD
/JetHT/Run2016H-03Feb2017_ver2-v1/MINIAOD
/JetHT/Run2016H-03Feb2017_ver3-v1/MINIAOD
/JetHT/Run2017B-17Nov2017-v1/MINIAOD
/JetHT/Run2017C-17Nov2017-v1/MINIAOD
/JetHT/Run2017D-17Nov2017-v1/MINIAOD
/JetHT/Run2017E-17Nov2017-v1/MINIAOD
/JetHT/Run2017F-17Nov2017-v1/MINIAOD

A. Appendix: Data Sets and MC Samples

The data sets used in the analysis are listed in table A.1. Overall 77.3 fb^{-1} of data collected by the CMS experiment has been analyzed in this work.

A list of generated samples for the signals is in table A.2. The considered phenomenologies are the bulk gravitons ($G_{\text{bulk}} \to \text{WW(ZZ)}$) generated for the bulk scenario [4,5,185] of the RS model of warped extra dimensions [2,3], and the heavy new bosons (W' and Z') that can be part of an heavy vector triplet [13] or can be mass degenerate as a vector singlet [186,187].

Two free parameters characterize the bulk graviton model: the mass of the first Kaluza–Klein (KK) excitation of a spin-2 boson, and the ratio $\tilde{\kappa} = \kappa/\overline{\text{M}}_{\text{Pl}}$, with κ being the unknown curvature scale of the extra dimension and $\overline{\text{M}}_{\text{Pl}} = \text{M}_{\text{Pl}}/\sqrt{8\pi}$ the reduced Planck mass. A scenario with $\tilde{\kappa} = 0.5$ [56] is considered in this thesis.

The HVT framework generically represents a large number of models with the specific models formulated in terms of a few parameters: three coefficients c_{F}, c_{H} and g_{V}. For the analysis presented here, samples were simulated in the HVT model B, corresponding to $g_{\text{V}} = 3$, $c_{\text{H}} = -0.98$, and $c_{\text{F}} = 1.02$ [13]. All simulated samples are produced with a relative resonance width of 0.1%, in order to be within the validity of the narrow-width approximation. Monte Carlo simulated events of the bulk graviton and HVT signals are generated at LO in QCD with MadGraph5_aMC@NLO versions 2.2.2 and 2.4.3 [120] and the hadronization and

showering is simulated with PYTHIA8 versions 8.205 and 8.230 [188], for 2016 and 2017 detector conditions, respectively.

Simulated samples of the SM background processes are used to optimize the analysis and create the background templates. Simulations for the main QCD multijet background, as well as the minor backgrounds from V+jets and $t\bar{t}$ are used in the analysis. The QCD multijet production is simulated with four different generator configurations:

1. using purely PYTHIA8 for the generation of a p_T-ordered QCD multijet sample

2. using the LO mode of MADGRAPH5_AMC@NLO [189] matched and showered with PYTHIA8 for the generation of an H_T-ordered QCD multijet sample

3. using POWHEG [127, 190–192] matched and showered with PYTHIA8 for the generation of QCD multijet sample NLO in QCD

4. using HERWIG++ 2.7.1 [129] with the CUETHS1 tune [125].

In addition three different samples of Top quark pair production are used for the analysis presented in this thesis:

1. $t\bar{t}$ production generated using POWHEG [193], showered with PYTHIA8 at NLO

2. $t\bar{t}$ production using MADGRAPH5_AMC@NLO interfaced with PYTHIA8 as shower generator

3. $t\bar{t}$ production using PYTHIA8 as a standalone generator

The first sample is an all hadronic sample used in the main analysis described in this thesis, while the second and third sample are inclusive and used for the scale factor measurement described in Section 4.2.7.

The production of W+jets and Z+jets is simulated at LO with MADGRAPH5_AMC@NLO matched and showered with PYTHIA8.

All samples are processed through a GEANT4-based [130] simulation of the CMS detector. To simulate the effect of additional pp collisions within the same or adjacent bunch crossings (pileup), additional inelastic events are generated using PYTHIA8 and superimposed on the hard-scattering events. The MC simulated events are weighted to reproduce the distribution of the number of reconstructed pileup vertices observed in the 2016 and 2017 data separately. The NNPDF 3.0 [110] LO parton distribution functions (PDFs) are used together with the CUETP8M1 [125] and CP5 [126] underlying event tunes in PYTHIA8 for 2016 and 2017 conditions, respectively.

Table A.2.: A list of signal samples used for the analysis with the number of events generated and the theoretical cross section of the model.

Sample name	Number of events	Cross section [pb]
/BulkGravToWW_narrow_M-1000_13TeV-madgraph	276858	0.0205
/BulkGravToWW_narrow_M-1200_13TeV-madgraph	299910	0.0068
/BulkGravToWW_narrow_M-1400_13TeV-madgraph	30 000	0.0026
/BulkGravToWW_narrow_M-1600_13TeV-madgraph	287956	0.0012
/BulkGravToWW_narrow_M-1800_13TeV-madgraph	299796	0.0005
/BulkGravToWW_narrow_M-2000_13TeV-madgraph	299814	0.0002
/BulkGravToWW_narrow_M-2500_13TeV-madgraph	299624	4.4857e-05
/BulkGravToWW_narrow_M-3000_13TeV-madgraph	299290	9.8249e-06
/BulkGravToWW_narrow_M-3500_13TeV-madgraph	298912	41.976e-07
/BulkGravToWW_narrow_M-4000_13TeV-madgraph	298118	24.382e-07
/BulkGravToWW_narrow_M-4500_13TeV-madgraph	29708	20.897e-07
/BulkGravToWW_narrow_M-5000_13TeV-madgraph	28906	-
/BulkGravToWW_narrow_M-5500_13TeV-madgraph	28988	-
/BulkGravToWW_narrow_M-6000_13TeV-madgraph	28020	-
/BulkGravToZZToZhadZhad_narrow_M-1000_13TeV-madgraph	299912	0.01025
/BulkGravToZZToZhadZhad_narrow_M-1200_13TeV-madgraph	299922	0.00342
/BulkGravToZZToZhadZhad_narrow_M-1400_13TeV-madgraph	299904	0.00131
/BulkGravToZZToZhadZhad_narrow_M-1600_13TeV-madgraph	299864	0.00057
/BulkGravToZZToZhadZhad_narrow_M-1800_13TeV-madgraph	289486	0.00024
/BulkGravToZZToZhadZhad_narrow_M-2000_13TeV-madgraph	299796	0.00012
/BulkGravToZZToZhadZhad_narrow_M-2500_13TeV-madgraph	299588	0.0000224
/BulkGravToZZToZhadZhad_narrow_M-3000_13TeV-madgraph	275934	0.0000049
/BulkGravToZZToZhadZhad_narrow_M-3500_13TeV-madgraph	298914	0.0000021
/BulkGravToZZToZhadZhad_narrow_M-4000_13TeV-madgraph	282354	0.0000012
/BulkGravToZZToZhadZhad_narrow_M-4500_13TeV-madgraph	29650	0.0000010
/BulkGravToZZToZhadZhad_narrow_M-5000_13TeV-madgraph	29412	-
/BulkGravToZZToZhadZhad_narrow_M-5500_13TeV-madgraph	28994	-
/BulkGravToZZToZhadZhad_narrow_M-6000_13TeV-madgraph	27970	-
/WprimeToWZToWhadZhad_narrow_M-1000_13TeV-madgraph	30000	4.5416e-01
/WprimeToWZToWhadZhad_narrow_M-1200_13TeV-madgraph	30000	2.5035e-01
/WprimeToWZToWhadZhad_narrow_M-1400_13TeV-madgraph	30000	1.3897e-01
/WprimeToWZToWhadZhad_narrow_M-1600_13TeV-madgraph	30000	7.9267e-02
/WprimeToWZToWhadZhad_narrow_M-1800_13TeV-madgraph	30000	4.6459e-02
/WprimeToWZToWhadZhad_narrow_M-2000_13TeV-madgraph	30000	2.7865e-02
/WprimeToWZToWhadZhad_narrow_M-2500_13TeV-madgraph	30000	8.3702e-03
/WprimeToWZToWhadZhad_narrow_M-3000_13TeV-madgraph	30000	2.6828e-03
/WprimeToWZToWhadZhad_narrow_M-3500_13TeV-madgraph	30000	8.8805e-04
/WprimeToWZToWhadZhad_narrow_M-4000_13TeV-madgraph	30000	2.8831e-04
/WprimeToWZToWhadZhad_narrow_M-4500_13TeV-madgraph	30000	8.8805e-05
/WprimeToWZToWhadZhad_narrow_M-5000_13TeV-madgraph	30000	-
/WprimeToWZToWhadZhad_narrow_M-5500_13TeV-madgraph	30000	-
/WprimeToWZToWhadZhad_narrow_M-6000_13TeV-madgraph	30000	-
/ZprimeToWW_narrow_M-1000_13TeV-madgraph	30000	2.297105e-01
/ZprimeToWW_narrow_M-1200_13TeV-madgraph	30000	1.249109e-01
/ZprimeToWW_narrow_M-1400_13TeV-madgraph	30000	6.836332e-02
/ZprimeToWW_narrow_M-1600_13TeV-madgraph	30000	3.843727e-02
/ZprimeToWW_narrow_M-1800_13TeV-madgraph	30000	2.221072e-02
/ZprimeToWW_narrow_M-2000_13TeV-madgraph	30000	1.314597e-02
/ZprimeToWW_narrow_M-2500_13TeV-madgraph	30000	3.840101e-03
/ZprimeToWW_narrow_M-3000_13TeV-madgraph	30000	1.213251e-03
/ZprimeToWW_narrow_M-3500_13TeV-madgraph	30000	4.015317e-04
/ZprimeToWW_narrow_M-4000_13TeV-madgraph	30000	1.360964e-04
/ZprimeToWW_narrow_M-4500_13TeV-madgraph	22176	0.440964e-04
/ZprimeToWW_narrow_M-5000_13TeV-madgraph	19320	-
/ZprimeToWW_narrow_M-5500_13TeV-madgraph	17500	-
/ZprimeToWW_narrow_M-6000_13TeV-madgraph	16618	-

B. Appendix: Cross Checks for the Signal Modeling

The utilized signal modeling relies on two separate fitting procedures: the distributions for the jet mass and the dijet invariant mass for different signal models are fitted for the simulated mass points and the parameters of these fit functions are interpolated between mass points, by fitting them in turn as functions of the available signal mass points. For each of the four signal models the masses 1200, 1400, 1600, 1800, 2000, 2500, 3000, 3500, 4000, 4500, 5000 and 5500 GeV were simulated. For each of the simulated samples three separate fits are conducted: the distribution of the jet mass of jet-1 and jet-2 as well as the dijet invariant mass distribution are fitted with a dCB function. Since a random labeling of jets in the event was adapted for the analysis, the distributions of the jet mass are almost identical between jet-1 and jet-2, except for statistical fluctuations. Since the limit calculation relies on a signal model for any mass point between 1200 and 5200 GeV the shapes obtained from MC simulation have to be further interpolated to mass points for which no MC sample was generated. This is done using polinomial fits for each dCB parameter as a function of the resonance mass m_{X}. To test this two-step procedure a goodness-of-fit test is conducted between the shapes derived from the above described procedure and a toy with 1000 signal events following the distributions from MC simulation. The results of this test are shown in Figure B.1, B.2 and B.3 for the dijet invariant mass and different signal models, showing good agreement between the modeling and the simulated distributions. Figures B.4, B.5 and B.6 show the same test for the jet mass in the HPHP category, while Figures B.7, B.8 and B.9 show the jet mass in the HPLP category.

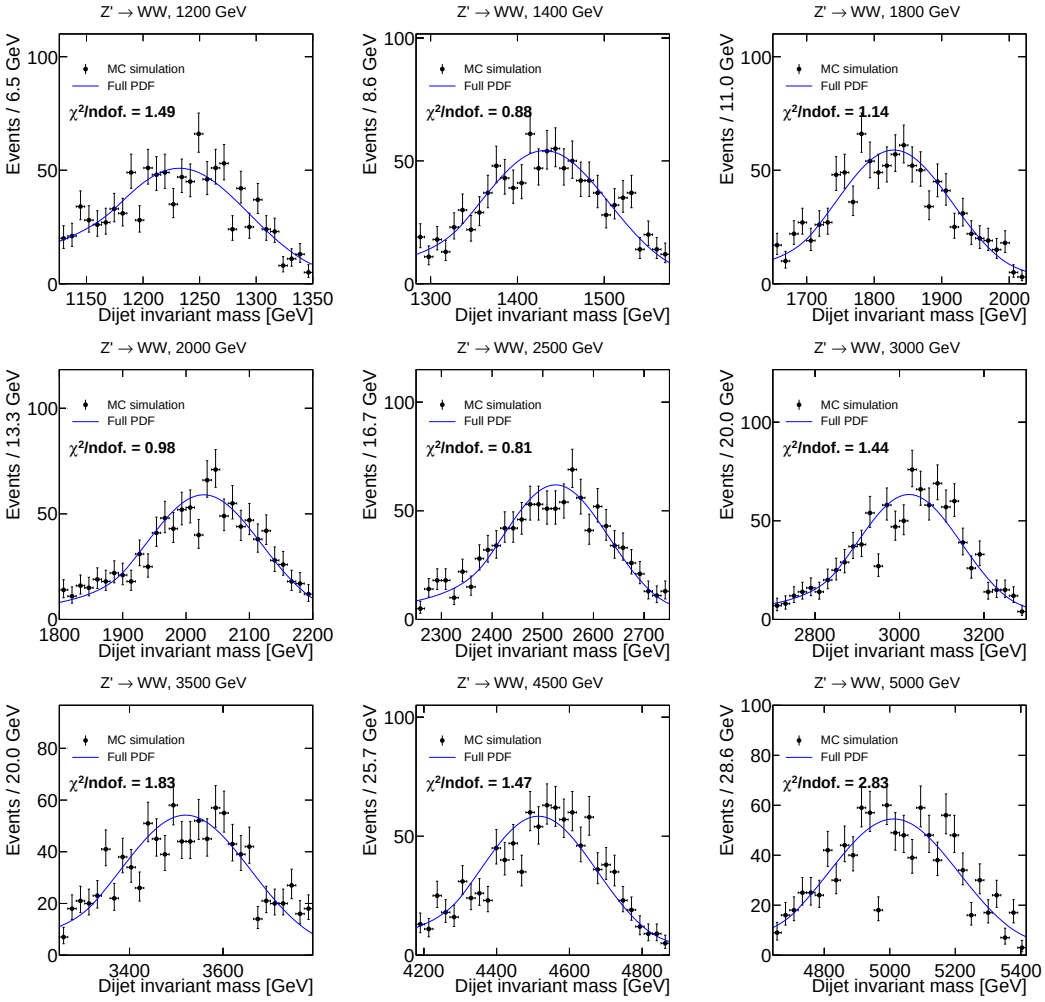

Figure B.1.: Comparison between the final signal model and the dijet invariant mass distribution from MC simulation for 1000 signal events. Note that no additional fit is carried out for this comparison. The gof test is conducted for Z′ → WW signal resonances.

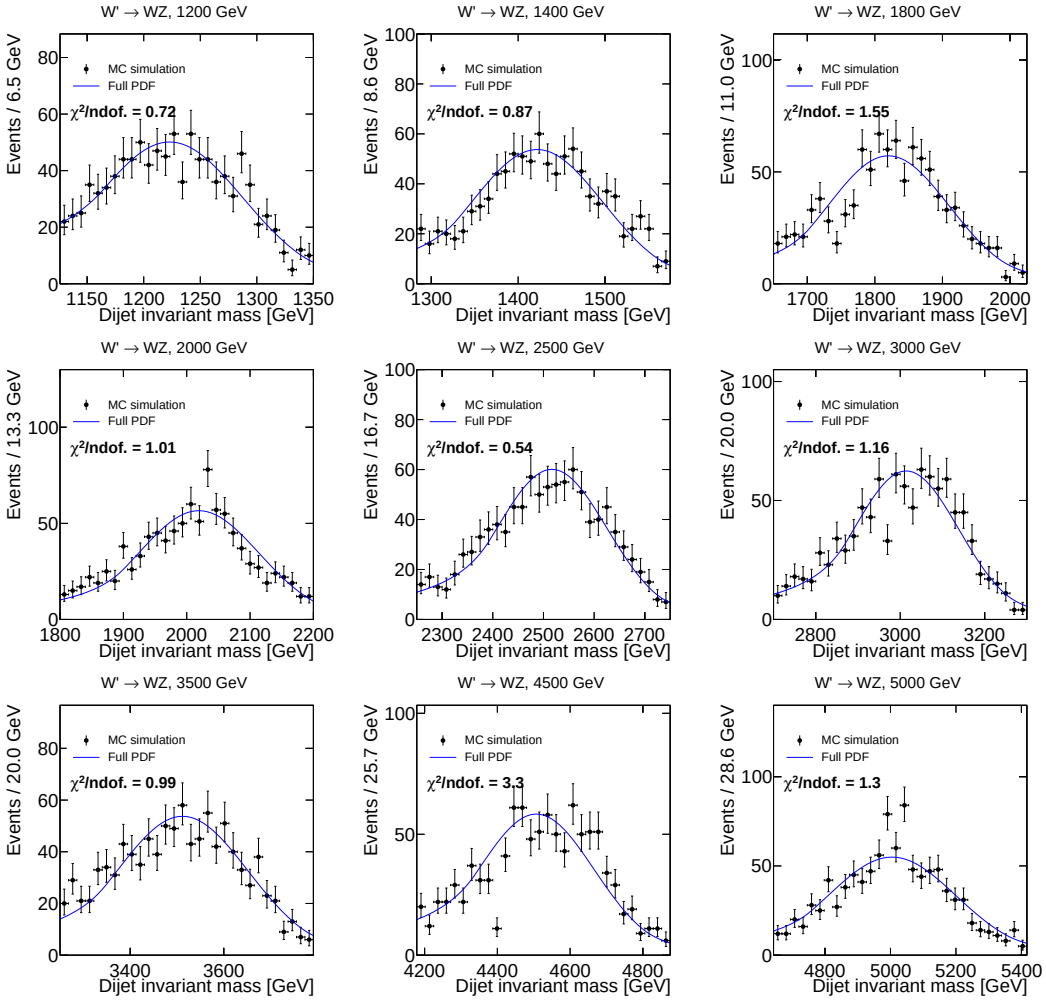

Figure B.2.: Comparison between the final signal model and the dijet invariant mass distribution from MC simulation for 1000 signal events. Note that no additional fit is carried out for this comparison. The gof test is conducted for $W' \to WZ$ signal resonances.

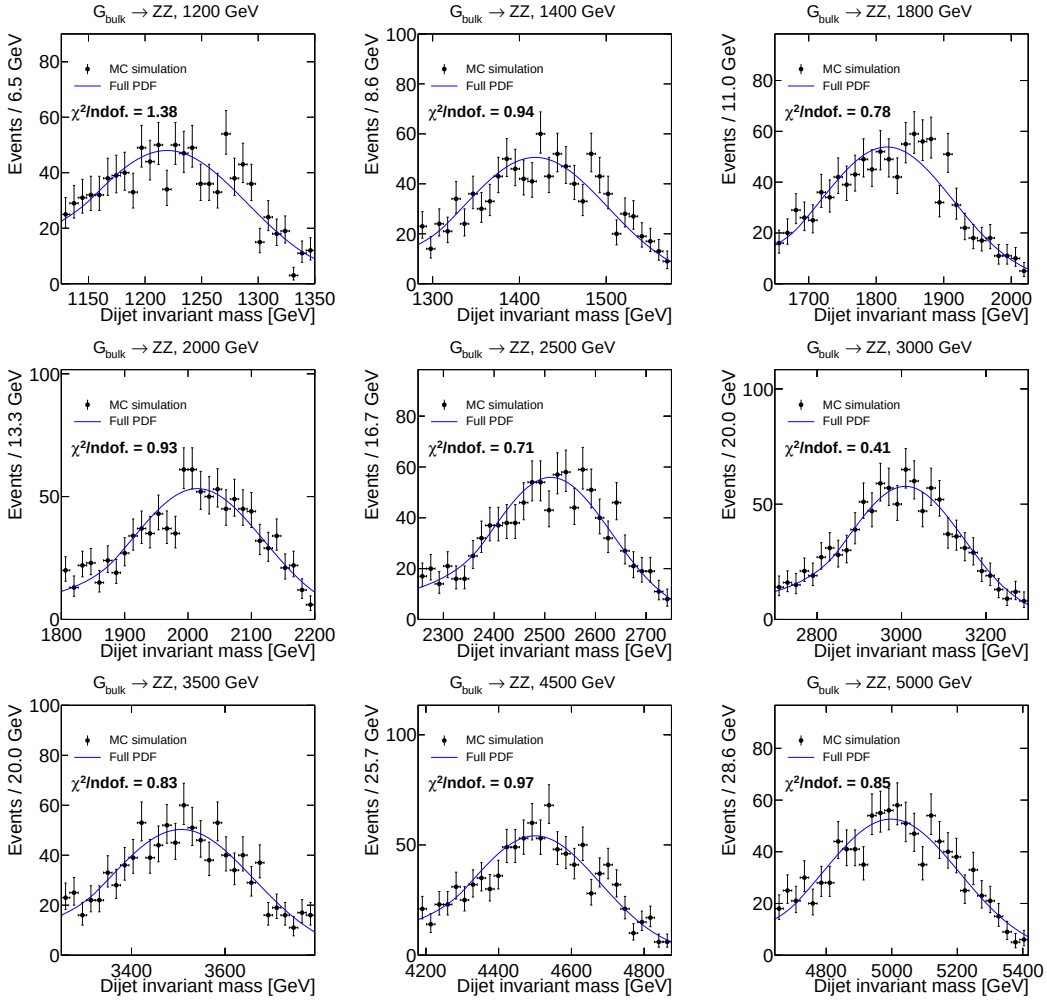

Figure B.3.: Comparison between the final signal model and the dijet invariant mass distribution from MC simulation for 1000 signal events. Note that no additional fit is carried out for this comparison. The gof test is conducted for $G_{bulk} \rightarrow ZZ$ signal resonances.

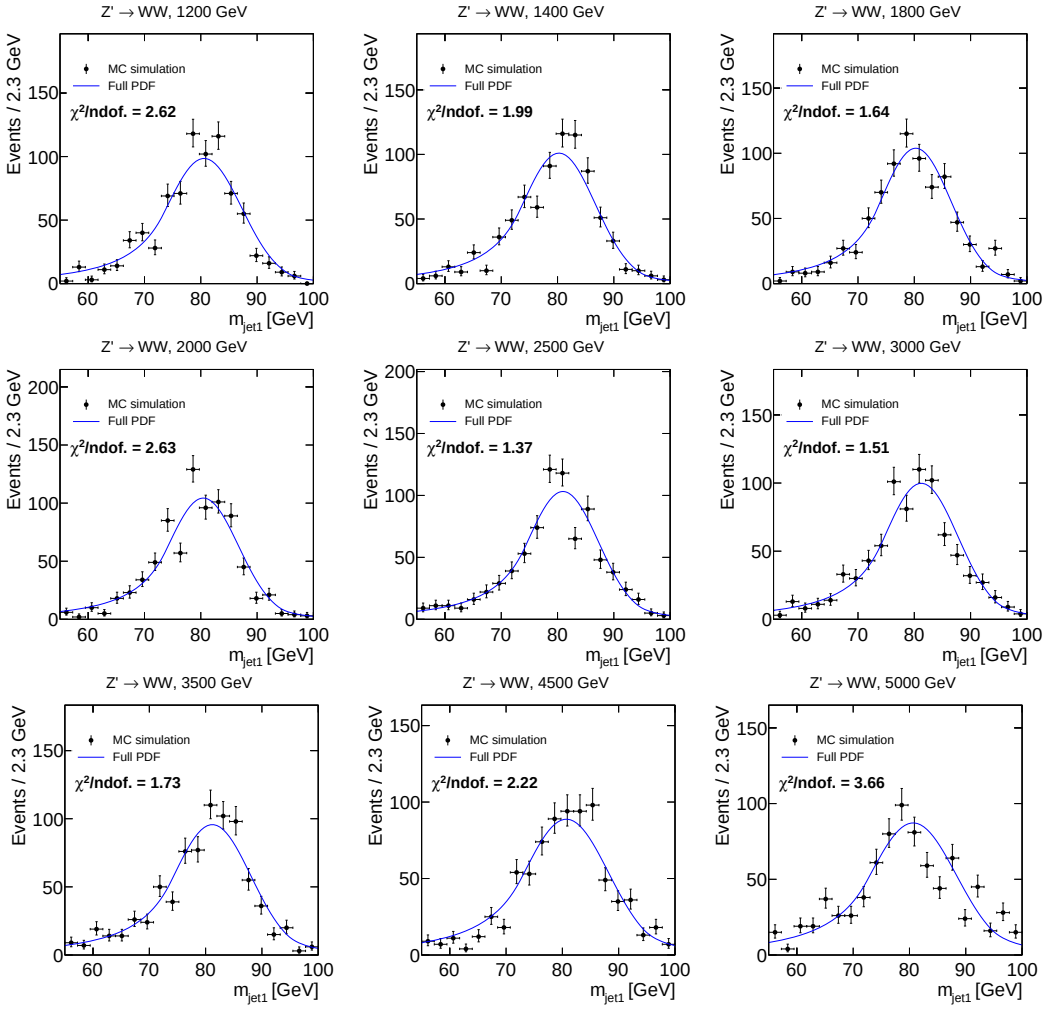

Figure B.4.: Comparison between the final signal model and the jet mass distribution from MC simulation for 1000 signal events in the HPHP category. Note that no additional fit is carried out for this comparison. The gof test is conducted for Z′ → WW signal resonances. The distibutions are shown for the jet mass of jet-1, however, due to the random labeling of jets in the event, the distributions and shapes for jet-2 are essentially the same.

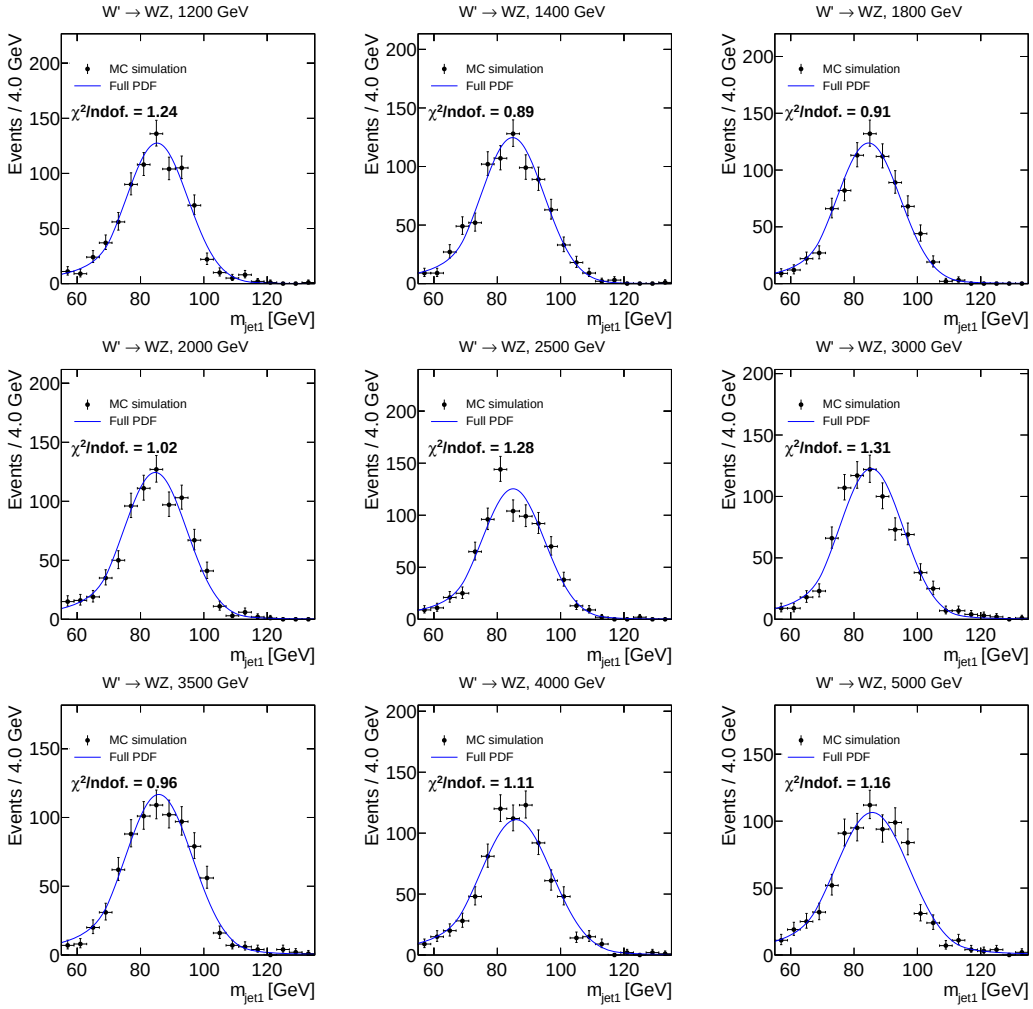

Figure B.5.: Comparison between the final signal model and the jet mass distribution from MC simulation for 1000 signal events in the HPHP category. Note that no additional fit is carried out for this comparison. The gof test is conducted for W′ → WZ signal resonances. The distibutions are shown for the jet mass of jet-1, however, due to the random labeling of jets in the event, the distributions and shapes for jet-2 are essentially the same.

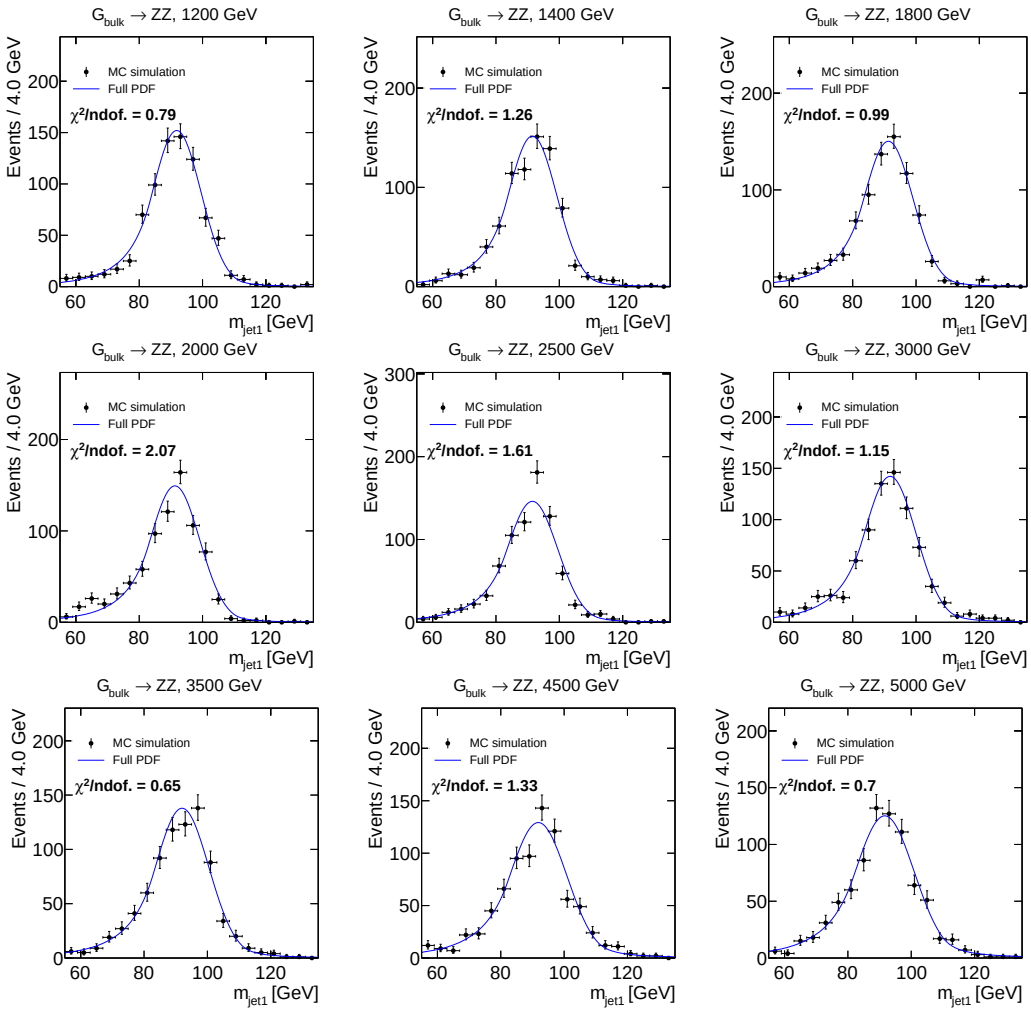

Figure B.6.: Comparison between the final signal model and the jet mass distribution from MC simulation for 1000 signal events in the HPHP category. Note that no additional fit is carried out for this comparison. The gof test is conducted for $G_{bulk} \rightarrow ZZ$ signal resonances. The distibutions are shown for the jet mass of jet-1, however, due to the random labeling of jets in the event, the distributions and shapes for jet-2 are essentially the same.

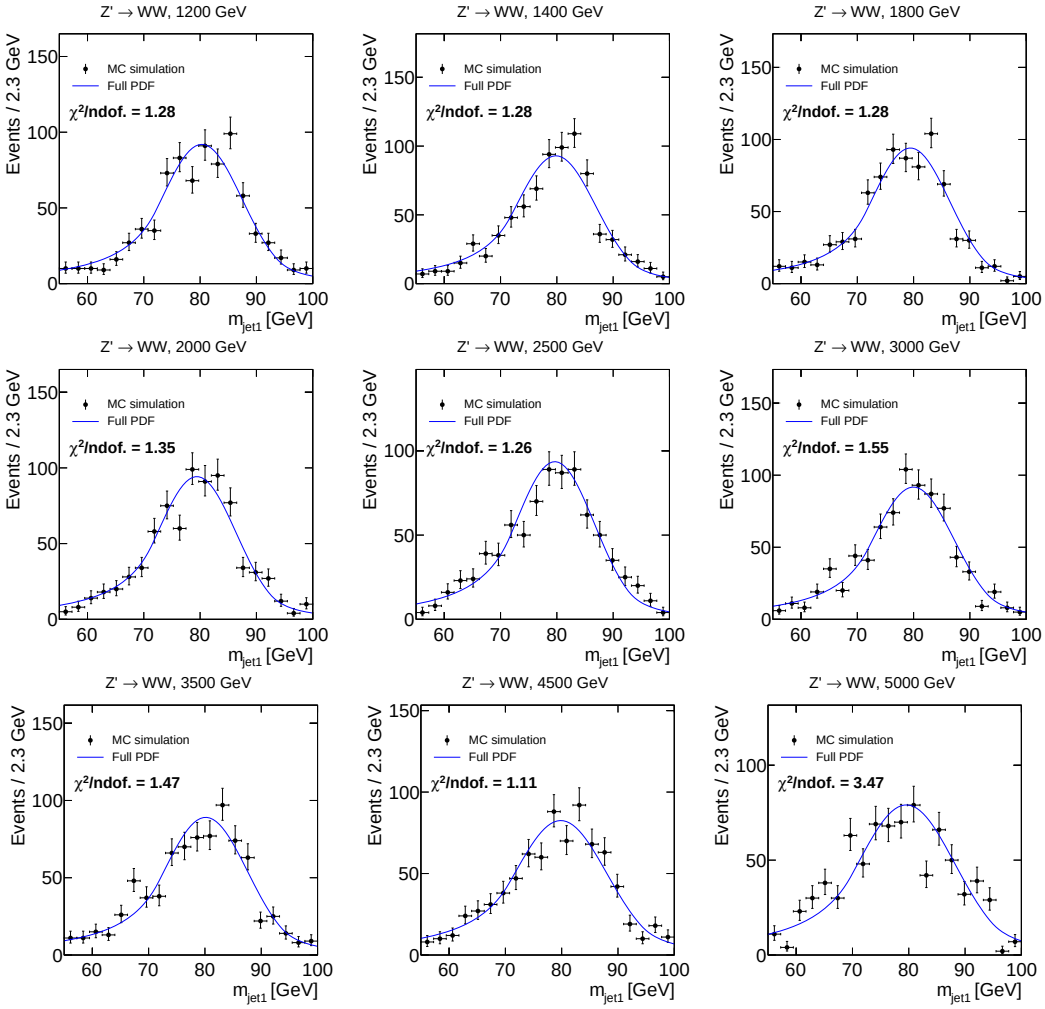

Figure B.7.: Comparison between the final signal model and the jet mass distribution from MC simulation for 1000 signal events in the HPLP category. Note that no additional fit is carried out for this comparison. The gof test is conducted for Z′ → WW signal resonances. The distibutions are shown for the jet mass of jet-1, however, due to the random labeling of jets in the event, the distributions and shapes for jet-2 are essentially the same.

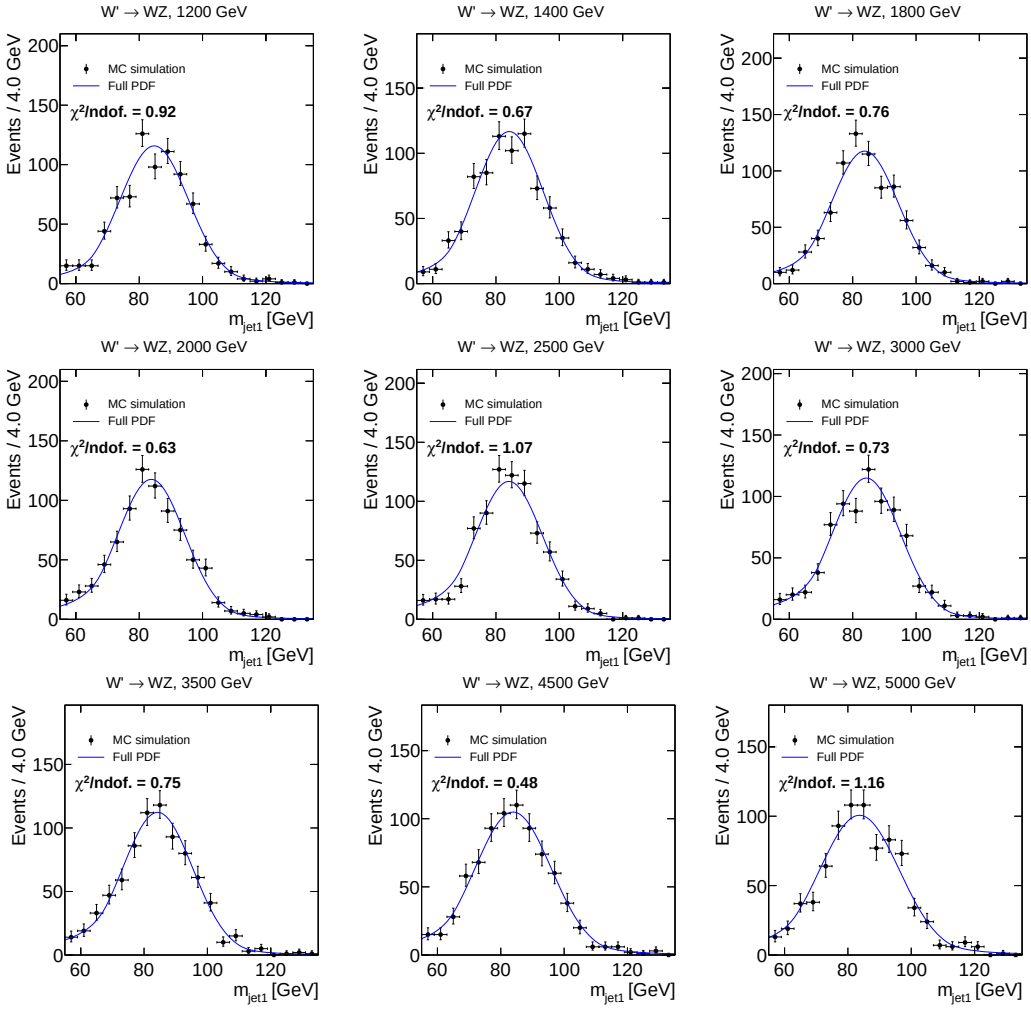

Figure B.8.: Comparison between the final signal model and the jet mass distribution from MC simulation for 1000 signal events in the HPLP category. Note that no additional fit is carried out for this comparison. The gof test is conducted for W′ → WZ signal resonances. The distibutions are shown for the jet mass of jet-1, however, due to the random labeling of jets in the event, the distributions and shapes for jet-2 are essentially the same.

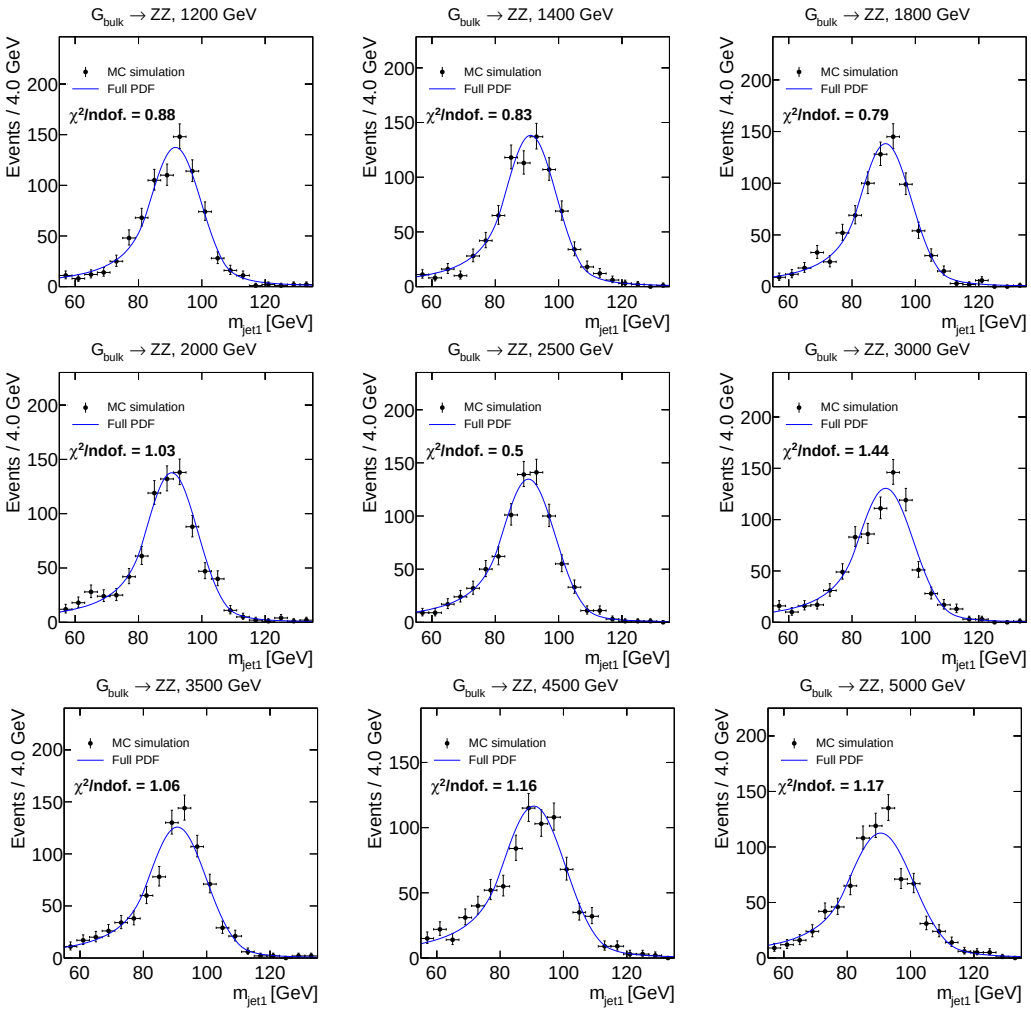

Figure B.9.: Comparison between the final signal model and the jet mass distribution from MC simulation for 1000 signal events in the HPLP category. Note that no additional fit is carried out for this comparison. The gof test is conducted for $G_{bulk} \rightarrow ZZ$ signal resonances. The distibutions are shown for the jet mass of jet-1, however, due to the random labeling of jets in the event, the distributions and shapes for jet-2 are essentially the same.

C. Appendix: Post-Fit Results in the LPLP Data Sideband

The validity of the fit method is tested in an orthogonal control-region in data, which is defined by demanding both jets to pass the purity selections of $0.43 < \tau_{21}^{\mathrm{DDT}} < 0.79$. This LPLP category allows the testing of the fitting procedure in a region that is not expected to contain any significant signal contribution. The fits shown in the following were conducted using LPLP templates built in exactly the same way as is done for the main fit in the HPLP category. However, since this category also contains only negligible amounts of the minor V+jets and $\mathrm{t\bar{t}}$ backgrounds the fits only use the model for the QCD multijet background. For these tests the data set recorded in 2016 is utilized. The projections on m_{jet1} are omitted since they are equivalent to the m_{jet2} projections except for statistical fluctuations. The corresponding ratio distribution defined as the number of events in data divided by the number of events expected from the fit is shown below each mass plot, as well as the uncertainty of the fit (yellow band).

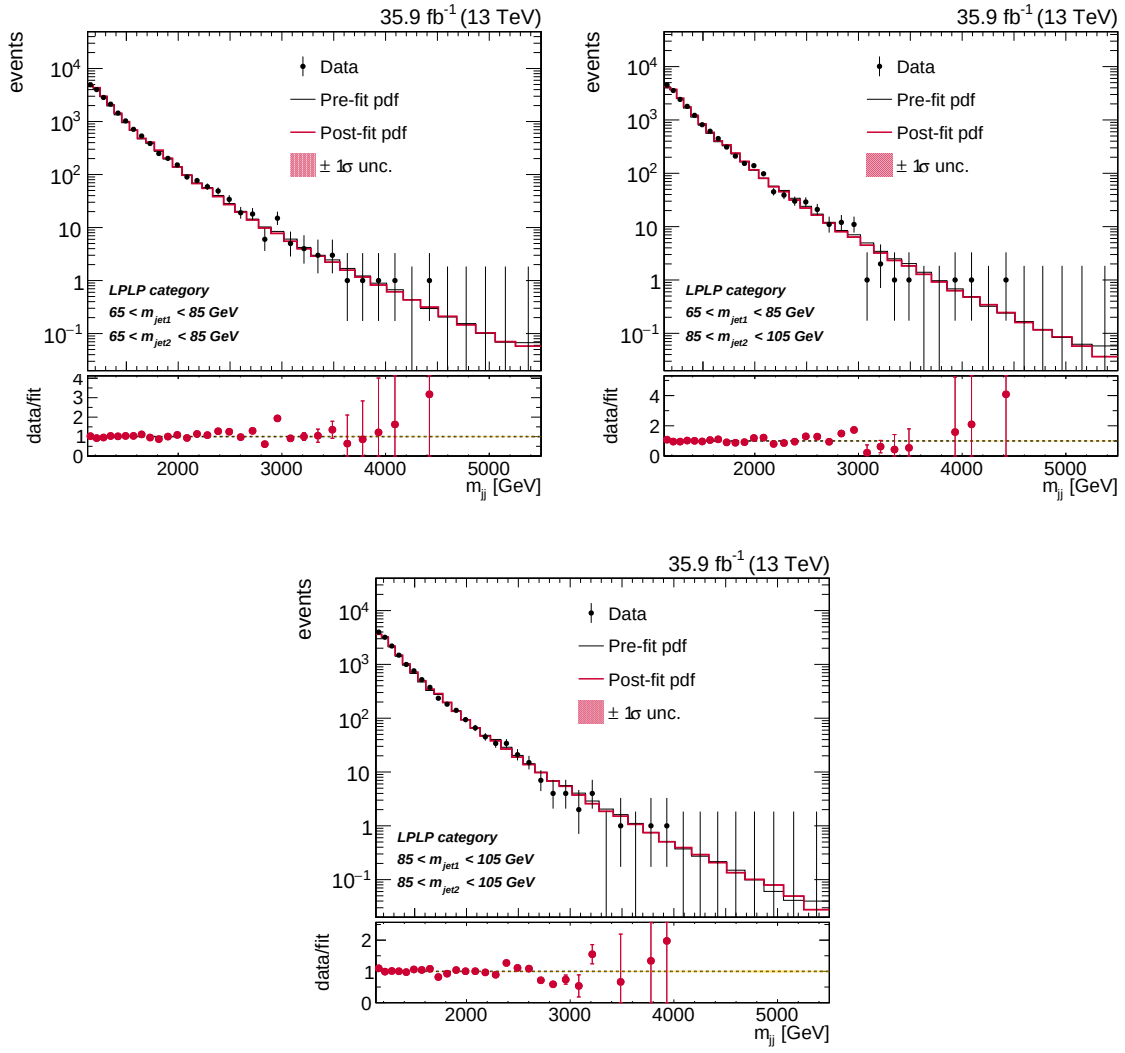

Figure C.1.: The post-fit distributions obtained from a fit to 2016 data in a low purity control region. The conditional projections on m_{jj} are shown for different regions of m_{jet1} and m_{jet2} in the signal region defined by $65 \leq m_{\mathrm{jet}} \leq 105$.

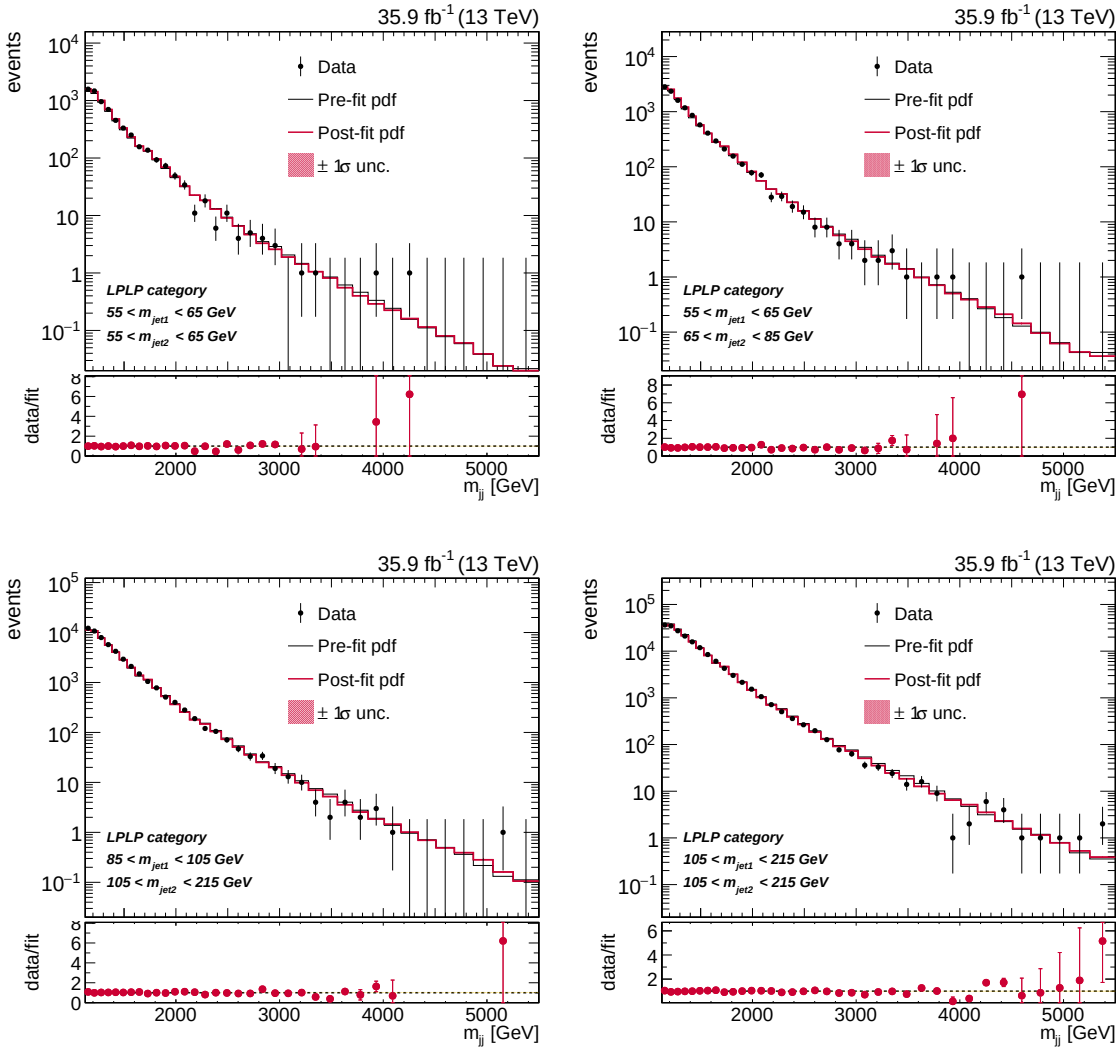

Figure C.2.: The post-fit distributions obtained from a fit to 2016 data in a low purity control region. The conditional projections on m_{jj} are shown for different regions of m_{jet1} and m_{jet2} outside of the signal region.

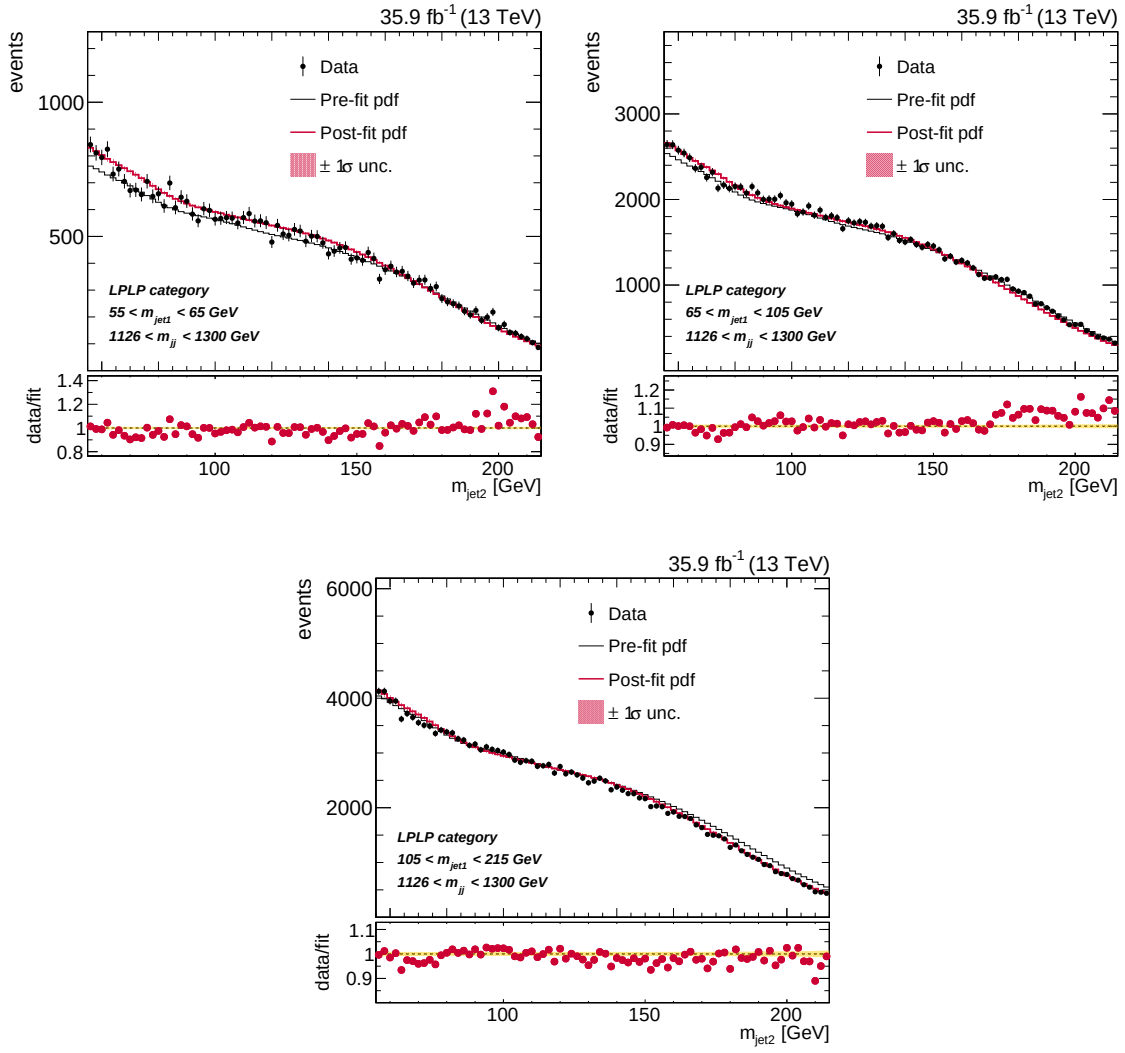

Figure C.3.: The post-fit distributions obtained from a fit to 2016 data in a low purity control region. The conditional projections of m_{jet2} are shown for m_{jj} between 1126 and 1300 GeV and slices of m_{jet1}.

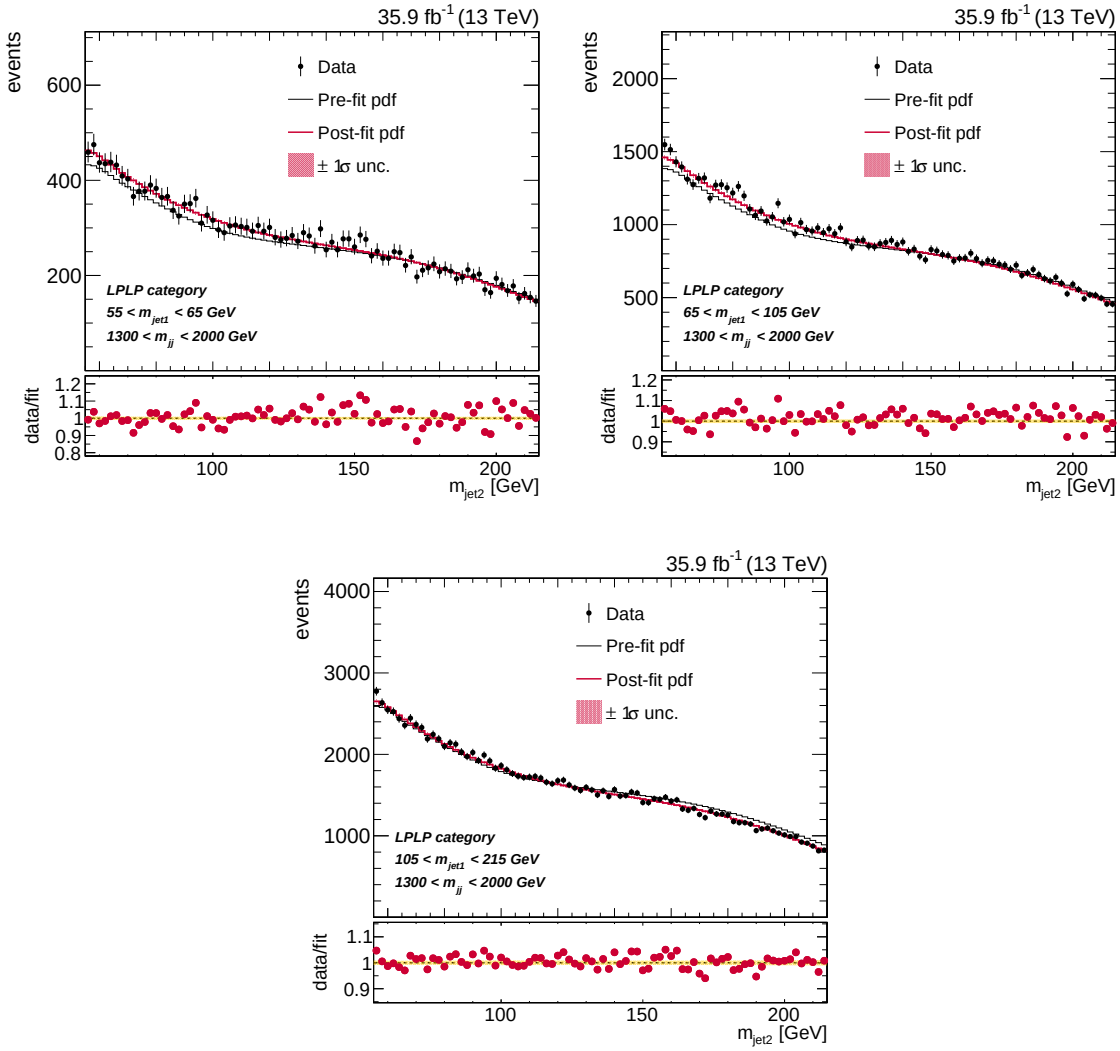

Figure C.4.: The post-fit distributions obtained from a fit to 2016 data in a low purity control region. The conditional projections of m_{jet2} are shown for m_{jj} between 1300 and 2000 GeV and slices of m_{jet1}.

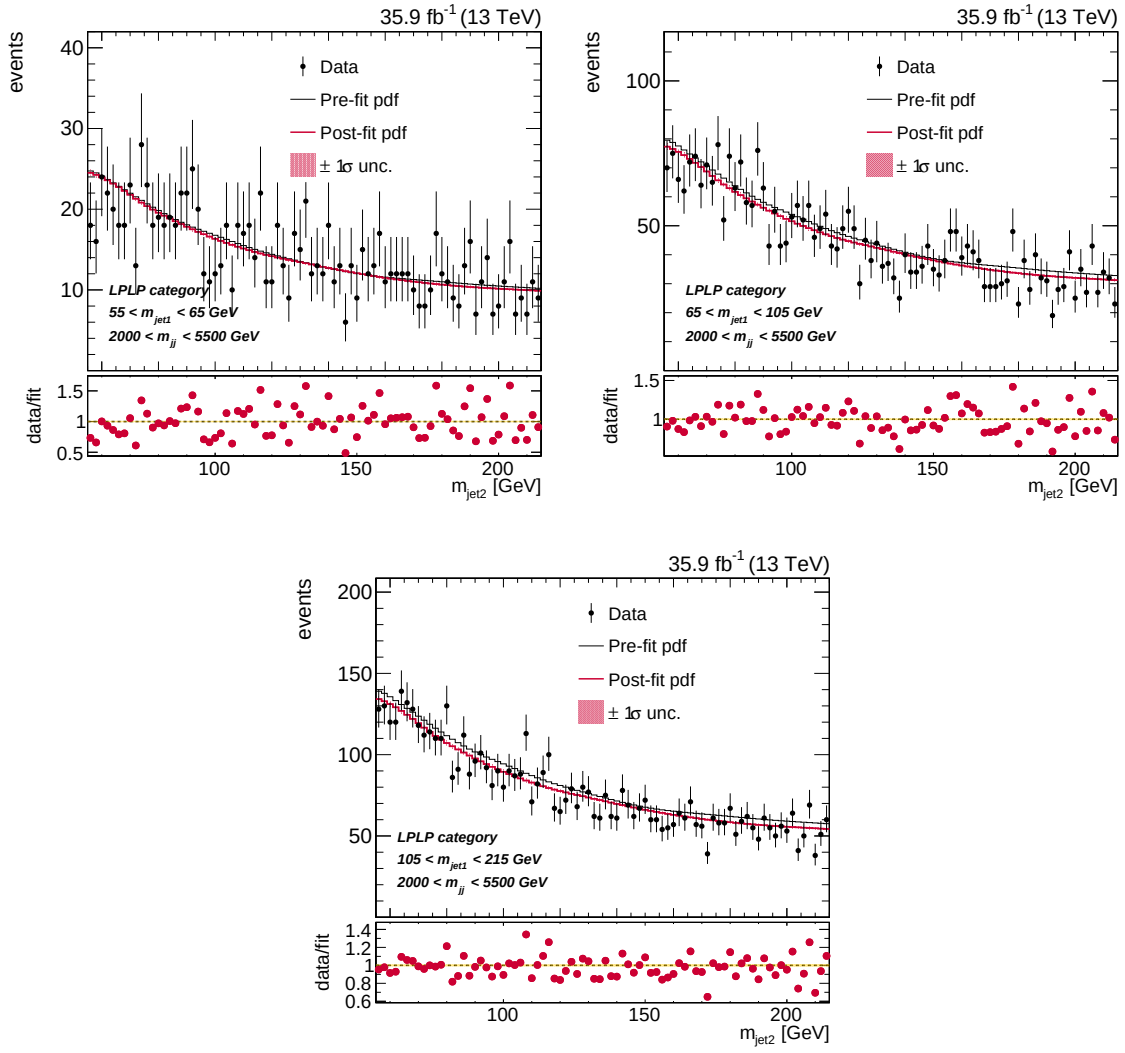

Figure C.5.: The post-fit distributions obtained from a fit to 2016 data in a low purity control region. The conditional projections of m_{jet2} are shown for m_{jj} between 2000 and 5500 GeV and slices of m_{jet1}.

D. Appendix: Tests of the Fitting Procedure

Figs. D.1 to D.4 show a fit of the full background model to the V+jets MC simulation. Projections are shown for a variety of conditional m_{jet} and m_{jj} intervals, showing good agreement between the model and MC simulation. The goodness-of-fit values for all shown projections are quoted in Table D.1.

In Figs. D.5 to D.8, the result of a signal+background fit to a background only toy is shown. The toy data distribution is generated from different MC simulation samples, namely a PYTHIA8 simulation sample in Fig. D.5, a HERWIG++ QCD multijet sample in Fig. D.6, a sample simulated using MADGRAPH5_AMC@NLO in Fig. D.7 and finally a NLO POWHEG sample shown in Fig. D.8. The background shape uncertainty is shown as a gray shaded band, and the statistical uncertainties of the data or pseudo-data are shown as vertical bars. The corresponding pull distribution (Data-fit)/σ is shown below each mass plot, where $\sigma = \sqrt{\sigma^2_{\text{data}} - \sigma^2_{\text{fit}}}$ for each bin in order to ensure a Gaussian distribution of pulls [180].

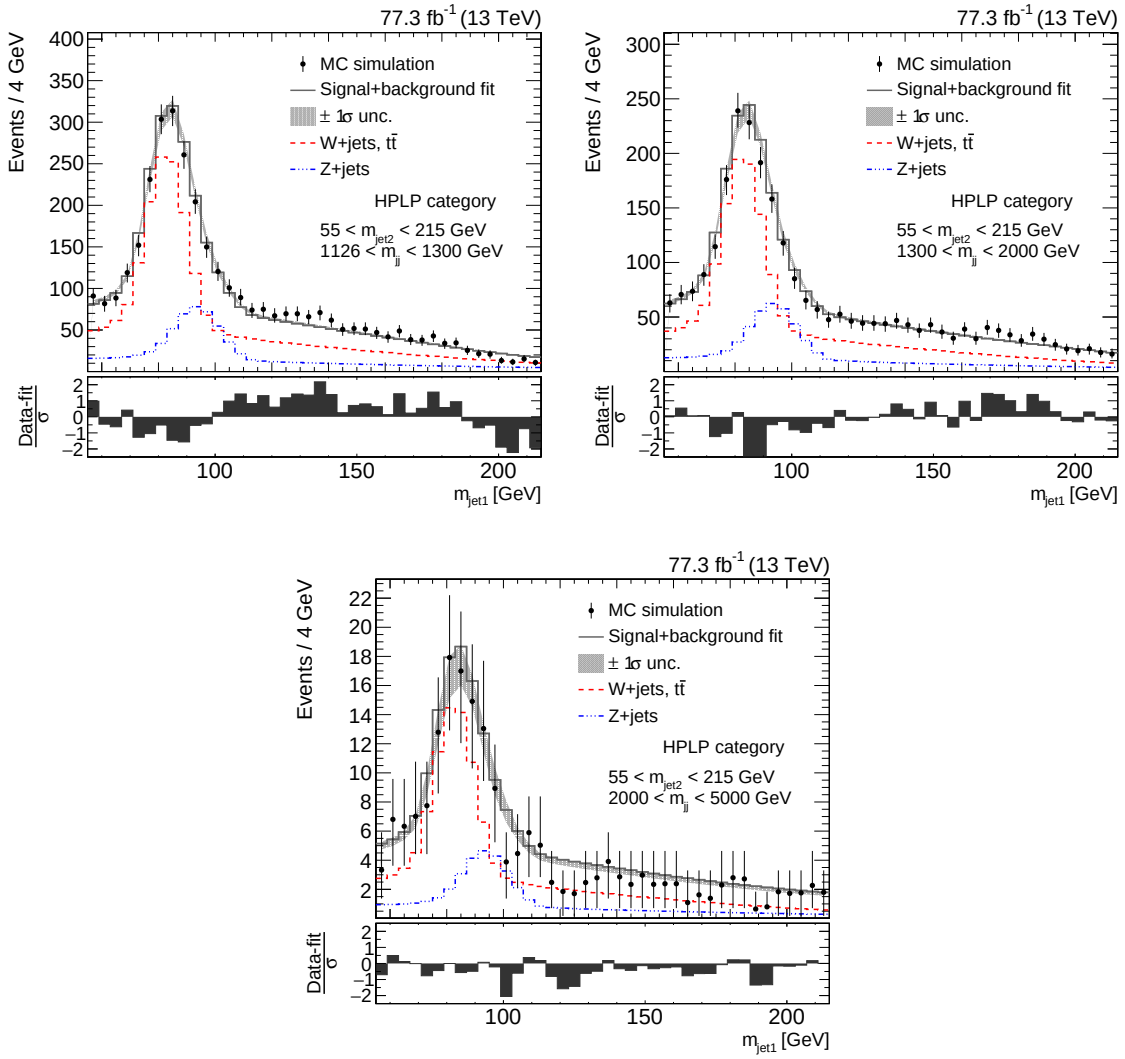

Figure D.1.: Conditional projections on m_{jet1} for the post-fit distribution of the complete background model (gray line) to the MC simulation of the V+jets backgrounds (black markers) for the low purity category. Shown here are conditional projections for different slices in the dijet invariant mass.

Table D.1.: The results of goodness-of-fit tests for different projections of the three-dimensional phase-space using the background model for V+jets processes fitted to the corresponding distribution in MC simulation. The results of a χ^2 test are shown for different conditional projections of the three-dimensional phase space.

projection	m_{jet1} (GeV)	m_{jet2} (GeV)	m_{jj} (GeV)	χ^2/ndof	p-value (%)
m_{jj}	55-215	55-215	2000-5000	0.30	99.815
m_{jet1}	55-215	55-215	2000-5000	0.39	99.979
m_{jet2}	55-215	55-215	2000-5000	0.47	99.81
m_{jj}	55-215	55-215	1300-2000	0.26	98.434
m_{jet1}	55-215	55-215	1300-2000	0.58	98.365
m_{jet2}	55-215	55-215	1300-2000	0.59	98.248
m_{jj}	55-215	55-215	1126-1300	0.72	54.155
m_{jet1}	55-215	55-215	1126-1300	1.11	28.95
m_{jet2}	55-215	55-215	1126-1300	0.82	78.376
m_{jj}	55-105	55-105	1126-5500	0.52	98.718
m_{jet1}	55-105	55-105	1126-5500	1.08	36.776
m_{jet2}	55-105	55-105	1126-5500	0.80	65.626
m_{jj}	55-105	105-215	1126-5500	0.26	99.999
m_{jet1}	55-105	105-215	1126-5500	0.52	91.307
m_{jet2}	55-105	105-215	1126-5500	0.94	55.404
m_{jj}	55-105	55-65	1126-5500	0.381	99.773
m_{jet1}	55-105	55-65	1126-5500	0.264	99.59
m_{jet2}	55-105	55-65	1126-5500	0.330	80.365
m_{jj}	55-215	105-215	1126-5500	0.53	98.404
m_{jet1}	55-215	105-215	1126-5500	1.67	0.519
m_{jet2}	55-215	105-215	1126-5500	0.95	53.487
m_{jj}	55-215	85-105	1126-5500	0.326	99.977
m_{jet1}	55-215	85-105	1126-5500	0.732	89.463
m_{jet2}	55-215	85-105	1126-5500	1.06	38.553
m_{jj}	55-215	65-85	1126-5500	0.2702	99.997
m_{jet1}	55-215	65-85	1126-5500	0.517	99.508
m_{jet2}	55-215	65-85	1126-5500	0.296	93.898
m_{jj}	55-215	55-65	1126-5500	0.398	99.733
m_{jet1}	55-215	55-65	1126-5500	0.356	99.994
m_{jet2}	55-215	55-65	1126-5500	1.259	28.651
m_{jj}	55-215	55-215	1126-5500	0.331	99.987
m_{jet1}	55-215	55-215	1126-5500	1.061	36.638
m_{jet2}	55-215	55-215	1126-5500	0.930	59.714
		HPHP			
m_{jj}	55-215	55-215	1126-5500	0.155	100.0
m_{jet1}	55-215	55-215	1126-5500	0.425	99.946
m_{jet2}	55-215	55-215	1126-5500	0.394	99.979

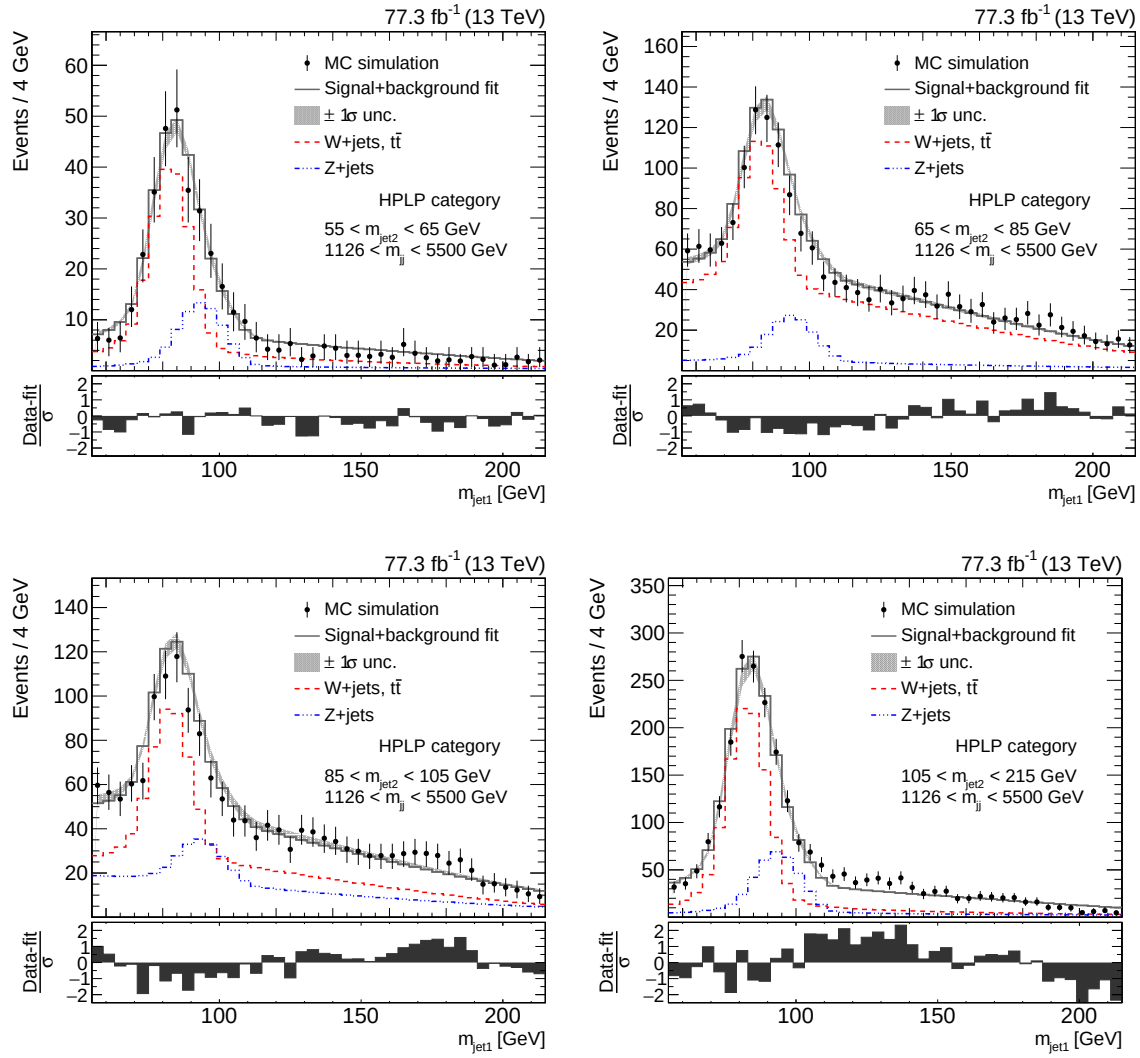

Figure D.2.: Conditional projections on m_{jet1} for the post-fit distribution of the complete background model (gray line) to the MC simulation of the V+jets backgrounds (black markers) for the low purity category.

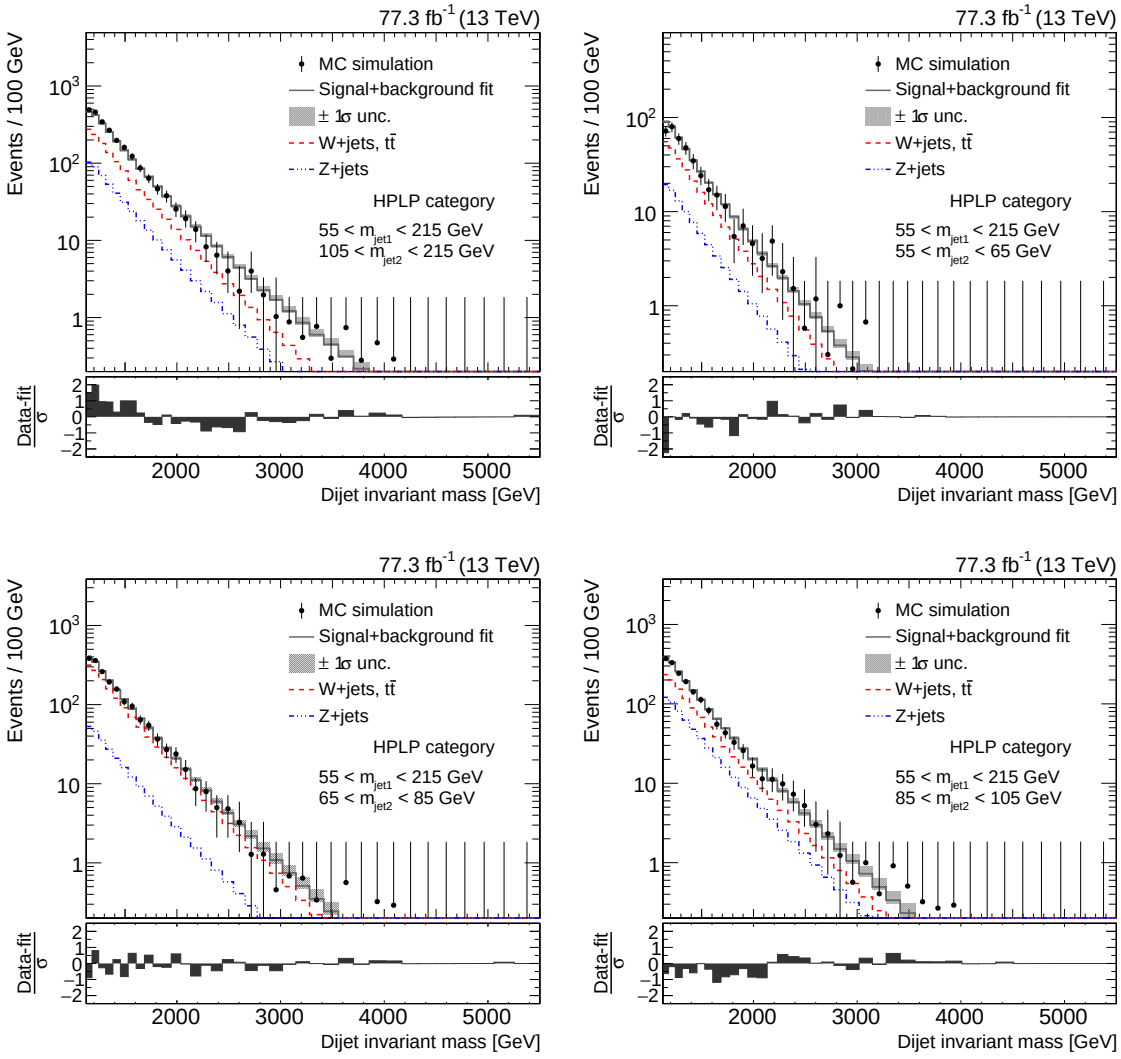

Figure D.3.: Conditional projections on m_{jj} for the post-fit distribution of the complete background model (gray line) to the MC simulation of the V+jets backgrounds (black markers) for the low purity category. The projections on the dijet invariant mass for different slices of m_{jet2} are shown.

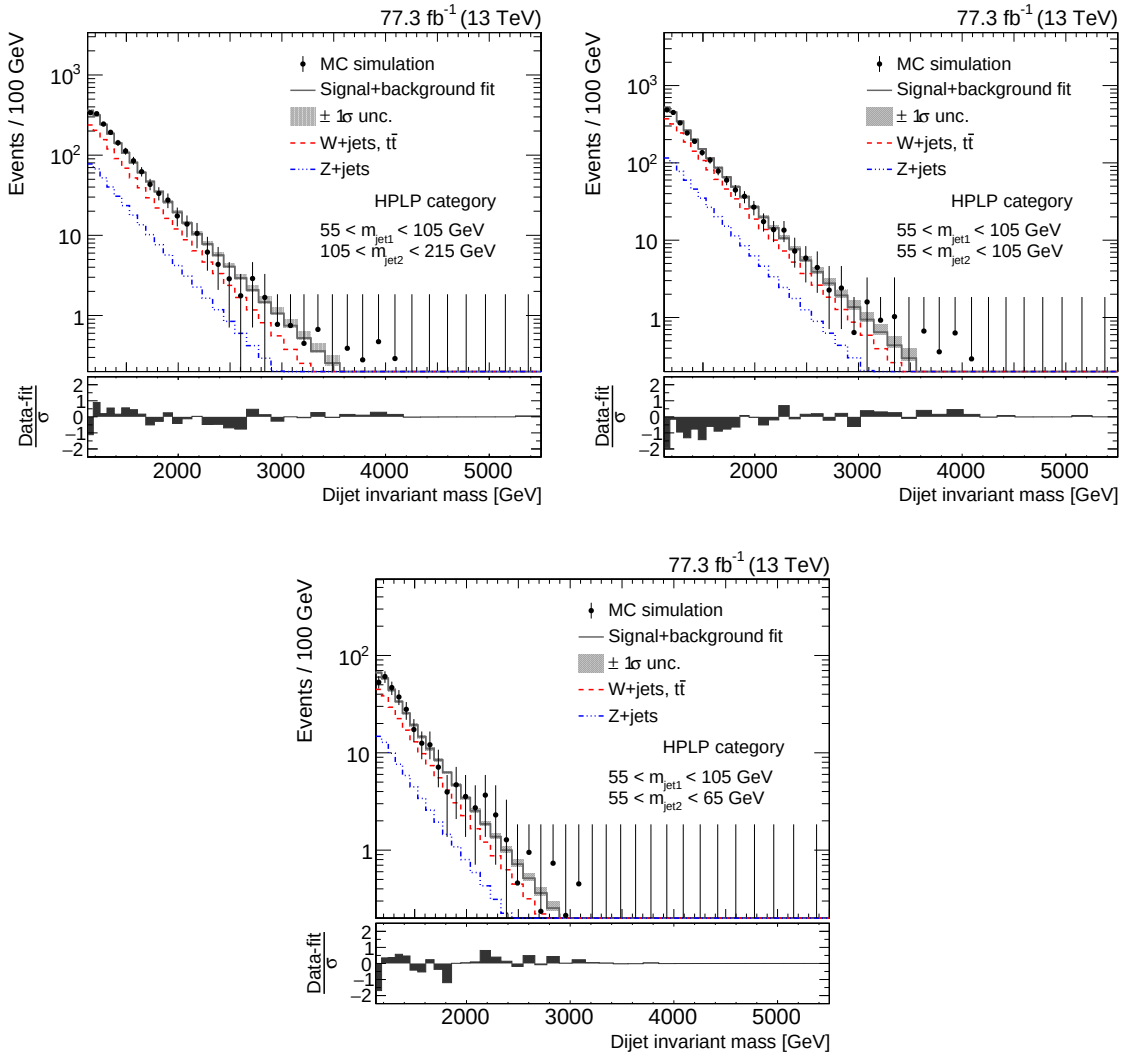

Figure D.4.: Conditional projections on m_{jj} for the post-fit distribution of the complete background model (gray line) to the MC simulation of the V+jets backgrounds (black markers) for the low purity category. The projections on the dijet invariant mass for different slices of m_{jet1} and m_{jet2} are shown.

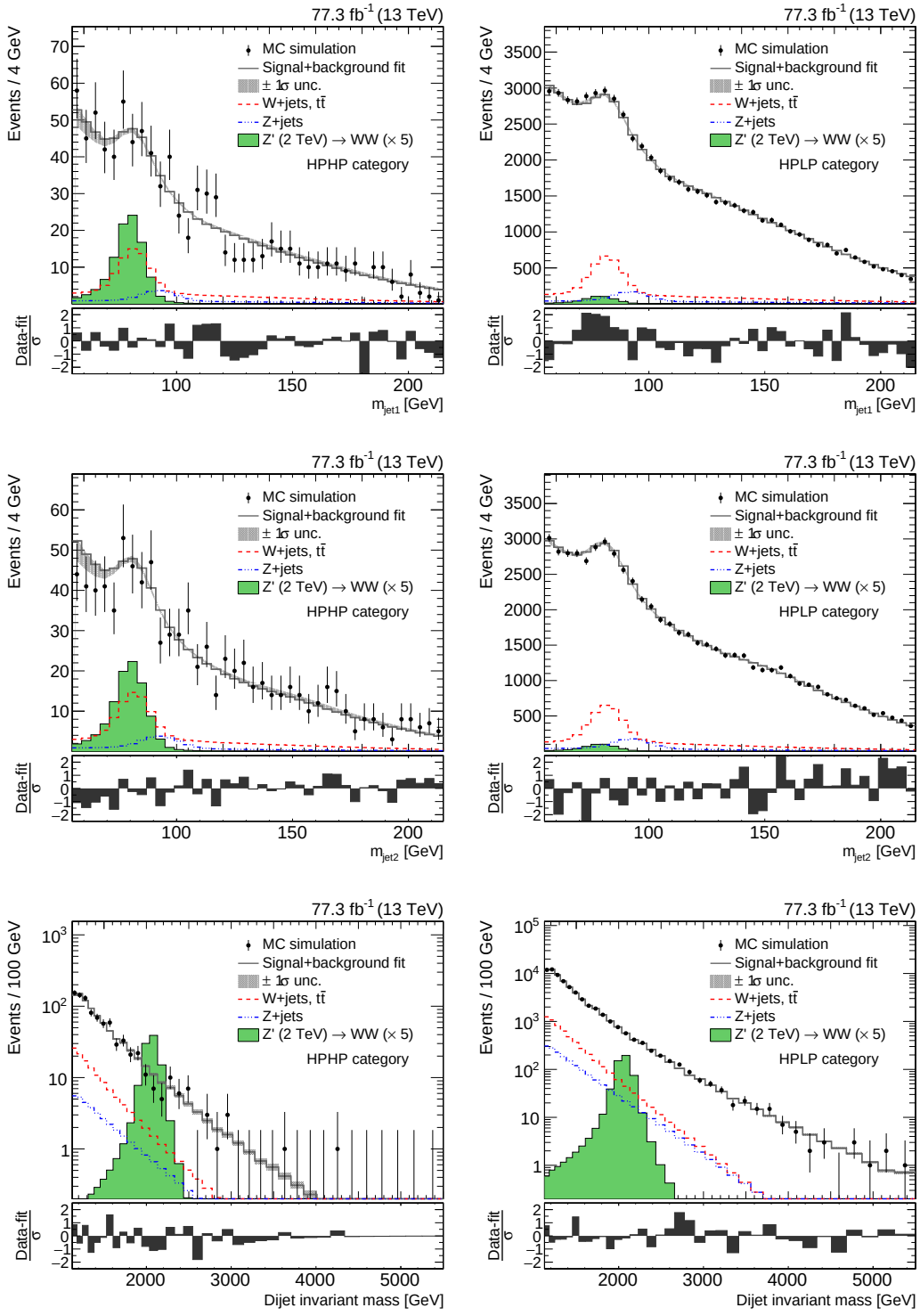

Figure D.5.: Distributions obtained from a combined fit to 2016 and 2017 toy data sets generated following the distribution derived from a QCD PYTHIA8 multijet sample. The projections of m_{jet1} (top), m_{jet2} (middle) and m_{jj} (bottom) are shown separately for the HPHP (left) and HPLP (right) category.

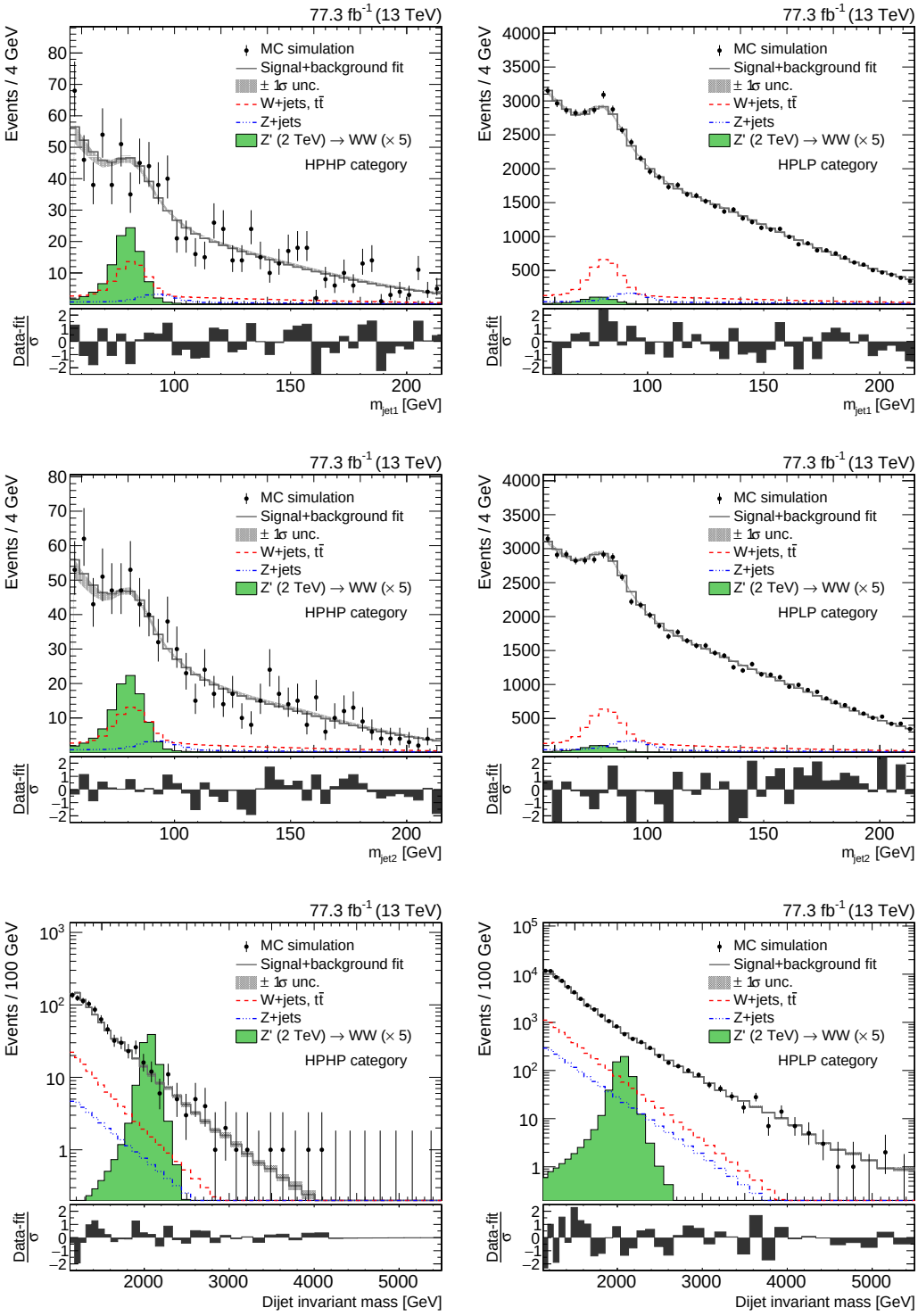

Figure D.6.: Distributions obtained from a combined fit to 2016 and 2017 toy data sets generated following the distribution derived from a QCD HERWIG++ multijet sample. The projections of m_{jet1} (top), m_{jet2} (middle) and m_{jj} (bottom) are shown separately for the HPHP (left) and HPLP (right) category.

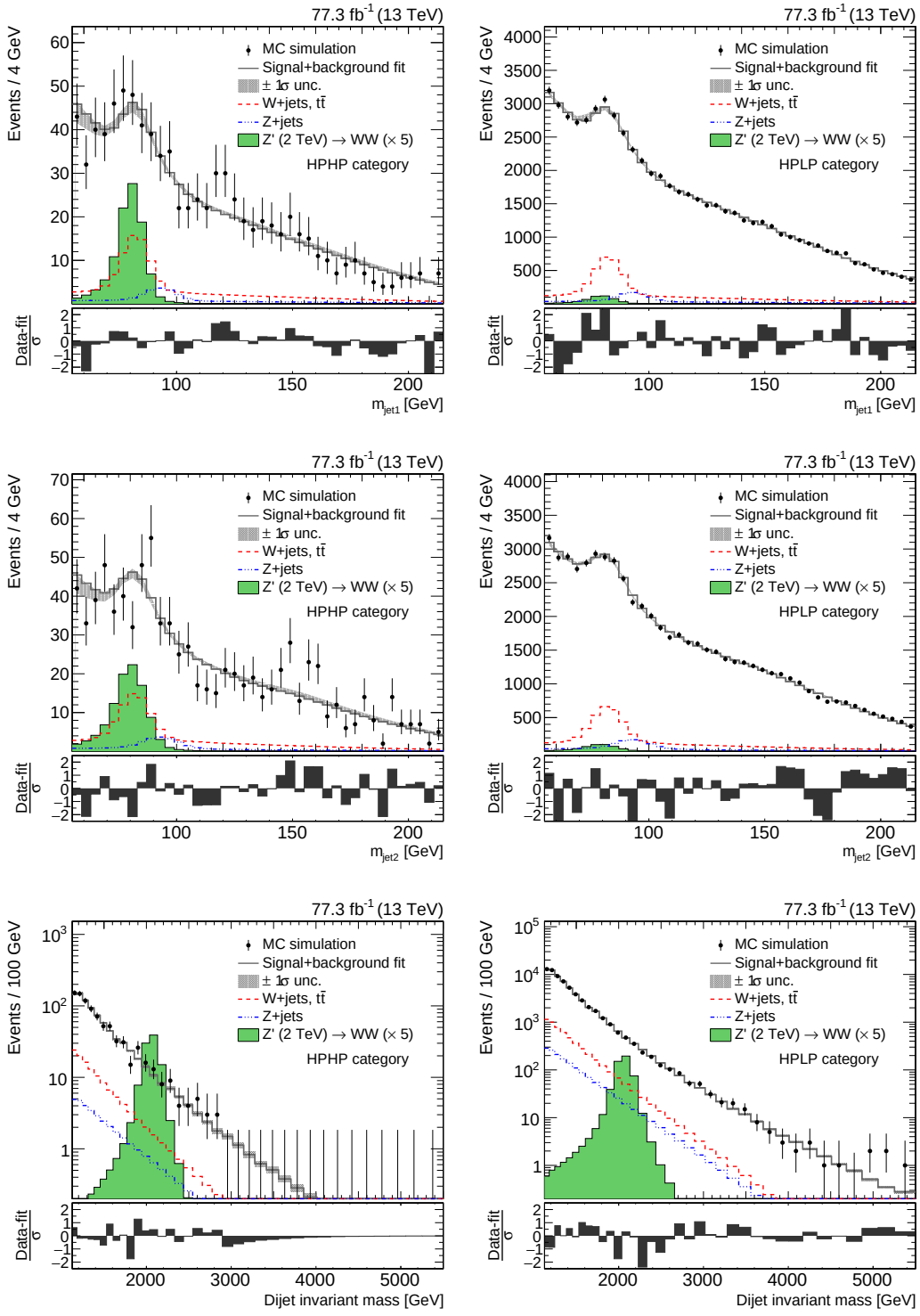

Figure D.7.: Distributions obtained from a combined fit to 2016 and 2017 toy data sets generated following the distribution derived from a QCD MADGRAPH5_AMC@NLO multijet sample. The projections of m_{jet1} (top), m_{jet2} (middle) and m_{jj} (bottom) are shown separately for the HPHP (left) and HPLP (right) category.

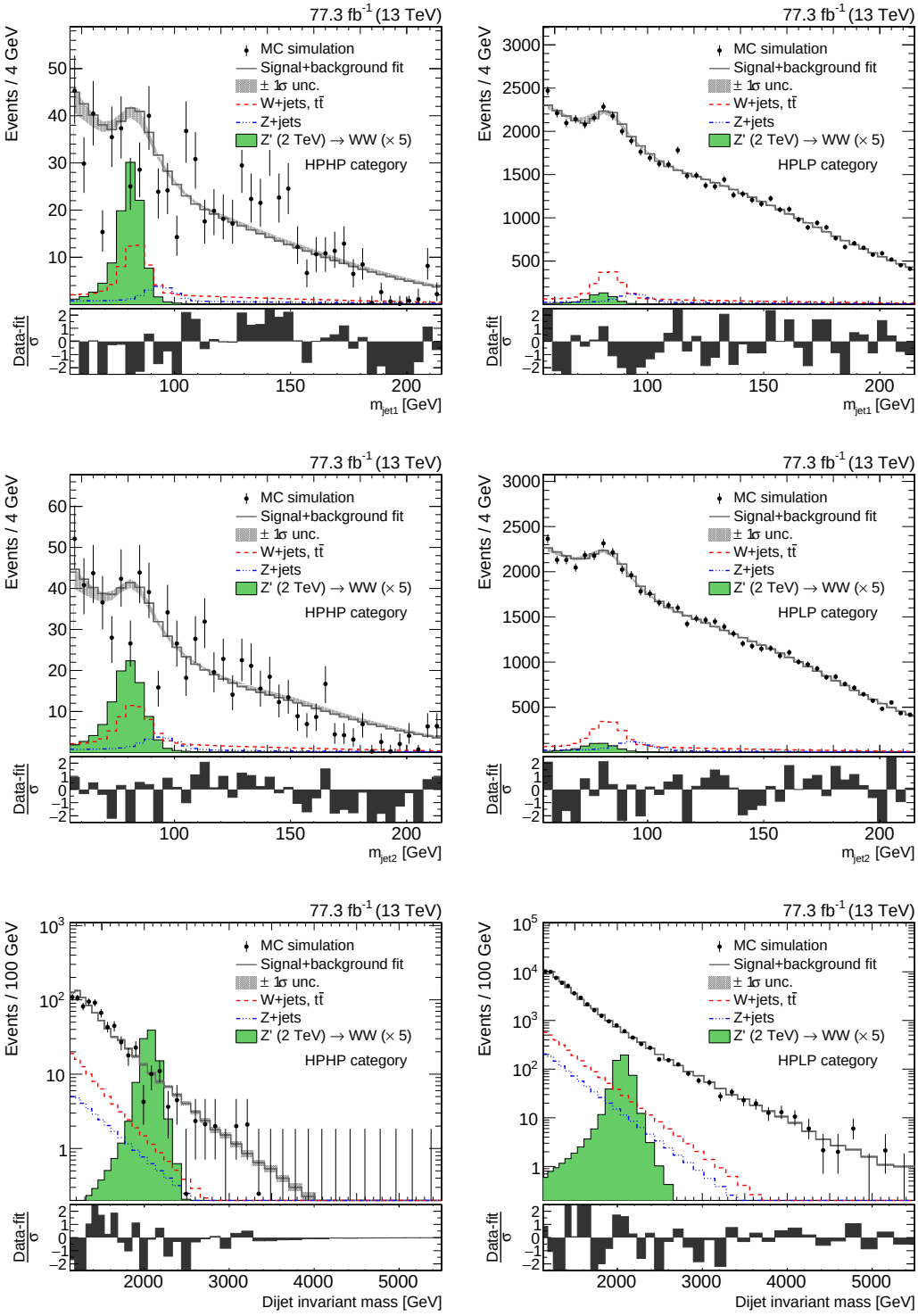

Figure D.8.: Distributions obtained from a combined fit to 2016 and 2017 toy data sets generated following the distribution derived from a QCD POWHEG multijet sample. The projections of m_{jet1} (top), m_{jet2} (middle) and m_{jj} (bottom) are shown separately for the HPHP (left) and HPLP (right) category.

E. Appendix: Results of a previous Diboson Search Utilizing a Different Background Estimation Method with 35.9 fb^{-1} of Data Recorded in 2016

Previous results for searches for heavy resonances decaying to VV or Vq in the all-jets final state were obtained with a different methodology, see Ref. [35] for more detail. As in the main analysis discussed in this thesis, the vector bosons are assumed to be highly boosted, thus large-radius AK8 jets are used in the reconstruction of events. The analysis briefly described here and detailed in Ref. [35] also utilizes substructure techniques for the tagging of events, specifically a double- and single-tag category are defined depending on whether one or two jets need to pass τ_{21} selection cuts. This enables the search for diboson resonances and resonances of the form $X \to q\mathrm{V}$, which can arise in the context of excited quark (q*) models. In this Vq channel the quark jet candidate is not subjected to a groomed mass or substructure based selection.

Jets used in the analysis are required to have a $p_\mathrm{T} > 200\,\mathrm{GeV}$, an angular separation $\Delta R > 0.8$ from any leptons in the event, and the two selected jets need a separation of $|\Delta\eta_{jj}| < 1.3$. The invariant dijet mass is required to be larger than 1050 GeV in order to reach the trigger plateau, see Figure E.1.

To further enhance the analysis sensitivity high-purity (HP) V-jets are selected by requiring $\tau_{21} \leq 0.35$, and low-purity (LP) V-jets are selected by requiring $0.35 < \tau_{21} < 0.75$. These working points are chosen to optimize the significance of the search for mass points below 2.5 (2.2) TeV in the double- (single-) tag region, where the significance achieved with this selection is within 10% of the maximal significance attained using the optimal selection value for each mass point. The second threshold of 0.75 is chosen to retain $> 95\%$ of signal events thus ensuring that the expected significance at high invariant masses is close to maximal. Events in the Vq channel are classified according to these two categories. For the VV channel, events are required to have at least one HP-tagged V-jet, and are divided into high purity (HPHP) or low purtiy (HPLP) events, depending on whether the other V-jet is HP or LP tagged.

The V-jets are further classified according to their jet mass, where the V-jet is considered a W candidate if its jet mass falls between $65 - 85\,\mathrm{GeV}$ and a Z boson candidate if its jet mass falls between $85 - 105\,\mathrm{GeV}$. All jets with a V tag are required to fall into one of the two categories. Because of jet mass resolution effects, up to 30% of W (Z) bosons are reconstructed in the Z (W) mass window. For this reason, all categories are combined in the limit setting procedure independent of the model prediction. Figure E.2 shows a comparison

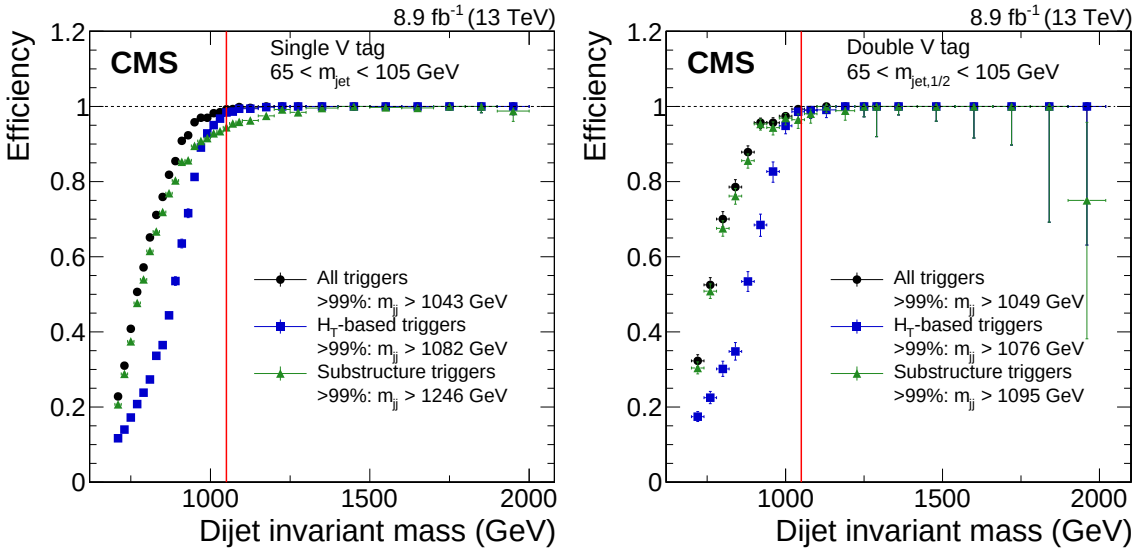

Figure E.1.: The trigger efficiency as a function of the dijet invariant mass of the two jets with highest transverse momenta in the event. The efficiency for the single-tag category is shown on the left, the one for the double-tag category on the right. The green triangle denotes the event selection efficiency using only substucture based triggers, the blue rectangles denote the event selection efficiency using only H_{T} based triggers, and the black circles denote the efficiency when all triggers are combined. Figure published in Ref. [35].

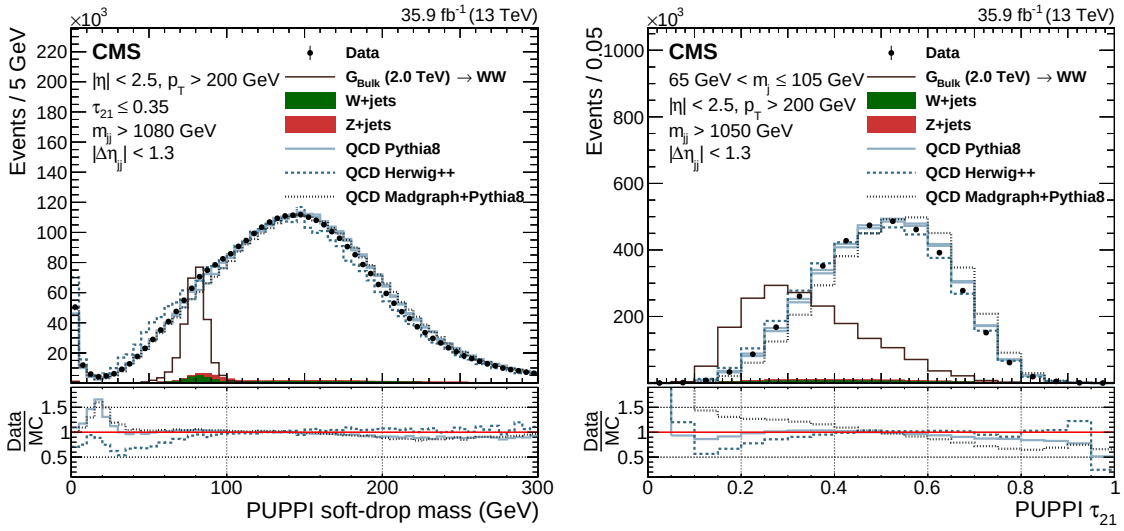

Figure E.2.: Comparison between data and different MC simulated samples for QCD multijet processes. Figure published in Ref. [35].

between data and MC simulated samples of background processes for the jet mass of the jet with the highest transvese momentum (left) and the τ_{21} distribution (right). The jet mass distribution is shown with a cut on τ_{21} $\leq$0.35 applied, thus showing an explicit mass sculpting for the QCD multijet background processes.

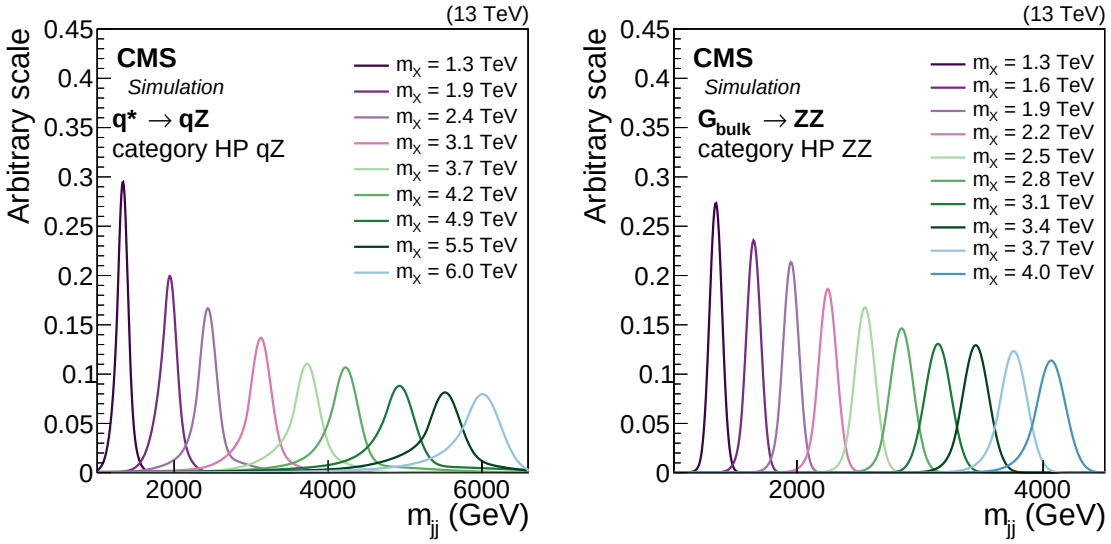

Figure E.3.: The fit results for the signal shapes in the single- (left) and double-tag (right) categories. The shapes are shown for an examplary q$*$ $\rightarrow$ qZ and a G_{bulk} $\rightarrow$ ZZ signal process. Figure published in Ref. [35].

The final categorization in purity and mass categories (WW, WZ, ZZ, qW, and qZ) yields a total of six orthogonal classes of events for the double-tag analysis and four classes of events for the single-tag analysis.

The invariant mass of the dijet system is further calculated. The presence of signal events can be inferred from the observation of a localized excess in the dijet invariant mass (m_{jj}) distribution. The signal is modeled with a dCB function, while the m_{jj} background distribution is modeled using either a monotonically falling function with two, or three parameters, in a completely data-driven approach. Figure E.3 shows the modeling of the signal shapes used in the analysis, for both single- and double-tag categories separately. To parametrize shapes for possible mass points for which no MC simulation was generated, the dijet invariant mass distributions are interpolated between the available mass points, utilizing a cubic interpolation between histograms generated with available mass points. The resulting histograms are then fitted using a dCB function.

Neither data control regions nor simulated background samples are used directly by this method, however, the chosen fit functions and the number of parameters used in each category are determined based on a Fisher F-test with 10% CL utilizing a data control region, defined by both jets failing all purity selections, as well as on QCD multijet events in simulation. The final analytical functions used for the modelling of the backgrounds are of the form

$$\frac{dN}{dm_{jj}} = \frac{P_0}{(m_{jj}/\sqrt{s})^{P_1}} \text{ (2-par. form)}, \tag{E.1}$$

$$\frac{dN}{dm_{jj}} = \frac{P_0(1-m_{jj}/\sqrt{s})^{P_2}}{(m_{jj}/\sqrt{s})^{P_1}} \text{ (3-par. form)}, \tag{E.2}$$

with the fit parameters $P_{0/1/2}$ and the center-of-mass energy $\sqrt{s}$. However, a number of alternative functions and the same function class using up to five fit parameters are tested in the Fisher F-test.

Table E.1.: Summary of the systematic uncertainties for the analysis and their impact on the event yield in the signal region and on the reconstructed m_{jj} shape (mean and width). Effects of PDF and scale uncertainties on the signal cross sections are assigned to the theory prediction instead of being included in the limit setting. Table published in Ref. [35].

Source	Relevant quantity	Uncertainty %			
		HP+HP	HP+LP	HP+j	LP+j
Jet energy scale	Resonance shape	2	2	2	2
Jet energy resolution	Resonance shape	6	7	4	3
PDF	Resonance shape	5	7	13	8
Jet energy scale	Signal yield	< 1		< 1	
Jet energy resolution	Signal yield	< 1		< 1	
Jet mass scale	Signal yield	< 2		< 1	
Jet mass resolution	Signal yield	< 6		< 8	
Pileup	Signal yield	2			
PDF (acceptance)	Signal yield	2			
Integrated luminosity	Signal yield	2.5			
Jet mass scale	Migration	< 36		< 10	
Jet mass resolution	Migration	< 25		< 7	
V tagging τ_{21}	Migration	22	33	11	22
V tagging p_T-dependence	Migration	19-40	14-29	9-23	4-11
PDF and scales (W′ and Z′)	Theory	2-18		N/A	
PDF and scales (bulk graviton)	Theory	8-78		N/A	
PDF and scales (q*)	Theory	N/A		1-61	

The background for this search is completely dominated by QCD multijet production where one or two of the jets are misidentified as V-jets. The smaller backgrounds of V+jets, $t\bar{t}$ and SM VV production are negligible for this search compared to the overwhelming number of QCD events, i.e., the overall contribution to the number of events in the signal region from all minor backgrounds is smaller than 3% of all background events. The limits are calculated using a simultaneous binned maximum likelihood fit of the background and signal model to the m_{jj} spectrum, with the binning used following the resolution of the CMS HCAL. The m_{jj} spectrum is fitted starting from $m_{jj} > 1080\,\text{GeV}$ to ensure $> 99\%$ trigger efficiency and avoid any bias from trigger inefficiencies, while the endpoint of the fit is chosen to extend at least to one bin after the dijet event in data with the highest invariant mass.

The fit results for background-only fits to data in different analysis categories are shown in Figure E.4 and E.5 for the double-tag categories and in Figure E.6 for the single-tag categories.

A summary of systematic uncertainties for this analysis can be found in Table E.1.

No significant deviations above the standard model expectation were found. The 95% CL upper limits on the production cross section set in this analysis can be found in Figure E.7.

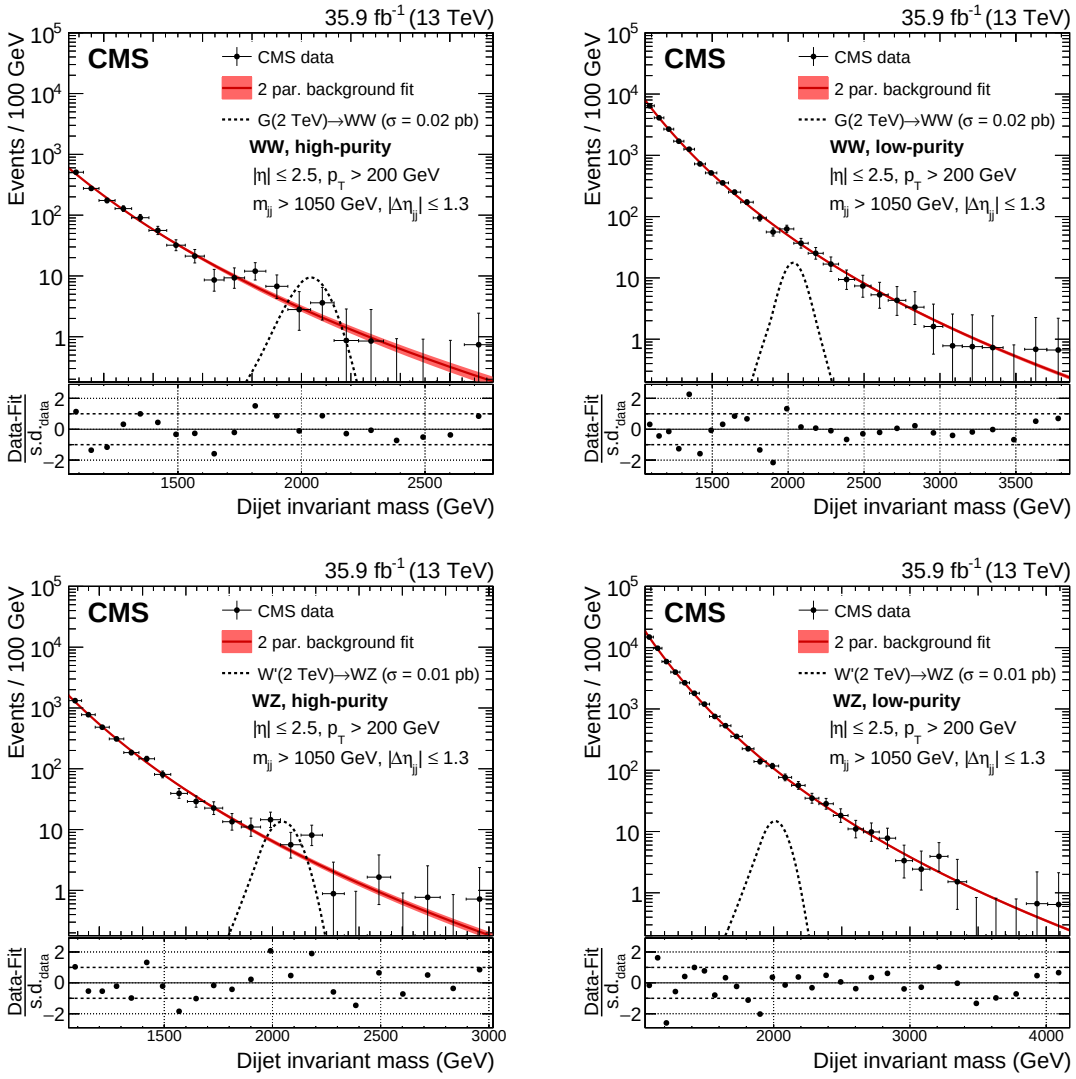

Figure E.4.: The dijet invariant mass distribution in data for the WW and WZ categories. The solid red curve represents the results of a background-only fit to data, with the shaded red area representing the uncertainty of the fit. The dashed line shows the signal shape for a bulk graviton of mass 2 TeV. The lower panels show the corresponding pull distributions, quantifying the agreement between a background-only fit and the data. Note that these fits do not represent the best fit hypotheses used in the statistical analysis where signal-plus-background fits are performed. Figure published in Ref. [35].

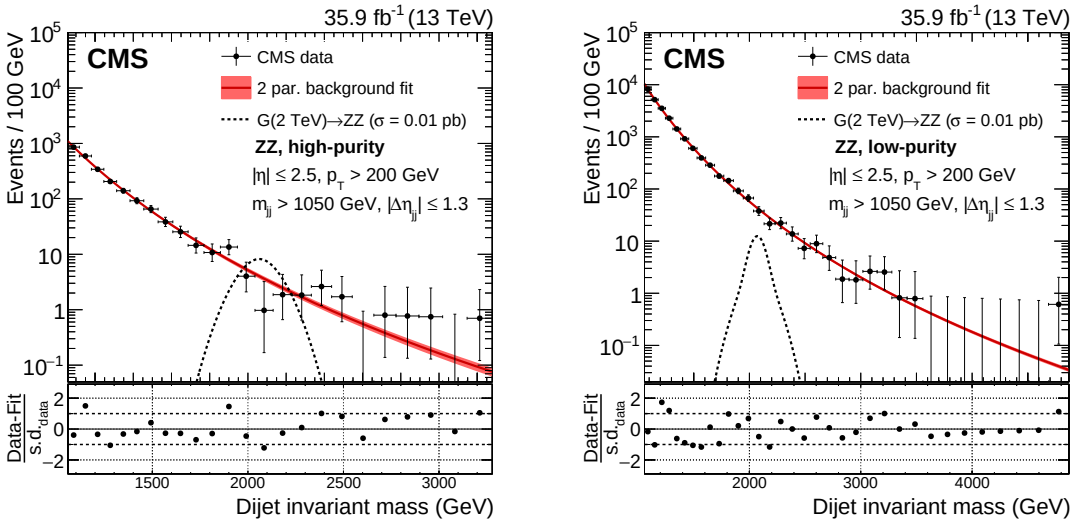

Figure E.5.: The dijet invariant mass distribution in data for the ZZ categories. The solid red curve represents the results of a background-only fit to data, with the shaded red area representing the uncertainty of the fit. The dashed line shows the signal shape for a bulk graviton of mass 2 TeV. The lower panels show the corresponding pull distributions, quantifying the agreement between a background-only fit and the data. Note that these fits do not represent the best fit hypotheses used in the statistical analysis where signal-plus-background fits are performed. Figure published in Ref. [35].

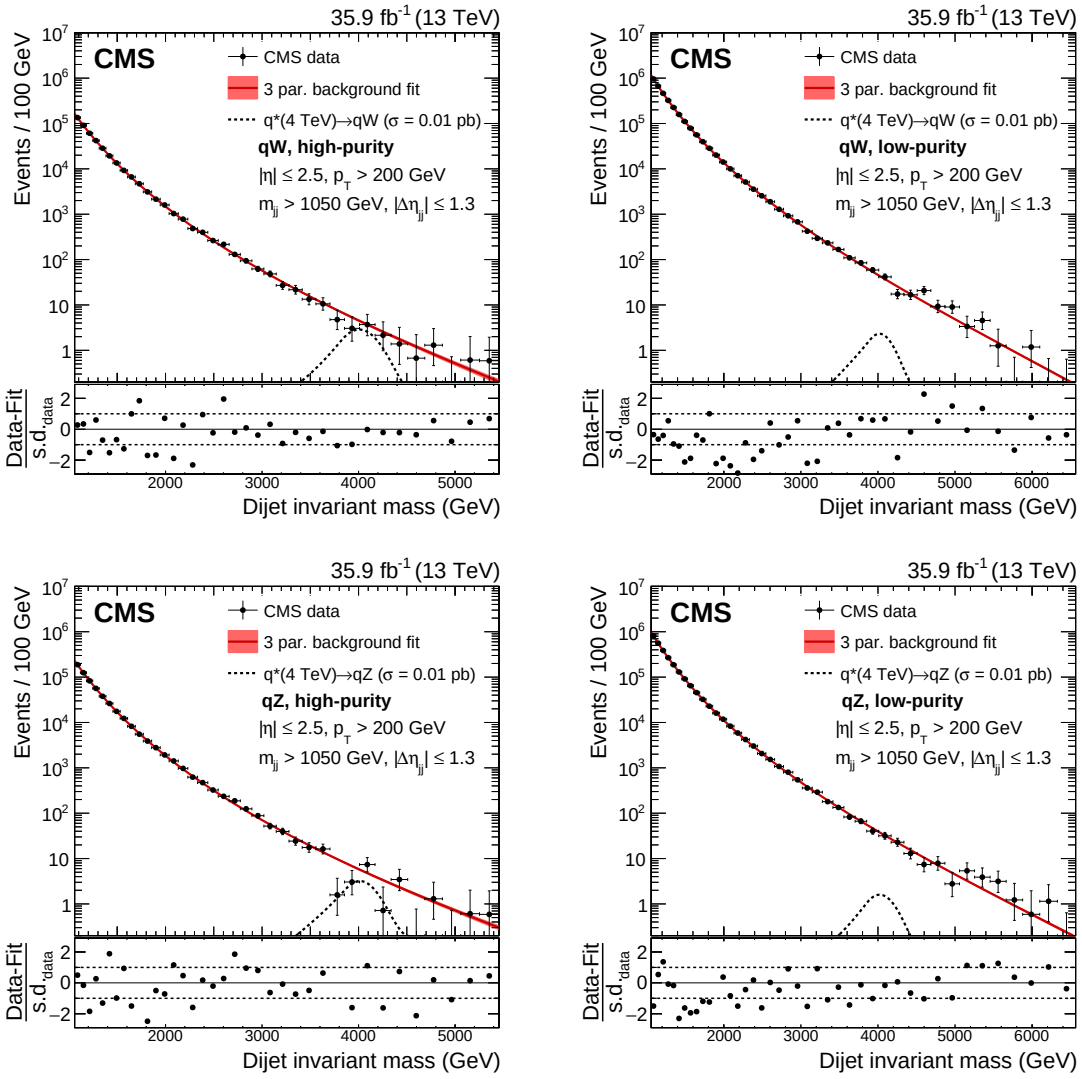

Figure E.6.: The dijet invariant mass distribution in data for the single-tag categories. The solid red curve represents the results of a background-only fit to data, with the shaded red area representing the uncertainty of the fit. The dashed line shows the signal shape for an exited quark of mass 4 TeV. The lower panels show the corresponding pull distributions, quantifying the agreement between a background-only fit and the data. Note that these fits do not represent the best fit hypotheses used in the statistical analysis where signal-plus-background fits are performed. Figure published in Ref. [35].

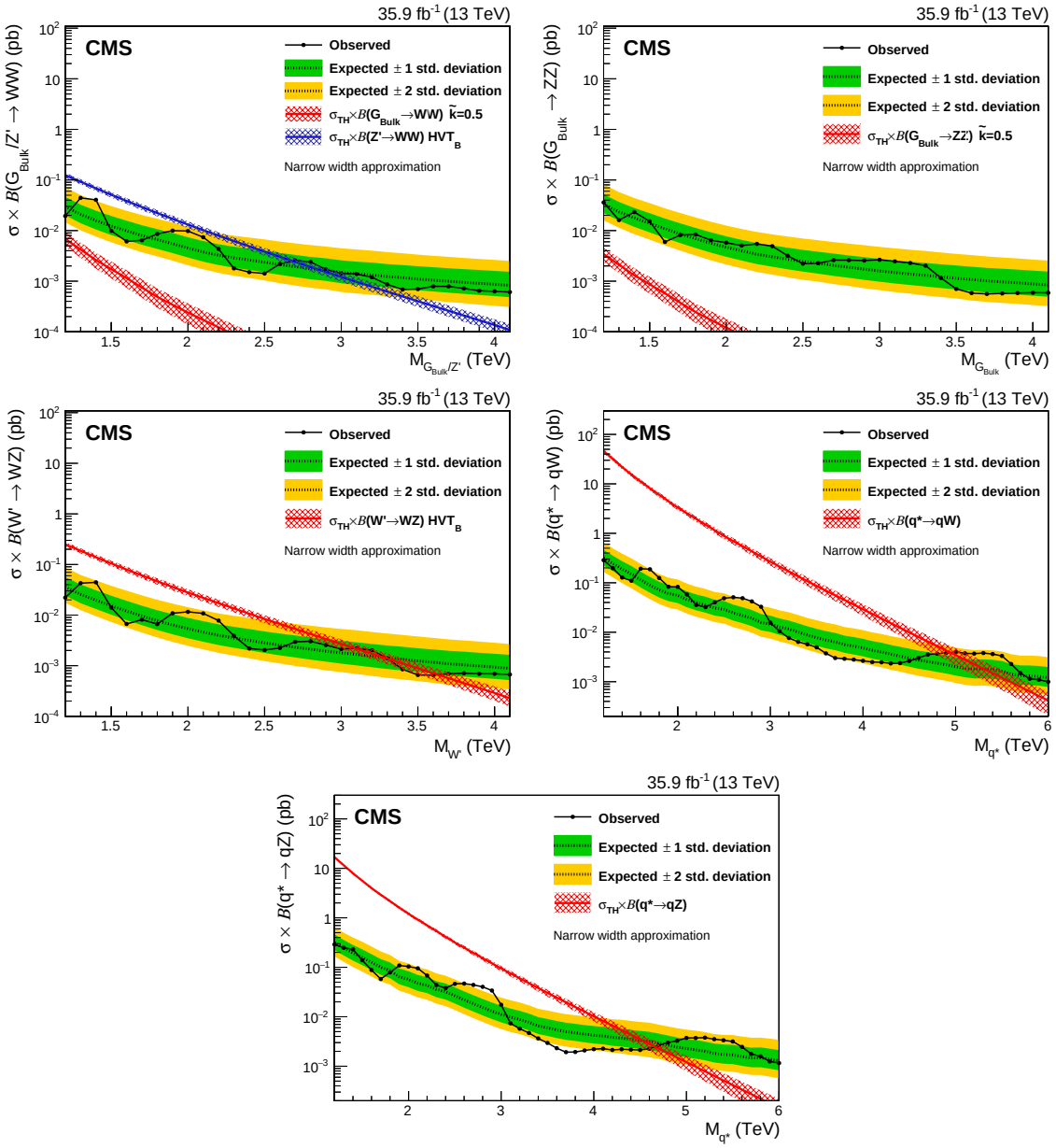

Figure E.7.: Observed (black solid) and expected (black dashed) 95% C.L. upper limits on the production cross section of a narrow-width resonance decaying to a pair of vector bosons (or qV) for different signal hypotheses. Limits are set (upper left plot) on a spin-1 neutral Z′ and a spin-2 resonance decaying into WW, and compared with the prediction of the HVT model B (blue line) and a bulk graviton model with $\tilde{k} = 0.5$ (red line). Limits are also set in the context of a bulk graviton decaying into ZZ (upper right) and a spin-1 charged resonance decaying into WZ (middle left) and compared with the predictions of the models. Upper limits on the production cross section for excited quarks are shown for $q^* \to qW$ ($q^* \to qZ$) on the middle right (lower) figures. Signal cross section uncertainties are displayed as cross-hatched bands. Figure published in Ref. [35].

List of Figures

0.1. Verbesserung der Ausschlussgrenzen. III
0.2. Ergebnisse für Ausschlussgrenzen auf Zwei-Boson Resonanzen. IV

1.1. Schematic of the profile structure of WED models. 14
1.2. The Feynman graphs for the production of a hypothetical spin-2 resonance. . 15
1.3. Branching fractions for a bulk graviton model. 16
1.4. Polarizations for the bulk graviton model. 17
1.5. Production diagrams at the LHC for the HVT model. 19
1.6. Production cross sections at the LHC for the HVT model. 20
1.7. Branching fractions for the HVT model. 21
1.8. Overview of diboson searches conducted by the CMS Collaboration. 22
1.9. 2016 Combination of diboson and dilepton searches (CMS Collaboration). . . 23

2.1. Schematic distributions of a test statistic. 28

3.1. A schematic of the LHC complex. 34
3.2. Mean number of pileup interactions per punch crossing. 35
3.3. Cumulative luminosity versus day delivered to the CMS experiment for pp collisions. 36
3.4. A schematic of the CMS detector. 37
3.5. Schematic layout of the CMS tracker. 39
3.6. Schematic layout of the CMS ECAL. 40
3.7. Schematic layout of the CMS HCAL. 43
3.8. Schematic layout of the CMS Muon System. 44
3.9. Data Acquisition at the CMS Collaboration. 45
3.10. Illustration of the Worldwide LHC Computing Grid. 46

4.1. A schematic view of the stages of MC event generation. 47
4.2. A schematic representation of a proton-proton collision. 48
4.3. The NNPDF3.1 NLO parton distribution functions. 51
4.4. Sketch of a jet origination from a pp collision. 57
4.5. Illustration of infrared and collinear safety in jet clustering algorithms. 58
4.6. Stages of jet energy corrections applied by the CMS Collaboration. 59
4.7. An illustration of the structure of a b quark jet. 61
4.8. Distribution of the jet mass before and after applying grooming algorithms. . 62
4.9. The p_{T} dependence of the soft drop grooming algorithm. 63
4.10. Corrections for the soft drop p_{T} dependence derived in a Z' signal sample. . . 64
4.11. Schematic of the substructure of fat jets. 65
4.12. An illustration of jet substructure techniques. 66
4.13. Comparison of τ_N between W-jets and QCD-jets. 67
4.14. Profile distribution of τ_{21} subjettiness in AK8 jets. 67

5.1. Schematic of the background and signal topologies in a 3D diboson search. . . 71
5.2. Feynman graphs for resonant diboson production. 72
5.3. Selected Feynman graphs for QCD multijet processes. 73
5.4. Representative Feynman graphs contributing to the W+jets background. . . . 73
5.5. The LO Feynman diagrams for $t\bar{t}$ production. 74
5.6. The LO Feynman graphs for SM diboson production. 74
5.7. The event selection efficiency as a function of the jet mass for trimmed mass triggers only. 76
5.8. The event selection efficiency as a function of the dijet invariant mass. 77
5.9. Comparison between the dijet invariant mass resolutions using different pileup subtraction methods. 78
5.10. Boson tagging efficiency and misidentification as a function of the number of pileup vertices. 78
5.11. Comparison of data distributions to MC simulation. 80
5.12. Mass sculpting using different substructure taggers. 81
5.13. Distribution of ρ' for QCD and V+jets. 82
5.14. ROC curve for τ_{21}^{DDT} performance. 82
5.15. Optimal τ_{21}^{DDT} cuts as a function of signal mass. 83
5.16. Scale factor measurement for τ_{21}^{DDT}. 86
5.17. Parametrization of the signal fits. 88
5.18. The signal modeling. 89
5.19. The signal efficiency as a function of the signal mass. 90
5.20. Goodness-of-fit tests for $\mathrm{G_{bulk}} \rightarrow \mathrm{WW}$ signal processes in the dijet invariant mass. 91
5.21. Goodness-of-fit tests tests for $\mathrm{G_{bulk}} \rightarrow \mathrm{WW}$ signal processes in the jet mass for the HPHP category. 92
5.22. Goodness-of-fit tests for $\mathrm{G_{bulk}} \rightarrow \mathrm{WW}$ signal processes in the jet mass for the HPLP category. 93
5.23. Distributions of the SM background processes on m_{jet} and m_{jj}. 100
5.24. The mass scale and resolution for an inclusive p_{T} selection. 101
5.25. Parametrization of the mass scale and resolution as a function of $p_{\mathrm{T}}^{\mathrm{gen}}$. 102
5.26. Conditional 2D probabilities for QCD multijet processes. 103
5.27. Comparison of the 1D kernel to MC simulation. 103
5.28. Comparison of QCD simulation to the kernels. 104
5.29. Alternative shapes for the QCD multijet background (HPLP). 105
5.30. Alternative shapes for the QCD multijet background (HPHP). 105
5.31. Stack plots showing the subdominant V+jets backgrounds. 107
5.32. One-dimensional kernels for the V+jets background compared to MC simulation. 109
5.33. Comparison of the dijet invariant mass spectrum with corrections and without corrections for V+jets background processes. 110
5.34. Fits to the V+jets resonant m_{jet} distribution. 110
5.35. Comparison between the final jet mass shapes for signal and V+jets background processes. 111
5.36. Fits to the V+jets non-resonant m_{jet} distribution. 112
5.37. Closure tests of the V+jets background model (HPHP). 113
5.38. Post-fit distribution for a low purity control-region in 2016 data. 120
5.39. Goodness of fit test for the low-purity control-region. 121
5.40. Likelihood distributions for background-only toys. 123

5.41. Pulls of the fitted nuisance parameters for the QCD multijet background shapes and different toy data sets. . . . 124
5.42. Pulls of the fitted nuisance parameters for the V+jets background shapes and different toy data sets. . . . 125
5.43. Pulls of the fitted nuisance parameters for the signal shapes and different toy data sets. . . . 126
5.44. Pulls of the fitted nuisance parameters for the background normalizations for different toy data sets. . . . 127
5.45. Pulls of the fitted nuisance parameters for the signal normalizations for different toy data sets. . . . 128
5.46. Bias tests for different QCD multijet background simulations. . . . 129
5.47. Post-fit projections for the HPHP category. . . . 131
5.48. Post-fit projections for the HPLP category. . . . 132
5.49. Post-fit projections for the signal region of $65 < m_{\text{jet}} < 105$ in the HPHP and HPLP categories. . . . 133
5.50. Pulls for the combined signal+background fit. . . . 135
5.51. Goodness-of-fit test for the signal region. . . . 136
5.52. Final limits for a bulk graviton model. . . . 136
5.53. Final limits for the HVT model B. . . . 137
5.54. Observed and expected upper limits for a bulk graviton model. . . . 137
5.55. Observed and expected upper limits for a V' HVT model. . . . 138
5.56. Exclusion limits in the HVT coupling plane. . . . 138
5.57. Comparison of expected 95% CL upper limits. . . . 139
5.58. Comparison of expected 95% CL upper limits. . . . 139

6.1. Comparison to limits obtained by the ATLAS Collaboration. . . . 141
6.2. Projections on full Run II-III luminosities. . . . 143

B.1. Goodness-of-fit tests for $Z' \to WW$ signal processes in the dijet invariant mass. 150
B.2. Goodness-of-fit tests for $W' \to WZ$ signal processes in the dijet invariant mass. 151
B.3. Goodness-of-fit tests for $G_{\text{bulk}} \to ZZ$ signal processes in the dijet invariant mass. 152
B.4. Goodness-of-fit tests for $Z' \to WW$ signal processes in the jet mass. . . . 153
B.5. Goodness-of-fit tests for $W' \to WZ$ signal processes in the jet mass. . . . 154
B.6. Goodness-of-fit tests for $G_{\text{bulk}} \to ZZ$ signal processes in the jet mass. . . . 155
B.7. Goodness-of-fit tests for $Z' \to WW$ signal processes in the jet mass for the HPLP category. . . . 156
B.8. Goodness-of-fit tests for $W' \to WZ$ signal processes in the jet mass for the HPLP category. . . . 157
B.9. Goodness-of-fit tests for $G_{\text{bulk}} \to ZZ$ signal processes in the jet mass for the HPLP category. . . . 158

C.1. Post-fit distributions for a low purity control-region in 2016 data. . . . 160
C.2. Post-fit distributions for a low purity control-region in 2016 data. . . . 161
C.3. Post-fit distributions for a low purity control-region in 2016 data. . . . 162
C.4. Post-fit distributions for a low purity control-region in 2016 data. . . . 163
C.5. Post-fit distributions for a low purity control-region in 2016 data. . . . 164

D.1. Conditional projections of a fit to the V+jets MC simulation. . . . 166
D.2. Conditional projections of a fit to the V+jets MC simulation. . . . 168

D.3. Conditional projections of a fit to the V+jets MC simulation. 169
D.4. Conditional projections of a fit to the V+jets MC simulation. 170
D.5. Fit to background toys using QCD PYTHIA8 simulation. 171
D.6. Fit to background toys using QCD HERWIG++ simulation. 172
D.7. Fit to background toys using QCD MADGRAPH5_AMC@NLO simulation. 173
D.8. Fit to background toys using QCD POWHEG simulation. 174

E.1. Trigger efficiencies for 2016 data. 176
E.2. Data to MC simulation comparison of the PUPPI jet mass and the τ_{21} distribution. 176
E.3. Signal shapes for the single- and double-tag category. 177
E.4. Fits to m_{jj} for the 1D fit method, double-tag category. 179
E.5. Fits to m_{jj} for the 1D fit method, double-tag ZZ category. 180
E.6. Fits to m_{jj} for the 1D fit method, single-tag category. 181
E.7. Limits extracted using the 1D fit method on 35.9 fb^{-1} of data recorded in 2016. 182

List of Tables

1.1. The quark content of the SM. 5
1.2. The leptons of the SM. 5
1.3. The boson content of the SM. 6

5.1. Jet quality requirements. 79
5.2. The V-tagging efficiency scale factors. 85
5.3. Summary of the systematic uncertainties. 114
5.4. 119
5.5. Yields extracted from the 3D fit method. 134

A.1. List of data sets used for the analysis. 145

A.2. List of signal samples used for the analysis. 147

D.1. Goodness-of-fit tests for the V+jets background model. 167

E.1. Systematic uncertainties in the previous analysis of the 2016 recorded data. . 178

Bibliography

[1] **Particle Data Group** Collaboration, M. e. a. Tanabashi, "Review of particle physics," *Phys. Rev. D* **98** (Aug, 2018) 030001. https://link.aps.org/doi/10.1103/PhysRevD.98.030001.

[2] L. Randall and R. Sundrum, "A Large mass hierarchy from a small extra dimension," *Phys. Rev. Lett.* **83** (1999) 3370–3373, arXiv:hep-ph/9905221 [hep-ph].

[3] L. Randall and R. Sundrum, "An Alternative to Compactification," *Phys. Rev. Lett.* **83** (1999) 4690–4693, arXiv:hep-th/9906064 [hep-th].

[4] K. Agashe, H. Davoudiasl, G. Perez, and A. Soni, "Warped Gravitons at the LHC and Beyond," *Phys. Rev.* **D76** (2007) 036006, arXiv:hep-ph/0701186 [hep-ph].

[5] A. L. Fitzpatrick, J. Kaplan, L. Randall, and L.-T. Wang, "Searching for the Kaluza-Klein Graviton in Bulk RS Models," *JHEP* **09** (2007) 013, arXiv:hep-ph/0701150 [hep-ph].

[6] R. Contino, D. Marzocca, D. Pappadopulo, and R. Rattazzi, "On the effect of resonances in composite Higgs phenomenology," *JHEP* **10** (2011) 081, arXiv:1109.1570 [hep-ph].

[7] B. Bellazzini, C. Csaki, J. Hubisz, J. Serra, and J. Terning, "Composite Higgs Sketch," *JHEP* **11** (2012) 003, arXiv:1205.4032 [hep-ph].

[8] E. Accomando, L. Fedeli, S. Moretti, S. De Curtis, and D. Dominici, "Charged di-boson production at the LHC in a 4-site model with a composite Higgs boson," *Phys. Rev.* **D86** (2012) 115006, arXiv:1208.0268 [hep-ph].

[9] J. L. Hewett and T. G. Rizzo, "Low-Energy Phenomenology of Superstring Inspired E(6) Models," *Phys. Rept.* **183** (1989) 193.

[10] T. G. Rizzo, "Z' phenomenology and the LHC," in *Proceedings of Theoretical Advanced Study Institute in Elementary Particle Physics : Exploring New Frontiers Using Colliders and Neutrinos (TASI 2006): Boulder, Colorado, June 4-30, 2006*, pp. 537–575. 2006. arXiv:hep-ph/0610104 [hep-ph]. http://www-public.slac.stanford.edu/sciDoc/docMeta.aspx?slacPubNumber=slac-pub-12129.

[11] **CMS** Collaboration, A. M. Sirunyan *et al.*, "Combination of CMS searches for heavy resonances decaying to pairs of bosons or leptons," arXiv:1906.00057 [hep-ex]. submitted to PLB.

[12] H. Davoudiasl and T. G. Rizzo, "Bulk physics at a graviton factory," *Phys. Lett.* **B512** (2001) 100–106, arXiv:hep-ph/0104199 [hep-ph].

[13] D. Pappadopulo, A. Thamm, R. Torre, and A. Wulzer, "Heavy Vector Triplets: Bridging Theory and Data," *JHEP* **09** (2014) 060, arXiv:1402.4431 [hep-ph].

[14] **CMS** Collaboration, V. Khachatryan *et al.*, "Search for massive resonances in dijet systems containing jets tagged as W or Z boson decays in pp collisions at $\sqrt{s} = 8$ TeV," *JHEP* **08** (2014) 173, arXiv:1405.1994 [hep-ex].

[15] **CMS** Collaboration, V. Khachatryan *et al.*, "Search for massive resonances decaying into pairs of boosted bosons in semi-leptonic final states at $\sqrt{s} = 8$ TeV," *JHEP* **08** (2014) 174, arXiv:1405.3447 [hep-ex].

[16] **CMS** Collaboration, V. Khachatryan *et al.*, "Search for new resonances decaying via WZ to leptons in proton-proton collisions at $\sqrt{s} = 8$ TeV," *Phys. Lett.* **B740** (2015) 83–104, arXiv:1407.3476 [hep-ex].

[17] **CMS** Collaboration, A. M. Sirunyan *et al.*, "Search for massive resonances decaying into WW, WZ or ZZ bosons in proton-proton collisions at $\sqrt{s} = 13$ TeV," *JHEP* **03** (2017) 162, arXiv:1612.09159 [hep-ex].

[18] **CMS** Collaboration, A. M. Sirunyan *et al.*, "Search for a heavy resonance decaying to a pair of vector bosons in the lepton plus merged jet final state at $\sqrt{s} = 13$ TeV," *JHEP* **05** (2018) 088, arXiv:1802.09407 [hep-ex].

[19] **CMS** Collaboration, V. Khachatryan *et al.*, "Search for Narrow High-Mass Resonances in Proton–Proton Collisions at $\sqrt{s} = 8$ TeV Decaying to a Z and a Higgs Boson," *Phys. Lett.* **B748** (2015) 255–277, arXiv:1502.04994 [hep-ex].

[20] **CMS** Collaboration, A. M. Sirunyan *et al.*, "Search for heavy resonances that decay into a vector boson and a Higgs boson in hadronic final states at $\sqrt{s} = 13$ TeV," *Eur. Phys. J.* **C77** no. 9, (2017) 636, arXiv:1707.01303 [hep-ex].

[21] **CMS** Collaboration, V. Khachatryan *et al.*, "Search for heavy resonances decaying into a vector boson and a Higgs boson in final states with charged leptons, neutrinos, and b quarks," *Phys. Lett.* **B768** (2017) 137–162, arXiv:1610.08066 [hep-ex].

[22] **CMS** Collaboration, V. Khachatryan *et al.*, "Search for a massive resonance decaying into a Higgs boson and a W or Z boson in hadronic final states in proton-proton collisions at $\sqrt{s} = 8$ TeV," *JHEP* **02** (2016) 145, arXiv:1506.01443 [hep-ex].

[23] **CMS** Collaboration, V. Khachatryan *et al.*, "Search for massive WH resonances decaying into the $\ell\nu\mathrm{b}\overline{\mathrm{b}}$ final state at $\sqrt{s} = 8$ TeV," *Eur. Phys. J.* **C76** no. 5, (2016) 237, arXiv:1601.06431 [hep-ex].

[24] **CMS** Collaboration, V. Khachatryan *et al.*, "Search for heavy resonances decaying to

two Higgs bosons in final states containing four b quarks," *Eur. Phys. J.* **C76** no. 7, (2016) 371, arXiv:1602.08762 [hep-ex].

[25] **ATLAS** Collaboration, G. Aad *et al.*, "Search for WZ resonances in the fully leptonic channel using pp collisions at sqrt(s) = 8 TeV with the ATLAS detector," *Phys. Lett.* **B737** (2014) 223–243, arXiv:1406.4456 [hep-ex].

[26] **ATLAS** Collaboration, G. Aad *et al.*, "Search for resonant diboson production in the $\ell\ell q\bar{q}$ final state in pp collisions at $\sqrt{s} = 8$ TeV with the ATLAS detector," *Eur. Phys. J.* **C75** (2015) 69, arXiv:1409.6190 [hep-ex].

[27] **ATLAS** Collaboration, G. Aad *et al.*, "Search for production of WW/WZ resonances decaying to a lepton, neutrino and jets in pp collisions at $\sqrt{s} = 8$ TeV with the ATLAS detector," *Eur. Phys. J.* **C75** no. 5, (2015) 209, arXiv:1503.04677 [hep-ex]. [Erratum: Eur. Phys. J.C75,370(2015)].

[28] **ATLAS** Collaboration, G. Aad *et al.*, "Search for high-mass diboson resonances with boson-tagged jets in proton-proton collisions at $\sqrt{s} = 8$ TeV with the ATLAS detector," *JHEP* **12** (2015) 055, arXiv:1506.00962 [hep-ex].

[29] **ATLAS** Collaboration, M. Aaboud *et al.*, "Search for heavy resonances decaying to a W or Z boson and a Higgs boson in the $q\bar{q}^{(\prime)}b\bar{b}$ final state in pp collisions at $\sqrt{s} = 13$ TeV with the ATLAS detector," *Phys. Lett.* **B774** (2017) 494–515, arXiv:1707.06958 [hep-ex].

[30] **ATLAS** Collaboration, M. Aaboud *et al.*, "Search for diboson resonances with boson-tagged jets in pp collisions at $\sqrt{s} = 13$ TeV with the ATLAS detector," *Phys. Lett.* **B777** (2018) 91–113, arXiv:1708.04445 [hep-ex].

[31] **ATLAS** Collaboration, G. Aad *et al.*, "Search for a new resonance decaying to a W or Z boson and a Higgs boson in the $\ell\ell/\ell\nu/\nu\nu + b\bar{b}$ final states with the ATLAS detector," *Eur. Phys. J.* **C75** no. 6, (2015) 263, arXiv:1503.08089 [hep-ex].

[32] **ATLAS** Collaboration, M. Aaboud *et al.*, "Searches for heavy diboson resonances in pp collisions at $\sqrt{s} = 13$ TeV with the ATLAS detector," *JHEP* **09** (2016) 173, arXiv:1606.04833 [hep-ex].

[33] **ATLAS** Collaboration, M. Aaboud *et al.*, "Search for new resonances decaying to a W or Z boson and a Higgs boson in the $\ell^+\ell^- b\bar{b}$, $\ell\nu b\bar{b}$, and $\nu\bar{\nu}b\bar{b}$ channels with pp collisions at $\sqrt{s} = 13$ TeV with the ATLAS detector," *Phys. Lett.* **B765** (2017) 32–52, arXiv:1607.05621 [hep-ex].

[34] **CMS** Collaboration, A. M. Sirunyan *et al.*, "Search for massive resonances decaying into WW, WZ, ZZ, qW, and qZ with dijet final states at $\sqrt{s} = 13$ TeV," *Phys. Rev.* **D97** no. 7, (2018) 072006, arXiv:1708.05379 [hep-ex].

[35] **CMS** Collaboration, A. M. Sirunyan *et al.*, "Search for massive resonances decaying into WW, WZ, ZZ, qW, and qZ with dijet final states at $\sqrt{s} = 13$ TeV," *Phys. Rev. D*

97 no. CMS-B2G-17-001. CMS-B2G-17-001-003, (Aug, 2017) 072006. 25 p. https://cds.cern.ch/record/2280069. All the figures and tables, including additional supplementary figures, can be found at http://cms-results.web.cern.ch/cms-results/public-results/publications/B2G-17-001/ (CMS Public Pages).

[36] S. L. Glashow, "Partial Symmetries of Weak Interactions," *Nucl. Phys.* **22** (1961) 579–588.

[37] E. Fermi, "Versuch einer Theorie der β-Strahlen. I," *Zeitschrift für Physik* **88** no. 3, (Mar, 1934) 161–177. https://doi.org/10.1007/BF01351864.

[38] P. W. Higgs, "Broken Symmetries and the Masses of Gauge Bosons," *Phys. Rev. Lett.* **13** (Oct, 1964) 508–509.

[39] F. Englert and R. Brout, "Broken symmetry and the mass of gauge vector mesons," *Phys. Rev. Lett.* **13** (Aug, 1964) 321–323. https://link.aps.org/doi/10.1103/PhysRevLett.13.321.

[40] J. Goldstone *et al.*, "Broken symmetries," *Phys. Rev.* **127** (Aug, 1962) 965–970. http://link.aps.org/doi/10.1103/PhysRev.127.965.

[41] S. Weinberg, "A model of leptons," *Phys. Rev. Lett.* **19** (Nov, 1967) 1264–1266. https://link.aps.org/doi/10.1103/PhysRevLett.19.1264.

[42] M. Kobayashi and T. Maskawa, "CP-Violation in the Renormalizable Theory of Weak Interaction," *Prog. of Theor. Phys.* **49** no. 2, (1973) 652–657, http://ptp.oxfordjournals.org/content/49/2/652.full.pdf+html.

[43] K. Krasnov and R. Percacci, "Gravity and Unification: A review," *Class. Quant. Grav.* **35** no. 14, (2018) 143001, arXiv:1712.03061 [hep-th].

[44] W. de Boer, "Grand unified theories and supersymmetry in particle physics and cosmology," *Prog. Part. Nucl. Phys.* **33** (1994) 201–302, arXiv:hep-ph/9402266 [hep-ph].

[45] G. 't Hooft, "The Evolution of Quantum Field Theory, From QED to Grand Unification," *Adv. Ser. Direct. High Energy Phys.* **26** (2016) 1–27, arXiv:1503.05007 [hep-th].

[46] S. F. King, "Unified Models of Neutrinos, Flavour and CP Violation," *Prog. Part. Nucl. Phys.* **94** (2017) 217–256, arXiv:1701.04413 [hep-ph].

[47] H. Andernach and F. Zwicky, "English and Spanish Translation of Zwicky's (1933) The Redshift of Extragalactic Nebulae," *arXiv e-prints* (Nov, 2017) arXiv:1711.01693, arXiv:1711.01693 [astro-ph.IM].

[48] V. Trimble, "Existence and Nature of Dark Matter in the Universe," *Ann. Rev. Astron. Astrophys.* **25** (1987) 425–472.

[49] P. J. E. Peebles and B. Ratra, "The Cosmological constant and dark energy," *Rev. Mod. Phys.* **75** (2003) 559–606, arXiv:astro-ph/0207347 [astro-ph]. [,592(2002)].

[50] L. Baudis, "The search for dark matter," *European Review* **26** no. 1, (2018) 70–81.

[51] C. Giunti and M. Laveder, "Neutrino mixing," arXiv:hep-ph/0310238 [hep-ph].

[52] A. D. Sakharov, "Violation ofCPin variance,casymmetry, and baryon asymmetry of the universe," *Soviet Physics Uspekhi* **34** no. 5, (May, 1991) 392–393. https://doi.org/10.1070%2Fpu1991v034n05abeh002497.

[53] M. Shaposhnikov, "Baryon asymmetry of the universe in standard electroweak theory," *Nuclear Physics B* **287** (1987) 757 – 775. http://www.sciencedirect.com/science/article/pii/0550321387901271.

[54] M. B. Gavela, P. Hernandez, J. Orloff, and O. Pene, "Standard model CP violation and baryon asymmetry," *Mod. Phys. Lett.* **A9** (1994) 795–810, arXiv:hep-ph/9312215 [hep-ph].

[55] C. Bär, *Elementare Differentialgeometrie*. 3. Auflage. Walter de Gruyter, 2010.

[56] A. Oliveira, "Gravity particles from Warped Extra Dimensions, a review. Part I - KK Graviton," arXiv:1404.0102 [hep-ph].

[57] A. Pasini, "A conceptual introduction to the Kaluza-Klein theory," *European Journal of Physics* **9** no. 4, (Oct, 1988) 289–296. https://doi.org/10.1088%2F0143-0807%2F9%2F4%2F007.

[58] E. Accomando, D. Becciolini, S. De Curtis, D. Dominici, and L. Fedeli, "W' production at the LHC in the 4-site Higgsless model," *Phys. Rev.* **D84** (2011) 115014, arXiv:1107.4087 [hep-ph].

[59] A. Falkowski, C. Grojean, A. Kaminska, S. Pokorski, and A. Weiler, "If no Higgs then what?," *JHEP* **11** (2011) 028, arXiv:1108.1183 [hep-ph].

[60] K. Agashe, H. Davoudiasl, S. Gopalakrishna, T. Han, G.-Y. Huang, G. Perez, Z.-G. Si, and A. Soni, "LHC Signals for Warped Electroweak Neutral Gauge Bosons," *Phys. Rev.* **D76** (2007) 115015, arXiv:0709.0007 [hep-ph].

[61] K. Agashe, S. Gopalakrishna, T. Han, G.-Y. Huang, and A. Soni, "LHC Signals for Warped Electroweak Charged Gauge Bosons," *Phys. Rev.* **D80** (2009) 075007, arXiv:0810.1497 [hep-ph].

[62] F. James, "Monte Carlo theory and practice," *Reports on Progress in Physics - REP PROGR PHYS* **43** (09, 1980) 1145–1189.

[63] R. T. D. Pappadopulo, A. Thamm and A. Wulzer, "Tools for the study of heavy vector triplets," July, 2014. http://rtorre.web.cern.ch/rtorre/Riccardotorre/vector_triplet_t.html.

[64] **CMS** Collaboration, "Common note on searches for new diboson resonances in semileptonic and hadronic final states at $\sqrt(s) = 13$ TeV." AN-17-196, 2017.

[65] **CMS** Collaboration, "CMS Beyond-two-generations (B2G) Public Physics Results - Dibosons," May, 2019. https://twiki.cern.ch/twiki/bin/view/CMSPublic/PhysicsResultsB2GDibosons.

[66] **ATLAS** Collaboration, M. Aaboud *et al.*, "Combination of searches for heavy resonances decaying into bosonic and leptonic final states using 36 fb^{-1} of proton-proton collision data at $\sqrt{s} = 13$ TeV with the ATLAS detector," *Phys. Rev.* **D98** no. 5, (2018) 052008, arXiv:1808.02380 [hep-ex].

[67] G. Bohm and G. Zech, *Einfürung in Statistik und Messwertanalyse für Physiker*. Verlag Deutsches Elektronen-Synchotron in der Helmholzgemeinschaft, D-22603 Hamburg, 2006.

[68] G. Cowan, "Statistics for Searches at the LHC," in *Proceedings, 69th Scottish Universities Summer School in Physics : LHC Phenomenology (SUSSP69): St.Andrews, Scotland, August 19-September 1, 2012*, pp. 321–355. 2013. arXiv:1307.2487 [hep-ex].

[69] T. Junk, "Confidence level computation for combining searches with small statistics," *Nucl. Instrum. Methods. Section A: Accelerators, Spectrometers, Detectors and Associated Equipment* **434** no. 2, (1999) 435 – 443.

[70] G. Cowan *et al.*, "Asymptotic formulae for likelihood-based tests of new physics," *Eur. Phys. J.* **C71** (2011) 1554, arXiv:1007.1727 [physics.data-an]. [Erratum: Eur. Phys. J.C73,2501(2013)].

[71] M. Baak, S. Gadatsch, R. Harrington, and W. Verkerke, "Interpolation between multi-dimensional histograms using a new non-linear moment morphing method," *Nucl. Instrum. Meth.* **A771** (2015) 39–48, arXiv:1410.7388 [physics.data-an].

[72] S. Baker and R. D. Cousins, "Clarification of the use of chi-square and likelihood functions in fits to histograms," *Nuclear Instruments and Methods in Physics Research* **221** no. 2, (1984) 437 – 442. http://www.sciencedirect.com/science/article/pii/0167508784900164.

[73] W. A. Rolke, A. M. Lopez, and J. Conrad, "Limits and confidence intervals in the presence of nuisance parameters," *Nucl. Instrum. Meth.* **A551** (2005) 493–503, arXiv:physics/0403059 [physics].

[74] R. D. Cousins and V. L. Highland, "Incorporating systematic uncertainties into an upper limit," *Nucl. Instrum. Meth.* **A320** (1992) 331–335.

[75] J. S. Conway, "Incorporating Nuisance Parameters in Likelihoods for Multisource Spectra," in *Proceedings, PHYSTAT 2011 Workshop on Statistical Issues Related to Discovery Claims in Search Experiments and Unfolding, CERN,Geneva, Switzerland 17-20 January 2011*, pp. 115–120. 2011. arXiv:1103.0354 [physics.data-an].

[76] The ATLAS Collaboration, The CMS Collaboration, The LHC Higgs Combination Group, "Procedure for the LHC Higgs boson search combination in Summer 2011," Tech. Rep. CMS-NOTE-2011-005. ATL-PHYS-PUB-2011-11, CERN, Geneva, Aug, 2011. https://cds.cern.ch/record/1379837.

[77] A. L. Read, "Presentation of search results: the CLs technique," *Journal of Physics G: Nuclear and Particle Physics* **28** no. 10, (Sep, 2002) 2693–2704. https://doi.org/10.1088%2F0954-3899%2F28%2F10%2F313.

[78] A. Wald, "Tests of Statistical Hypotheses Concerning Several Parameters When the Number of Observations is Large," *AMS* **54** (1943) 426–482.

[79] M. Benedikt, P. Collier, V. Mertens, J. Poole, and K. Schindl, *LHC Design Report*. CERN Yellow Reports: Monographs. CERN, Geneva, 2004. http://cds.cern.ch/record/823808.

[80] S. Myers and E. Picasso, "The design, construction and commissioning of the CERN large Electron–Positron collider.," *Contemporary Physics* **31** no. 6, (1990) 387–403. https://doi.org/10.1080/00107519008213789.

[81] C. Lefèvre, "The CERN accelerator complex. Complexe des accélérateurs du CERN," Dec, 2008. https://cds.cern.ch/record/1260465.

[82] **ATLAS** Collaboration, G. Aad *et al.*, "The ATLAS Experiment at the CERN Large Hadron Collider," *JINST* **3** (2008) S08003.

[83] **ALICE** Collaboration, K. Aamodt *et al.*, "The ALICE experiment at the CERN LHC," *JINST* **3** (2008) S08002.

[84] **LHCb** Collaboration, A. A. Alves, Jr. *et al.*, "The LHCb Detector at the LHC," *JINST* **3** (2008) S08005.

[85] **LHCb** Collaboration, *LHCb : Technical Proposal*. Tech. Proposal. CERN, Geneva, 1998. http://cds.cern.ch/record/622031.

[86] **TOTEM** Collaboration, "The TOTEM experiment at the CERN large hadron collider," *Journal of Instrumentation* **3** no. 08, (Aug, 2008) S08007–S08007. https://doi.org/10.1088%2F1748-0221%2F3%2F08%2Fs08007.

[87] **MoEDAL** Collaboration, V. A. Mitsou, "The MoEDAL experiment at the LHC: status and results," *J. Phys. Conf. Ser.* **873** no. 1, (2017) 012010, arXiv:1703.07141 [hep-ex].

[88] **LHCf** Collaboration, E. Berti, "The LHCf experiment: present status and physics results," arXiv:1710.03991 [hep-ex].

[89] **CMS** Collaboration, Feb, 2019. https://twiki.cern.ch/twiki/bin/view/CMSPublic/LumiPublicResults.

[90] G. Apollinari, I. Béjar Alonso, O. Brüning, M. Lamont, and L. Rossi, *High-Luminosity Large Hadron Collider (HL-LHC): Preliminary Design Report*. CERN Yellow Reports: Monographs. CERN, Geneva, 2015. http://cds.cern.ch/record/2116337.

[91] **CMS** Collaboration, S. Chatrchyan *et al.*, "The CMS Experiment at the CERN LHC," *JINST* **3** (2008) S08004.

[92] **CMS** Collaboration, March, 2019. http://cms.web.cern.ch/news/cms-detector-design.

[93] **CMS** Collaboration, *CMS, tracker technical design report*. 1998. http://weblib.cern.ch/abstract?CERN-LHCC-98-6.

[94] **CMS** Collaboration, V. Veszpremi, "Operation and performance of the CMS tracker," *JINST* **9** (2014) C03005, arXiv:1402.0675 [physics.ins-det].

[95] D. Sprenger, M. Weber, R. Adolphi, R. Brauer, L. Feld, K. Klein, A. Ostaptchuk, S. Schael, and B. Wittmer, "Validation of Kalman Filter alignment algorithm with cosmic-ray data using a CMS silicon strip tracker endcap," *JINST* **5** no. arXiv:1003.5460. CMS-NOTE-2010-002, (Mar, 2010) P06007. 11 p. https://cds.cern.ch/record/1256099.

[96] A. Saha, "Phase 1 upgrade of the CMS pixel detector," *Journal of Instrumentation* **12** no. 02, (Feb, 2017) C02033–C02033. https://doi.org/10.1088%2F1748-0221%2F12%2F02%2Fc02033.

[97] **CMS** Collaboration, *The CMS electromagnetic calorimeter project: Technical Design Report*. Technical Design Report CMS. CERN, Geneva, 1997. http://cds.cern.ch/record/349375.

[98] **CMS** Collaboration, S. Chatrchyan *et al.*, "Performance and Operation of the CMS Electromagnetic Calorimeter," *JINST* **5** (2010) T03010, arXiv:0910.3423 [physics.ins-det].

[99] **CMS** Collaboration, *The CMS hadron calorimeter project: Technical Design Report*. Technical Design Report CMS. CERN, Geneva, 1997. https://cds.cern.ch/record/357153.

[100] V. D. Elvira, "Measurement of the Pion Energy Response and Resolution in the CMS HCAL Test Beam 2002 Experiment," Tech. Rep. CMS-NOTE-2004-020, CERN, Geneva, Sep, 2004. https://cds.cern.ch/record/800406.

[101] **CMS** Collaboration, S. Chatrchyan *et al.*, "Performance of the CMS Hadron Calorimeter with Cosmic Ray Muons and LHC Beam Data," *JINST* **5** (2010) T03012, arXiv:0911.4991 [physics.ins-det].

[102] **CMS** Collaboration, "Performance of CMS muon reconstruction in pp collision events at $\sqrt{s} = 7$ TeV," *JINST* **7** no. CMS-MUO-10-004. CMS-MUO-10-004. CERN-PH-EP-2012-173, (Jun, 2012) P10002. 81 p. https://cds.cern.ch/record/1456510. Comments: Submitted to the Journal of Instrumentation.

[103] **CMS** Collaboration, S. Chatrchyan *et al.*, "CMS Data Processing Workflows during an Extended Cosmic Ray Run," *JINST* **5** (2010) T03006, arXiv:0911.4842 [physics.ins-det].

[104] **CMS** Collaboration, V. Khachatryan *et al.*, "The CMS trigger system," *JINST* **12** no. 01, (2017) P01020, arXiv:1609.02366 [physics.ins-det].

[105] **CMS** Collaboration, "CMS Computing Model," July, 2018. https://twiki.cern.ch/twiki/bin/view/CMSPublic/WorkBookComputingModel.

[106] I. Bird, "Computing for the large hadron collider," *Annual Review of Nuclear and Particle Science* **61** no. 1, (2011) 99–118. https://doi.org/10.1146/annurev-nucl-102010-130059.

[107] N. Bartosik, "Event simulation in HEP experiments." http://bartosik.pp.ua/hep_sketches/event_simulation. Accessed: 2016-09-13.

[108] J. M. Butterworth *et al.*, "Hard Processes in Proton-Proton Collisions at the Large Hadron Collider," *Ann. Rev. Nucl. Part. Sci.* **62** (2012) 387–405, arXiv:1202.0583 [hep-ex].

[109] **CMS** Collaboration, V. Khachatryan *et al.*, "Measurement of the underlying event activity using charged-particle jets in proton-proton collisions at sqrt(s) = 2.76 TeV," *JHEP* **09** (2015) 137, arXiv:1507.07229 [hep-ex].

[110] **NNPDF** Collaboration, R. D. Ball *et al.*, "Parton distributions for the LHC Run II," *JHEP* **04** (2015) 040, arXiv:1410.8849 [hep-ph].

[111] **NNPDF** Collaboration, R. D. Ball, E. R. Nocera, and R. L. Pearson, "Nuclear Uncertainties in the Determination of Proton PDFs," *Eur. Phys. J.* **C79** no. 3, (2019) 282, arXiv:1812.09074 [hep-ph].

[112] **NNPDF** Collaboration, R. D. Ball *et al.*, "Parton distributions from high-precision collider data," *Eur. Phys. J.* **C77** no. 10, (2017) 663, arXiv:1706.00428 [hep-ph].

[113] S. Hoeche *et al.*, "Matching parton showers and matrix elements," in *HERA and the LHC: A Workshop on the implications of HERA for LHC physics: Proceedings Part A*.

2006. arXiv:hep-ph/0602031 [hep-ph]. https://inspirehep.net/record/709818/files/arXiv:hep-ph_0602031.pdf.

[114] B. Andersson, G. Gustafson, G. Ingelman, and T. Sjöstrand, "Parton Fragmentation and String Dynamics," *Phys. Rept.* **97** (1983) 31–145.

[115] B. Andersson, "The Lund model," *Camb. Monogr. Part. Phys. Nucl. Phys. Cosmol.* **7** (1997) 1–471.

[116] B. Andersson, S. Mohanty, and F. Soderberg, "Recent developments in the Lund model," in *36th Annual Winter School on Nuclear and Particle Physics (PINP 2002) and 8th St. Petersburg School on Theoretical Physics St. Petersburg, Russia, February 25-March 3, 2002*. 2002. arXiv:hep-ph/0212122 [hep-ph].

[117] D. Amati and G. Veneziano, "Preconfinement as a property of perturbative qcd," *Physics Letters B* **83** no. 1, (1979) 87 – 92. http://www.sciencedirect.com/science/article/pii/0370269379908967.

[118] J. Alwall *et al.*, "A Standard format for Les Houches event files," *Comput. Phys. Commun.* **176** (2007) 300–304, arXiv:hep-ph/0609017 [hep-ph].

[119] A. Buckley *et al.*, "General-purpose event generators for LHC physics," *Phys. Rept.* **504** (2011) 145–233, arXiv:1101.2599 [hep-ph].

[120] J. Alwall, R. Frederix, S. Frixione, V. Hirschi, F. Maltoni, O. Mattelaer, H. S. Shao, T. Stelzer, P. Torrielli, and M. Zaro, "The automated computation of tree-level and next-to-leading order differential cross sections, and their matching to parton shower simulations," *JHEP* **07** (2014) 079, arXiv:1405.0301 [hep-ph].

[121] J. Alwall, M. Herquet, F. Maltoni, O. Mattelaer, and T. Stelzer, "MadGraph 5 : Going Beyond," *JHEP* **06** (2011) 128, arXiv:1106.0522 [hep-ph].

[122] K. Hagiwara *et al.*, "HELAS and MadGraph/MadEvent with spin-2 particles," *Eur. Phys. J.* **C56** (2008) 435–447, arXiv:0805.2554 [hep-ph].

[123] P. de Aquino *et al.*, "Simulating graviton production at hadron colliders," *JHEP* **06** (2011) 132, arXiv:1101.5499 [hep-ph].

[124] T. Sjöstrand *et al.*, "High-energy physics event generation with PYTHIA 6.1," *Comput. Phys. Commun.* **135** (2001) 238–259, arXiv:hep-ph/0010017 [hep-ph].

[125] **CMS** Collaboration, V. Khachatryan *et al.*, "Event generator tunes obtained from underlying event and multiparton scattering measurements," *Eur. Phys. J. C.* **76** (2016) 155, arXiv:1512.00815 [hep-ex].

[126] **CMS** Collaboration, A. M. Sirunyan *et al.*, "Extraction and validation of a new set of CMS PYTHIA8 tunes from underlying-event measurements," arXiv:1903.12179 [hep-ex].

[127] S. Alioli, K. Hamilton, P. Nason, C. Oleari, and E. Re, "Jet pair production in POWHEG," *JHEP* **04** (2011) 081, arXiv:1012.3380 [hep-ph].

[128] C. Oleari, "The POWHEG-BOX," *Nucl. Phys. Proc. Suppl.* **205-206** (2010) 36–41, arXiv:1007.3893 [hep-ph].

[129] M. Bahr *et al.*, "Herwig++ Physics and Manual," *Eur. Phys. J.* **C58** (2008) 639–707, arXiv:0803.0883 [hep-ph].

[130] **GEANT4** Collaboration, S. Agostinelli *et al.*, "GEANT4: A Simulation toolkit," *Nucl. Instrum. Meth.* **A506** (2003) 250–303.

[131] J. Allison *et al.*, "Geant4 developments and applications," *IEEE Trans. Nucl. Sci.* **53** (2006) 270.

[132] **CMS** Collaboration, A. M. Sirunyan *et al.*, "Particle-flow reconstruction and global event description with the CMS detector," *JINST* **12** no. 10, (2017) P10003, arXiv:1706.04965 [physics.ins-det].

[133] **CMS** Collaboration, F. Beaudette, "The CMS Particle Flow Algorithm," in *Proceedings, International Conference on Calorimetry for the High Energy Frontier (CHEF 2013): Paris, France, April 22-25, 2013*, pp. 295–304. 2013. arXiv:1401.8155 [hep-ex].

[134] P. Billoir, "Progressive track recognition with a kalman-like fitting procedure," *Computer Physics Communications* **57** no. 1, (1989) 390 – 394. http://www.sciencedirect.com/science/article/pii/001046558990249X.

[135] T. Speer, K. Prokofiev, R. Fruhwirth, W. Waltenberger, and P. Vanlaer, "Vertex fitting in the CMS tracker,".

[136] K. Rose, "Deterministic annealing for clustering, compression, classification, regression, and related optimization problems," *Proceedings of the IEEE* **86** no. 11, (Nov, 1998) 2210–2239.

[137] R. Frühwirth, W. Waltenberger, and P. Vanlaer, "Adaptive Vertex Fitting," Tech. Rep. CMS-NOTE-2007-008, CERN, Geneva, Mar, 2007. https://cds.cern.ch/record/1027031.

[138] **CMS** Collaboration, "Jets at CMS and determination of their energy scale.," April, 2019. https://cms.cern/news/jets-cms-and-determination-their-energy-scale.

[139] G. C. Blazey *et al.*, "Run II jet physics," in *QCD and weak boson physics in Run II. Proceedings, Batavia, USA, March 4-6, June 3-4, November 4-6, 1999*, pp. 47–77. 2000. arXiv:hep-ex/0005012 [hep-ex]. http://lss.fnal.gov/cgi-bin/find_paper.pl?conf-00-092.

[140] G. P. Salam and G. Soyez, "A Practical Seedless Infrared-Safe Cone jet algorithm," *JHEP* **05** (2007) 086, arXiv:0704.0292 [hep-ph].

[141] Y. L. Dokshitzer *et al.*, "Better jet clustering algorithms," *JHEP* **08** (1997) 001, arXiv:hep-ph/9707323 [hep-ph].

[142] M. Cacciari, G. P. Salam, and G. Soyez, "The anti-k_t jet clustering algorithm," *JHEP* **04** (2008) 063, arXiv:0802.1189 [hep-ph].

[143] **CMS** Collaboration, "Jet algorithms performance in 13 TeV data," Tech. Rep. CMS-PAS-JME-16-003, CERN, Geneva, 2017. https://cds.cern.ch/record/2256875.

[144] **CMS** Collaboration, V. Khachatryan *et al.*, "Jet energy scale and resolution in the CMS experiment in pp collisions at 8 TeV," *JINST* **12** no. 02, (2017) P02014, arXiv:1607.03663 [hep-ex].

[145] **CMS** Collaboration, S. Chatrchyan *et al.*, "Determination of Jet Energy Calibration and Transverse Momentum Resolution in CMS," *JINST* **6** (2011) P11002, arXiv:1107.4277 [physics.ins-det].

[146] **CMS** Collaboration, "Pileup Removal Algorithms," Tech. Rep. CMS-PAS-JME-14-001, CERN, Geneva, 2014. https://cds.cern.ch/record/1751454.

[147] **CMS** Collaboration, H. Kirschenmann, "Jet performance in CMS," Tech. Rep. CMS-CR-2013-325, CERN, Geneva, Oct, 2013. https://cds.cern.ch/record/1627818.

[148] D. Bertolini, P. Harris, M. Low, and N. Tran, "Pileup Per Particle Identification," *JHEP* **10** (2014) 059, arXiv:1407.6013 [hep-ph].

[149] **CMS** Collaboration, S. Chatrchyan *et al.*, "Identification of b-quark jets with the CMS experiment," *JINST* **8** (2013) P04013, arXiv:1211.4462 [hep-ex].

[150] **CMS** Collaboration, A. M. Sirunyan *et al.*, "Identification of heavy-flavour jets with the CMS detector in pp collisions at 13 TeV," *JINST* **13** no. 05, (2018) P05011, arXiv:1712.07158 [physics.ins-det].

[151] D. Krohn, J. Thaler, and L.-T. Wang, "Jet Trimming," *JHEP* **02** (2010) 084, arXiv:0912.1342 [hep-ph].

[152] S. D. Ellis, C. K. Vermilion, and J. R. Walsh, "Recombination Algorithms and Jet Substructure: Pruning as a Tool for Heavy Particle Searches," *Phys. Rev.* **D81** (2010) 094023, arXiv:0912.0033 [hep-ph].

[153] A. J. Larkoski, S. Marzani, G. Soyez, and J. Thaler, "Soft Drop," *JHEP* **05** (2014) 146, arXiv:1402.2657 [hep-ph].

[154] M. Dasgupta, A. Fregoso, S. Marzani, and G. P. Salam, "Towards an understanding of jet substructure," *JHEP* **09** (2013) 029, arXiv:1307.0007 [hep-ph].

[155] **ATLAS** Collaboration, S. Schramm, "Searches for new physics using jet substructure in ATLAS and CMS," Tech. Rep. ATL-PHYS-PROC-2018-163, CERN, Geneva, Nov, 2018. https://cds.cern.ch/record/2648893.

[156] J. Thaler *et al.*, "Identifying Boosted Objects with N-subjettiness," *JHEP* **03** (2011) 015, arXiv:1011.2268 [hep-ph].

[157] V. Khachatryan *et al.*, "Identification techniques for highly boosted W bosons that decay into hadrons," *JHEP* **12** (2014) 017, arXiv:1410.4227 [hep-ex].

[158] J. Dolen, P. Harris, S. Marzani, S. Rappoccio, and N. Tran, "Thinking outside the ROCs: Designing Decorrelated Taggers (DDT) for jet substructure," *JHEP* **05** (2016) 156, arXiv:1603.00027 [hep-ph].

[159] **CMS** Collaboration, "A multi-dimensional search for new heavy resonances decaying to boosted WW, WZ, or ZZ boson pairs in the dijet final state at 13 TeV," Tech. Rep. arXiv:1906.05977. CMS-B2G-18-002-003, CERN, Geneva, Jun, 2019. http://cds.cern.ch/record/2678480. Submitted to EPJC. All figures and tables can be found at http://cms-results.web.cern.ch/cms-results/public-results/publications/B2G-18-002 (CMS Public Pages).

[160] **CMS** Collaboration, "Search for heavy resonances decaying to pairs of vector bosons in the l nu q qbar final state with the CMS detector in proton-proton collisions at sqrt s = 13 TeV," Tech. Rep. CMS-PAS-B2G-16-029, CERN, Geneva, 2017. http://cds.cern.ch/record/2296237.

[161] J. Ngadiuba, "Search for Diboson Resonances with CMS and Pixel Barrel Detector Calibration and Upgrade," Mar, 2017. https://cds.cern.ch/record/2646850. Presented 06 Apr 2017.

[162] T. Årrestad, "A novel multidimensional search for diboson resonances in the boosted dijet final state and encoding jet substructure with machine learning," Mar, 2019. Presented 14 Mar 2017.

[163] **CMS** Collaboration, "Tracking and Primary Vertex Results in First 7 TeV Collisions," Tech. Rep. CMS-PAS-TRK-10-005, CERN, Geneva, 2010. http://cds.cern.ch/record/1279383.

[164] C. M. POG, "MET Filter Recommendations for Run II," Juli, 2019. https://twiki.cern.ch/twiki/bin/viewauth/CMS/MissingETOptionalFiltersRun2.

[165] M. Cacciari, G. P. Salam, and G. Soyez, "FastJet User Manual," *Eur. Phys. J.* **C72** (2012) 1896, arXiv:1111.6097 [hep-ph].

[166] **CMS** Collaboration, C. Collaboration, "Pileup mitigation at CMS in 13 TeV data,".

[167] **CMS** Collaboration, A. M. Sirunyan *et al.*, "Performance of the CMS muon detector and muon reconstruction with proton-proton collisions at $\sqrt{s} = 13$ TeV," *JINST* **13** no. 06, (2018) P06015, arXiv:1804.04528 [physics.ins-det].

[168] **CMS** Collaboration, V. Khachatryan *et al.*, "Performance of Electron Reconstruction and Selection with the CMS Detector in Proton-Proton Collisions at $\sqrt{s} = 8$ TeV," *JINST* **10** no. 06, (2015) P06005, arXiv:1502.02701 [physics.ins-det].

[169] G. Punzi, "Sensitivity of searches for new signals and its optimization," *eConf* **C030908** (2003) MODT002, arXiv:physics/0308063 [physics]. [,79(2003)].

[170] **CMS** Collaboration, "Jet Performance in pp Collisions at 7 TeV," Tech. Rep. CMS-PAS-JME-10-003, CERN, Geneva, 2010. http://cds.cern.ch/record/1279362.

[171] **CMS** Collaboration, V. Khachatryan *et al.*, "Measurement of differential cross sections for top quark pair production using the lepton+jets final state in proton-proton collisions at 13 TeV," *Phys. Rev.* **D95** no. 9, (2017) 092001, arXiv:1610.04191 [hep-ex].

[172] S. Das, "A simple alternative to the Crystal Ball function," arXiv:1603.08591 [hep-ex].

[173] **CMS** Collaboration, "Search for massive resonances decaying into pairs of boosted W and Z bosons at $\sqrt{s} = 13$ TeV," CMS Physics Analysis Summary CMS-PAS-EXO-15-002, 2015. http://cds.cern.ch/record/2117062?ln=en.

[174] S. Kallweit, J. M. Lindert, P. Maierhöfer, S. Pozzorini, and M. Schönherr, "NLO electroweak automation and precise predictions for W+multijet production at the LHC," *JHEP* **04** (2015) 012, arXiv:1412.5157 [hep-ph].

[175] S. Kallweit, J. M. Lindert, P. Maierhöfer, S. Pozzorini, and M. Schöherr, "NLO QCD+EW predictions for V+jets including off-shell vector-boson decays and multijet merging," *JHEP* **04** (2016) 021, arXiv:1511.08692 [hep-ph].

[176] S. Kallweit, J. M. Lindert, S. Pozzorini, M. Schönherr, and P. Maierhöfer, "NLO QCD+EW automation and precise predictions for V+multijet production," in *Proceedings, 50th Rencontres de Moriond, QCD and high energy interactions*, p. 121. 2015. arXiv:1505.05704 [hep-ph]. https://inspirehep.net/record/1372103/files/arXiv:1505.05704.pdf.

[177] M. Cacciari, S. Frixione, M. L. Mangano, P. Nason, and G. Ridolfi, "The t anti-t cross-section at 1.8-TeV and 1.96-TeV: A Study of the systematics due to parton densities and scale dependence," *JHEP* **04** (2004) 068, arXiv:hep-ph/0303085 [hep-ph].

[178] S. Catani, D. de Florian, M. Grazzini, and P. Nason, "Soft gluon resummation for Higgs boson production at hadron colliders," *JHEP* **07** (2003) 028, arXiv:hep-ph/0306211 [hep-ph].

[179] A. Buckley, J. Ferrando, S. Lloyd, K. Nordström, B. Page, M. Rüfenacht, M. Schönherr, and G. Watt, "LHAPDF6: parton density access in the LHC precision era," *Eur. Phys. J.* **C75** (2015) 132, arXiv:1412.7420 [hep-ph].

[180] L. Demortier and L. Lyons, "Everything you always wanted to know about pulls," Tech. Rep. CDF/ANAL/PUBLIC/5776, CDF, 2002. http://physics.rockefeller.edu/luc/technical_reports/cdf5776_pulls.pdf.

[181] **ATLAS** Collaboration, "Search for diboson resonances in hadronic final states in 79.8 fb^{-1} of pp collisions at $\sqrt{s} = 13$ TeV with the ATLAS detector," Tech. Rep. ATLAS-CONF-2018-016, CERN, Geneva, Jun, 2018. https://cds.cern.ch/record/2621302.

[182] **ATLAS** Collaboration, G. Aad *et al.*, "Search for diboson resonances in hadronic final states in 139 fb^{-1} of pp collisions at $\sqrt{s} = 13$ TeV with the ATLAS detector," arXiv:1906.08589 [hep-ex].

[183] J. A. Aguilar-Saavedra, "Profile of multiboson signals," *JHEP* **5** (May, 2017) 66. https://doi.org/10.1007/JHEP05(2017)066.

[184] K. Agashe, J. H. Collins, P. Du, S. Hong, D. Kim, and R. K. Mishra, "Detecting a Boosted Diboson Resonance," *JHEP* **11** no. arXiv:1809.07334, (Sep, 2018) 027. 33 p. http://cds.cern.ch/record/2639898.

[185] O. Antipin, D. Atwood, and A. Soni, "Search for RS gravitons via $W_L W_L$ decays," *Phys. Lett. B* **666** (2008) 155, arXiv:0711.3175 [hep-ph].

[186] C. Grojean, E. Salvioni, and R. Torre, "A weakly constrained W' at the early LHC," *JHEP* **07** (2011) 002, arXiv:1103.2761 [hep-ph].

[187] E. Salvioni, G. Villadoro, and F. Zwirner, "Minimal Z' models: present bounds and early LHC reach," *JHEP* **11** (2009) 068, arXiv:0909.1320 [hep-ph].

[188] T. Sjöstrand, S. Ask, J. R. Christiansen, R. Corke, N. Desai, P. Ilten, S. Mrenna, S. Prestel, C. O. Rasmussen, and P. Z. Skands, "An introduction to PYTHIA 8.2," *Comput. Phys. Commun.* **191** (2015) 159, arXiv:1410.3012 [hep-ph].

[189] J. Alwall, S. Höche, F. Krauss, N. Lavesson, L. Lönnblad, F. Maltoni, M. L. Mangano, M. Moretti, C. G. Papadopoulos, F. Piccinini, S. Schumann, M. Treccani, J. Winter, and W. M., "Comparative study of various algorithms for the merging of parton showers and matrix elements in hadronic collisions," *Eur. Phys. J. C* **53** (2008) 473, arXiv:0706.2569 [hep-ph].

[190] P. Nason, "A new method for combining NLO QCD with shower Monte Carlo algorithms," *JHEP* **11** (2004) 040, arXiv:hep-ph/0409146 [hep-ph].

[191] S. Frixione, P. Nason, and C. Oleari, "Matching NLO QCD computations with parton shower simulations: the POWHEG method," *JHEP* **11** (2007) 070, arXiv:0709.2092 [hep-ph].

[192] S. Alioli, P. Nason, C. Oleari, and E. Re, "A general framework for implementing NLO calculations in shower Monte Carlo programs: the POWHEG BOX," *JHEP* **06** (2010) 043, arXiv:1002.2581 [hep-ph].

[193] S. Alioli, S.-O. Moch, and P. Uwer, "Hadronic top-quark pair-production with one jet and parton showering," *JHEP* **01** (2012) 137, arXiv:1110.5251 [hep-ph].

Danksagung

Zunächst möchte ich Prof. Dr. Thomas Müller dafür danken mir die Möglichkeit gegeben zu haben in seiner Arbeitsgruppe sowohl meine Promotion als auch Masterarbeit durchzuführen. Seine Unterstützung sowohl bei der Präsentation meiner Arbeit auf interressanten Konferenzen, als auch bei der Weiterbildung auf zahlreichen Schulen und Workshops die ich in meiner Zeit am Institut besuchen dürfte war jederzeit wertvoll. Im besonderen möchte ich mich für die Möglichkeit bedanken ein halbes Jahr am CERN in Genf zu verbringen, meinen Horizont zu erweitern und einzigartige Erfahrungen zu sammeln beim Austausch mit Physikern aus aller Welt.

Mein besonderer Dank gilt PD. Dr. Matthias Mozer, für die unermüdliche Betreuung, seine wissenschaftliche, moralische und organisatorische Unterstützung und die stete Beantwortung von Fragen und Problemen.

Desweiteren möchte ich den aktuellen Mitgliedern dieser Arbeitsgruppe meinen Dank aussprechen, fur die hervorragende Arbeitsatmosphähre am Institut, den regen Austausch von Ideen, Vorschlägen und Verbesserungen in den regelmässigen Gruppen-meetings und die stete Untersützung bei Fragen un Unklarheiten. Im besonderen möchte ich mich hier noch bei Prof. Dr. Thomas Müller, Dr. Roger Wolf, Dr. Thorsten Chwalek, Dr. Nils Faltermann, Denise Müller, Kevin Flöh und Darius Bühler bedanken für das unermüdliche Korrekturlesen dieser Arbeit.

PD. Dr. Roger Wolf möchte ich für die Übernahme meines Korreferats und die direkte Betreuung und die herzliche Aufnahme in seine Gruppe im letzten Jahr meiner Arbeit danken.

Ich möchte mich außerdem bei allen Mitgliedern des ETP bedanken, für die stets angenehme Arbeitsatmosphäre und insbesondere bei Frau Bräunling und dem Admin-Team, die für einen stets reibungslosen Ablauf im organisatorischen und technischen Bereich sorgten. Hier möchte ich mich besonders bei Matthias Schnepf bedanken, der für Probleme mit der Desktop-Cloud, mit der große Teile dieser Arbeit berechnet wurden, immer mit einer schnellen und zuverlässigen Lösung aufwarten konnte.

In addition, I want to thank the people in the CMS collaboration that contributed to this work, especially Dr. Jennifer Ngadiabu, Dr. Thea Årrestad, Dr. Clemens Lange, Prof. Dr. Andreas Hinzmann, Irene Zoi and Anna Benecke. My sincere thanks to you all, for the excellent collaboration.

Zuletzt möchte ich mich noch bei meinen Eltern bedanken, ohne deren stete Untersützung mein Studium, und damit diese Promotion, nicht möglich gewesen wäre.